

IMPERIAL

Spirals, defects, rolls and bands;
Transitional Rayleigh-Bénard Poiseuille flows
using spectral/ hp element methods

IMPERIAL COLLEGE LONDON
DEPARTMENT OF AERONAUTICS

Author:

Chi Hin Chan

Supervisor:

Professor Spencer J. Sherwin

Co-Supervisor

Professor Yongyun Hwang

April 2025

Ph.D. Thesis

Abstract

Contents

1	Introduction	6
1.1	Overview	6
1.2	Transitional wall-bounded shear flows	9
1.2.1	Linear Stability Analysis	9
1.2.2	Nonlinear dynamical systems	13
1.2.3	Spatiotemporal transitional flows	15
1.3	Rayleigh-Bénard convection	17
1.4	Rayleigh-Bénard Poiseuille (RBP) flows	22
1.4.1	Thesis Outline	25
2	Numerical Techniques	27
2.1	Method of weighted residuals	27
2.2	Galerkin Projection	29
2.3	Spectral/ <i>hp</i> element method	31
2.3.1	Domain partition	31
2.3.2	Standard Elements	31
2.3.3	Global assembly	33
2.3.4	Local basis expansions	35
2.3.5	Gaussian quadrature	38
2.3.6	Numerical differentiation	39
2.3.7	Example in 1D	40
2.4	Numerical techniques for solving the Navier-Stokes equations	42
2.4.1	Velocity Correction Scheme	42
2.4.2	Fourier spectral/ <i>hp</i> modes	44
2.4.3	Maintaining fluid flow through a channel	45
2.5	Stability analysis of the Navier-Stokes equations	49
2.5.1	Algorithms for linear stability analysis	49
2.5.2	Edge tracking	53
3	Transitional Rayleigh-Bénard Poiseuille flows	56
3.1	Introduction	56
3.1.1	Rayleigh-Bénard Poiseuille (RBP) flows	56

3.1.2	Rayleigh-Bénard convection (RBC)	57
3.1.3	Plane Poiseuille flows (PPF)	58
3.1.4	Objectives and organisation	58
3.2	Problem formulation	59
3.2.1	Governing equations	59
3.2.2	Numerical Methods	59
3.2.3	<i>Ra-Re</i> sweep	60
3.2.4	Linear Stability Analysis	60
3.3	<i>Ra-Re</i> Phase Space	61
3.3.1	Classification	61
3.3.2	Spatiotemporal intermittent rolls	63
3.3.3	Coexistence with turbulent bands	65
3.4	The role of longitudinal rolls	67
3.4.1	The thermally-assisted sustaining process (TASP) in a confined domain	67
3.4.2	Variation of <i>Ra</i> and <i>Re</i> on the thermally sustained turbulent process within $\Gamma = \pi/2$	74
3.4.3	Extending to large domains, $\Gamma = 4\pi$	78
3.5	Conclusions	81
4	The state space structure of Spiral Defect Chaos	83
4.1	Introduction	83
4.1.1	Multiple convection states	83
4.1.2	Spiral defect chaos	84
4.1.3	Scope of this study	85
4.2	Problem formulation	86
4.2.1	Rayleigh-Benard convection (RBC)	86
4.2.2	Numerical method	86
4.2.3	Linear stability analysis of ISRs	87
4.3	Transient SDC and elementary states in minimal domain	88
4.4	Multiplicity of edge states	94
4.5	Unstable ideal straight rolls	99
4.5.1	Pathways leading to ISRs - heteroclinic orbits	103
4.5.2	Pathways leading to elementary states	106
4.5.3	A pathway to SDC in an extended domain $\Gamma = 4\pi$	108
4.6	Concluding remarks	113
5	Conclusions	115
A	Appendices	116
A.1	Non-dimensionalisation	116
A.2	Governing equations for Rayleigh-Bénard convection	116

A.3	Projection methods for Navier-Stokes equations	117
A.4	Simulation parameters for Ra - Re sweep	118
A.5	First- and second-order statistics of the buoyancy- and shear-driven regime	120
A.5.1	Buoyancy-driven regime	120
A.5.2	Shear-driven regime	120
A.6	Growth rates of primary instabilities	124
A.7	Verification of linear stability analysis	124
A.8	Other elementary states and ISRs	125

Chapter 1

Introduction

1.1 Overview

Fluid motions driven by buoyancy and frictional forces belongs to broad class of flows known as thermoconvective shear flows. These flows exhibit rich behaviour, and are of interest in both engineering and meteorology applications spanning across a broad range of length scales. At small scales, around $L \sim 1\text{cm}$, the thermoconvection flows are relevant to the cooling of microprocessing chips. In such systems, the fluid acts medium to dissipate heat, experiences shear forces from the confining walls, and buoyancy from heating. One of the major innovation in this industry is in squeezing more transistors onto a single chip, resulting to a doubling of transistors on a single chip roughly every two years, according to Moore's law. However, one of the major limitations on further miniaturisation is the challenge of dissipating the excessive heat generated. Fluids, such as air, water or refrigerant, are often used to transport heat away from the components, thereby preventing overheating [Kennedy and Zebib, 1983, Ray and Srinivasan, 1992]. At intermediate length scales, $L \sim 1\text{m}$, the interaction between buoyancy and frictional forces is important in the fabrication of uniform thin films in chemical vapour deposition (CVD) [Evans and Greif, 1991, Jensen et al., 1991]. The CVD process typically involves a reactive gases carried by inert gases which flows through a channel with a heated substrate. Upon heating, the reactant gases react chemically at substrate and deposits material, forming thin films, such as silicon layers. A key challenge in the CVD process is achieving a uniform deposition and maintaining sharp interfaces between layers. The interactions between shear and buoyancy forces often gives rise to boundary layers and thermoconvective rolls, which can disrupt uniform deposition, affecting film quality. At large scales, $L \sim 1\text{km}$, the thermoconvective shear flows can be observed in the atmosphere such as the cloud streets over the Norwegian Sea. These parallel bands of cumulus clouds can stretch over hundreds of kilometres. They form when relatively warm sea surfaces heat up the colder air blowing from the North [nor]. As the colder air is heated, it rises upwards whilst carrying water vapour. As it reaches a certain altitudes, $L \sim 1 - 10\text{km}$, the water vapour condenses into visible clouds, while the cooler air falls towards the sea. This circulation is organised into parallel rotating parallel columns of air, forming distinct cloud streets.

The common thread among the examples discussed above is the interaction between shear and buoyancy forces driven fluid motion - the central focus of this thesis. By restricting our analysis to these

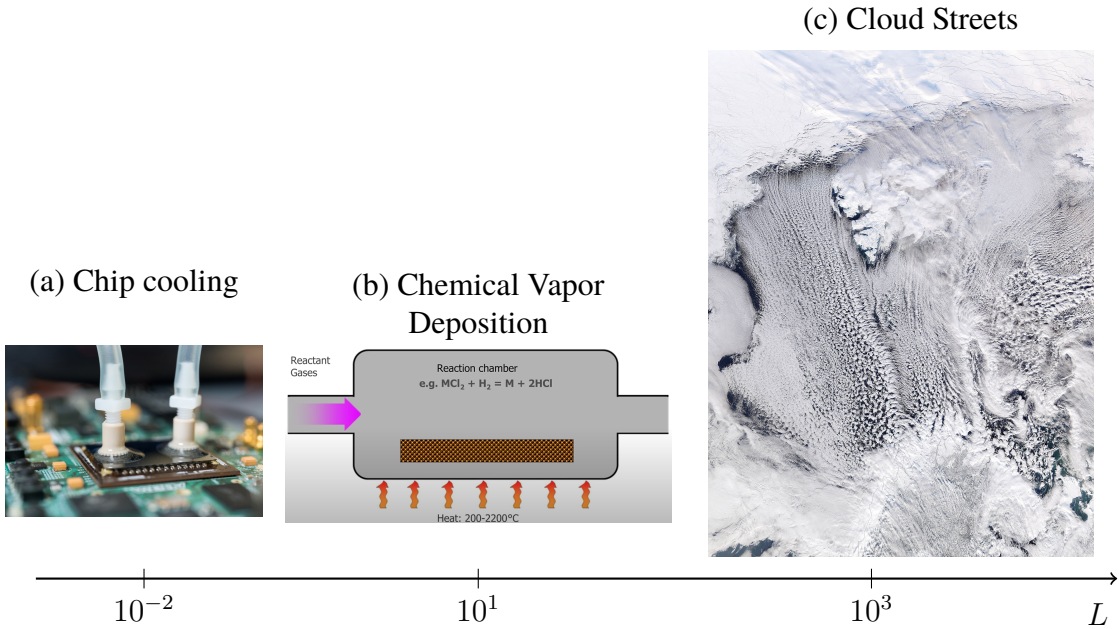


Figure 1.1: Fluid flow due to shear and buoyancy forces across length scales, $L \in [1\text{cm}, 1\text{km}]$, such as (a) chip cooling, (b) chemical vapour deposition and (c) formation of cloud streets.

two mechanisms, we neglect other physical mechanisms such as phase change, chemical reactions and evaporation, which may be significant in the context of cooling microprocessors, chemical vapour deposition, and atmospheric boundary layers respectively [Vallis et al., 2019]. To consider this interaction, we consider an idealised setup without geometric complexity, known to as the Rayleigh-Bénard-Poiseuille (RBP) flow. This system describes the fluid motion confined between two infinitely extended parallel plates, heated from below and cooled from the top, with an additional pressure gradient driving the flow. The RBP configuration combines two paradigmatic flow configurations; the classical Rayleigh-Bénard convection (RBC), driven purely by buoyancy, and plane Poiseuille flow (PPF), driven purely by shear. While the onset of convection in RBC, and the transition to subcritical shear-driven turbulence in PPF have been both extensively studied, the transitional regime in which both forces interact remains less understood. Gaining insights into this regime can have implications for various applications across a range of scales mentioned previously.

The RBP configuration is illustrated in figure 1.1, where $z^*, y^*, x^*, L_z, L_x, d, h$ refer to the streamwise, spanwise, wall-normal coordinates, length, span, depth and half-height of the domain respectively. We note that the asterisks*, refer to variables in dimensional form. The flow is driven by a pressure gradient along the streamwise z^* direction, $\Delta P^* = P^*|_{z^*=0} - P^*|_{z^*=L_z} < 0$, leading to the formation of a laminar Poiseuille flow, $w^*(y^*)$, for a sufficiently small ΔP . In this study, we will only consider fully-developed flow, where the boundary layer from the top and the bottom wall meets at the midplane, $y^* = 0$, and entrance effects are neglected. The RBP configuration is also unstably stratified, such that the temperature difference between the lower, T_L , and upper wall, T_U , is always positive, $\Delta T = T_L - T_U > 0$, leading to a stable linear conduction profile along the wall-normal direction, $T(y^*)$, if ΔT is kept sufficiently small.

In the absence of a pressure gradient, the RBP configuration reduces to the classical Rayleigh-

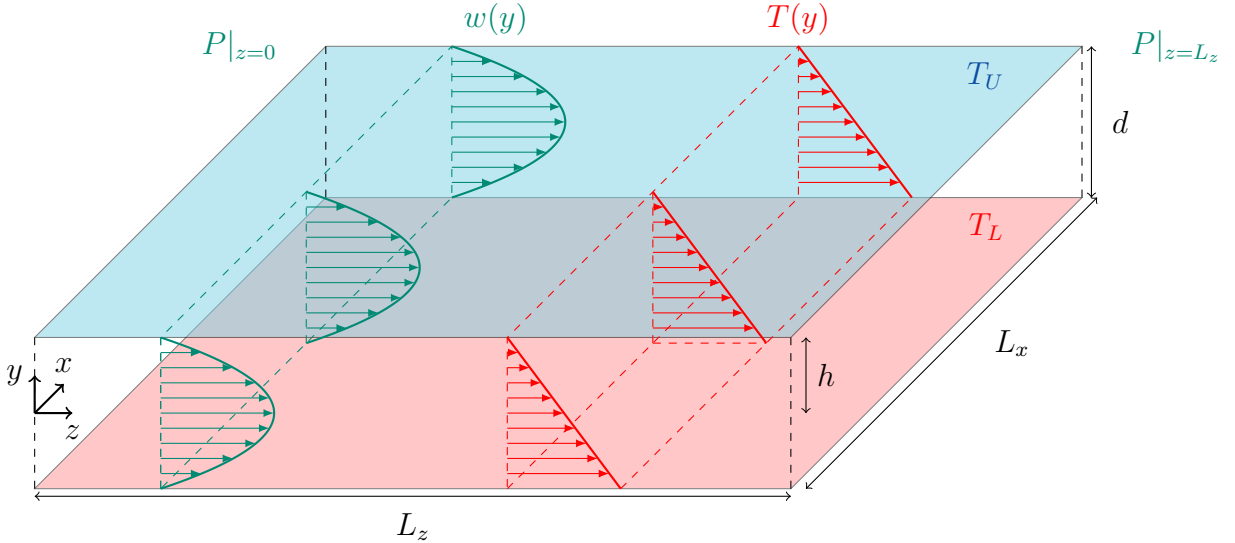


Figure 1.2: The Rayleigh-Bénard Poiseuille (RBP) flow configuration.

Bénard convection problem, bringing about buoyancy-driven convection for a sufficiently large unstable stratification. In the limiting case without unstable stratification, $\Delta T = 0$, the system reduces to the wall-bounded plane Poiseuille flow (PPF), where the transition towards subcritical shear-driven turbulence may be expected for a sufficiently large pressure gradient.

For instance, do buoyancy forces promote the transition to shear-driven turbulence and how does shear influence the convection? To describe the motion of the fluid in RBP configurations, we consider non-dimensionalised Navier-Stokes equations with Boussinesq approximations,

$$\frac{\partial \mathbf{u}}{\partial t} + (\mathbf{u} \cdot \nabla) \mathbf{u} = -\nabla p + \frac{1}{Re} \nabla^2 \mathbf{u} + \frac{Ra}{Re^2 Pr} \theta, \quad (1.1a)$$

$$\frac{\partial \theta}{\partial t} + (\mathbf{u} \cdot \nabla) \theta = \frac{1}{Re Pr} \nabla^2 \theta, \quad (1.1b)$$

$$\nabla \cdot \mathbf{u} = 0. \quad (1.1c)$$

where $\mathbf{u}(\mathbf{x})$, $\theta(\mathbf{x})$, $p(\mathbf{x})$ refers to the nondimensionalised velocity, temperature and pressure respectively. The key control parameters for RBP flows are the Rayleigh number, Ra , Reynolds number, Re , Prandtl number Pr , which are defined as follows,

$$Ra = \eta g d^3 \Delta T / \nu \kappa, \quad Re = W_c h / \nu, \quad Pr = \kappa / \nu, \quad \Gamma = L / 2d, \quad (1.2)$$

where η , g , ΔT , ν , κ , W_c , h , d , L are the thermal expansion coefficient, acceleration due to gravity, temperature difference between the bottom and top wall, kinematic viscosity, thermal diffusivity, laminar centreline velocity, domain's half-depth, full-depth, length or span respectively.

We describe important historical of hydrodynamic stability of planar shear flows and their theoretical frameworks in §1.2. Theoretical frameworks used in the study of stability of flow such as linear stability, nonlinear dynamical systems and spatiotemporal character of transitional shear flows

will be outlined. This followed the historical developments of Rayleigh-Bénard convection (RBC), where concepts of the stability of fluid flows will be utilised in §1.3. After which, we describe the historical developments of RBP flows §1.4, and the outline of the thesis will be give in §1.4.1.

1.2 Transitional wall-bounded shear flows

Wall-bounded shear flows concerns the motion of the fluid flowing in parallel to walls, typically bounded by one or more walls. The fluid closest to the wall comes to a rest, satisfying the no-slip boundary condition in the presence of a wall. As a consequence, a velocity gradient in the direction perpendicular from the wall develops, where the fluid layer becomes *sheared* due to the presence of the wall - referred to wall-bounded sheared flows. Example of wall-bounded shear flows include the pressure-driven plane Poiseuille flow (or channel flow), Hagen-Poiseuille (or pipe) flows, plane Couette flow and flat plate boundary layers. These geometrically simple examples enables a convenient framework amenable to the mathematical analysis of fluid motion subjected to shear. Depending on the degree of shear, the fluid motion can be either laminar, where the fluid layers move in smooth parallel 'laminates', or turbulent, characterised by chaotic eddying motions. We also note that there is a transitional regime where both states can coexist discuss later. A central question is predicting the transition from the laminar regime to the turbulence.

The earliest investigation into this transition dates back to the pipe flow experiments of [Reynolds \[1883\]](#). In his experimental setup, the flow speed through the pipe could be controlled by regulating the inlet pressure, while injecting dye to visualise the flow, as illustrated in figure 1.3(a). At low speeds, the fluid remained laminar, resulting to a single streak of steady dye in figure 1.3(b). As the speed increased, the dye begin to exhibit irregular 'sinuous' motions interspersed with laminar regions shown in figure 1.3(c). This is now referred to as the transitional/intermittent regime, alternating between the laminar and turbulent states. Beyond a critical speed, the dye breaks down entirely into chaotic 'eddies', mixing with the surrounding fluid and discolouring the flow with dye downstream in figure 1.3(d). This regime is now identified as turbulence.

Reynolds conjectured that the threshold between the laminar, transitional and turbulent regimes could be characterised by the Reynolds number, $Re = UD/\nu$, where U is the centerline velocity in the pipe, D , the pipe diameter and ν , the kinematic viscosity. He observed that flow through the pipe remained 'stable' and laminar for $Re < 1900$, while it became 'unstable' and turbulent for $Re > 2000$ [[Reynolds, 1895](#)]. His remarks led to the concept of the stability of fluid flows.

1.2.1 Linear Stability Analysis

Following Reynolds' experiment, interest towards the mathematical analysis of the stability of fluid flows grew in early 20st century. The mathematical approach typically begins by decomposing the velocity field, $\mathbf{u}(\mathbf{x}, t)$, into a laminar (base) state, $U(y)$ (assumed to depend only on the wall-normal direction here), and the velocity perturbations, $\mathbf{u}'(\mathbf{x}, t)$, with pressure similarly decomposed as,

$$\mathbf{u}(\mathbf{x}) = U(y) + \mathbf{u}'(\mathbf{x}, t), \quad \text{and} \quad p(\mathbf{x}, t) = P(x) + p'(\mathbf{x}, t). \quad (1.3)$$

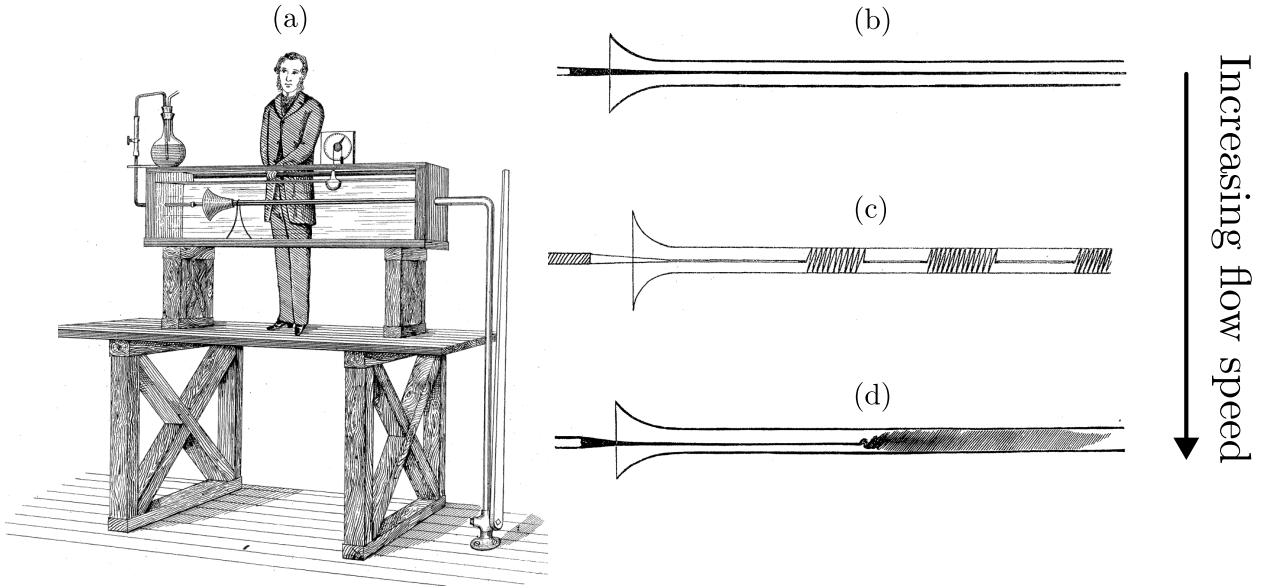


Figure 1.3: (a) Osbourne Reynolds pipe experiment with the dye injection apparatus, illustrating the (b) laminar flow, (c) intermittent regime and (d) turbulent flow as the flow speed is increased, taken from [Reynolds, 1883].

Next, we substitute the formulations for the decomposed velocity and pressure into the Navier-Stokes equations of equation (1.1) and drop the nonlinear perturbations terms $(\mathbf{u}' \cdot \nabla)\mathbf{u}'$,

$$\frac{\partial \mathbf{u}'}{\partial t} + (\mathbf{U} \cdot \nabla) \mathbf{u}' + (\mathbf{u}' \cdot \nabla) \mathbf{U} = -\nabla p' + \frac{1}{Re} \nabla^2 \mathbf{u}', \quad (1.4a)$$

$$\nabla \cdot \mathbf{u}' = 0, \quad (1.4b)$$

resulting to the linearised Navier-Stokes equations. This commonly followed by introducing a wavelike ansatz (mode) defined by streamwise and spanwise wavenumbers, α, β and complex frequency, ω . In general two ways to analyse the linearised Navier-Stokes equations by considering the behaviour of each mode independently in §1.2.1 and their coupled dynamics in §1.2.1

Modal analysis

It is convenient to eliminate the pressure terms by transforming equation (1.4) using the wall-normal perturbation velocity, v' , and wall-normal vorticity, $\eta' = \partial u'/\partial z - \partial w'/\partial x$, variables. Using (v, η) , introduce an ansatz (mode) for them,

$$v'(\mathbf{x}, t) = \tilde{v}(y) e^{i(\alpha x + \beta z - \omega t)}, \quad \text{and} \quad \eta'(\mathbf{x}, t) = \tilde{\eta}(y) e^{i(\alpha x + \beta z - \omega t)}. \quad (1.5)$$

where α, β, ω denotes the streamwise and spanwise wavenumbers, and complex frequency (i.e. $\omega = \omega_r + i\omega_i$), respectively. Next, we substitute the ansatz into equation 1.4, leading to the classical Orr-Sommerfeld and Squire equations [Orr, 1907, Sommerfeld, 1909, Squire, 1933, Schmid and

[Henningson, 2001](#)],

$$\left[-i\omega \begin{pmatrix} k^2 - \mathcal{D}^2 & 0 \\ 0 & 1 \end{pmatrix} + \begin{pmatrix} \mathcal{L}_{OS} & 0 \\ i\beta U' & \mathcal{L}_{SQ} \end{pmatrix} \right] \begin{pmatrix} \tilde{v} \\ \tilde{\eta} \end{pmatrix} = 0, \quad (1.6)$$

where \mathcal{L}_{OS} and \mathcal{L}_{SQ} refers to the Orr-Sommerfeld and Squire operators given as,

$$\mathcal{L}_{OS} = i\alpha U(k^2 - \mathcal{D}^2) + i\alpha U'' + \frac{1}{Re}(k^2 - \mathcal{D}^2)^2, \quad (1.7a)$$

$$\mathcal{L}_{SQ} = i\alpha U + \frac{1}{Re}(k^2 - \mathcal{D}^2). \quad (1.7b)$$

$k^2, \mathcal{D}, U', U''$ denotes the sum of squared wavenumbers, $k^2 = \alpha^2 + \beta^2$, differential operator in y , first- and second- derivative of the laminar velocity, respectively. Equation (1.6) is simply an eigenvalue problem which could be represented as,

$$\mathbf{L}\tilde{\mathbf{q}} = i\omega \mathbf{M}\tilde{\mathbf{q}} \quad (1.8)$$

where,

$$\mathbf{L} = \begin{pmatrix} \mathbf{L}_{OS} & 0 \\ i\beta U' & \mathcal{L}_{SQ} \end{pmatrix}, \quad \mathbf{M} \begin{pmatrix} k^2 - \mathcal{D}^2 & 0 \\ 0 & 1 \end{pmatrix}, \quad \tilde{\mathbf{q}} = \begin{pmatrix} \tilde{v} \\ \tilde{\eta} \end{pmatrix}. \quad (1.9)$$

and $i\omega$ refers to the eigenvalue. The aim of linear stability analysis is to determine the critical Reynolds number, Re_c , which is defined as the lowest value of Re over α and β , such that $Im[\omega] = 0$. For $Re > Re_c$, perturbations could grow exponentially, departing from the laminar state. In other words, we consider the behaviour of each $\alpha - \beta$ mode independently, herein referred to as *modal* analysis. Squire's theorem implies that for any unstable three-dimensional perturbations, $\beta \neq 0$, there exist an unstable two-dimensional perturbation, $\beta = 0$ with a lower Re_c [[Squire, 1933](#)]. Therefore, the unstable perturbations of wall-bounded shear flows at Re_c must be two-dimensional. The theoretical calculations was first perform by [Tollmien \[1928\]](#) and [Schlichting \[1933\]](#) for a flat-plate boundary layer flow, yielding a critical Reynolds number based on streamwise distance x of $Re_{x,c} = Ux_c/\nu = 520$ [[Schlichting and Gersten, 2017](#)]. In their honour, the unstable two-dimensional perturbations of the Orr-Sommerfeld operator is referred to as Tollmien-Schlichting (T.S) waves. For plane Poiseuille flow [[Orszag, 1971](#)] with a critical wavenumber of $\alpha_c = 1.02$. However, turbulence in plane Poiseuille flows have been observed at much lower Reynolds number, $Re \sim 1000 - 2000$, contradicting the results from linear stability analysis. Likewise, the onset of turbulence appear near $Re_{x,c} \approx 5 \times 10^5$ for flat plat boundary layer. A similar result holds for the plane Couette flow [[Meseguer and Trefethen, 2003](#)]. Despite its limitation, linear analysis analysis succeeds in predicting the critical Rayleigh number in Rayleigh-Bénard convection.

Non-modal stability

One of a major limitation of linear stability analysis considered above is that it treats each eigenmode independently, referred to as *modal* analysis. However, the interaction between decaying eigenmodes

may lead to a short-term amplification of perturbations, before eventually decaying. This phenomenon is referred to as *transient growth*, and the method of analysis is referred to as *non-modal* analysis, related to the normality of the linear Orr-Sommerfeld operator [Schmid, 2007]. To demonstrate an

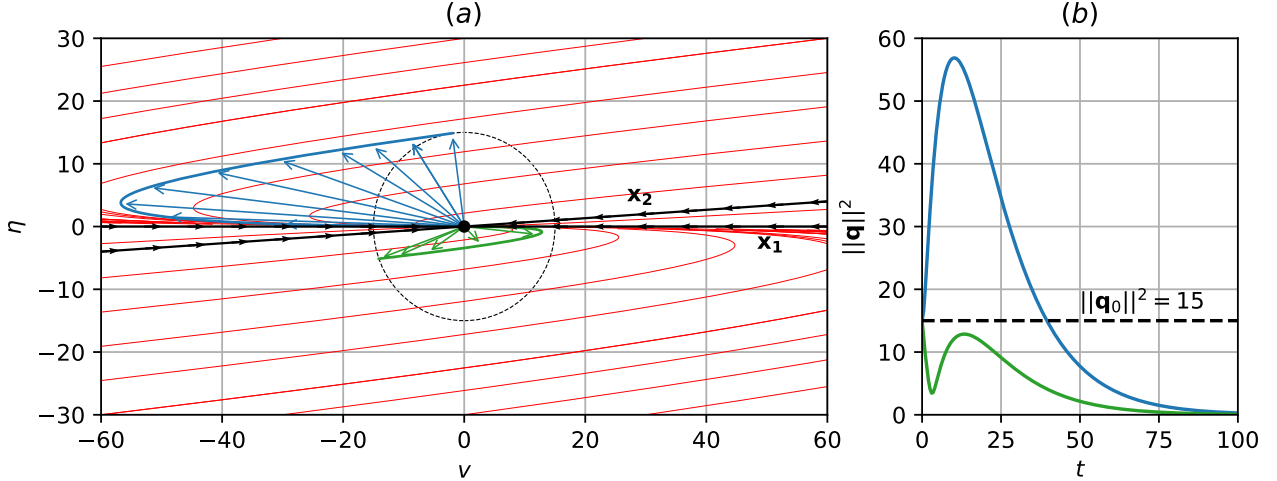


Figure 1.4: (a) The phase portrait of the toy model with $Re = 15$, (b) Transient growth.

example of transient growth, we consider a two-dimensional toy model governing the time-evolution of \mathbf{q} ,

$$\frac{d}{dt} \begin{pmatrix} v \\ \eta \end{pmatrix} = \begin{pmatrix} -\frac{1}{Re} & -1 \\ 0 & -\frac{2}{Re} \end{pmatrix} \begin{pmatrix} v \\ \eta \end{pmatrix}, \quad (1.10)$$

where Re refers to the Reynolds number. The toy model has negative eigenvalues, $(\lambda_1, \lambda_2) = (-1/Re, -2/Re)$, and unit eigenvectors $\mathbf{x}_1 = (1, 0)$, $\mathbf{x}_2 = \frac{1}{\sqrt{Re^2+1}}(Re, 1)$. Judging from the negative eigenvalues, we conclude that $\mathbf{q}(t)$ will decay exponentially. However, as $Re \rightarrow \infty$, they become increasingly non-orthogonal approaching each other such that the angle between \mathbf{x}_1 and \mathbf{x}_2 tends towards 0. At $Re = 15$, the eigenvector pairs, \mathbf{x}_1 and \mathbf{x}_2 , are highly non-orthogonal, becoming almost linearly dependent shown in figure 1.4(a). For a randomly selected initial condition with an energy-norm of $\|\mathbf{q}_0\|_2 = 15$, where $\|\cdot\|_2$ refers to the L2-norm, the trajectory in green decays exponentially for $t \in [0, 100]$ in figure 1.4(b). In contrast, for a specifically chosen initial condition shown as the blue trajectory, $\|\mathbf{q}\|_2$ is amplified nearly four times before decaying exponentially. The toy model demonstrates the significance of transient growth for a specifically chosen initial condition.

The goal of non-modal stability analysis is to search over all initial conditions, $\tilde{\mathbf{q}}_0$, leading to the maximum amplification factor at time t , resulting in an optimisation problem,

$$G(t) = \max_{\tilde{\mathbf{q}}_0 \neq 0} \frac{\langle \tilde{\mathbf{q}}(t), \tilde{\mathbf{q}}(t) \rangle}{\langle \tilde{\mathbf{q}}_0, \tilde{\mathbf{q}}_0 \rangle}, \quad \text{s.t. } \langle \tilde{\mathbf{q}}_0, \tilde{\mathbf{q}}_0 \rangle = 1, \quad (1.11)$$

where, $\langle \cdot, \cdot \rangle$ refers to the inner-product defined as,

$$\langle \mathbf{x}, \mathbf{y} \rangle = \int_{\Omega} \mathbf{x}^H \mathbf{y} \, d\Omega, \quad (1.12)$$

and \mathbf{x}^H refers to the complex conjugate transpose of \mathbf{x} . By considering the linearised operator of (1.6), we can define a linear time invariant operator given as,

$$\tilde{\mathbf{q}}(t) = \mathcal{A}(t)\tilde{\mathbf{q}}_0, \quad (1.13)$$

which takes the solution from initial conditions, $\tilde{\mathbf{q}}_0$, to $\tilde{\mathbf{q}}(t)$ at time t . Substituting the expression above into equation (1.11),

$$G(t) = \max_{\tilde{\mathbf{q}}_0 \neq 0} \frac{\langle \mathcal{A}(t)\tilde{\mathbf{q}}_0, \mathcal{A}(t)\tilde{\mathbf{q}}_0 \rangle}{\langle \tilde{\mathbf{q}}_0, \tilde{\mathbf{q}}_0 \rangle} = \langle \tilde{\mathbf{q}}_0, \mathcal{A}^\dagger(t)\mathcal{A}(t)\tilde{\mathbf{q}}_0 \rangle = \lambda_{max}(\mathcal{A}^\dagger\mathcal{A}) \quad (1.14)$$

where $\mathcal{A}^\dagger(t)$ refers to the adjoint of $\mathcal{A}(t)$. The maximum amplification factor $\max G(t)$ is the largest eigenvalue, λ_{max} , of $\mathcal{A}^\dagger\mathcal{A}$, and the eigenvalue problem is given as,

$$\mathcal{A}^\dagger(t)\mathcal{A}(t)\tilde{\mathbf{q}}_0 = \lambda\tilde{\mathbf{q}}_0, \quad (1.15)$$

where $\tilde{\mathbf{q}}_0$ refers to the eigenvector denoting the optimal initial condition. For a detailed derivation of the optimal initial conditions or forcing, the reader is referred to [Butler and Farrell, 1992, Schmid, 2007]. An alternative method of computing transient growth is computing the pseudospectral of linear operators discussed in [Trefethen, 1997], outside the scope of this thesis.

Both two-dimensional, $\beta = 0$, and three-dimensional, $\beta \neq 0$, non-modal stability analysis have been studied.

In the two-dimensional form, the optimal initial conditions are in the form of near wall vortices tilted upstream, transiently energised referred to as the Orr-mechanism [Orr, 1907, Farrell, 1988, Reddy et al., 1993]. In the three-dimension form, streamwise vortices, acting as optimal initial conditions lead to the optimal response in the form of streamwise streaks [Reddy and Henningson, 1993]. Contrary to linear stability analysis which confers two-dimensional perturbations as linearly unstable, the key result in this analysis is that three-dimensional initial conditions, $\alpha = 0$, confer the optimal initial conditions leading to large transient growth at subcritical Reynolds numbers. Figure.. shows this.

The width of the streaks happen to be robustly occur around 100 wall units, the characteristics spacing identified in many experiments [Kline, Panton, Bandyopadhyay]

The optimal initial conditions involve streamwise vortices which amplify streaks, related to the lift-up effect [Ellingsen and Palm, 1975, Brandt, 2014]. These modal and nonmodal mechanisms above highlight developments based on linear methods.

1.2.2 Nonlinear dynamical systems

In the previous section, we have examined the transition process based linear mechanisms. Unfortunately, for canonical shear flow configurations, the transition process is subcritical where linear stability theory fails to predict the onset of turbulence. Furthermore, the transition to turbulence is ultimately governed fully nonlinear nature of the Navier-Stokes equations. Hence, we turn to a nonlinear dynamical systems point of view of this transition process, inspired from Hopf's vision

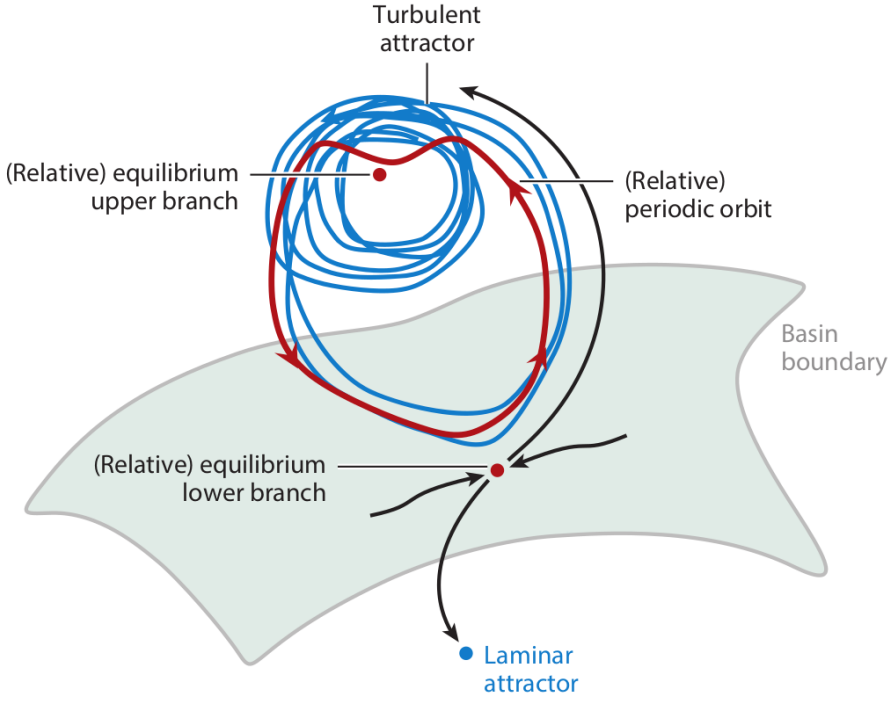


Figure 1.5: The state space organising of the upper and lower branch. Turbulence is interpreted as solution trajectories wander around the upper branch, orbiting around a network unstable invariant states. The lower branch acts as a boundary between the turbulent attractor and laminar attractor, an attractor on the edge referred to as the edge state. Taken from [Graham and Floryan, 2021].

of transition, where turbulence emerge as a chaotic trajectory after succeeding Hopf bifurcations.. [CHECK THIS DESCRIPTION...] However, this bifurcation cannot happen in the subcritical In this view, turbulence is interpreted as a solution trajectory evolving through a phase space composed of a network such non-trivial nonlinear solutions, commonly referred to as exact coherent states (ECS) or invariant solutions [Graham and Floryan, 2021].

In the context of parallel shear flows, Nagata was the first to discover a pair of unstable equilibrium solutions in plane Couette flow by smoothly following (homotopy) from a Taylor-Couette configuration [Nagata, 1990]. This pair consist of an unstable upper branch and lower branch emerging as a saddle-node bifurcation near $Re \approx 500$, and is disconnected from the stable laminar solution. The lower branch refers to its proximity towards the stable laminar state in phase space. A travelling-wave solution in plane Couette flow also later found by the same author [Nagata, 1997]. A family of equilibrium and travelling waves solutions was found for plane Couette and plane Poiseuille flows under various boundary conditions (i.e. stress-free, slip and no-slip) where identified by [Waleffe, 2001, 2003].

While these unstable solutions demonstrate good agreements with results from DNS such as the spanwise length scales, and mean and fluctuations, they do not capture the dynamical processes. Periodic orbits defined by time-dependent solutions that have been identified in plane Couette flow [Kawahara and Kida, 2001], describing a single regeneration cycle similar to the self-sustaining process. The chaotic trajectories of turbulence have been found to be embedded within invariant

solutions and their connections between them known as heteroclinic orbits, offering a robust view of the building-blocks of turbulence [Gibson et al., 2008, 2009, Viswanath, 2007, Halcrow et al., 2009, Graham and Floryan, 2021]

In the context of this transitional flows, the lower branch solution can be thought of separating the turbulent attractor from the laminar state. It's an attractor that resides on the edge of turbulence, defined as an edge state. The graphical representation of this edge is shown in figure 1.5.

These invariant solutions commonly take the form of equilibria, travelling waves, periodic and relative periodic orbits. It is well established that coherent motions defined by flow patterns that persist in space and time play an important role in the transport of momentum and heat. In parallel shear flows, these coherent structures typically appear as near-walls streaks and quasi-streamwise rollers. A persistent, quasi-periodic cycle between the regeneration of streaks and rolls, referred to as the *self-sustaining process*, appears to be a fundamental mechanism in sustaining wall-bounded turbulence *self-sustaining process* [Hamilton et al., 1995]. This mechanism is described by the generation of streaks due to quasi-streamwise rollers by redistributing the mean. These streaks become linearly unstable and breakdown, and through a nonlinear process regenerates the quasi-streamwise rollers, closing the cycle.

1.2.3 Spatiotemporal transitional flows

This section describes the inherent spatiotemporal intermittent description of turbulence in transitional wall-bounded shear flows commonly reported in large extended domains where the span is about fifty times the half-height of a plane Poiseuille channel, $L/h \gtrsim 50$. In this regime, turbulence is characterised by the coexistence of turbulent and laminar structures. Examples of such are found in canonical shear flow systems such as plane Couette flows [Prigent et al., 2003, Barkley and Tuckerman, 2005, 2007, Tuckerman and Barkley, 2011, Duguet et al., 2010, Reetz et al., 2019], Taylor-Couette flows [Prigent and Dauchot, 2002, Prigent et al., 2003], pipe flows [Avila et al., 2010, 2011, Song et al., 2017, Avila et al., 2023] and plane Poiseuille flows [Tsukahara et al., 2014a,c, Tuckerman et al., 2014, Tsukahara et al., 2014b, Gomé et al., 2020, Paranjape, 2019, Paranjape et al., 2020, 2023].

We will focus on the plane Poiseuille flow configuration, where the spatiotemporal intermittent patterns are referred to as oblique turbulent-laminar bands illustrated in figure 1.6 at $Re = 1400$ for $L/h = 16\pi$. The bright and dark regions highlights coexisting spatially localised turbulent and laminar regions. These turbulent-laminar bands occur over a range of Reynolds numbers, and its precise range is likely dependent on the domain's aspect ratio [Tsukahara et al., 2014b, Tuckerman et al., 2014, Paranjape et al., 2023]. Near the upper Re threshold of this regime, the domain is fully engulfed by developed turbulent regions, referred to uniform, featureless turbulence appearing at $Re = 1800$ in figure 1.6(a). As Re decreases towards $Re = 1050$, turbulent-laminar bands persist in figures 1.7(b-f). In this region, turbulent-laminar bands angles have been observed to be inclined between $20^\circ \sim 30^\circ$, with streamwise wavelengths of $\sim 60h$, and spanwise wavelengths of $\sim 20h - 30h$ [Tsukahara et al., 2014b]. To study the preference of angles, zzz performed linear stability analysis of bands and showed that preferred angle at .. degrees. Below certain Re threshold, the spatially turbulent regions spontaneously decay where the flow relaminarises asymptotically [Tuckerman et al.,

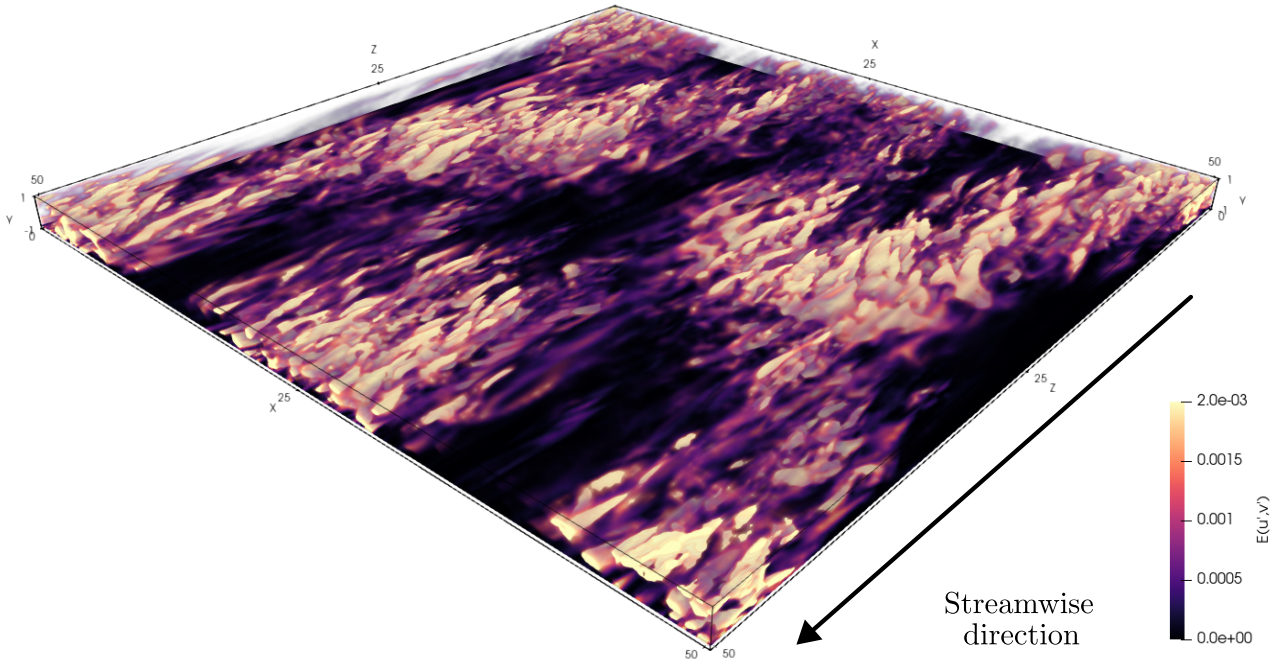


Figure 1.6: A snapshot of turbulent-laminar bands at $Re = 1400$ in a large domain $L/d = 8\pi$, depicting its spatiotemporal intermittent nature. Isovolumetric renderings are based on the spanwise, u' , and wall-normal, v' , perturbation kinetic energy, $E(u', v') = 1/2(u'^2 + v'^2)$, where the perturbation velocities are defined about the laminar state $\mathbf{u}'(\mathbf{x}, t) = \mathbf{u}(\mathbf{x}, t) - U_{lam}(y)$.

2014]. This decay is shown in $Re = 1000$ near $t = 1600$ in figure 1.7(g).

Inspired from previous studies of turbulent-laminar bands in plane Couette flows [Barkley and Tuckerman, 2005, Reetz et al., 2019], narrow domains, titled orthogonally to the band angles were considered to investigate their dynamics [Tuckerman et al., 2014, Paranjape et al., 2020, 2023]. In narrow-tilted domains inclined at 24° , the turbulent-bands convect at about $\sim 1\%$ of the bulk velocity, propagating either upstream or downstream, above or below a critical $Re \sim 1000$, independent of domain sizes for $L_z \geq 100h$ [Tuckerman et al., 2014, Gomé et al., 2020]. The characteristic spanwise wavelengths of turbulent-laminar bands are dependent on Re , appearing at $\lambda_z \sim 20h$ for $Re \geq 1400$ and $\lambda_z \sim 40h$ for $Re \leq 1100$. Indeed, between $1300 < Re < 1400$ the bands appear to alternate between two different band-widths [Tuckerman et al., 2014], merging and splitting continuously. This points towards a band splitting event in between $Re = 1100$ and $Re = 1400$, reminiscent of a puff splitting in pipe flows [Avila et al., 2011].

On the other hand, turbulent bands appear to decay at $Re = 830$ [Gomé et al., 2020], and at $re = 1100$ but surviving for $re = 1000$ [Tuckerman et al., 2014], suggesting that turbulent bands decay spontaneously. [Gomé et al., 2020] computed the probability distributions of turbulent band decay, $P(\Delta t^d)$, where Δt^d refers to the time it takes for decay. One of the key insights is that the

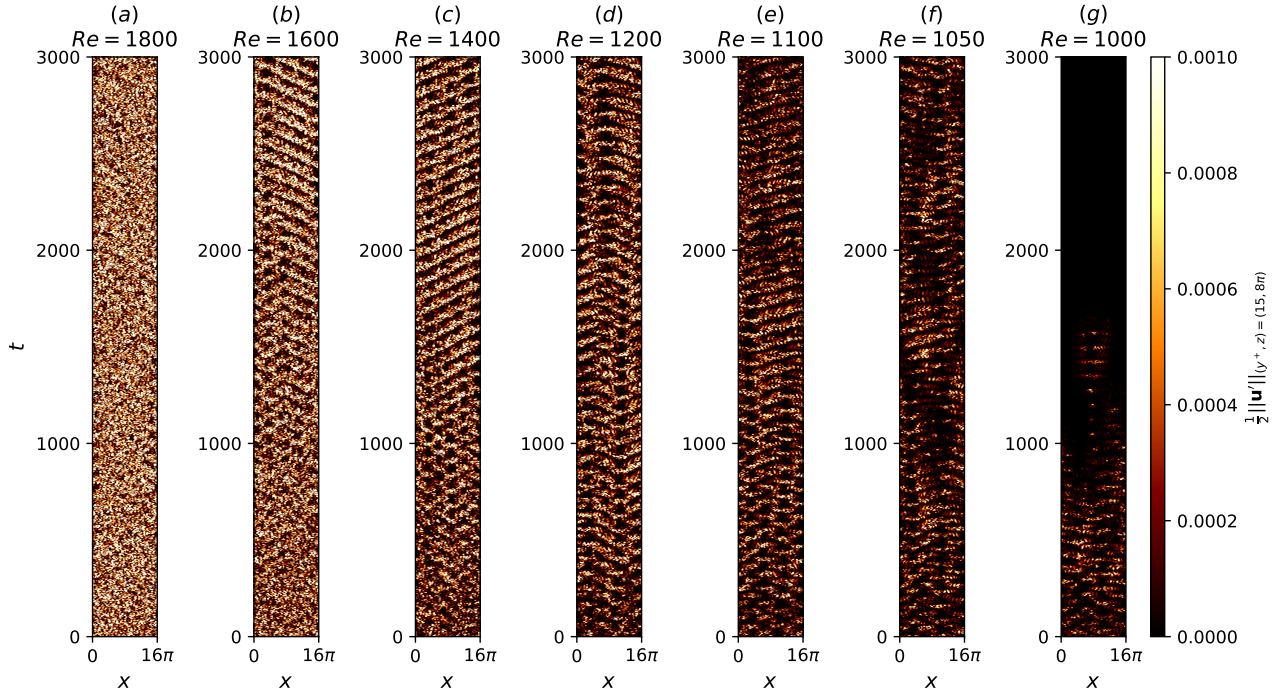


Figure 1.7: Turbulent-laminar bands for $t \in [0, 3000]$ in large domains $(L_x, L_z) = (16\pi, 16\pi)$ at (a) $Re = 1800$, (b) $Re = 1600$, (c) $Re = 1400$, (d) $Re = 1200$, (e) $Re = 1100$, (f) $Re = 1050$, (g) $Re = 1000$.

probability distributions of turbulent band decay mimicks a memoryless Poisson distribution,

$$P(\Delta t^d) = \exp(-\Delta t^d/\tau^d(Re)), \quad (1.16)$$

where $\tau^d(Re)$ refers to the mean lifetime for decay as a function of Re . Similarly, the probability distribution for band splitting also follows a Poisson distribution, $P(\Delta t^s) = \exp(-\Delta t^s/\tau^s(Re))$, where $\tau^s(Re)$ refers to the mean lifetime of a splitting event dependent on Re . The mean survival lifetime of a band decaying, τ^d , and splitting, τ^s , depends superexponentially on Re , i.e. $\tau^{d,s} = \exp(\exp(Re))$. This superexponential dependence is presented in figure 1.8, with a crossover point at $Re_{cross} \approx 965$. This crossover point refers to equal mean survival lifetime of a band de suggesting a critical Re for the onset of turbulent bands. While there has substantial progress made towards understanding the behaviour of periodic turbulent-laminar bands in narrow-tilted domains, recently studies of isolated turbulent bands (ITBs) indicate differed behaviour. Notably, ITBs persist at $Re \approx 700$ for $t = 10000$ (far beyond figure 1.8, characterised by streak generating head, and a diffusive upstream tail. [Xiong et al., 2015, Tao et al., 2018, Shimizu and Manneville, 2019, Xiao and Song, 2020].

1.3 Rayleigh-Bénard convection

Rayleigh-Bénard convection (RBC) is a paradigmatic fluid configuration describing the motion of the fluid confined between two infinite-parallel plates heated from below and cooled from the top. As

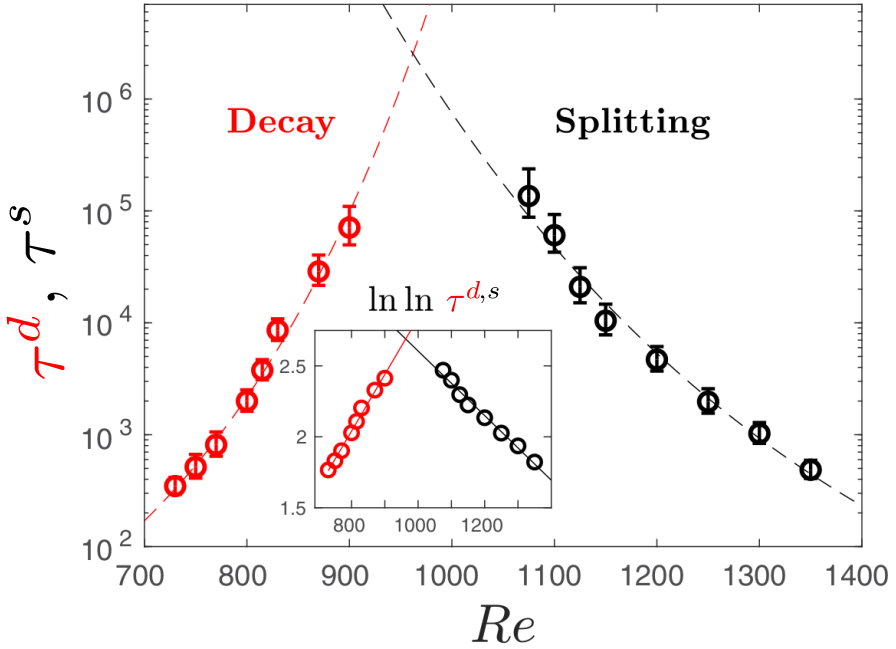


Figure 1.8: The mean decay times (red), τ^d , and mean splitting times (black), τ^s , as a function of Reynolds number, leading to a crossover point at $Re \approx 965$, adapted from [Gomé et al., 2020].

the bottom plate is heated, the bottom layer fluid becomes more buoyant and tends to rise, while the colder top fluid layer is becomes relatively less buoyant and tends to sink, leading to an overturning of layers. Viscous forces between neighbouring fluid parcels act to resist the motion. As buoyancy overcomes these viscous forces, the fluid layers overturn, resulting in the initiation of buoyancy-driven convection, the physical mechanism underpinning RBC.

One of the earliest experimental studies dedicated to buoyancy-driven convection was conducted by Henri Bénard [Bénard, 1901], who observed the formation of hexagonal convection cells above a certain temperature threshold ΔT . These hexagonal patterns are referred to as Bénard cells are illustrated in figure 1.9(a) (adapted from [Koschmieder and Pallas, 1974]). Subsequently, Rayleigh [1916] carried out one of first linear stability analyses of buoyancy-driven convection, predicting the onset of convection at a critical Rayleigh number of $Ra_c = 657.5$. However, Rayleigh's analysis assumed an idealised free-free boundary conditions, which differed from the rigid-free setup of Bénard's experiment. The linear stability analysis for rigid-free configuration was later performed by Jeffreys [1928] yielding a higher critical Rayleigh number of $Ra_c = 1058$. In the rigid-rigid configuration, the critical Rayleigh number increases further to $Ra_c = 1708$ [Pellew and Southwell, 1940]. The Rayleigh number in Bénard's original experiment was found to be 300 to 1500 smaller than Ra_c for the free-free and rigid-free cases [Wesfreid, 2017]. This contradiction, not recognised by Bénard at the time, lies in the significant role of surface tension in thin fluid layers exposed to air, now known as Bénard-Maragoni (BM) convection [Block, 1956, Cloot and Lebon, 1984, Manneville, 2006, Wesfreid, 2017]. In BM convection, fluid motion is primarily driven by surface tension gradients due to variations of temperature, forming hexagonal cells, as in figure 1.9(a). The preference for hexagonal cells in BM convection was later confirmed based on weakly nonlinear stability analysis [Cloot and Lebon, 1984]. As the fluid layer becomes thicker, surface-tension effects diminish and

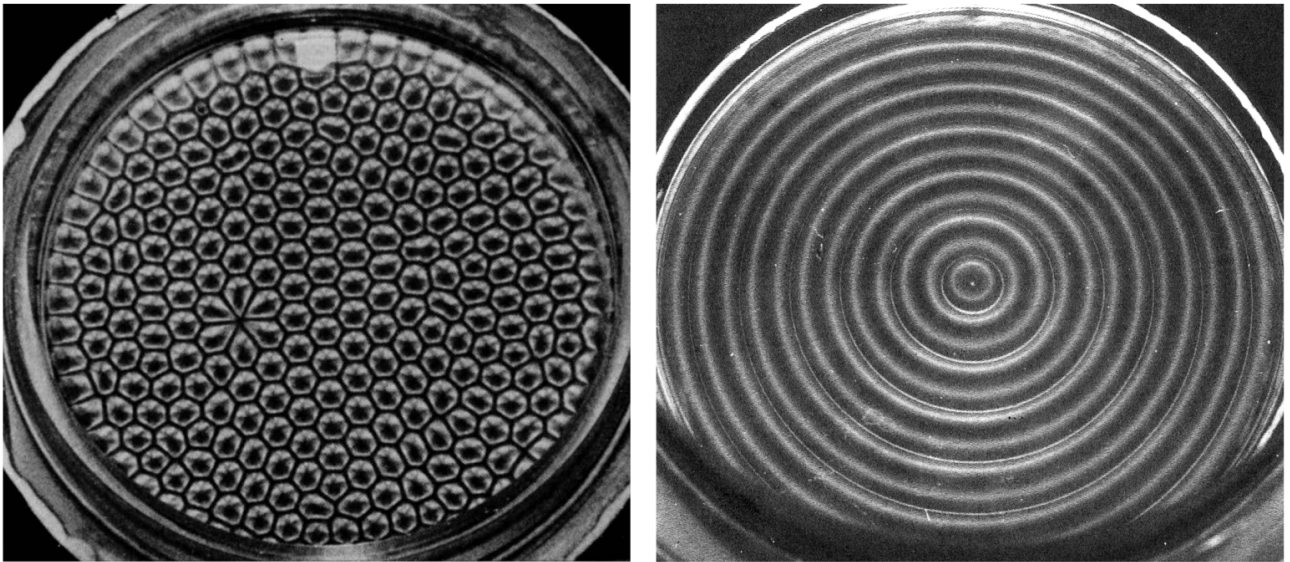


Figure 1.9: (a) Surface tension driven convection leading to the onset of hexagonal Bénard cells in a thin layer of silicone oil, heated from below and cooled by ambient air. A diamond defect appears, likely caused by plate imperfections. (b) Buoyancy driven convection in rigid plates, resulting to concentric convection rolls at 2.9 times the critical Rayleigh number. Both experiments were performed by Koschmieder and Pallas [1974], and the convection patterns were illuminated by aluminum powder, where the dark and bright regions refer to vertical and horizontal motions respectively. These higher resolution images were taken from [Van Dyke and Van Dyke, 1982].

buoyancy-driven convection becomes dominant. Similarly, placing a rigid lid on top of a thin fluid layer suppresses surface-tension effects, also resulting in buoyancy-driven convection. The preferred convection patterns based on weakly nonlinear stability analysis are the two-dimensional parallel rolls, now referred to as ideal straight rolls (ISRs) [Schlüter et al., 1965, Bodenschatz et al., 2000]. In circular containers, the ISRs conform to the geometry of the boundaries, forming concentric convection rolls illustrated in figure 1.9(b). Interestingly, hexagonal cells have been observed in buoyancy-driven flows of non-Boussinesq fluids [Hoard et al., 1970, Bodenschatz et al., 2000]. In this thesis, I will consider RBC with rigid-rigid boundary conditions with for which the critical Rayleigh number is $Ra_c = 1708$. Notably, the corresponding critical wavelength is $q_c = 3.12/d$ (or $\lambda_c \approx 2d$), suggesting that distance separating the plates, d , dictates the length of a single roll, $l_{roll} = \lambda_c/2 \approx d$.

As mentioned earlier, stationary ISRs near q_c emerge just above Ra_c , based on weakly nonlinear stability analysis. [Eckhaus, 1965, Schlüter et al., 1965]. However, this prediction contradicted by the emergence of time-dependent oscillatory ISRs in experiments [Rossby, 1969, Willis and Deardorff, 1970] at $Ra = 9200$ (or roughly five times Ra_c), where weakly nonlinear stability becomes inapplicable far from threshold. To address this, a direct secondary stability analysis was employed to study the stability of ISRs further from Ra_c , based on Galerkin analysis [Busse, 1972]. The results from the analysis is described by the Busse balloon, which illustrates the stability boundaries of ISRs as a function of Ra and Pr and roll wavenumber, α , shown figure 1.10 [Busse, 1978]. The boundaries of the Busse balloon are described by a range of secondary instabilities, each arising from different physical mechanisms [Busse, 1978]. At large Prandtl numbers, $Pr = O(10^2)$, the zig-zag (ZZ)

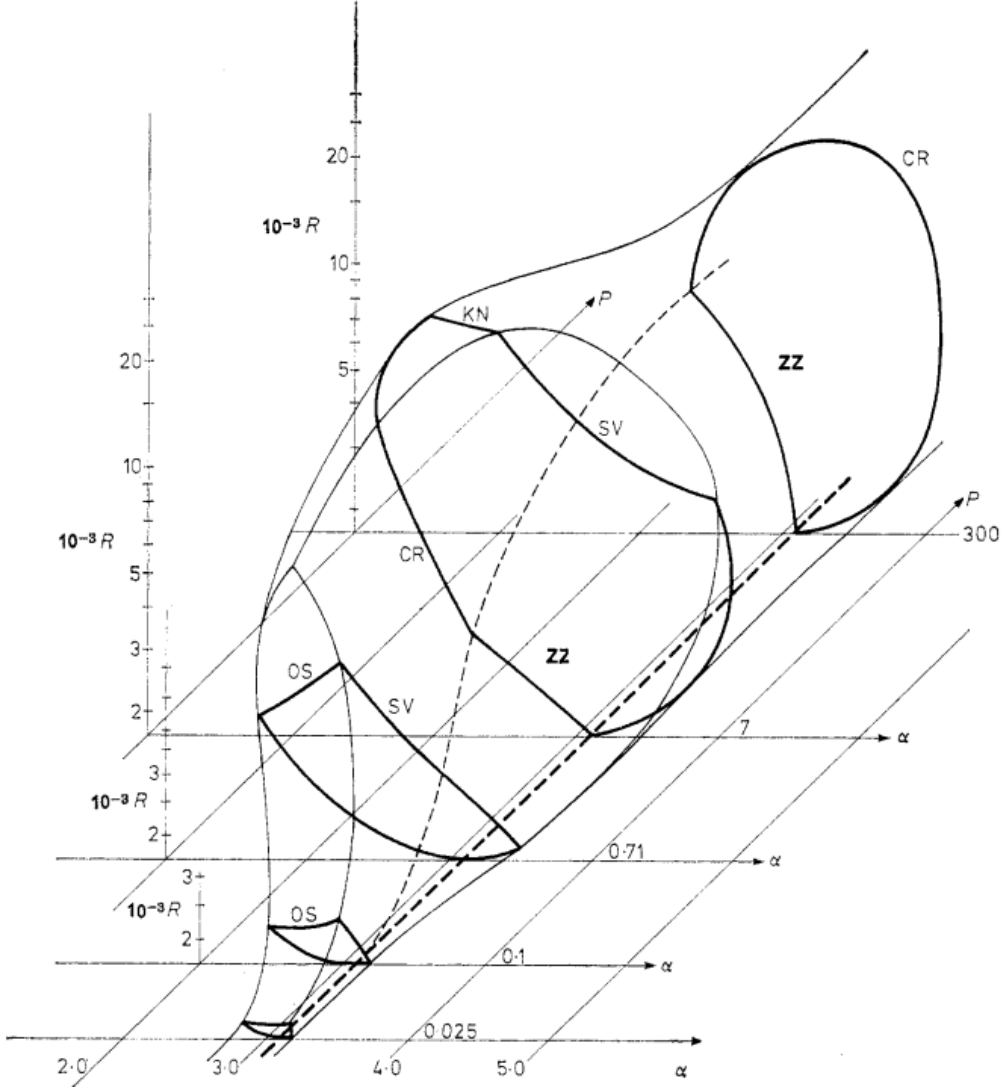


Figure 1.10: The Busse balloon describes the stability boundaries of ISRs in a $\varepsilon - q$ space. For larger wavenumbers, the instability mechanism is described by the skewed-varicose (SV) instability. For smaller wavenumbers, the instability mechanism is described by the Eckhaus instability. For large ε , the instability is described by the onset of oscillatory instability. Busse balloon digitised from [Plapp, 1997] for $Pr \approx 1$.

and cross-roll (CR) instabilities delimits the balloon for small and large roll wavenumbers. The zig-zag instabilities cause zig-zag undulations while the CR instabilities generate rolls orthogonal to the underlying ISR structure, effectively increasing or decreasing the roll wavenumber respectively [Busse and Whitehead, 1971]. Examples of these instabilities at $Pr = 100$ are illustrated in figure 1.11(a,b).

At moderate Prandtl numbers, $Pr = O(1)$, the Busse balloon is bounded by the skewed varicose (SV) for high roll wavenumbers and the oscillatory (OS) instability at large Ra . The skewed-varicose (SV) instability leads to roll-pinchig where pinched rolls merged into a single roll, reducing roll wavenumber while the oscillatory instability leads to the onset of an oscillatory ISRs. Examples of the respective instabilities at $Pr = 1$ are shown in figure 1.11(c,d). At higher wavenumbers, the skewed varicose (SV) instability becomes relevant at intermediate Prandtl numbers, characterised by roll pinching and merging that effectively reduces the roll wavenumber. Finally, the Eckhaus

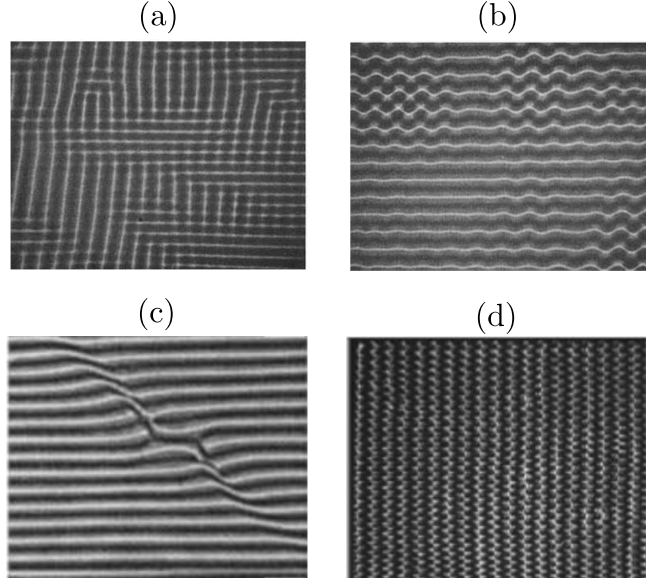


Figure 1.11: ISRs experiencing (a) cross-roll instability at $Ra = 3000, Pr = 100$ and (b) zig-zag instability at $Ra = 3600, Pr = 100$ [Busse and Whitehead, 1971]. (c) Skew-varicosed instability at $Ra = 5568, Pr = 1$ [Plapp, 1997], and (d) oscillatory instability at $Ra = 10384, Pr = 1$ [Cakmur et al., 1997a].

instability (not shown), related to the symmetry of the system, appears close to the Ra_c , leading a disturbance parallel to the underlying rolls which either creates or destroy rolls such that the resultant roll wavenumber adheres to the stability boundaries [Lowe and Gollub, 1985]. Near $Pr = 1$, the Eckhaus instability coincides with the crossroll instability (figure 6 from Bodenschatz et al. [2000], adapted from Plapp [1997].) In this thesis, we focus on fluids with $Pr = 1$, where the skewed-varicose, Eckhaus and cross-roll instabilities typically arises. The stability boundaries of the Busse balloon have been experimentally verified [Busse and Whitehead, 1971, Croquette, 1989a, Plapp, 1997]. However, the exact roll wavenumbers of ISRs exhibits hysteresis. As Ra is was continuously modified, the ISRs with wavenumbers that are outside of the stability boundaries of the Busse balloon, undergo spontaneous rolls dislocations from various secondary instabilities described above. These instabilities either increase or decrease the roll wavenumber, adhering to the the stability boundaries of the Busse balloon. The hysteretic behaviour indicates that the roll wavenumber of the ISRs is strongly dependent on the system's history [Bodenschatz et al., 2000].

It is worth noting that the solutions in the form of ISRs appear to be an exception rather than the rule [Croquette, 1989b]. The coexistence of multiple ‘non-ISR’ states, in the form of squares, travelling/stationary targets, giant rotating spirals, and oscillatory convection patterns have been found over several years [Le Gal et al., 1985, Croquette, 1989a, Plapp, 1997, Hof et al., 1999, Rüdiger and Feudel, 2000, Borońska and Tuckerman, 2010a,b]. Investigation of cylindrical RBC with small aspect-ratio ($\Gamma = 2$) found eight stationary states (at the same $Ra = 142000$), and two oscillatory states ($Ra > 14200$) [Hof et al., 1999]. These findings were later supported by numerical experiments and bifurcation analyses [Ma et al., 2006, Borońska and Tuckerman, 2010a,b]. In particular, bifurcation analyses performed by Ma et al. [2006], revealed twelve stable branches in the form of symmetric and asymmetric convection rolls near onset ($Ra \leq 2500$), with the potential emergence of hundreds of

branches at higher Rayleigh numbers, $Ra \leq 30000$ [Borońska and Tuckerman, 2010b].

In larger domains ($\Gamma \geq 28$), giant rotating spirals were identified and thoroughly investigated [Plapp and Bodenschatz, 1996, Plapp et al., 1998]. Experimental and numerical studies of RBC with varying sidewall boundary conditions (i.e. thermally insulating, conducting an no-slip) [Tuckerman and Barkley, 1988, Siggers, 2003, Paul et al., 2003, Bouillé et al., 2022], non-Boussinesq convection [Bodenschatz et al., 1992], and rotational effects [Hu et al., 1997] were investigated, where multiple states were also reported. More recently, Reetz and Schneider [2020], Reetz et al. [2020] computed up to sixteen stable and unstable invariant states and identified heteroclinic orbits between the multiple states in an inclined RBC. The existence of multiple stable states apart from ISRs suggest that RBC forms a multiple bistable systate above Ra_c . To complicate matter further, an intrinsic chaotic state of convection was discovered.

In the late 1990s, convection rolls exhibiting spatio-temporal chaotic behaviour known as spiral defect chaos (SDC) are found in the same stability boundaries where ISRs were expected [Morris et al., 1993, Hu et al., 1993, Decker et al., 1994, Hu et al., 1995, Morris et al., 1996, Cakmur et al., 1997a, Ahlers, Egolf et al., 1998, 2000, Chiam et al., 2003, Vitral et al., 2020]. Notably only carefully prepared experiment setups led to ISRs while uncontrolled initial conditions yield SDC. It is well established that SDC exists as intrinsic attractor of RBC, independent of sidewall conditions Morris et al. [1996], forming a bistable system with ISRs [Cakmur et al., 1997a] across a range of Ra at Pr illustrated in figure 1.12. However, the SDC attractor have been found to be unstable at $Pr = 4$, decaying towards ISRs over long periods [Bajaj et al., 1997]. SDC has also been modelled in numerical simulations of the two-dimensional Swift-Hohenberg equations [Swift and Hohenberg, 1977, Xi et al., 1993, Xi and Gunton, 1995, Schmitz et al., 2002, Karimi et al., 2011]. The critical Rayleigh number for the onset of SDC, Ra_s , depends on the domain's aspect ratio, and Prandtl number [Hu et al., 1995, Bajaj et al., 1997, Cakmur et al., 1997b, Bodenschatz et al., 2000], and remain inconclusive. Notably, SDC has been reported in large domains ($\Gamma \gtrsim 20$), implying that there is a minimal Γ for SDC to occur [Bodenschatz et al., 2000], supporting the dependence of the Ra_s on Γ . The chaotic properties of SDC is also dependent of aspect ratio, where the leading Lyapunov exponents decreases with aspect ratio [Egolf et al., 2000, Paul et al., 2007]. Investigations into the spatial-temporal description of SDC such as the averaged roll-curvature Hu et al. [1995], probability distribution of spirals Ecke et al. [1995], Liu and Ahlers [1996] and correlation length-/time-scales [Morris et al., 1993, 1996, Cakmur et al., 1997b] have been undertaken. Specifically, the correlation length-scales [Morris et al., 1993, 1996, Cakmur et al., 1997b] scales exponentially with Ra , suggesting that onset of SDC from ISRs mimicks a phase transition. Spatiotemporal chaotic behaviour similar to SDC has been found also in other pattern-formation systems such as rotational RBC Hu et al. [1997], dielectric barrier discharge Dong et al. [2005] and advection diffusion reaction systems Affan and Friedrich [2014].

1.4 Rayleigh-Bénard Poiseuille (RBP) flows

The neutral stability curves in the Rayleigh-Bénard Poiseuille (RBP) comprising of both plane Poisueille flow (PPF) and Rayleigh-Béanrd convection (RBC) systems, are bounded by the onset

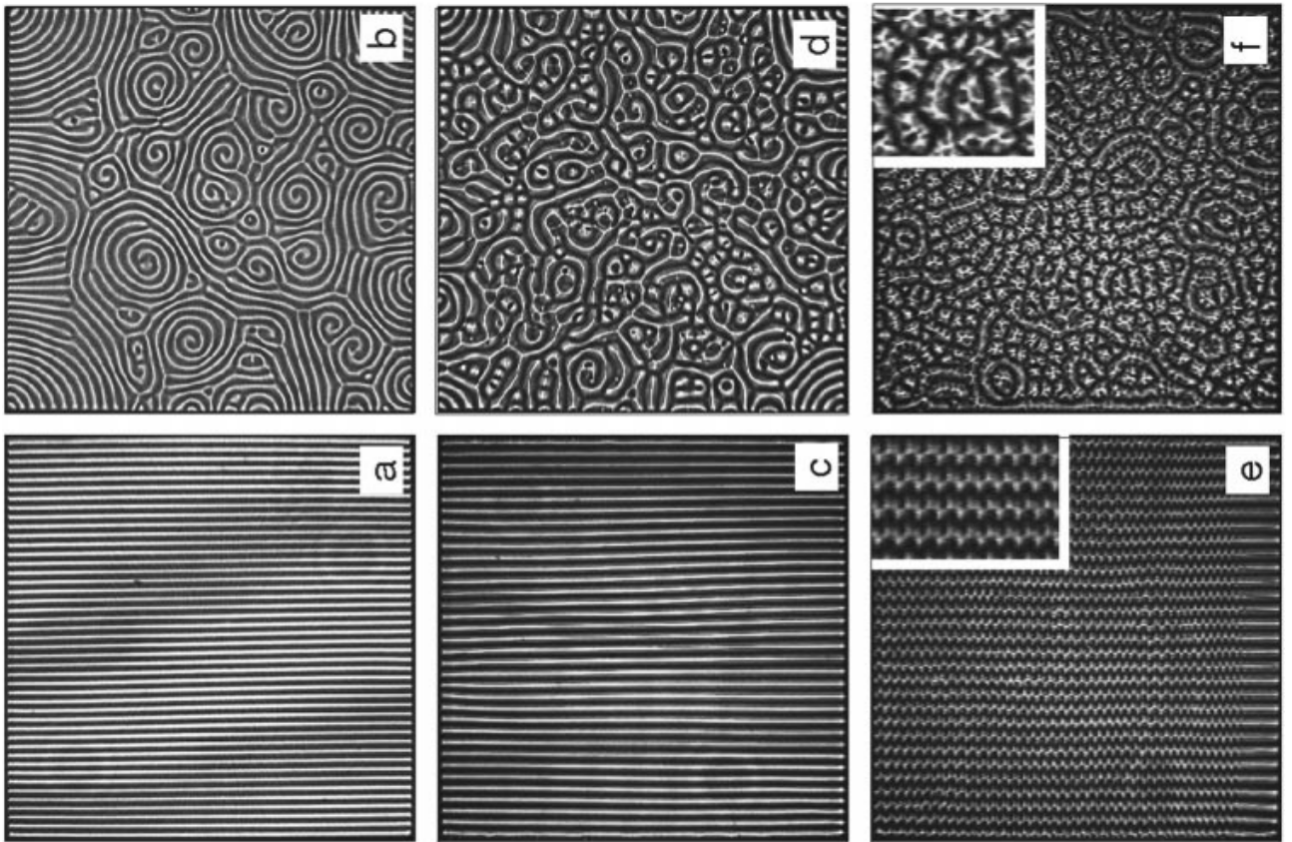


Figure 1.12: The coexistence of spiral defect chaos (SDC, top row) and ideal straight rolls (ISRs, bottom row) at (a,b) $Ra = 3279$, (c,d) $Ra = 6832$ and (e,f) $Ra = 10384$. The domain size is $\Gamma = 50$ and $Pr = 1$, adapted from Cakmur et al. [1997a].

of Tollmien-Schlichting waves at $Re_c = 5772.22$ [Orszag, 1971], and by the onset of convection rolls at $Ra_c = 1708$ [Pellew and Southwell, 1940], respectively. The imposed mean Poiseuille flow in the RBP system breaks the rotational invariance of the convection rolls, categorising them based on their orientation to the mean flow direction, namely: longitudinal ($\alpha = 0, \beta \neq 0$), transverse ($\alpha \neq 0, \beta = 0$) and oblique rolls ($\alpha \neq 0, \beta \neq 0$). The primary instabilities leading to these rolls were first investigated by Gage and Reid [1968] in an infinitely extended layer. For the onset of longitudinal rolls, the linearised system reduces to that of RBC. Hence, the critical Rayleigh number for the onset of longitudinal rolls remains the same, $Ra_{\parallel} = Ra_c = 1708.8$ with a critical wavenumber, $\alpha_{\parallel} = \alpha_c = 3.13$ [Pellew and Southwell, 1940, Kelly, 1994], independent of both Reynolds number, Re , and Prandtl number Pr . In contrast, the onset of transverse rolls exhibits a critical Rayleigh number, $Ra_{\perp} = f(Re, Pr)$, that increases with Re and is dependent on Pr [Gage and Reid, 1968, Müller et al., 1992, Nicolas et al., 1997]. The critical Rayleigh number for the onset of obliqued rolls can be obtained by applying a Squire transformation [Squire, 1933] to the linearised problem for transverse rolls. For a given Ra , the corresponding critical Re for the onset of oblique rolls is higher than that of transverse rolls [Gage and Reid, 1968]. The neutral stability curves associated with the transverse rolls (TR), oblique rolls (OR) and longitudinal rolls (LR) are shown in figure 1.13.

Experimental observations of the onset of longitudinal rolls have been reported in channels with large transverse aspect ratios (i.e span-to-depth) [Akiyama et al., 1971, Ostrach and Kamotani, 1975,

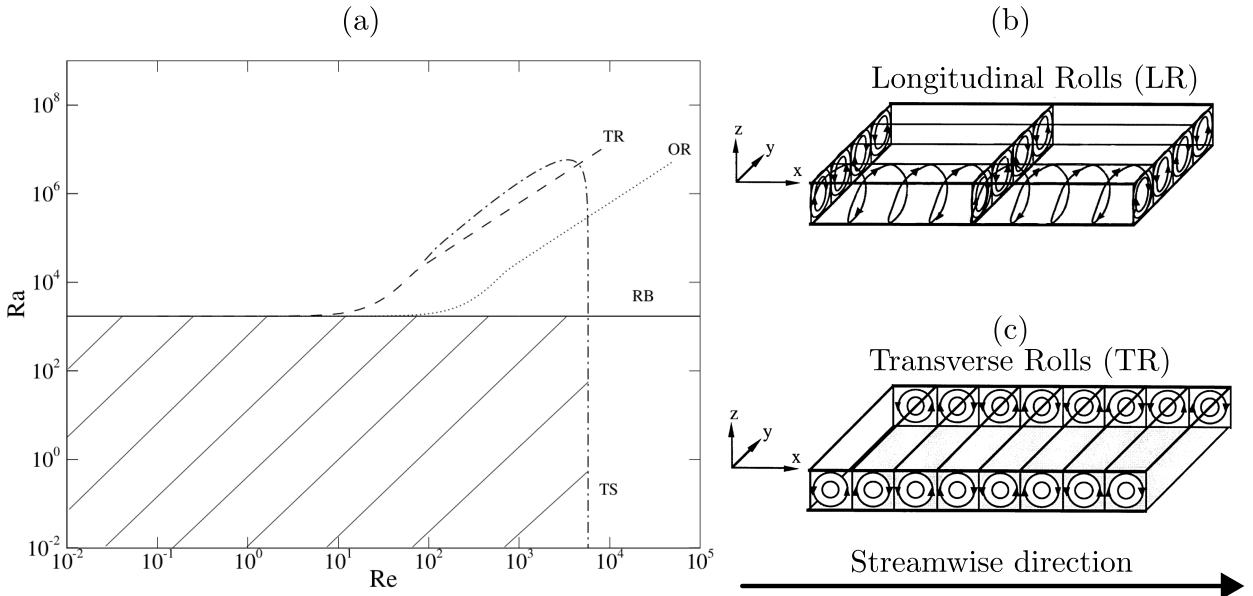


Figure 1.13: (a) Neutral stability curves of longitudinal rolls (LR), oblique rolls (OR), transverse rolls (TR) and Tollmien-Schlichting (TS) waves, adapted from John Soundar Jerome et al. [2012]. The shaded area refers to damped perturbations. Sketch of (b) longitudinal and (c) transverse rolls, adapted from Kelly [1994].

Fukui et al., 1983], while the onset of transverse rolls are observed in narrower channels [Luijckx et al., 1981, Ouazzani et al., 1989, 1990]. Indeed, linear stability analysis conducted for finite channels revealed that critical Rayleigh number Ra_{\parallel} remains independent for transverse aspect ratios greater than five, and increases quickly below that. Therefore, the critical Rayleigh number for onset of transverse rolls, Ra_{\perp} , is lower than Ra_{\parallel} in narrow channels for small Reynolds numbers [Nicolas et al., 2000], providing support for the preference of transverse rolls in narrow channels. Ouazzani et al. [1990] reported laminar Poiseuille flow in the Ra, Re parameter space where transverse rolls are expected based on temporal linear stability analysis. This contraction was addressed by Müller et al. [1992], who showed that transverse rolls can be either convectively or absolutely unstable, and the boundary between them matches with the experimental results of Ouazzani et al. [1990]. By considering the response from three-dimensional impulse, Carrière and Monkewitz [1999] further demonstrated that the longitudinal rolls, unlike the transverse rolls, are always convectively unstable. Nonmodal stability analysis of subcritical RBP, $Ra < Ra_c$, $Re < Re_c$, performed by John Soundar Jerome et al. [2012] revealed that the optimal transient growth is primarily dominated by streamwise rollers of plane Poiseuille flow [Reddy and Henningson, 1993], with a spanwise wavenumber of $\beta_{opt} \approx 2.05$. The maximum amplification factor, G_{max} increases modestly with Ra , and the critical wavenumber approaches, α_{\parallel} , indicative of longitudinal rolls. Since longitudinal rolls are the dominant primary instability for $Re > 0$ in infinite domains, their secondary stability have been analysed by Clever and Busse [1991]. Their study revealed the presence of a secondary, time-dependent wavy instability near $Re \sim 100$ [Clever and Busse, 1991], leading to the onset of tertiary solutions in the form of wavy rolls. These have been observed experimentally and was found to be convectively unstable [Pabiou et al., 2003, 2005, Nicolas et al., 2010]. Clever and Busse [1991] also speculated that the wavy rolls are

less efficient at transporting heating than longitudinal rolls at the same control parameters, confirmed numerically [Nicolas et al., 2012]. The impact of finite transverse aspect ratios on the onset of wavy rolls have been also studied [Xin et al., 2006, Nicolas et al., 2010], where the critical Ra was found to be approximatgely 1.5 times higher than that in an infinite domain Clever and Busse [1991]. The influence of external excitations on the development length of wavy rolls have been explored. An increase in external excitation amplitude have shown to reduced the required development length of wavy rolls [Nicolas et al., 2010, 2012]. More recently, studies of turbulent RBP flows showed that shear-driven turbulence can enhance heat fluxes [Scagliarini et al., 2014, 2015, Pirozzoli et al., 2017]. Extensions of the RBP configuration, such as flows over wavy walls or with sinusoidal thermal forcing have been investigated, potentially offering a reduction in drag and enhancing heat transport [Hossain et al., 2012, Hossain and Floryan, 2016, 2020]. For a comprehensive overview of RBP flows, the reader is referred to the reviews by Kelly [1994] and Nicolas [2002].

1.4.1 Thesis Outline

In this thesis, I am particularly focused on the transition behaviour of fluid flow driven by shear and bouyancy, addressing questions related to the onset of instabilities due to shear and buoyancy, and the (possible) competitive between shear and buoyancy driven instabilities. I would like to preface that while this thesis is dealing with onset of instabilities, it does not clearly indicate that the onset of such instabilities necessarily lead to turbulence, hence, for terminology sake, we shall be looking into transitional regimes where the fluid neither laminar nor turbulent. The main motivations are two-folds, both from an academic and applied point-of-view. Within academia, the onset and transition to turbulence in Rayleigh-Bénard Poiseuille flows remains poorly understand. Whilst there had been significant progress in our understand of transition to turbulence in independent setups, Rayleigh-Bénard convection and plane Poiseuille flows, their combined effects are not known. The thesis is structured into the follow, Chapter 1 is the introduction with literature review, chapter 2 methodology assosicated with the spectral/ hp -element method, chapter 3 with results related to the the Rayleigh and Reynolds number sweep, chapter 4 with a specific focus on the bistability between spiral defect chaos and ideal straight rolls and finally chapter 5 with concluding remarks.

1. Academic motivation - flow structures, statistics, transition.
2. Application motivation - shear, heat transfer. Chip cooling, thin-film fabrication and atmospheric boundary layer.

We seek to investigate the influence of unstable stratification quantified by Rayleigh number Ra , on the behaviour tubulent-laminar bands. The onset of convection occurs at a critical Rayleigh number of $Ra_c > 1708$, in the form of a pair of convection rolls. When aligned in the streamwise direction, the convection rolls are seemingly analogous to a pair of counter-rotating vortices, an optimal initial condition for transient growth. Our investigation naturally answers a few questions related to turbulent-laminar bands. For example, does the onset of turbulent-laminar bands, Re_{cr} decrease with increasing Ra ? Do Ra -effects influence the structure of turbulent-laminar bands i.e band angle/width?

The answers to our research will have important implications Rayleigh-Bénard Poiseuille flows, ubiquitous in atmospheric, geophysical and engineering flows.

Chapter 2

Numerical Techniques

We will discuss the fundamentals of numerical methods relevant to solving the Navier-Stokes equations. We begin the discussion of the weighted of residuals (§2.1) and the spatial discretisation using spectral/*hp* element methods in one dimension (§2.3). This is followed by techniques for solving the Navier-Stokes equations (§2.4), introducing the velocity-correction scheme, enforcing a constant flow rate and the quasi-3D approach for semi-homogeneous domains. This chapter concludes with numerical techniques for the stability analysis of the Navier-Stokes equations (§2.5), including eigenvalue computation and edge tracking.

2.1 Method of weighted residuals

Spatial discretisation errors, or residuals, arises as one seeks an approximate solution to some partial differential equation (PDE). The method of weighted residual provides a generic mathematical framework in which constraints on the residual could be applied flexibly, defining the spatial discretisation scheme and its convergence properties. In summary, we approximate the solution of PDE by considering a finite expansion of a suitable basis, to which its coefficients are sought after by minimising the inner product between the PDE and a test (or weight) function. To demonstrate this, we consider a linear partial differential equation as,

$$\mathbf{L}[u(x)] = 0, \quad x \in \Omega, \tag{2.1}$$

where \mathbf{L} refers to a linear spatial differential operator subjected to some boundary conditions within the domain, Ω , while $u(x)$ refers to the exact solution of \mathbf{L} . Examples of PDEs with linear spatial differential operators include the Laplace equation, $\nabla^2 u = 0$, Poisson equation, $\nabla^2 u = f$, and the Helmholtz equation, $\nabla^2 u + \lambda u = f$. We suppose that the exact solution $u(x)$ can be approximated (discretised) by N finite number of basis (or expansion) functions, $\Phi(x)$.

$$u(x) \approx u^\delta(x) = \sum_{i=0}^{N-1} \hat{u}_i \Phi_i(x), \tag{2.2}$$

where $u^\delta(x)$ refers to the approximate solution of $u(x)$, consisting of a linear combination of the product between the i^{th} basis coefficient, \hat{u}_i , and the i^{th} global basis expansion, $\Phi_i(x)$, defined within Ω . Since $u^\delta(x)$ is an approximate solution of equation (2.5), we expect a residual (or ‘error’) between the exact solution, $u(x)$, and $u^\delta(x)$,

$$\mathbf{L}[u^\delta(x)] = R[u^\delta(x)], \quad (2.3)$$

where $R[u^\delta(x)]$ refers to the residual which depends on the approximate solution $u^\delta(x)$ and varying within Ω . In other words, equation (2.5) might not be satisfied everywhere in Ω . We need to place restrictions on the residual, such that it the residual approaches zero, $R \rightarrow 0$, and the approximate solution approaches the exact solution, $u^\delta(x) \rightarrow u(x)$. The method of residuals places a restriction on the residual by applying an inner product between the governing equation, and N test (or weight) functions, $v_j(x)$, and setting it to zero,

$$(v_j(x), R[u^\delta(x)]) = 0, \quad j = 0, \dots, N - 1. \quad (2.4)$$

Definition 2.1.1 (Inner product). The inner product between two functions $f(x)$ and $g(x)$ is,

$$(f, g) = \int_{\Omega} f(x)g(x)dx.$$

By setting equation (2.4) to zero, it becomes a system of N ordinary differential equations, where the N basis coefficients, \hat{u}_i . The choice of test function defines the projection methods, and examples of projection methods are shown in table 2.1. We emphasise that the method of weighted residuals merely describes the projection method, but does not specify the type of basis expansions, as we will discuss later in §2.3. The choice of projection method coupled with suitable basis expansions will have different solution convergence properties. A particular interest is on how quickly the residual vanishes as the number of basis expansions increases. For instance, by considering the Galerkin method coupled with Fourier expansions, one can expect exponential convergence, desirable for an efficient representation of turbulent dynamics.

Weight functions	Projection method
$v_j(x) = \delta(x - x_j)$	Collocation
$v_j(x) = \begin{cases} 1 & \text{if } x \in \Omega_j \\ 0 & \text{if } x \notin \Omega_j \end{cases}$	Finite-Volume
$v_j(x) = \phi_j$	Galerkin
$v_j(x) = \frac{\partial R}{\partial \hat{u}_j}$	Least-squares

Table 2.1: Examples of weight functions and projection methods

2.2 Galerkin Projection

The Galerkin projection remains a standard projection method in the context of the finite element method, where the test functions, $v(x)$, are chosen to be lie in the same functional space as the global basis functions, $\Phi(x)$. To demostrate the Galerkin projection method, we consider that the differential operator earlier in equation (2.1) as a 1D Helmholtz equation,

$$\mathbf{L}[u(x)] \equiv \frac{\partial^2 u(x)}{\partial x^2} - \lambda u(x) - f(x) = 0, \quad x \in \Omega := [0, l] \quad (2.5a)$$

$$u(0) = g_D, \quad \left. \frac{\partial u}{\partial x} \right|_{x=l} = g_N. \quad (2.5b)$$

where λ is a real positive constant, $f(x)$ is a forcing function, and Ω refers to the spatial domain bounded between 0 and l . To ensure that problem is well posed, Dirichlet and Neumann boundary conditions, g_D and g_N , are imposed at $x = 0$ and $x = l$ respectively. Equation 2.5 is commonly referred to as the strong or classical form.

The subsequent step in Galerkin projection methods is take the inner product of the equation (2.5) with a test function, $v(x)$, that satisfies the homogeneous Dirichlet boundary conditions by definition, i.e. $v(0) = 0$, and setting the inner product to zero,

$$(v(x), \mathbf{L}[u(x)]) = \int_0^l v \left[\frac{\partial^2 u(x)}{\partial x^2} - \lambda u(x) + f(x) \right] dx = 0. \quad (2.6)$$

This step is equivalent to applying the method of weighted residuals (§2.1), where $u(x)$ could refer to the approximate solution, $u^\delta(x)$. Next, we perform integration by parts,

$$\underbrace{\int_0^l \frac{\partial v}{\partial x} \frac{\partial u}{\partial x} dx}_{a(v,u)} + \underbrace{\int_0^l \lambda v u dx}_{f(v)} = \underbrace{\int_0^l v f dx}_{f(v)} + \left[v \frac{\partial u}{\partial x} \right]_0^l. \quad (2.7)$$

This equation is typically referred to as the weak ¹ form of equation (2.5). In compact notation, we define the bilinear and linear forms as,

$$a(v, u) = f(v), \quad (2.8a)$$

where $a(v, u)$ and $f(v)$ are typically referred to as the strain energy and forcing function in structural mechanics, required to remain finite. To ensure this, we restrict the choice of solutions $u(x)$ to lie in the solution space, \mathcal{U} , defined as

$$\mathcal{U} := \{u \mid u \in H^1(\Omega), u(0) = g_D\}, \quad (2.9)$$

¹The notions of the *weak* and *strong* are refers to the smoothness (regularity) required of admissible solutions. In the weak formulation, the highest derivative involved is up to first-order, so the solution space is H^1 . This space is generally larger than that of the strong formulation, which required $u \in H^2(\Omega)$. Since $H^2(\Omega) \subset H^1(\Omega)$ the weak formulation imposeds a ‘less stringent’ constraint of the solution space of admissible functions.

where $u \in H^1$ refers to functions of u belonging to Sobolev space of order 1, and satisfying the Dirichlet condition, $u(0) = g_D$, at $x = 0$.

Definition 2.2.1 (Sobolev space). We define Sobolev space of order $n \geq 1$ on Ω ,

$$H^n(\Omega) = \{u \mid u \in L_2(\Omega), D^\alpha u \in L_2(\Omega), \forall \alpha : \alpha \leq n\},$$

where $D^\alpha u$ refers to derivatives up to order α and $L_2(\Omega)$ refers to functions that are square integrable.

Definition 2.2.2 (L_2 space). The space $L_2(\Omega)$ refers to functions that are square integrable,

$$(u, u)_{L_2} = \int_{\Omega} |u(x)|^2 d\Omega < \infty. \quad (2.10)$$

We consider admissible functions up to the first derivatives, the highest order derivative in the weak formulation of equation (2.6). Similarly, the space of test functions, \mathcal{V} , is defined as,

$$\mathcal{V} := \{v \mid v \in H^1, v(0) = 0\}, \quad (2.11)$$

where $v \in H^1$ are refer to test functions belonging to the Sobolev the space of order 1, and is defined to be zero, $v(0) = 0$ on Dirichlet boundary condition, $x = 0$. The generalised weak form is therefore finding $u(x) \in \mathcal{U}$, such that

$$a(v, u) = f(v), \quad \forall v \in \mathcal{V}. \quad (2.12)$$

At this point, equation (2.12) is infinite dimension as the function spaces, \mathcal{U} and \mathcal{V} , contain infinitely many functions. To obtain an approximate solution, $u^\delta(x)$, we restrict ourselves to finite dimensional subspaces, $\mathcal{U}^\delta \subset \mathcal{U}$, and $\mathcal{V}^\delta \subset \mathcal{V}$. The problem is then to find $u^\delta \in \mathcal{U}^\delta$, such that

$$a(v^\delta, u^\delta) = f(v^\delta), \quad v^\delta \in \mathcal{V}^\delta. \quad (2.13)$$

Here, the subspaces $u^\delta \in \mathcal{U}^\delta$ and $v^\delta \in \mathcal{V}^\delta$ are not the same, compare equations (2.9) and (2.11), necessary for the standard Galerkin projection procedure where they should lie in the same subspace. To ensure that they belong to the same space, we lift the solution u^δ into two parts,

$$u^\delta = u^{\mathcal{H}} + u^{\mathcal{D}}. \quad (2.14)$$

where $u^{\mathcal{H}} \in \mathcal{V}^\delta$ satisfies the homogeneous Dirichlet condition (e.g. is zero on Dirichlet boundaries), belonging to the same subsapce as $v^\delta \in \mathcal{V}^\delta$, while $u^{\mathcal{D}} \in \mathcal{U}^\delta$ satisfies the Dirichlet boundary conditions $u^{\mathcal{D}}(0) = g_D$. Hence, the standard Galerkin projection method is to search for the homogeneous solution, $u^{\mathcal{H}} \in \mathcal{V}^\delta$, such that,

$$a(v^\delta, u^{\mathcal{H}}) = f(v^\delta) - a(v^\delta, u^{\mathcal{D}}). \quad (2.15)$$

This concludes the classical Galerkin formulation. Under certain assumptions of a , a solution is guaranteed under the Lax-Milgram theorem [Lax and Milgram, 1955].

2.3 Spectral/ hp element method

We have described the procedure for approximating a solution of a PDE using the classical Galerkin projection technique. However, the spatial discretisation scheme, related to the choice of basis (and test) functions, remains undiscussed. In this section, we discuss the spectral/ hp element method [Patera, 1984], where the solution is partitioned into a set of non-overlapping finite elements of size h , consisting of a linear combination of continuous orthogonal polynomial functions up to order P . It leverages the geometric flexibility of classical finite-element methods, allowing for the representation of complex engineering geometries, and the exponential (spectral) convergence properties of classical spectral methods, where the solution error decreases exponentially. Suppose we consider $P + 1$ linearly independent polynomials spanning the polynomial space of \mathcal{P}_P , the error of a smooth solution with element size of h and polynomial order P has the property of [Karniadakis and Sherwin, 2005],

$$\|u(x) - u^\delta(x)\| \leq Ch^P \|u(x)\| \approx O(h^P). \quad (2.16)$$

where C is some constant. Equation 2.16 implies that the error decreases linearly with h , and exponentially with P . This section is organised into domain partition, standard elements, assembly process, modal and nodal expansion functions, numerical integration and differentiation, concluding with an example in 1D.

2.3.1 Domain partition

The first step concerns the partitioning the domain into a set of (finite) elemental regions. We consider an example in one dimension within Ω , and partition it into a set of N_{el} elements, where Ω^e , refers to the elemental partitions with $1 \geq e \geq N_{el}$, such that they meet at their boundaries and do not overlap,

$$\Omega = \bigcup_{e=1}^{N_{el}} \Omega^e, \quad \text{where } \bigcap_{e=1}^{N_{el}} \Omega^e = \emptyset \quad (2.17)$$

where the e^{th} element is defined as,

$$\Omega^e = \{x \mid x_{e-1} \geq x \geq x_e\}. \quad (2.18)$$

Each element can be represented by a linear combination of orthogonal basis expansions. The basis expansions can be either modal or nodal expansions, as we shall see later.

2.3.2 Standard Elements

In general, we expect to work with non-uniform elements that may have arbitrarily shapes, making the definition of basis expansions potentially unwieldy. To simplify the formulation, it is convenient to define a *standard* element,

$$\Omega_{st} = \{\xi \mid -1 \geq \xi \geq 1\}, \quad (2.19)$$

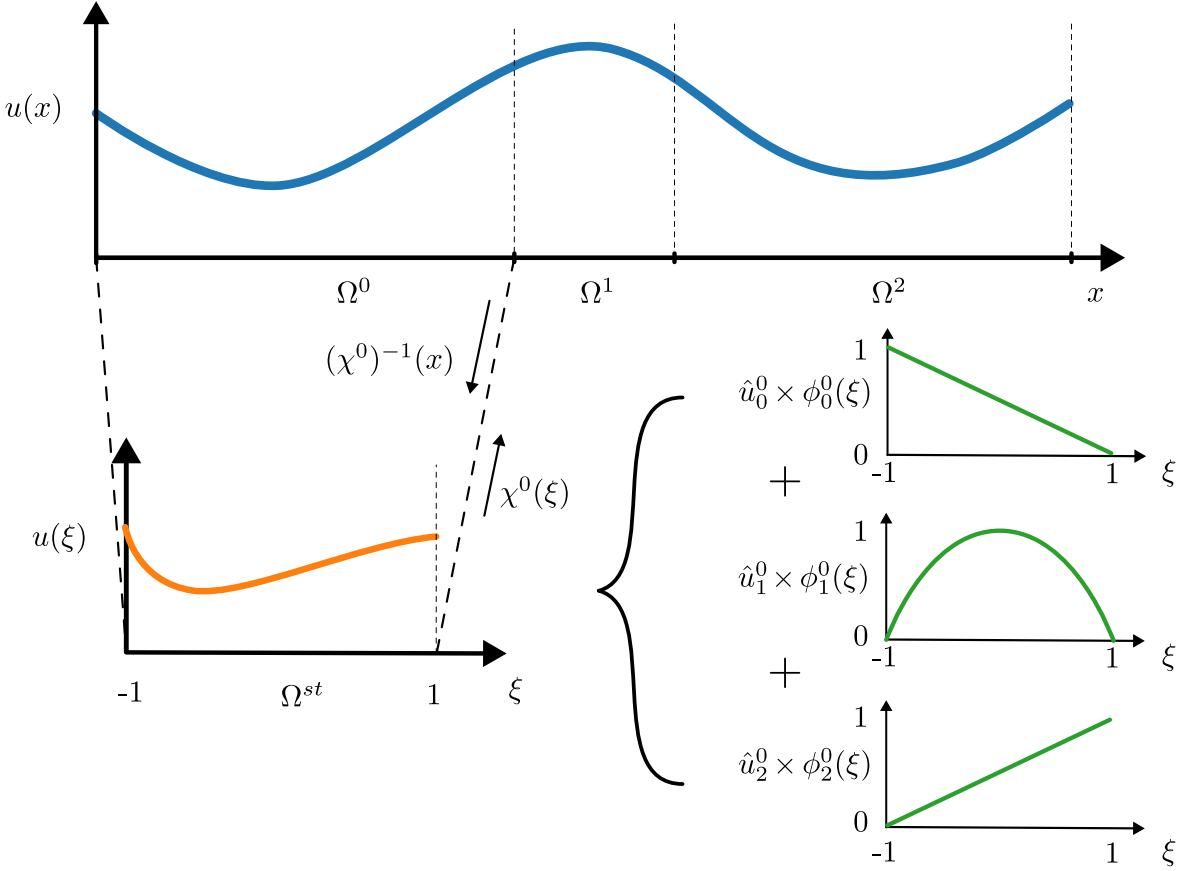


Figure 2.1: A spectral/ hp element representation of $u(x)$, consisting of three non-overlapping finite elements, each containing a linear combination of local expansion bases of up to $P = 2$.

where Ω_{st} refers to the standard element defined in local coordinates, $\xi \in [-1, 1]$. Within this standard element, the formulation of basis expansions, as well as differential and integration operations, can be carried out in the local coordinate system ξ , before mapping the solution back to the global domain, x . We can map the standard element into any arbitrary global coordinates based on a linear mapping $\chi^e : \Omega_{st} \rightarrow \Omega$,

$$x = \chi^e(\xi) = \frac{1 - \xi}{2}x_e + \frac{1 + \xi}{2}x_{e+1}, \quad \xi \in \Omega_{st} \quad (2.20)$$

which has an analytical inverse, $(\chi^e)^{-1}(x)$,

$$\xi = (\chi^e)^{-1}(x) = 2 \frac{x - x_{e-1}}{x_e - x_{e-1}} - 1, \quad x \in \Omega^e. \quad (2.21)$$

For illustration purposes, we consider that the standard element can be represented by three local basis expansions of polynomial order of up to $P = 2$,

$$\phi_0^e(\xi) = \frac{1 - \xi}{2}, \quad \phi_1^e(\xi) = (1 + \xi)(1 - \xi), \quad \phi_2^e(\xi) = \frac{1 + \xi}{2}, \quad (2.22)$$

where ϕ_0^e, ϕ_1^e and ϕ_2^e refers to the linear and quadratic local basis expansions of the e^{th} element. These local basis expansions is illustrated in figure 2.1. We note that the formulations of local basis

expansion here is merely an example. In practice, the local basis expansions are usually chosen to have orthogonality properties under a certain inner product. The approximate solution is now represented as,

$$u^\delta(x) = \sum_{e=0}^{N_{el}-1} \sum_{i=0}^P \hat{u}_i^e \phi_i^e(\chi^e(\xi)). \quad (2.23)$$

where \hat{u}_i^e refers to the local expansion basis coefficients. The approximate solution, $u^\delta(x)$, now lie within the solution space \mathcal{U}^δ defined as,

$$\mathcal{U}^\delta := \{u^\delta \mid u^\delta \in H^1, u^\delta(\chi^e(\xi)) \in \phi_i^e(\xi), \forall i : 0 \leq i \leq P, \forall e : 0 \leq e \leq N_{el}\} \quad (2.24)$$

2.3.3 Global assembly

In this section, we introduce the concept of global assembly (or direct stiffness summation) which relates the global basis expansions (equation (2.2)), $\Phi_i(x)$, to the local basis expansions (equation (2.23)), $\phi_i^e(x)$, where the solution can be approximated using either formulation,

$$u^\delta(x) = \sum_{i=0}^{N-1} \hat{u}_i \Phi_i(x) = \sum_{e=0}^{N_{el}-1} \sum_{i=0}^P \hat{u}_i^e \phi_i^e(\chi^e(\xi)). \quad (2.25)$$

In general, we can represent the global and local basis coefficients each as a column vector,

$$\hat{\mathbf{u}}_g = \begin{pmatrix} \hat{u}_0 \\ \vdots \\ \hat{u}_N \end{pmatrix}, \quad \hat{\mathbf{u}}_l = \begin{pmatrix} \hat{\mathbf{u}}^0 \\ \vdots \\ \hat{\mathbf{u}}^{N_{el}-1} \end{pmatrix}, \quad (2.26)$$

where $\hat{\mathbf{u}}^e = (\hat{u}_0^e, \dots, \hat{u}_P^e)^T$, $\hat{\mathbf{u}}_g \in \mathbb{R}^N$, $\hat{\mathbf{u}}_l \in \mathbb{R}^{N_{loc}}$ and $N_{loc} = N_{el}(P + 1)$. As there can be more global degrees of freedom than local degrees of freedom, $N > N_{loc}$, we need to impose some conditions on the local expansion coefficients. One of the common approach is to enforce C^0 continuity across elemental boundaries, referred to as the continuous Galerkin projection. Following the definition of local basis expansions in equation (2.22), this condition can be supplemented using,

$$\hat{u}_P^{e-1} = \hat{u}_0^e. \quad (2.27)$$

The graphical representation of this condition enforcing C^0 continuity between the element boundaries for three finite elements with $P = 2$ local basis expansions, and the relationship between global and local basis coefficients are shown in figure 2.2. We can relate the global and local basis coefficients with an assembly matrix, $\mathbf{A} \in \mathbb{R}^{N_{loc} \times N}$,

$$\hat{\mathbf{u}}_l = \mathbf{A} \hat{\mathbf{u}}_g. \quad (2.28)$$

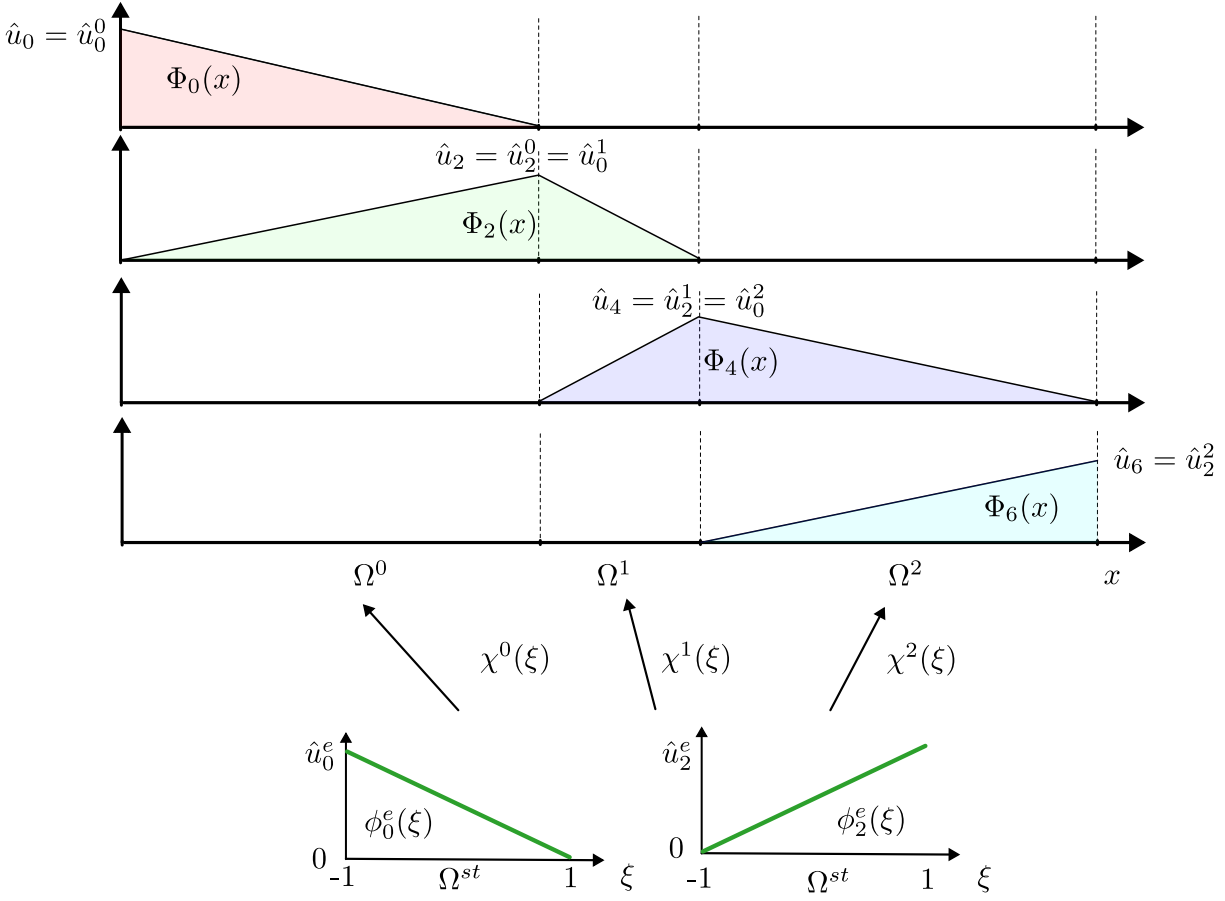


Figure 2.2: A graphical representation of C^0 across elemental boundaries and the relationship between local basis coefficients, u_0^e, u_2^e , and global basis expansions, u_i .

In the case for $P = 2$ and three finite elements as in the case of figures 2.1 and 2.2, the assembly matrix and the vectors of global and local basis coefficients are given as,

$$\hat{\mathbf{u}}_l = \begin{pmatrix} \hat{u}_0^0 \\ \hat{u}_1^0 \\ \hat{u}_2^0 \\ \hat{u}_0^1 \\ \hat{u}_1^1 \\ \hat{u}_2^1 \\ \hat{u}_0^2 \\ \hat{u}_1^2 \\ \hat{u}_2^2 \end{pmatrix}, \quad \mathbf{A} = \begin{pmatrix} 1 & 0 & 0 & 0 & 0 & 0 & 0 \\ 0 & 1 & 0 & 0 & 0 & 0 & 0 \\ 0 & 0 & 1 & 0 & 0 & 0 & 0 \\ 0 & 0 & 1 & 0 & 0 & 0 & 0 \\ 0 & 0 & 0 & 1 & 0 & 0 & 0 \\ 0 & 0 & 0 & 0 & 1 & 0 & 0 \\ 0 & 0 & 0 & 0 & 1 & 0 & 0 \\ 0 & 0 & 0 & 0 & 0 & 1 & 0 \\ 0 & 0 & 0 & 0 & 0 & 0 & 1 \end{pmatrix}, \quad \hat{\mathbf{u}}_g = \begin{pmatrix} \hat{u}_0 \\ \hat{u}_1 \\ \hat{u}_3 \\ \hat{u}_4 \\ \hat{u}_5 \\ \hat{u}_6 \end{pmatrix}, \quad (2.29)$$

The assembly matrix \mathbf{A} ‘scatters’ the global degrees of freedom to local degrees of freedom, while the transpose of it, \mathbf{A}^T , performs the reverse, referred to as global assembly. For example, we wish to perform integration in the domain Ω ,

$$\mathbf{I}_g[j] = (\Phi_j(x), u^\delta(x)), \quad (2.30)$$

where $\mathbf{I}_g \in \mathbb{R}^N$ refers to a vector containing the integral between $\Phi_i(x)$ and $u^\delta(x)$. This is related to first performing integration using local expansion basis within standard elements, and then assembling using \mathbf{A}^T ,

$$\mathbf{I}_g = \mathbf{A}^T \mathbf{I}_l, \quad (2.31a)$$

where,

$$\mathbf{I}_g = \begin{bmatrix} \mathbf{I}_0 \\ \vdots \\ \mathbf{I}_{N_g-1} \end{bmatrix}, \quad \mathbf{I}_l = \begin{bmatrix} \mathbf{I}^0 \\ \vdots \\ \mathbf{I}^{N_{el}-1} \end{bmatrix}, \quad \text{with} \quad \mathbf{I}^e = \begin{bmatrix} \int_{-1}^1 \phi_0^e(\xi) u(\chi^e) \frac{d\chi^e}{d\xi} d\xi \\ \vdots \\ \int_{-1}^1 \phi_{P-1}^e(\xi) u(\chi^e) \frac{d\chi^e}{d\xi} d\xi \end{bmatrix}, \quad (2.31b)$$

and $\mathbf{I}_l \in \mathbb{R}^{N_{loc}}$ refer to the vector of integration operations performed within a standard element. In the spectral/ hp element approach, we perform integration and differentiation using local basis expansions within a standard element. After doing so, we assemble the local operations from the standard element to the global domain by using \mathbf{A}^T , as we shall show later using a 1D example. We note that the structure of assembly matrix is generally sparse, where the entries either contain 0, 1 or -1 in multidimensional formulation. Therefore, the assembly matrix is not constructed in practice, and a mapping array is used instead.

2.3.4 Local basis expansions

The choice of local basis expansions, $\phi_i^e(\xi)$, concerns the representation of the solution, and the convergence properties of the numerical solver, in particular, the condition number of the mass and laplacian matrices. In general, the local basis expansions can be classified into two groups, either *modal* or *nodal* expansions.

Modal expansions

Modal expansions, or hierarchical expansions, describes a set of expansion basis where an expansion set (\mathcal{X}_{P-1}^δ) of order $P - 1$, is contained within a set (\mathcal{X}_P^δ) of order P , e.g. $\mathcal{X}_{P-1}^\delta \subset \mathcal{X}_P^\delta$. An example of modal expansions are the Jacobi polynomials, $P_p^{\alpha,\beta}(x)$, representing a family of solutions to the Sturm-Liouville problem within, $x \in [-1, 1]$. The Jacobi polynomials become symmetric for $\alpha = \beta$, referred to ultraspheric polynomials. Special cases of ultraspheric polynomials are the Legendre polynomials, $\alpha = \beta = 1$, and the Chebyshev polynomials, $\alpha = \beta = 1/2$. Within the Nektar++ framework, we utilise the *modified* basis, constructed using on the Jacobi polynomials and modified (hence its name) by linear expansions given as,

$$\phi_p(\xi) \rightarrow \psi_p(\xi) = \begin{cases} \frac{1-\xi}{2} & \text{for } p = 0 \\ \left(\frac{1-\xi}{2}\right) \left(\frac{1+\xi}{2}\right) P_{p-1}^{1,1}(\xi) & \text{for } 0 < p < P \\ \frac{1+\xi}{2} & \text{for } p = P, \end{cases} \quad (2.32)$$

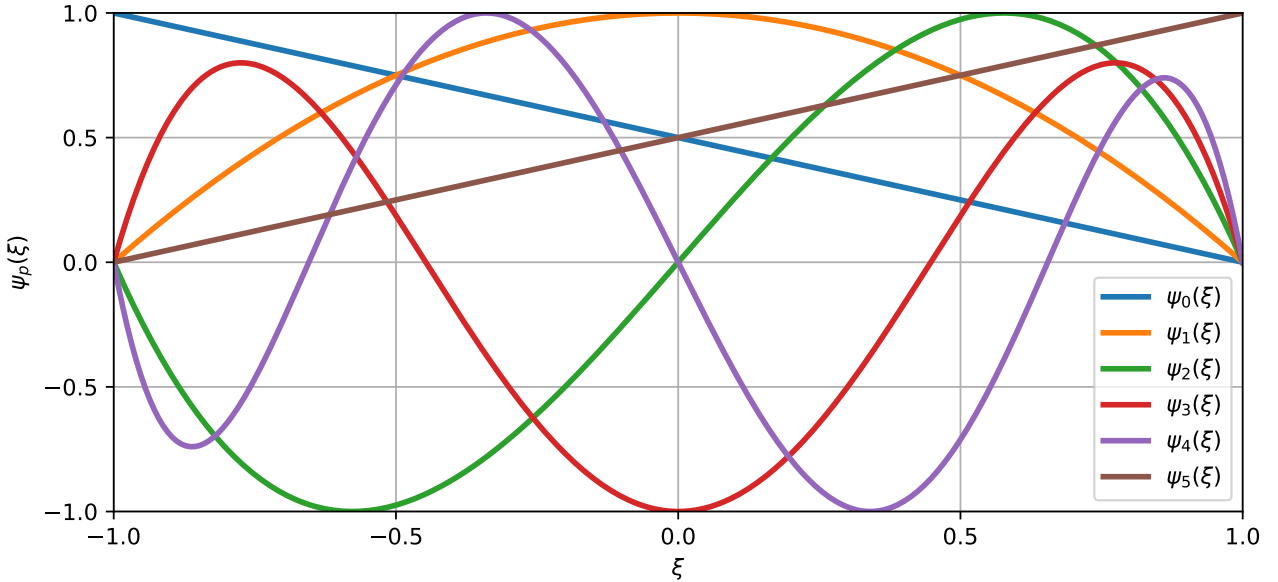


Figure 2.3: The modified basis for up to $P = 5$ normalised to $-1 \leq \psi_p \leq 1$.

We note that $\phi_p(\xi)$ refers to a general local expansion basis while $\psi_p(\xi)$ to definition of the modified basis. The one-dimensional expansion modes of the modified basis of up to $P = 5$ is shown in figure 2.3. The linear modes, corresponding to $p = 0$ and $p = P$, are the only expansions which has a magnitude of at the boundaries, referred to as boundary modes. The modified basis for $0 < p < P$, are clearly hierarchical, and have non-zero values except at the boundaries, referred to as interior/bubble modes.

Nodal expansions

Nodal expansions are basis expansions that are non-hierarchical, $\mathcal{X}_{P-1}^\delta \not\subset \mathcal{X}_P^\delta$. An example of nodal expansions are the Lagrange polynomials,

$$\phi_p(\xi) \rightarrow h_p(\xi) = \frac{\prod_{q=0, q \neq p}^P (\xi - \xi_q)}{\prod_{q=0, q \neq p}^P (\xi_p - \xi_q)} \quad (2.33)$$

The Lagrange polynomials, $h_p(\xi)$, are particular attractive as it has a unit value at discrete nodal values, ξ_q , and zero everywhere else, $h_p(\xi_q) = \delta_{pq}$, which implies that

$$u^\delta(\xi_q) = \sum_{p=0}^P \hat{u}_p h_p(\xi_q) = \sum_{p=0}^P \hat{u}_p \delta_{pq} = \hat{u}_q, \quad (2.34)$$

where the Lagrange coefficient \hat{u}_q is the same as the value evaluated at the node ξ_q . The nodal values, ξ_q , are based on the Gauss-Lobatto-Legendre (GLL) points which will be defined later in §2.3.5. Figure 2.4 presents Lagrange expansions evaluated along the GLL points.

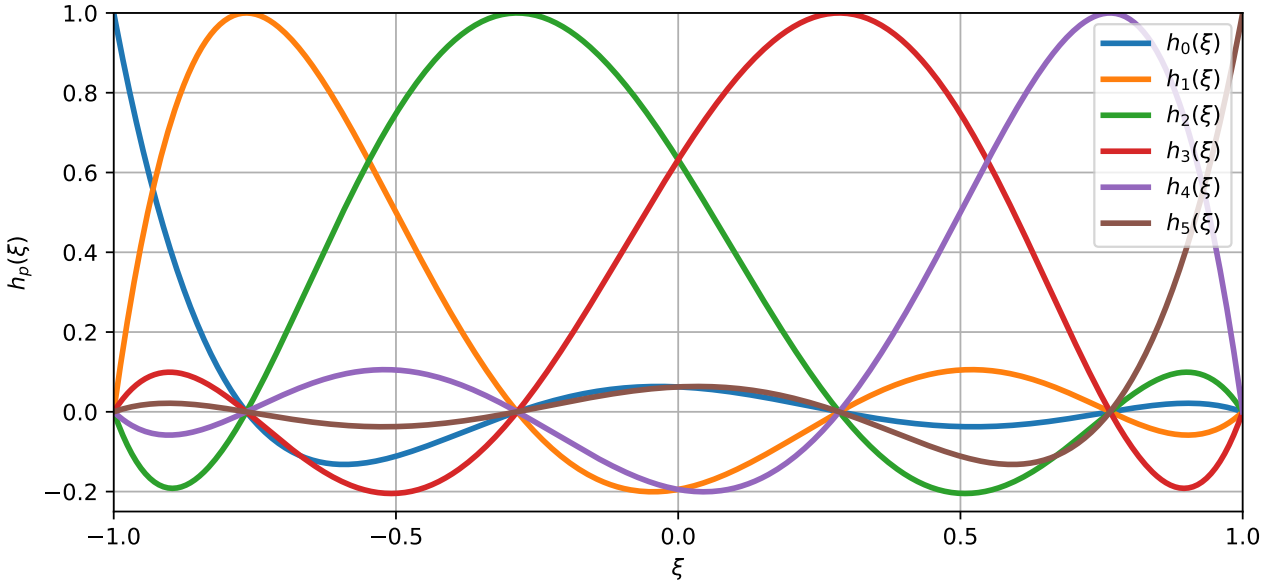


Figure 2.4: Lagrange polynomials for $P = 5$ with nodal values along GLL points.

Multi-dimensional expansions

We have introduced modal and nodal expansions in one dimension, and its extension to multi-dimensions bases can be generalised using a tensorial expansion of the local expansion bases. The standard element in a two dimensional quadrilateral, \mathcal{Q}^2 , and a three dimensional hexahedral \mathcal{H}^3 , are given as,

$$\mathcal{Q}^2 = \{-1 \leq \xi_1, \xi_2 \leq 1\}, \quad \mathcal{H}^3 = \{-1 \leq \xi_1, \xi_2, \xi_3 \leq 1\} \quad (2.35)$$

where ξ_1, ξ_2, ξ_3 refers to the local coordinates in multi-dimensions. Thus, the multi-dimensional expansion bases for quadrilaterals and hexadrals using modified bases are simply a tensor product of the one dimensional modified bases,

$$\phi_{pq}(\xi_1, \xi_2) = \psi_q(\xi_1)\psi_q(\xi_2), \quad \text{and} \quad \phi_{pqr}(\xi_1, \xi_2, \xi_3) = \psi_q(\xi_1)\psi_q(\xi_2)\psi_r(\xi_3). \quad (2.36)$$

An example of the modal tensorial bases, for $p = q = 4$ in a standard quadrilateral element is shown in figure 2.5. While we have discussed the tensorial the expansions for regular domains such as the standard quadrilateral and hexahedral elements, the extensions for simplex domains such as triangles, tetrahedrals, prisms and pyramids commonly used to represent complex geometries, are less straightforward. The challenge for simplexes is that the local coordinates, ξ_1, ξ_2, ξ_3 , become dependent where a direct tensorial expansion becomes unwieldy. Instead, a collapsed coordinate system is introduced, providing a transformation from a standard simplex element to a standard regular element. In this thesis, we utilise quadrilateral elements. The reader is referred to [Karniadakis and Sherwin \[2005\]](#) for more details about the multi-dimensional formulation of regular and simplex elements.

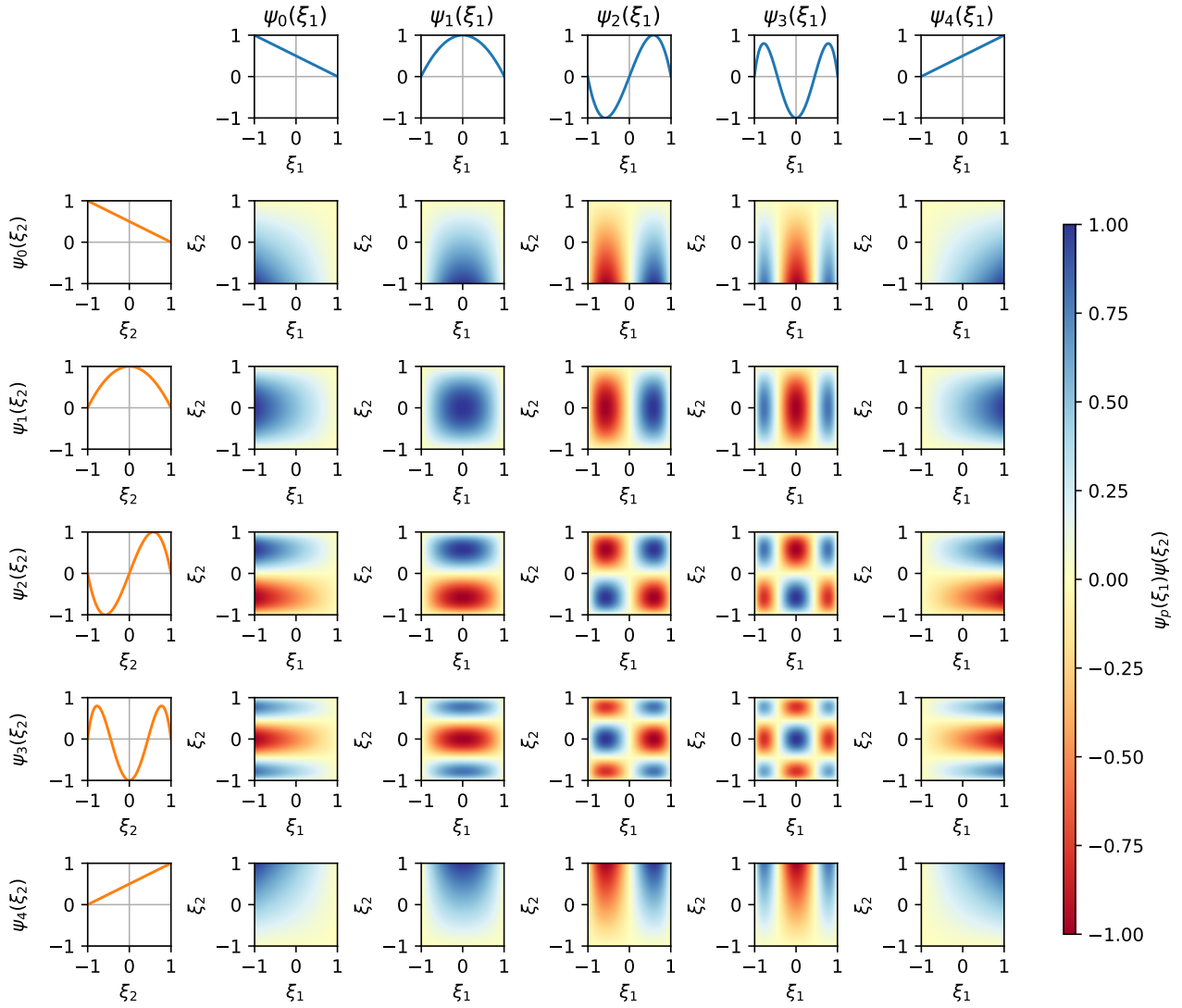


Figure 2.5: Two dimensional modified basis with $p = q = 4$ in a standard quadrilateral, $-1 \leq \xi_1, \xi_2 \leq 1$. The modified bases are normalised to $-1 \leq \phi_{pq} \leq 1$.

2.3.5 Gaussian quadrature

In the Galerkin formulation, we perform integration between basis functions routinely, and an efficient numerical technique is sought after. Suppose we want to approximate the integral of a function, $u(\xi)$, in a standard element numerically given as,

$$\int_{-1}^1 u(\xi) \, d\xi = \sum_{i=0}^{Q-1} w_i u(\xi_i) + R(u). \quad (2.37)$$

The premise is determine the optimal number of quadrature points, Q , integration weights, w_i , and zeros, ξ_i , in which the integral error, $R(u)$, can be minimised. If $u(\xi)$ is of polynomial order of P , we may expect that we require at least $P + 1$ equispaced points to represent $u(\xi)$ sufficiently. Using Gaussian quadrature rules, we can approximate an integral of a function of order P , with far fewer than $P + 1$ points with specific integration weights and zeros. In general, Gaussian quadrature rules

can be grouped into three categories: Gauss, Gauss-Radau and Gauss-Lobatto quadrature. The main difference between the three categories are on the inclusion of the end points. Gauss quadrature rule evaluates the integral without the end points $\xi = \pm 1$. Gauss-Radau quadrature rule either select one of the end points, typically at $\xi = -1$. Gauss-Lobatto quadrature rule consider both end points. We will only focus on describing the Gauss-Lobatto quadrature rules and the zeros of Jacobi polynomials known as the Gauss-Lobatto-Jacobi quadrature rules given as,

$$\xi_i^{\alpha,\beta} = \begin{cases} -1 & i = 0, \\ \xi_{i-1,Q-2}^{\alpha+1,\beta+1} & i = 1, \dots, Q-2, \\ 1, & i = Q-1, \end{cases} \quad (2.38a)$$

$$w_i^{\alpha,\beta} = \begin{cases} (\beta + 1)C_{0,Q-2}^{\alpha,\beta}, & i = 0, \\ C_{i,Q-2}^{\alpha,\beta}, & i = 1, \dots, Q-2, \\ (\alpha + 1)C_{Q-1,Q-2}^{\alpha,\beta}, & i = Q-1, \end{cases} \quad (2.38b)$$

$$C_{i,Q-2}^{\alpha,\beta} = \frac{2^{\alpha+\beta+1}\Gamma(\alpha+Q)\Gamma(\beta+Q)}{(Q-1)(Q-1)!\Gamma(\alpha+\beta+Q+1)[P_{Q-1}^{\alpha,\beta}(\xi_i)]^2} \quad (2.38c)$$

where $w_i^{\alpha,\beta}$, $\xi_i^{\alpha,\beta}$ are the zeros (or sometimes referred to as quadrature points) and weights of the Gauss-Lobatto-Jacobi quadrature rules, and Γ refers to the Gamma function. For $\alpha = \beta = 0$, the quadrature points is known as the Gauss-Lobatto-Legendre (GLL) points, typically employed for Lagrange polynomials. By evaluating the integral using the zeros and integrations weights defined above, we can obtain an exact integral of the function $u(\xi)$, of polynomial order P , with at least $Q \geq (P+3)/2$ quadrature points.

2.3.6 Numerical differentiation

In the same fashion as Gaussian quadrature rules, we want to evaluate the derivative of a function, $u^\delta(\xi)$ numerically. Suppose that we want to differentiate in x using local coordinates given as,

$$\frac{du^\delta(\xi)}{dx} = \frac{du^\delta(\xi)}{d\xi} \frac{d\xi}{dx} = \sum_{p=0}^P \hat{u}_p \frac{d\phi_p(\xi)}{d\xi} \frac{d\xi}{dx}, \quad (2.39)$$

where $d\xi/dx$ is the jacobian. The main step in involves evaluating the derivative of the local expansion bases, $d\phi_p(\xi)/d\xi$, referred to as collocation differentiation as differentiation is performed in physical space. Suppose that we express the solution of polynomial order P with modified polynomials, $\phi_p(\xi) \rightarrow \psi_p(\xi)$, through a set of $Q \geq P+1$ quadrature points, the derivative in discrete local coordinates is expressed as,

$$\left. \frac{du^\delta(\xi)}{d\xi} \right|_{\xi=\xi_i} = \sum_{j=0}^{Q-1} \hat{u}_j \left. \frac{d\psi_j(\xi)}{d\xi} \right|_{\xi=\xi_i} = \sum_{j=0}^{Q-1} D_{ij} \hat{u}_j, \quad (2.40)$$

where D_{ij} refers to the differential matrix containing values of the derivative of the basis at discrete quadrature points given as,

$$D_{ij} = \frac{dh_j(\xi)}{d\xi} \Big|_{\xi=\xi_i}, \quad (2.41)$$

which is often pre-computed. To differentiate a function, $u(\xi)$, we typically need to construct the differential matrices, and the general representation of the differential matrix is,

$$D_{ij} = \begin{cases} \frac{p'_Q(\xi_i)}{p'_Q(\xi_j)} \frac{1}{\xi_i - \xi_j}, & i \neq j, \\ \frac{p''_Q(\xi_i)}{2p'_Q(\xi_i)}, & i = j. \end{cases} \quad (2.42)$$

where $p'_Q(\xi_i), p''_Q(\xi_i)$ refers to the first and second differentiative of Jacobi polynomials evaluated at the quadrature points ξ_i .

2.3.7 Example in 1D

We have outlined the basic formulation of spectral/ hp element methods in a single dimension. To conclude the section on spectral/ hp element methods, we will describe its solution procedure, converting the weak form of the Helmholtz equation into a system of linear equations, and introduce the mass and laplacian matrices. Starting from the weak form,

$$\underbrace{\lambda \int_{-1}^1 v^\delta u^H d\xi}_{\mathbf{M}^e \hat{\mathbf{u}}^e} + \underbrace{\int_{-1}^1 \frac{\partial v^\delta}{\partial \xi} \frac{\partial u^H}{\partial \xi} d\xi}_{\mathbf{L}^e \hat{\mathbf{u}}^e} = \underbrace{\int_{-1}^1 v^\delta f d\xi}_{\hat{\mathbf{f}}^e} - \underbrace{\int_{-1}^1 \frac{\partial v^\delta}{\partial \xi} \frac{\partial u^D}{\partial \xi} d\xi}_{\mathbf{L}^0} + v(l)g_N, \quad (2.43)$$

we wish to seek the solution $u^H(\xi)$. Recall that the solution space of $u^H(\xi)$ and $v^\delta(\xi)$ are the same, following the standard Galerkin projection procedure. Suppose they can be discretised by spectral/ hp elements with e elements and local basis expansions of up to polynomial order P ,

$$u^H(\xi) = \sum_{i=0}^P \hat{u}_i^e \phi_i^e(\xi), \quad v^\delta(\xi) = \sum_{i=0}^P \hat{v}_i^e \phi_i^e(\xi). \quad (2.44)$$

Substituting into equation (2.43) and evaluating the first term on the left hand side through a set of Q quadrature points.

$$\begin{aligned} \int_{-1}^1 \sum_{i=0}^P \hat{v}_i^e \phi_i^e(\xi) \sum_{i=0}^P \hat{u}_i^e \phi_i^e(\xi) d\xi &= \sum_{q=0}^{Q-1} \left[\sum_{i=0}^P \hat{v}_i^e \phi_i^e(\xi_q) \sum_{i=0}^P \hat{u}_i^e \phi_i^e(\xi_q) \right] w_q^e \\ &= (\hat{\mathbf{v}}^e)^T (\mathbf{B}^e)^T \mathbf{W}^e \mathbf{B}^e \hat{\mathbf{u}}^e \\ &= \hat{\mathbf{v}}^T \mathbf{M}^e \hat{\mathbf{u}}^e \end{aligned} \quad (2.45)$$

where $\mathbf{M}^e = (\mathbf{B}^e)^T \mathbf{W} \mathbf{B}^e \in \mathbb{R}^{(P+1) \times (P+1)}$ refers to the elemental mass matrix, while $\mathbf{B}^e \in \mathbb{R}^{Q \times (P+1)}$ refers to the elemental basis matrix, and $\mathbf{W}^e \in \mathbb{R}^{Q \times Q}$, the elemental weight matrix, a diagonal matrix

consisting of discrete integration weights along Q quadrature points.

$$\mathbf{B}^e = \begin{bmatrix} \phi_0(\xi_0) & \cdots & \phi_P(\xi_0) \\ \vdots & \ddots & \vdots \\ \phi_0(\xi_Q) & \cdots & \phi_P(\xi_Q) \end{bmatrix}, \quad \mathbf{W}^e = \begin{bmatrix} w_0^e & & 0 \\ & \ddots & \\ 0 & & w_{Q-1}^e \end{bmatrix} \quad (2.46)$$

Next, we move onto the second term on the left hand side,

$$\begin{aligned} \int_{-1}^1 \sum_{i=0}^P \hat{v}_i^e \frac{d\phi_i^e}{d\xi} \sum_{i=0}^P \hat{u}_i^e \frac{d\phi_i^e}{d\xi} d\xi &= \sum_{q=0}^Q \left[\sum_{i=0}^P \hat{v}_i^e D_{qi}^e \phi_i^e(\xi_q) \sum_{i=0}^P \hat{u}_i^e D_{qi}^e \phi_i^e(\xi_q) \right] w_q^e \\ &= \hat{\mathbf{v}}^T (\mathbf{B}^e)^T (\mathbf{D}^e)^T \mathbf{W}^e \mathbf{D}^e \mathbf{B}^e \hat{\mathbf{u}}^e \\ &= \hat{\mathbf{v}}^T \mathbf{L}^e \hat{\mathbf{u}}^e \end{aligned} \quad (2.47)$$

where $\mathbf{L}^e = (\mathbf{B}^e)^T (\mathbf{D}^e)^T \mathbf{W}^e \mathbf{D}^e \mathbf{B}^e \in \mathbb{R}^{(P+1) \times (P+1)}$ refers to the elemental Laplacian matrix while $\mathbf{D}^e \in \mathbb{R}^{Q \times (P+1)}$ refers to the differential matrix defined in equation (2.42). Moving onto the first term on the right hand side,

$$\begin{aligned} \int_{-1}^1 \sum_{i=0}^P \hat{v}_i^e \phi_i^e(\xi) f^e(\xi) d\xi &= \sum_{q=0}^P \sum_{i=0}^P \hat{v}_i^e \phi_i^e(\xi_q) f^e(\xi_q) w_q^e, \\ &= \hat{\mathbf{v}}^T (\mathbf{B}^e)^T \mathbf{W}^e \mathbf{f}^e \\ &= \hat{\mathbf{v}}^T \hat{\mathbf{f}}^e, \end{aligned} \quad (2.48)$$

where $\hat{\mathbf{f}}^e$, is referred to the elemental forcing vector. As we bolt the elemental laplacian, mass matrices, and forcing vector, the system of linear equations within a standard element is given as,

$$[\lambda \mathbf{M}^e + \mathbf{L}^e] \hat{\mathbf{u}}^e = \hat{\mathbf{f}}^e. \quad (2.49)$$

We note that the boundary conditions have been omitted. To include the boundary conditions, we consider the full system of linear of equations consisting of e number of elements,

$$\lambda \underbrace{\begin{bmatrix} \mathbf{M}^0 + \mathbf{L}^0 & \mathbf{0} \\ \mathbf{0} & \ddots \\ \mathbf{0} & \mathbf{M}^{N_{el}-1} + \mathbf{L}^{N_{el}-1} \end{bmatrix}}_{\mathbf{M}_l + \mathbf{L}_l} \underbrace{\begin{bmatrix} \hat{\mathbf{u}}^0 \\ \vdots \\ \hat{\mathbf{u}}^{N_{el}-1} \end{bmatrix}}_{\hat{\mathbf{u}}_l} = \underbrace{\begin{bmatrix} \hat{\mathbf{f}}^0 \\ \vdots \\ \hat{\mathbf{f}}^{N_{el}-1} \end{bmatrix}}_{\hat{\mathbf{f}}_l} + \underbrace{\begin{bmatrix} \mathbf{L}^0 g_D \\ \vdots \\ \mathbf{0} \end{bmatrix}}_{\mathbf{g}_D} + \underbrace{\begin{bmatrix} \mathbf{0} \\ \vdots \\ g_N \end{bmatrix}}_{\mathbf{g}_N}, \quad (2.50)$$

where $\mathbf{M}_l \in \mathbb{R}^{N_{el}(P+1) \times N_{el}(P+1)}$, $\mathbf{L}_l \in \mathbb{R}^{N_{el}(P+1) \times N_{el}(P+1)}$, $\hat{\mathbf{u}}_l \in \mathbb{R}^{N_{el}(P+1)}$ refers to the local mass matrix, local laplacian matrix and the vector of local expansion coefficients. On the right hand side, $\hat{\mathbf{f}}_l \in \mathbb{R}^{N_{el}(P+1)}$, $\mathbf{g}_D^{N_{el}(P+1)}$, $\mathbf{g}_N^{N_{el}(P+1)}$ refers local forcing vector, Dirichlet and Neumann boundary conditions in vector form. Lastly, to ensure that the solution remains C^0 continuous across the elemental

boundaries, we perform the assembly process by using the assemble matrices (see §2.3.3),

$$\lambda \mathbf{A}^T (\mathbf{M}_l + \mathbf{L}_l) \mathbf{A} \hat{\mathbf{u}}_g = \mathbf{A}^T (\hat{\mathbf{f}}^l + \mathbf{g}_D + \mathbf{g}_N), \quad (2.51)$$

and obtain the solution for $\hat{\mathbf{u}}_g$.

2.4 Numerical techniques for solving the Navier-Stokes equations

2.4.1 Velocity Correction Scheme

The spatial discretisation of the Helmholtz operator and its numerical solution procedure has been discussed using the spectral/ hp element methods. Here, we describe the numerical methods that is used to solve the Navier-Stokes equations given as,

$$\frac{\partial \mathbf{u}}{\partial t} + (\mathbf{u} \cdot \nabla) \mathbf{u} = -\nabla p + \nu \nabla^2 \mathbf{u} + \mathbf{f} \quad (2.52a)$$

$$\nabla \cdot \mathbf{u} = 0, \quad (2.52b)$$

with boundary conditions,

$$\mathbf{u} = 0, \quad \text{on } \partial\Omega. \quad (2.52c)$$

Here, the primitive variables are velocity and pressure (\mathbf{u}, p) and we assumed unit density, $\rho = 1$, with the kinematic viscosity appearing as the control parameter. The time evolution of velocity is explicit expressed in equation (2.52a), but does not appear for the pressure, which is coupled to the velocity field, enforcing the incompressibility condition. Several strategies exist for addressing the coupled velocity-pressure fields by

1. Solving the coupled system such as the Uzawa algorithm,
2. Splitting methods,
3. Change of coordinates (e.g. vorticity-streamfunction approach).

We adopt splitting methods, which solves the of the Navier-Stokes equation by splitting them into ‘subequations’, and solving them sequentially. These methods, belonging to the broader family of projection methods introduced by Chorin [1967] and Témam [1969], and can be further classified into pressure-correction or velocity-correction schemes. This thesis employs the use of the high-order velocity-correction scheme introduced by Karniadakis et al. [1991]. We rewrite the incompressible Navier-Stokes equations in semi-discrete form with using linear and nonlinear operators as,

$$\frac{\partial \mathbf{u}}{\partial t} = \mathbf{N}(\mathbf{u}) - \nabla p + \nu \mathbf{L}(\mathbf{u}), \quad (2.53a)$$

$$\nabla \cdot \mathbf{u} = 0, \quad (2.53b)$$

with boundary conditions,

$$\mathbf{u}|_{\Omega} = 0, \quad \mathbf{u}(t = 0) = \mathbf{u}_0. \quad (2.53c)$$

The nonlinear, \mathbf{N} , linear, \mathbf{L} , operators are obtained from a suitable spatial-discretisation method such as the spectral/ hp element method. The nonlinear and linear operators are defined as,

$$\mathbf{N}(\mathbf{u}) \equiv -(\mathbf{u} \cdot \nabla)\mathbf{u} = -\frac{1}{2}[(\mathbf{u} \cdot \nabla)\mathbf{u} + \nabla \cdot (\mathbf{u}\mathbf{u})], \quad \mathbf{L}(\mathbf{u}) \equiv \nabla^2\mathbf{u}, \quad (2.54)$$

We note that the nonlinear terms are written in the skew-symmetric to minimise aliasing errors [Karniadakis et al., 1991]. To advance the velocity at time step, \mathbf{u}^n , to the next time step, \mathbf{u}^{n+1} , we integrate equation (2.53) over a time step Δt ,

$$\mathbf{u}^{n+1} - \mathbf{u}^n = \underbrace{\int_{t_n}^{t_{n+1}} \mathbf{N}(\mathbf{u}) dt}_{\Delta t \sum_{q=0}^{J_e-1} \beta_q \mathbf{N}(\mathbf{u}^{n-q})} - \underbrace{\int_{t_n}^{t_{n+1}} \nabla p dt}_{\Delta t \nabla \bar{p}^{n+1}} + \nu \underbrace{\int_{t_n}^{t_{n+1}} \mathbf{L}(\mathbf{u}) dt}_{\Delta t \sum_{q=0}^{J_i-1} \gamma_q \mathbf{L}(\mathbf{u}^{n+1-q})}. \quad (2.55)$$

The velocity correction scheme evaluates the underbraced terms in three successive independently from left to right independently, effectively ‘splitting’ equation (2.53) from this point onwards. The first step we perform is to extrapolate the advection velocities, by approximating the nonlinear terms using an explicit scheme such as the Adams-Bashforth family of J_e order,

$$\frac{\hat{\mathbf{u}} - \sum_{q=0}^{J_e-1} \alpha_q \mathbf{u}^{n-q}}{\Delta t} = \sum_{q=0}^{J_e-1} \beta_q \mathbf{N}(\mathbf{u}^{n-q}), \quad (2.56)$$

where $\hat{\mathbf{u}}$ is denotes the primary intermediate velocity field desired and α_e, β_e refers to the time integration coefficients for a prescribe J_e -th order, described later. After evaluting $\hat{\mathbf{u}}$, we move onto the second term in equation (2.55), which defines the pressure at time step $n + 1$ as,

$$\frac{\hat{\mathbf{u}} - \hat{\mathbf{u}}}{\Delta t} = -\nabla p^{n+1}. \quad (2.57)$$

$\hat{\mathbf{u}}$ denotes as the secondary intermediate velocity. In this single equation, we seek to obtain two unknown solutions, $\hat{\mathbf{u}}$ and p^{n+1} , which is ill-posed, and seek to impose certain restrictions. The splitting method assumes that the secondary intermediate velocity is divergence free, $\nabla \cdot \hat{\mathbf{u}} = 0$, and satisfies the Dirichlet boundary conditions normal to the boundary, $\hat{\mathbf{u}} \cdot \mathbf{n} = \mathbf{u}|_{\Omega} \cdot \mathbf{n}$. By considering the assumptions above and the divergence of equation (2.57), we obtain the pressure Poisson equation with the primary intermediate velocity acting as the forcing term,

$$\nabla^2 p^{n+1} = \nabla \cdot \left(\frac{\hat{\mathbf{u}}}{\Delta t} \right) \quad (2.58a)$$

and boundary conditions,

$$\frac{\partial p^{n+1}}{\partial n} = \mathbf{n} \cdot \left(\frac{\hat{\mathbf{u}} - \hat{\mathbf{u}}}{\Delta t} \right). \quad (2.58b)$$

While the pressure boundary condition (2.58b) is straightforward to evaluate, it is sensitive to large splitting errors [Karniadakis et al., 1991]. To overcome this, we consider a high-order boundary condition of pressure, obtained by taking the normal dot product of equation (2.53),

$$\frac{\partial p^{n+1}}{\partial t} = - \sum_{q=0}^{J_e-1} \beta_q \left[\frac{1}{\Delta t} \mathbf{u}^{n-q} + \nu [\nabla \times (\nabla \times \mathbf{u}^{n-q})] + (\mathbf{u}^{n-q} \cdot \nabla) \mathbf{u}^{n-q} \right] \cdot \mathbf{n}. \quad (2.59)$$

Notably, the linear operator is expressed as $\mathbf{L}(\mathbf{u}) = \nabla(\nabla \cdot \mathbf{u}) - \nabla \times (\nabla \times \mathbf{u})$, favouring numerical stability [Orszag et al., 1986, Karniadakis et al., 1991]. J_e is the order the explicit scheme as in equation (2.56). After solving for the pressure Poisson equation, the secondary intermediate velocity could be subsequently obtained using equation (2.57). After which, we can move onto the final substep in equation (2.55), by solving a Helmholtz equation for \mathbf{u}^{n+1} ,

$$\frac{\gamma_0 \mathbf{u}^{n+1} - \hat{\mathbf{u}}}{\Delta t} = \nu \sum_{q=0}^{J_i-1} \gamma_q \mathbf{L}(\mathbf{u}^{n+1-q}), \quad (2.60)$$

where the linear terms are treated based similar to the family of Adams-Moulton implicit scheme and J_i, γ_q denotes the order of the scheme and time integration coefficients, completing the velocity correction scheme. The time integration coefficients are determined from stiffly stable schemes shown in table 2.2, an improvement from the Adams-family schemes [Karniadakis et al., 1991]. The high

Coefficients	1^{st} order	2^{nd} order	3^{rd} order
γ_0	1	3/2	11/6
α_0	1	2	3
α_1	0	-1/2	-3/2
α_2	0	0	1/3
β_0	1	2	3
β_1	0	-1	-3
β_2	0	0	1

Table 2.2: Integration coefficient of stiffly stable schemes from Karniadakis et al. [1991].

order velocity correction scheme and be summarised in a three step process of the following,

$$\mathbf{u}^n \xrightarrow{\mathbf{N}(\mathbf{u}^n)} \hat{\mathbf{u}} \xrightarrow{\nabla^2 p} \hat{\mathbf{u}} \xrightarrow{\mathbf{L}(\hat{\mathbf{u}})} \mathbf{u}^{n+1},$$

evolving the velocity fields at time step n to $n + 1$.

2.4.2 Fourier spectral/ hp modes

Fourier-Chebyshev-Fourier type discretisation have been recognised as preferred method for performing direct numerical simulations (DNS) of transitional or turbulent channel flows [Kim et al., 1987] owing to its efficient representation of the inhomogeneous wall-normal directions and the homogeneous streamwise and spanwise directions, using Chebyshev and Fourier expansions respectively.

The Fourier spectral/ hp element method draws on this approach, where the homogeneous and

the inhomogeneous directions are represented by the Fourier expansions and spectral/ hp elements respectively. This approach has been commonly referred to as the Quasi-3D or (2.5D) approach, allowing for the representation of two inhomogeneous directions. For example, in the turbulent channel flows with riblets, the Fourier expansions are used to represent the periodic streamwise, while the spectral/ hp elements are used to discretise the wall-normal direction. In the analysis of three-dimensional wakes of cylinders where the Fourier expansions are treated in the spanwise directions. In this thesis, we routinely use the the Quasi-3D approach, consisting of the 2D spectral/ hp elements with 1D Fourier expansions are used to discretise the cross stream plane and streamwise flow respectively. The velocity and pressure in the spectral/ hp plane is described by two dimensional modified bases with Fourier expansions,

$$\begin{bmatrix} \mathbf{u}^\delta(x, y, z, t) \\ p^\delta(x, y, z, t) \end{bmatrix} = \sum_{k=0}^{N_z-1} \sum_{p=0}^P \sum_{q=0}^P \psi_p(x) \psi_q(y) e^{ik\beta z} \begin{bmatrix} \hat{\mathbf{u}}_{p,q,k}(t) \\ \hat{p}_{p,q,k}(t) \end{bmatrix} = \sum_{k=0}^{N_z-1} e^{ik\beta z} \begin{bmatrix} \tilde{\mathbf{u}}_k(x, y, t) \\ \tilde{p}_k(x, y, t) \end{bmatrix} \quad (2.61)$$

where $\beta = \frac{2\pi}{L_z}$ is the spanwise wavenumber, L_z the spanwise length, N_z the number of Fourier expansions. Substituting equation 2.61 into the Navier-Stokes equations and taking the Fourier transform (equivalently to the Galerkin projection with respect to Fourier expansion as a test function) yields a system of N_z decoupled equations, amenable for parallel processing,

$$\frac{\partial \tilde{\mathbf{u}}_k}{\partial t} = -\tilde{\nabla}_k \tilde{p}_k + \nu(\nabla_{x,y}^2 - k^2 \beta^2) \tilde{\mathbf{u}}_k - [\widehat{(\mathbf{u} \cdot \nabla) \mathbf{u}}]_k \quad (2.62a)$$

$$-k\beta \tilde{\nabla} \cdot \tilde{\mathbf{u}}_k = 0, \quad k = 0, \dots, N_z - 1 \quad (2.62b)$$

where, $\tilde{\nabla}_k = (\frac{\partial}{\partial x}, \frac{\partial}{\partial y}, ik\beta)$, $\nabla_{x,y}^2 = (\frac{\partial^2}{\partial x^2}, \frac{\partial^2}{\partial y^2})$ and $[(\widehat{\mathbf{u} \cdot \nabla}) \mathbf{u}]_k$ refers to the Fourier-transformed of the k^{th} nonlinear term.

2.4.3 Maintaining fluid flow through a channel

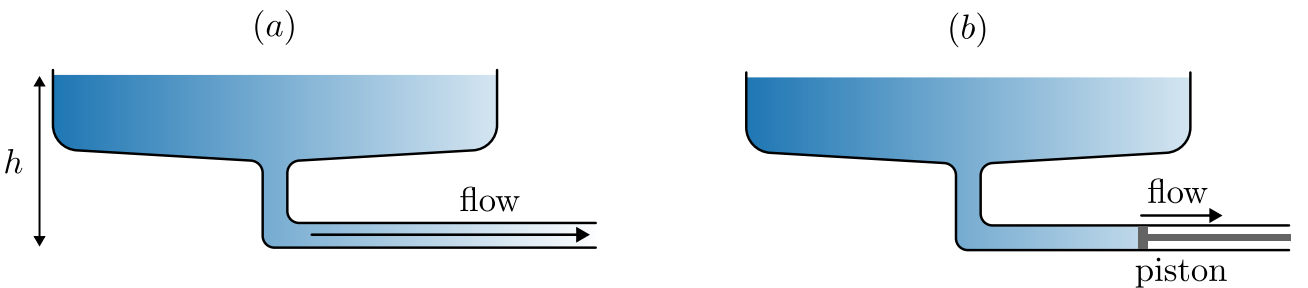


Figure 2.6: (a) Flow rate driven by a pressure gradient from an reservoir elevated by h . (b) Flow driven by a piston at a constant flow rate.

In general, there are two approaches to drive a fluid flow through a channel, either by maintaining a constant pressure drop, or a constant volumetric flux (flow rate). This difference is illustrated in figure 2.6, whereby the flow through the channel is driven by a constant pressure drop from an elevated

reservoir of constant height h in figure 2.6(a), while a piston moves at a constant speed rightwards, drawing fluid through the channel at a constant volumetric flux in figure 2.6(b).

Constant pressure via body-forcing

As we prescribe the homogeneous direction along the streamwise directions, a pressure drop cannot be prescribe directly. Instead, we substitute the constant pressure drop with a constant body force $\mathbf{f} = f_x \hat{\mathbf{e}}_x$ in the streamwise direction,

$$\frac{\partial u}{\partial t} + (u \cdot \nabla)u = -\nabla p + \nu \nabla^2 u + f_x, \quad (2.63)$$

The central question now becomes what is the magnitude of body force required a laminar or turbulent flow. To begin this discussion, we assume that we can decompose our flow variables into a mean and a fluctuating component,

$$u(x, y, t) = U(y) + u'(x, y, t), \quad (2.64)$$

where $U(y) = \langle u \rangle$ refers to the averaged velocity and $\langle \cdot \rangle = \frac{1}{TL_x L_z} \int \cdot dz dx dt$ refers to the temporal and span-averaged operator. The fluctuating component is defined with an average of 0, i.e. $\langle u' \rangle = 0$. Next, we substitute this decomposition into equation (2.63), and perform the averaging operation,

$$\begin{aligned} & \left\langle \frac{\partial(U + u')}{\partial t} + (U + u') \frac{\partial(U + u')}{\partial x} + (V + v') \frac{\partial(V + v')}{\partial y} \right. \\ & \left. = -\frac{\partial(P + p')}{\partial x} + \nu \nabla^2(U + u') + F_x + f'_x \right\rangle. \end{aligned} \quad (2.65)$$

For a statistically stationary turbulent (or laminar) channel flow with periodic streamwise boundary conditions, we can make the following assumptions:

1. stationary flow $\frac{\partial U}{\partial t} = 0$,
2. fully-developed in x , $\frac{\partial}{\partial x} \rightarrow 0$,
3. $\frac{\partial V}{\partial y} = 0$, as a consequence of continuity and the no-slip boundary condition.
4. $\langle u', v', w', p' \rangle = 0$, based on the definition of fluctuations,
5. $\frac{\partial p}{\partial x} = 0$ due to the enforced periodicity in x .

Applying the assumptions above, the mean momentum equations simplify into,

$$\langle F_x \rangle = \left\langle \frac{\partial(u'v')}{\partial y} \right\rangle - \nu \frac{\partial U^2}{\partial y^2}, \quad (2.66)$$

where the body force on the left-hand side balances the sum of Reynolds stresses and viscous diffusion on the right-hand side. Next, we integrate the expression from $y \in [-1, 1]$,

$$2F_x = [\langle u'v' \rangle]_{y=-1}^{y=1} + \nu \left[\frac{\partial U}{\partial y} \Big|_{y=1} - \frac{\partial U}{\partial y} \Big|_{y=-1} \right]. \quad (2.67)$$

The wall shear stress is defined by $\tau_w = \nu \frac{\partial U}{\partial y} \Big|_{y=1}$ (ρ is assumed to be 1), and it is antisymmetric about the channel centreline, $\nu \frac{\partial U}{\partial y} \Big|_{y=1} = -\nu \frac{\partial U}{\partial y} \Big|_{y=-1}$. Due to the no-slip condition, the Reynolds shear stresses is zero, i.e. $[u'v'] \Big|_{y=-1,1} = 0$. Hence, the expression above simplifies to,

$$\tau_w = F_x. \quad (2.68)$$

In other words, the body force F_x is balanced by the wall shear stress (drag), τ_w , along the channel walls. In the case of laminar flow, τ_w can be determined analytically, and the body force required for sustaining a laminar flow for a velocity profile of $u(y) = 1 - y^2$, is $F_x = -2\nu$. However, to determine the wall shear stress (and hence the magnitude of body force) is not as straightforward task for transitional or turbulent channel flow as there isn't an analytical expression for τ_w and its dependence on Reynolds number. Instead, we can only rely on empirical relations of turbulent channel flow between the skin friction coefficient, $c_f = \tau_w / \frac{1}{2} \rho U_c^2$ and Reynolds number Re_c from [Dean \[1978\]](#).

$$c_f = 0.00302 Re_c^{-1/4}, \quad (2.69)$$

where Re_c is the Reynolds number based on the laminar centerline velocity. Similarly, the skin

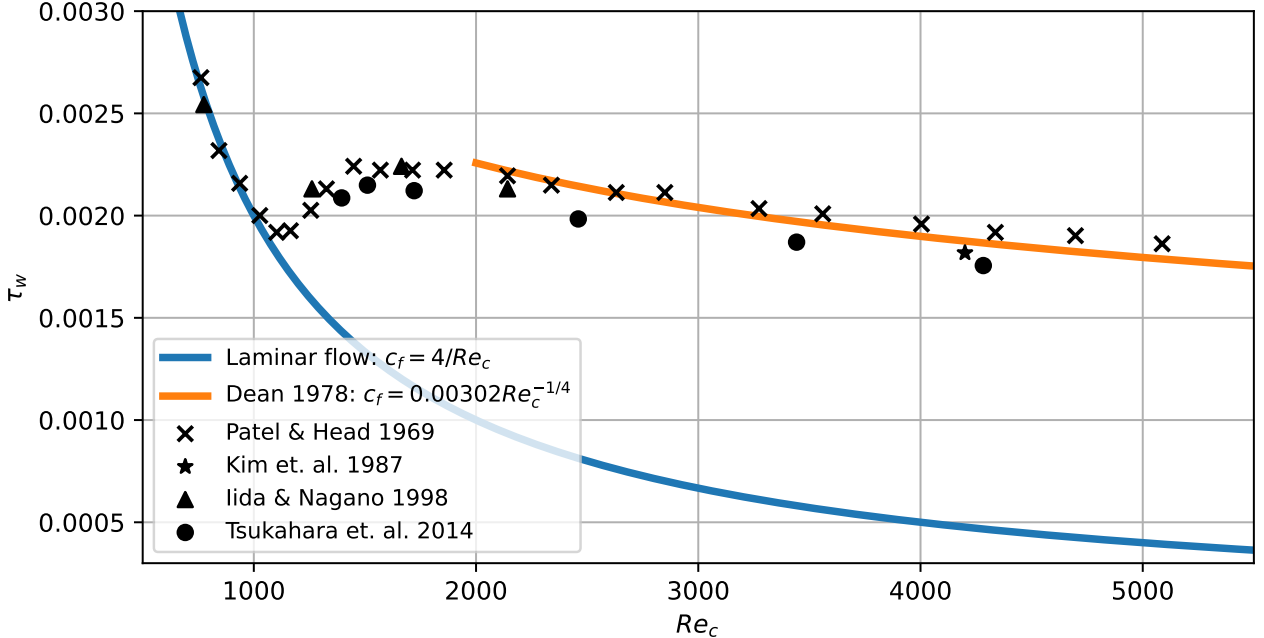


Figure 2.7: τ_w against Re_c using skin friction coefficients from [Dean \[1978\]](#) with $\rho = U_c = 1$. Experimental scatter points from [[Patel and Head, 1969](#), [Kim et al., 1987](#), [Iida and Nagano, 1998](#), [Tsukahara et al., 2014a](#)].

friction coefficient for the case of laminar flow is $c_f = 4/Re_c$ [Dean, 1978]. Figure 2.7 illustrates the relationship between τ_w and Re_c of channel flow using empirical relationship from Dean [1978] (here $\rho = U_c = 1$) and experimental data from Patel and Head [1969], Kim et al. [1987], Iida and Nagano [1998], Tsukahara et al. [2014a]. While the empirical relation for laminar flow, $Re_c \lesssim 1000$ and turbulent flow $Re_c \gtrsim 2000$ appears reasonably robust, the wall shear stress in the transitional region is lacking therefore, the body forcing approach is not preferred.

Constant volumetric flux

An alternative approach is to enforce a constant volumetric flux, illustrated using the piston method in figure 2.6(b). We employ the efficient Green's function approach introduced by Chu and Karniadakis [1993], and outline its solution procedure. The volumetric flux is defined as,

$$Q(\mathbf{u}) = \frac{1}{2\mu(R)} \int_R \mathbf{u} \cdot d\mathbf{s}, \quad (2.70)$$

where $Q(\cdot)$ refer to the flow rate operator through the surface R with surface area of $\mu(R)$. The idea is to append a correction velocity, \mathbf{u}_{corr} , to the velocity field at time step n , \mathbf{u}^n , such that the corrected solution, $\bar{\mathbf{u}}^n = \mathbf{u}^n + \mathbf{u}_{corr}$, has the desired volumetric flux $\bar{Q} = Q(\bar{\mathbf{u}}^n)$. While adding two solutions together is straightforward, the resultant velocity field may not directly satisfy the Navier-Stokes equations. Fortunately, we can leverage the velocity correction scheme which (in general) evaluates the nonlinear advection terms followed by a linear terms (pressure and dissipation). This process is summarised as,

$$\begin{cases} \frac{\partial \mathbf{u}}{\partial t} = \mathbf{N}(\mathbf{u}) \\ \mathbf{u}(\mathbf{x}, 0) = \mathbf{u}^n \end{cases} \xrightarrow{\hat{\mathbf{u}}(\mathbf{x}, \Delta t)} \begin{cases} \frac{\partial \mathbf{u}}{\partial t} = -\nabla p + \nu \mathbf{L}(\mathbf{u}) \\ \mathbf{u}(\mathbf{x}, 0) = \hat{\mathbf{u}}(\mathbf{x}, \Delta t), \end{cases} \quad (2.71)$$

where $\mathbf{u}(\mathbf{x}, 0) = \mathbf{u}^n$ and $\hat{\mathbf{u}}(\mathbf{x}, \Delta t)$ refer to the initial condition for the nonlinear advection terms, and the intermediate velocity, the initial condition for the linear terms, respectively. Since the second step correspond to solving the linear Stokes equation, any solution of the linear Stokes (such as \mathbf{u}_{corr}) added to the final solution will still satisfy the linear Stokes equations - a property of linear differential equations. We consider the linear Stokes equation governing the evolution of the correction velocity,

$$\frac{\partial \mathbf{u}_{corr}}{\partial t} = -\nabla p_{corr} + \nu \mathbf{L}(\mathbf{u}_{corr}) + \alpha^n \hat{\mathbf{e}}_x, \quad (2.72)$$

where α^n is the undetermined magnitude of body force at time step n in the streamwise direction, $\hat{\mathbf{e}}_x$, required to maintain the desired flow rate $\bar{Q} = Q(\mathbf{u}^n) + Q(\mathbf{u}_{corr})$. Since \mathbf{u}_{corr} is appended to \mathbf{u}^n , the initial condition for \mathbf{u}_{corr} must be $\mathbf{u}_{corr}(\mathbf{x}, 0) = 0$, so that \mathbf{u}^n remains compatible with the initial conditions in equation (2.71). Since α^n is undetermined, we normalise the equation with respect to α^n , yielding the linear Stokes equations with unit forcing,

$$\frac{\partial \mathbf{v}}{\partial t} = -\nabla \hat{p} + \nu \mathbf{L}(\mathbf{v}) + \hat{\mathbf{e}}_x, \quad \mathbf{v}(\mathbf{x}, 0) = \mathbf{0}, \quad (2.73)$$

where $\mathbf{v} = \mathbf{u}_{corr}/\alpha^n$ and $\hat{p} = p_{corr}/\alpha^n$. The corrected velocity field becomes

$$\bar{\mathbf{u}} = \mathbf{u} + \alpha^n \mathbf{v}^1, \quad (2.74)$$

where \mathbf{v}^1 is solution field obtained by solving equation (2.73) in the first time step. To match the target volumetric flux, \bar{Q} , we need to scale α^n such that,

$$\bar{Q} = Q(\bar{\mathbf{u}}^n) = Q(\mathbf{u}^n) + Q(\alpha^n \mathbf{v}^1). \quad (2.75)$$

which gives,

$$\alpha^n = \frac{\bar{Q} - Q(\mathbf{u}^n)}{Q(\mathbf{v}^1)}, \quad (2.76)$$

evaluated at every time step n . The Green's function approach is computationally efficient as we only need to compute \mathbf{v}^1 and $Q(\mathbf{v}^1)$ once during the first time step and reuse it for subsequent time steps. The process of adding the correction velocity at the end of velocity correction scheme can be summarised in the procedure as follows,

$$\mathbf{u}^n \xrightarrow{\mathbf{N}(\mathbf{u}^n)} \hat{\mathbf{u}} \xrightarrow{\nabla^2 p} \hat{\mathbf{u}} \xrightarrow{\mathbf{L}(\hat{\mathbf{u}})} \mathbf{u}^{n+1} \xrightarrow{\alpha^{n+1} \mathbf{v}^1} \bar{\mathbf{u}}^{n+1}.$$

2.5 Stability analysis of the Navier-Stokes equations

2.5.1 Algorithms for linear stability analysis

In this section, we present a general overview of the numerical procedure for linear stability analysis. Linear stability analysis examines the stability of a base flow by considering the evolution of infinitesimal perturbations. These perturbations in general, may either grow or decay exponentially, indicating whether the base flow is linearly unstable or stable respectively. In §1.2, we introduced linear stability analysis in the context of wall-bounded shear flows leading to the Orr-Sommerfeld equations, where the base flows depend on a single inhomogeneous and two homogeneous directions, commonly referred to as local² stability analysis. For example, the laminar Poiseuille flow, $U(y) = 1 - y^2$ and the laminar Couette flow $U(y) = y$, $y \in [-1, 1]$. For some flows such as boundary layers, wakes and jets, their base flows are not strictly parallel. By considering a weak dependence on the stream and spanwise directions, their stability are described by the parabolised stability equations [Herbert, 1997]. When the base flow depends on two spatially inhomogeneous directions, $U(x, y)$, or three spatially inhomogeneous directions, $U(x, y, z)$, the analysis of such states are commonly referred to as biglobal or triglobal stability analysis, respectively [Theofilis, 2003]. If the base flow is time-dependent, such as in the secondary instability of cylinder flows, we use Floquet stability analysis [Henderson and Barkley, 1996].

In this section, we consider a time-independent base flow and consider a generic decomposition

²Referring to being spatially local in the context of ‘real’ flows which are typically inhomogeneous in all directions

of the velocity field in three spatial dimensions,

$$\mathbf{u}(\mathbf{x}, t) = \mathbf{U}(\mathbf{x}) + \mathbf{u}'(\mathbf{x}, t), \quad (2.77)$$

where $\mathbf{U}(\mathbf{x})$, $\mathbf{u}'(\mathbf{x}, t)$ refers to the base flow and perturbations. Substituting this into the Navier-Stokes equations and linearising,

$$\frac{\partial \mathbf{u}'}{\partial t} = -(\mathbf{U} \cdot \nabla) \mathbf{u}' - (\mathbf{u}' \cdot \nabla) \mathbf{U} - \nabla p' + \frac{1}{Re} \nabla^2 \mathbf{u}', \quad (2.78a)$$

$$\nabla \cdot \mathbf{u}' = 0. \quad (2.78b)$$

This can be rewritten in as,

$$\frac{\partial}{\partial t} \mathbf{q}' = \mathcal{L} \mathbf{q}', \quad \mathcal{L} = \begin{bmatrix} -(\mathbf{U} \cdot \nabla) - (\nabla \mathbf{U}) + \frac{1}{Re} \nabla^2 & -\nabla \\ \nabla \cdot & 0 \end{bmatrix}, \quad (2.79)$$

where \mathcal{L} refer to the linearised operator and, $\mathbf{q}' = (\mathbf{u}', p')^T$. Assuming an initial perturbation, $\mathbf{q}'(\mathbf{x}, t = 0) = \mathbf{q}_0$, its evolution to time T is given by,

$$\mathbf{q}(\mathbf{x}', T) = \mathcal{A}(T, Re) \mathbf{q}_0, \quad \text{where } \mathcal{A}(T, Re) = \exp(\mathcal{L}T). \quad (2.80)$$

We assume that the perturbations can be represented as a normal mode,

$$\mathbf{q}'(\mathbf{x}, t) = \tilde{\mathbf{q}}(\mathbf{x}) \exp(\lambda t) + \text{c.c} \quad (2.81)$$

where $\lambda_j, \tilde{\mathbf{q}}_j(x)$ refer to the j^{th} eigenvalue and eigenmode, and c.c refers to the complex conjugate. Substituting the normal mode into equation (2.80), we obtain an eigenvalue problem,

$$\mathcal{A}(T, Re) \tilde{\mathbf{q}}_j = \mu_j \tilde{\mathbf{q}}_j, \quad \mu_j = \exp(\lambda_j T). \quad (2.82)$$

where μ_j refers to the eigenvalue of $\mathcal{A} = \exp(\mathcal{L}T)$, and we typically set $T = 1$ [Barkley et al., 2008]. The real component of the eigenvalues determine the stability of the base flow, which can be either,

1. Unstable: $\Re(\lambda) > 0$,
2. Stable: $\Re(\lambda) < 0$,
3. Neutral: $\Re(\lambda) = 0$.

This concludes the mathematical overview of linear stabiltiy analysis, and the challenge lies in the computing the eigenpairs of \mathcal{A} efficiently. For large matrices, $\mathcal{A} \in \mathbb{R}^{M \times M}$ (assuming it is real here for simplicity), direct eigenvalue solvers such as the QR algorithm costing $O(M^3)$ might be computationally infeasible. Another concern is that we are typically only interested in the most dangerous (leading) eigenvalues of largest real parts, and not the full spectrum. Lastly, we do not have access to \mathcal{A} in a time stepping based code.

Power Iteration Method

A simple method in computing the dominant eigenpair is the power iteration method,

Definition 2.5.1 (Power iteration). Given a diagonalisable matrix $\mathbf{A} \in \mathbb{R}^{n \times n}$ and a non-zero vector \mathbf{x}_0 , the sequence of matrix vector products between them (we neglect normalisation here),

$$\mathbf{A}\mathbf{x}_0, \mathbf{A}^2\mathbf{x}_0, \mathbf{A}^3\mathbf{x}_0, \dots, \mathbf{A}^k\mathbf{x}_0. \quad (2.83)$$

approaches the eigenvector of \mathbf{A} with the largest magnitude. i.e. $\tilde{\mathbf{x}}_1 = \lim_{k \rightarrow \infty} \mathbf{A}^k \mathbf{x}_0$. The dominant eigenvalue, λ_1 , can be computed using the Rayleigh quotient, $\lambda_1 = \frac{\tilde{\mathbf{x}}_1^T \mathbf{A} \tilde{\mathbf{x}}_1}{\tilde{\mathbf{x}}_1^T \tilde{\mathbf{x}}_1}$.

Arnoldi Method

We typically require two to four eigenpairs with the largest real parts. To compute more than one eigenpair, we utilise the Arnoldi method [Arnoldi, 1951], belonging to a class of Krylov subspace iterative methods, for performing a Hessenberg reduction.

Definition 2.5.2 (Krylov Subspaces). Given a matrix $\mathbf{A} \in \mathbb{R}^{n \times n}$ and a non-zero vector $\mathbf{x}_0 \in \mathbb{R}^n$, the k^{th} -Krylov subspace, $\mathcal{K}_n(\mathbf{A}, \mathbf{x}_0, k)$ is defined by,

$$\mathcal{K}_n(\mathbf{A}, \mathbf{x}_0, k) = \text{span}\{\mathbf{x}_0, \mathbf{A}\mathbf{x}_0, \mathbf{A}^2\mathbf{x}_0, \mathbf{A}^3\mathbf{x}_0, \dots, \mathbf{A}^{k-1}\mathbf{x}_0\}. \quad (2.84)$$

Definition 2.5.3 (Hessenberg reduction). The Hessenberg reduction is a matrix decomposition technique commonly used for the computing eigenpairs of matrices. Given a unsymmetric matrix $\mathbf{A} \in \mathbb{R}^{N \times N}$ (we assume that \mathbf{A} is real for simplicity), we seek a decomposition of the form,

$$\mathbf{A} = \mathbf{Q}\mathbf{H}\mathbf{Q}^T, \quad (2.85)$$

where,

- $\mathbf{H} \in \mathbb{R}^{N \times N}$ is an upper Hessenberg matrix (i.e. $a_{i,j} = 0$ for $i > j + 1$)
- $\mathbf{Q} \in \mathbb{R}^{N \times N}$ is an orthonormal matrix (i.e. $\mathbf{Q}^{-1} = \mathbf{Q}^T$), whose columns $\mathbf{q}_1, \dots, \mathbf{q}_N$, form an orthonormal basis.

The Hessenberg reduction shows that \mathbf{A} and \mathbf{H} are similar matrices, which have the same eigenvalues. If $\mathbf{Ax} = \lambda\mathbf{x}$, using $\mathbf{Q}^T = \mathbf{Q}^{-1}$ and multiplying (2.85) by \mathbf{x} ,

$$\mathbf{Ax} = \mathbf{Q}\mathbf{H}\mathbf{Q}^{-1}\mathbf{x} \Rightarrow \lambda\mathbf{x} = \mathbf{Q}\mathbf{H}\mathbf{Q}^{-1}\mathbf{x} \Rightarrow \lambda\mathbf{Q}^{-1}\mathbf{x} = \mathbf{H}\mathbf{Q}^{-1}\mathbf{x} \Rightarrow \lambda\mathbf{y} = \mathbf{Hy}. \quad (2.86)$$

Hence, $\lambda(\mathbf{A}) = \lambda(\mathbf{H})$, and their eigenvectors are related by $\mathbf{x} = \mathbf{Q}\mathbf{y}$.

The Arnoldi method generates a sequences of vectors $[\mathbf{u}_0, \mathbf{Au}_0, \dots, \mathbf{A}^{k-1}\mathbf{u}_0]$ that spans the k -dimensional Krylov subspace. These vectors, are known as Arnoldi vectors [Golub and Van Loan, 2013], and are used to construct an orthogonal matrix via the Gram-Schmidt process, $\mathbf{Q} = [\mathbf{q}_1, \mathbf{q}_2, \dots, \mathbf{q}_k] \in$

$\mathbb{R}^{M \times K}$. This is equivalent to performing a partial Hessenberg reduction of $\mathcal{A} = \mathbf{Q} \mathbf{H} \mathbf{Q}^T$, where the eigenvalues of $\mathcal{A} \in \mathbb{R}^{N \times N}$ can be approximated by a smaller Hessenberg matrix $\mathbf{H} \in \mathbb{R}^{k \times k}$, suitable for a direct eigenvalue computation using the QR algorithm. The k -step Arnoldi factorisation of \mathcal{A} gives,

$$\mathcal{A} \mathbf{Q}_k = \mathbf{Q}_k \mathbf{H}_k + \mathbf{r}_k \mathbf{e}_k^T, \quad (2.87)$$

where $\mathbf{H} \in \mathbb{R}^{k \times k}$ refers to the upper Hessenberg matrix, $\mathbf{e}_k = [0, \dots, 0, 1] \in \mathbb{R}^k$, and $\mathbf{r}_k \in \mathbb{R}^N$ is a residual vector. If $\mathbf{x} = \mathbf{Q}_k \mathbf{y}$, and $\mathbf{H}\mathbf{y} = \lambda\mathbf{y}$ then,

$$(\mathcal{A} - \mathbf{I}\lambda)\mathbf{x} = (\mathbf{e}_k^T \mathbf{y})\mathbf{r}_k. \quad (2.88)$$

In other words, the residual vector difference between the approximation of $\lambda(\mathcal{A})$, using $\lambda(\mathbf{H})$. If $\|\mathbf{r}_k\| = 0$, then $\lambda(\mathbf{H}) \subseteq \lambda(\mathcal{A})$.

We now present the Arnoldi method by generating k Arnoldi vectors,

$$\mathbf{T}_k = [\mathbf{u}_0, \mathbf{u}_1, \dots, \mathbf{u}_{k-1}] = \left[\mathbf{u}_0, \frac{\mathcal{A}(T, Re)\mathbf{u}_0}{\alpha_1}, \frac{\mathcal{A}(T, Re)\mathbf{u}_1}{\alpha_2}, \dots, \frac{\mathcal{A}(T, Re)\mathbf{u}_{k-1}}{\alpha_k} \right], \quad (2.89)$$

where α_j is scaled such that $\|\mathbf{u}_j\| = 1$. Following [Barkley et al., 2008], the projection of \mathcal{A} onto the Krylov subspace is given as,

$$\mathcal{A} \mathbf{T}_k = \mathbf{T}_{k+1} D_k^{(k+1)}, \quad (2.90)$$

where $D_k^{(k+1)} \in \mathbb{R}^{(k+1) \times k}$ is a shifted diagonal matrix with entries $D_{ij} = \alpha_i \delta_{i,j+1}$. We assume that \mathbf{T}_k and \mathbf{T}_{k+1} admit QR decompositions,

$$\mathcal{A} \mathbf{Q}_k \mathbf{R}_k = \mathbf{Q}_{k+1} \mathbf{R}_{k+1} D_k^{(k+1)}, \quad (2.91)$$

where $\mathbf{Q}_k \in \mathbb{R}^{N \times k}$, $\mathbf{R}_k \in \mathbb{R}^{k \times k}$ and $\mathbf{Q}_{k+1}, \mathbf{R}_{k+1}$ are similarly defined. The upper Hessenberg matrix $\mathbf{H}_k^{(k+1)} \in \mathbb{R}^{(k+1) \times k}$ is defined as,

$$\mathbf{H}_k^{(k+1)} = \mathbf{R}_{k+1} D_k^{(k+1)} \mathbf{R}_k^{-1}, \quad (2.92)$$

in which the last row of $\mathbf{H}_k^{(k+1)}$ only contains a single non-zero entry, $h^* = h_{k,k-1}$. By substituting the definition of the upper Hessenberg matrix and separating the last row of $\mathbf{H}_k^{(k+1)}$ we obtain,

$$\mathcal{A} \mathbf{Q}_k = \mathbf{Q}_k \mathbf{H}_k + h^* \mathbf{q}_k \mathbf{e}_k^T. \quad (2.93)$$

Equation (2.93) describes the projection of \mathcal{A} onto the Krylov subspace spanned by orthonormal bases \mathbf{Q}_k , yielding a smaller \mathbf{H}_k matrix. The accuracy of this approximation is dictated by the magnitude of the residual term, $h^* \mathbf{q}_k \mathbf{e}_k^T$. Assuming that \mathbf{H}_k is diagonalisable as $\mathbf{H}_k = \Psi_k \Lambda_k \Psi_k^{-1}$, we multiply equation (2.93) by Ψ_k ,

$$\mathcal{A} \mathbf{Q}_k \Psi_k = \mathbf{Q}_k \Psi_k \Psi_k^{-1} \mathbf{H}_k \Psi_k + h^* \mathbf{q}_k \mathbf{e}_k^T \Psi_k. \quad (2.94)$$

Simplifying the expression above we get,

$$\mathcal{A}\mathbf{V}_k = \mathbf{V}_k\Lambda_k + h^*\mathbf{q}_k\mathbf{e}_k^T\boldsymbol{\Psi}_k, \quad (2.95)$$

where Λ_k contains the k eigenvalues and $\mathbf{V}_k = \mathbf{Q}_k\boldsymbol{\Psi}_k$ the eigenvectors of \mathcal{A} . The error in approximating the j^{th} eigenpair is given by,

$$\varepsilon_j = \|\mathcal{A}\mathbf{v}_j - \lambda_j\mathbf{v}_j\| = \|h^*\mathbf{q}_k\mathbf{e}_k^T\psi_j\| = |h^*|\mathbf{v}_j[k-1]|, \quad (2.96)$$

where $\mathbf{v}_j[k-1]$ is the last component of the eigenvector \mathbf{v}_j .

Lastly, we are generally interested in obtaining the eigenpairs with the the largest real part. We introduce exponential power method [Tuckerman and Barkley, 2000], which is naturally considered by time stepping an initial perturbation \mathbf{q}'_0 from $t = 0$ to T ,

$$\mathbf{q}'(T) = \exp(\mathcal{L}T)\mathbf{q}'_0 = \mathcal{A}(T)\mathbf{q}'_0. \quad (2.97)$$

The dominant eigenvalues, μ , of \mathcal{A} obtained from the Arnoldi method described above, which correspond to the eigenvalue of the largest real part λ , of \mathcal{L} by $\mu = \exp(\lambda T)$, where T is typically set to 1. For further details on this algorithm, the reader is referred to Barkley et al. [2008] for more details.

In summary, the algorithm described above have been implemented in Nektar++, referred to as the ‘modified’ Arnoldi algorithm, which modifies the existing time-stepper code with a wrapper function that generates Arnoldi vectors and solves the Hessenberg matrix using the subroutine dgeev from LAPACK (Linear Algebra PACKage, [Anderson et al., 1999]). The modified Arnoldi algorithm has been verified against using a separate implementation based on the third-party package ARPACK (ARnoldi PACKage [Lehoucq et al., 1998]) [Rocco, 2014].

2.5.2 Edge tracking

In the section, we consider the dynamical system interpretation of transition, where the laminar state is separated by the turbulent state by an edge, referred to the edge of chaos. Along this edge, there could be attractors, sometimes in the form of travelling-waves, tori, and high-order invariant sets, known as the edge states. For the edge tracking, we use the bisection method [Skufca et al., 2006, Schneider et al., 2007, Khapko et al., 2016], with an initial condition given by

$$\mathbf{x}_0 = \chi\mathbf{x}_L + (1-\chi)\mathbf{x}_T \quad (2.98)$$

where \mathbf{x}_0 refers to an initial condition consisting of a weighted sum, $\chi \in [0, 1]$, between a laminar state, \mathbf{x}_L , and a turbulent state, \mathbf{x}_T . Since the laminar and turbulent state forms a bistable system, there could be (at least) one critical value of $\chi \in [0, 1]$, where the trajectory walks along the ‘edge’ between the turbulent and laminar state without decaying to either states. To find this χ_c , we perform n successive bisections between χ_L^n, χ_T^n , the upper and lower bounds such that the trajectory relaminaris or become turbulent respectively, where χ^n is updated by $\chi^n = \frac{1}{2}(\chi_L^n + \chi_T^n)$ At every n^{th} bisection,

it involves a stopping criteria, a tolerance based on the deviation of an observable (e.g. wall shear stresses) away from the initial condition. Then, a direct numerical simulation is reinitialised with an initial condition given by equation (2.98) For every successive bisection, the difference between two trajectories, $\Delta\chi^n = \chi_L^n - \chi_T^n$, decays like $\Delta\chi^n \sim 0.5^n$, and is related to the Lyapunov exponent of the edge

$$\Delta\chi \approx C \exp(\mu_e t) \quad (2.99)$$

where μ_e, C refers to the Lyapunov exponent of the edge and a constant. In practice, we consider $n = 10, 20$ and for $n = 10$, the solution along the edge is converged. After we determine the critical χ_c , we repeat the bisections step by replacing the laminar state, \mathbf{x}_L , and the turbulent state \mathbf{x}_T , which the solution trajectory with χ_L and χ_T , that has been terminated after exceeded the threshold. We refer this repetition as the number of ‘outer’ bisections, while the bisection for χ^n is referred to ‘inner bisections’ After a certain number of ‘outer’ bisections, the trajectory may converge towards an attractor, which may exist in a form of travelling-waves, periodic orbits or a chaotic attractor. This attractor sits along the edge is referred to as the edge state, a saddle acting as a separatrix between the turbulent and laminar attractor. We describe the algorithm of edge tracking in algorithm 2.5.2

Algorithm 1 Algorithm for edge tracking between a turbulent and laminar state

```
1: Initialise maxInBisects, maxOutBisects           ▷ Maximum inner and outer bisections
2: Initialise tol                                     ▷ Tolerance for stopping criteria (e.g., wall-shear stress)
3: outBisects ← 0
4: while outBisects < maxOutBisects do
5:   if outBisects == 0 then
6:      $\mathbf{x}_L, \mathbf{x}_T \leftarrow \text{input}()$                   ▷ Initial laminar and turbulent states
7:   end if
8:    $\chi_L \leftarrow 0, \chi_T \leftarrow 1, \chi \leftarrow \frac{1}{2}(\chi_L + \chi_T)$     ▷ Initialise bisection coefficients
9:    $\mathbf{x}_0 \leftarrow \chi \mathbf{x}_T + (1 - \chi) \mathbf{x}_L$                       ▷ Initialise initial condition
10:  inBisects ← 0
11:  while inBisects < maxInBisects do
12:    k ← 0,  $\Delta \leftarrow 10^6$ 
13:    while  $\Delta > \text{tol}$  do
14:       $\mathbf{x}_{k+1} \leftarrow \text{TimeIntegrate}(\mathbf{x}_k)$ 
15:       $\Delta \leftarrow |\mathbf{x}_{k+1} - \mathbf{x}_0|$                          ▷ Deviation from initial condition
16:      k ← k + 1
17:    end while
18:    if isTurbulent( $\mathbf{x}_k$ ) then                                ▷ Check if terminal state is turbulent
19:       $\chi_L \leftarrow \chi$                                          ▷  $\mathbf{x}_L$  gets larger weight
20:      if inBisects == maxInBisects - 1 then
21:         $\mathbf{x}_T \leftarrow \mathbf{x}_k$                                ▷ Save turbulent-leaning initial condition
22:        break
23:      end if
24:    else
25:       $\chi_T \leftarrow \chi$ 
26:      if inBisects == maxInBisects - 1 then
27:         $\mathbf{x}_L \leftarrow \mathbf{x}_k$                                ▷ Save laminar-leaning initial condition
28:        break
29:      end if
30:    end if
31:     $\chi \leftarrow \frac{1}{2}(\chi_L + \chi_T)$ 
32:     $\mathbf{x}_0 \leftarrow \chi \mathbf{x}_L + (1 - \chi) \mathbf{x}_T$           ▷ Update initial conditions
33:    inBisects++
34:  end while
35:  outBisects++
36: end while
```

Chapter 3

Transitional Rayleigh-Bénard Poiseuille flows

3.1 Introduction

RRayleigh-Bénard-Poiseuille (RBP) flows describe the motion of fluids confined between two extended parallel plates, heated from below and cooled from the top, with an imposed pressure gradient. This system combines classical Rayleigh-Bénard convection (RBC) and plane Poiseuille flow (PPF), driven by buoyancy and shear forces, respectively. In the limiting cases, the laminar solution can transition to convection rolls (RBC) or shear-driven turbulence (PPF), depending on whether buoyancy or shear forces dominate. Transition to turbulence in the regime where both forces interact remains largely unexplored. For instance, do buoyancy forces promote the transition to shear-driven turbulence?; how does shear influence the convection? Understanding the transition to turbulence in this regime can have implications for applications such as the fabrication of thin uniform films in chemical vapour deposition [??] and the cooling of electronic components [??].

3.1.1 Rayleigh-Bénard Poiseuille (RBP) flows

The non-dimensionalised parameters that govern the RBP flow are the Rayleigh number, $Ra = \eta g d^3 \Delta T / \nu \kappa$, Reynolds number, $Re = W_c h / \nu$, Prandtl number, $Pr = \kappa / \nu$, and the aspect ratio of the flow domain, $\Gamma = L / 2d$, where η , g , ΔT , ν , κ , W_c , h , d , L are the thermal expansion coefficient, acceleration due to gravity, temperature difference between the bottom and top wall, kinematic viscosity, thermal diffusivity, laminar centreline velocity, domain's half-depth, domain's full-depth, length (or span), respectively.

? first investigated the primary instabilities of RBP flows, which can be determined by Re , Ra , Pr , and the planar x - z perturbations wavenumbers α, β respectively. For a given Ra and Pr , the neutral stability curves are limited by the development of Tollmien-Schlichting waves for $Re \geq Re_{TS} = 5772.22$ [?], and convection rolls within $0 \leq Re < Re_{TS}$. Convection rolls can be categorised based on their orientation to the mean flow, namely, longitudinal ($\alpha = 0, \beta \neq 0$), transverse ($\alpha \neq 0, \beta = 0$) and oblique rolls ($\alpha \neq 0, \beta \neq 0$). The linearised system governing the onset of longitudinal rolls is analogous to the linearised RBC system, with a critical Rayleigh number, $Ra_{\parallel} = Ra_{RB} = 1708.8$ and critical wavenumber, $\alpha_{\parallel} = \alpha_{RB} = 3.13$ [??], independent of Re and Pr .

The critical Rayleigh number for oblique and transverse rolls matches that of RBC at $Re = 0$ due to horizontal isotropy, but increases as Re increases, depending on Pr , i.e., $Ra_{\perp} = f(Re, Pr)$ [??]. When spatially developing instabilities are considered, longitudinal rolls are always convectively unstable, and transverse rolls can become absolutely unstable [??]. Nonmodal stability analyses of subcritical RBP indicate that the optimal transient growth, G_{max} , increases gradually with Ra . The wavenumber of the optimal initial conditions, β_{max} , resembles that observed in shear flows [?], and gradually approaches the critical wavenumber of convection rolls, α_{\parallel} , as Ra increases [?]. For $Re > 0$, the longitudinal rolls appear as the dominant primary instability [?]. Secondary stability analyses of longitudinal rolls reveal a wavy instability near $Re \sim 100$ [?], leading to wavy longitudinal rolls, which are convectively unstable [??]. The influence of finite lateral extensions in RBP flows on the stability of longitudinal and transverse rolls [??], as well as wavy rolls [??], has been reported. In finite streamwise extensions of RBP flows, the onset of convection rolls and the heat flux variations due to entrance effects have been investigated [??]. More recently, shear-driven turbulence can enhance heat fluxes in turbulent RBP flows [??]. RBP flows with sinusoidal heating and wavy walls have also been studied [?]. For an in-depth discussion of RBP flows, see the reviews by ? and ?.

3.1.2 Rayleigh-Bénard convection (RBC)

In the limiting case of $Re = 0$, the RBP problem reduces to the buoyancy-driven Rayleigh-Bénard convection (RBC). We provide an overview of the key developments of RBC as a foundation for studying RBP flows at $Re = 0$. Beyond the onset, $Ra > Ra_{RB}$, the secondary stability characteristics of ideal straight rolls (ISRs), which are infinitely-parallel convection rolls, are described by the Busse balloon. This balloon defines the stability boundaries of ISRs based on their wavenumber, Ra and Pr . For $Pr = 1$ and $Ra_{RB} < Ra \lesssim 6000$, the secondary instabilities primarily modify the ISR wavenumber to remain within the boundaries of the Busse balloon. These include the cross-roll, Eckhaus, or skewed-varicose instabilities [??]. An oscillatory secondary instability emerges at $Ra \gtrsim 5500$, where a stationary ISR transitions into a time-dependent tertiary state, known as oscillatory ISRs [??], and these instabilities have been reported in experiments [????]. Notably, ISRs appear to be the exception rather than the norm as multiple convection patterns in the form of squares, targets, and oscillatory convection patterns have been reported, resulting in many multiple stable states in the same Ra parameter space where ISRs are expected [??????]. For large aspect ratios, $\Gamma \gtrsim 20$, convection rolls can exhibit spatiotemporal chaotic behaviour, known as spiral defect chaos (SDC) within the same Ra range [?????????]. It is now established that both SDC and ISR can coexist at the same Ra , forming a bistable system confirmed experimentally [?].

This study focuses on the influence of Re on the complex convection patterns of RBC within $Ra \in [0, 10000]$. Specifically, we investigate the impact of shear on the bistable system between SDC and ISRs, the stability boundaries of the Busse balloon, and the possible emergence of multiple 'non-ISR' states as Re increases.

3.1.3 Plane Poiseuille flows (PPF)

The other limiting case at $Ra = 0$ corresponds to the classical plane Poiseuille flow (PPF), and its relevance to RBP flows is discussed here. Turbulence in PPF is known to be subcritical, occurring at $Re \sim 1000$, well below the threshold $Re < Re_{TS}$ [??]. This could be due to the non-normality of the Orr-Sommerfeld equations, allowing disturbances to develop significant transient growth at $Re = 1000$ [??]. The optimal initial conditions involve streamwise vortices which amplify streaks, related to the lift-up effect [?]. These modal and nonmodal mechanisms above highlight developments based on linear methods. Utilising tools from nonlinear dynamics systems, turbulence could be viewed as chaotic trajectories around unstable nonlinear solutions known as invariant solutions or exact coherent structures [?????????]. We adopt this perspective as we analyse chaotic (turbulent) trajectories within a confined domain, $\Gamma = \pi/2$, motivated from the minimal flow unit from ?. In large domains, $\Gamma \gtrsim 20$, transitional PPF exhibits spatiotemporal intermittent turbulent-laminar bands, where turbulent and laminar regions can coexist [??????].

This study focuses on the impact of Ra on the transition to turbulence. For instance, could convection rolls, reminiscent of the optimal streamwise vortices [?], assist the transition towards subcritical turbulence?

3.1.4 Objectives and organisation

While the stability characteristics of laminar RBP flows have been well studied (see §3.1.1), its transition to shear-driven turbulence remains poorly understood and is the focus of this study. For instance, how do wavy rolls evolve as Re increases? Additionally, we also aim to bridge the gap between RBC (see §3.1.2), and PPF (see §3.1.3) by investigating the impact of Re on the bistability between SDC and ISRs in RBC, as well as the influence of Ra on turbulent-laminar bands in PPF. The main objective of this work is to perform direct numerical simulations (DNS) of transitional RBP flows within $Ra \in [0, 10000]$ and $Re \in [0, 2000]$ at $Pr = 1$ in both large and confined domains, $\Gamma = 4\pi, \Gamma = \pi/2$. This study is largely exploratory, focusing on identifying different flow regimes and providing key insights into their dynamical processes. Hence, we do not intend to perform bifurcation analysis due to the lack of prior knowledge of the phase space, which could lead to large computational costs.

The paper is organised as follows: in §3.2, we describe the problem formulation, governing equations, numerical methods and setup. In §3.3, we present the Ra - Re phase space, identifying five distinct regimes and their transition boundaries. We also introduce a new ‘intermittent roll’ regime and discuss the coexistence of longitudinal rolls with turbulent-laminar bands, highlighting the role of longitudinal rolls in transitional RBP flows. In §3.4, we investigate the unstable manifolds of longitudinal rolls in a confined domain, $\Gamma = \pi/2$, revealing dynamical connections between shear-driven turbulence, longitudinal rolls and the laminar state, and discuss its relevance to the larger domain. Finally, we conclude in §3.5, and propose directions for future work.

3.2 Problem formulation

3.2.1 Governing equations

We consider a layer of fluid sandwiched between two extended parallel plates of equal length and span, $L = L_x = L_z$, separated by depth, d (or two half heights, $h = d/2$), with a uniform upper and lower plate temperature T_U and T_L . The fluid is unstably stratified such that $\Delta T = T_L - T_U > 0$. The fluid has a density of ρ , kinetic viscosity, ν , thermal diffusivity κ . The governing equations are the non-dimensionalised Navier-Stokes equations with Boussinesq approximation given by,

$$\frac{\partial \mathbf{u}}{\partial t} + (\mathbf{u} \cdot \nabla) \mathbf{u} = -\nabla p + \frac{1}{Re} \nabla^2 \mathbf{u} + \frac{Ra}{8PrRe^2} \theta \mathbf{j}, \quad (3.1a)$$

$$\frac{\partial \theta}{\partial t} + (\mathbf{u} \cdot \nabla) \theta = \frac{1}{RePr} \nabla^2 \theta, \quad (3.1b)$$

$$\nabla \cdot \mathbf{u} = 0, \quad (3.1c)$$

with the following boundary conditions at the wall,

$$\mathbf{u}|_{y=\pm h} = 0, \quad \theta|_{y=-h} = 1, \quad \theta|_{y=h} = 0, \quad (3.2)$$

and periodic boundary conditions in the planar x and z directions. $\mathbf{u}(\mathbf{x}, t)$ denotes the non-dimensionalised velocity scaled by the laminar centreline velocity, W_c , i.e. $W_{lam}(y) = W_c(1 - y^2)$. $\mathbf{x} = (x, y, z)$ and t denote the non-dimensionalised spatial and temporal coordinates scaled by the half-height, h and the advective time scale, W_c/h , where x, y, z refers to the spanwise, wall-normal and streamwise directions, respectively. p refers to the non-dimensionalised pressure scaled by ρW_c^2 , and $\theta (\equiv (T - T_U)/\Delta T)$ refers to the non-dimensionalised temperature with T being the absolute temperature. \mathbf{j} denotes the unit vector in the y -direction. We note that the rescaled $Ra/8$ term in the momentum forcing terms is equivalent to the Rayleigh number scaled based on the half-depth, h , whereas Ra is scaled based on depth, d , as in classical RBC. The Rayleigh number, Ra , Reynolds number Re and Prandtl number, Pr are defined in §???. We set $Pr = 1$ in this study. For the Rayleigh-Bénard convection problem, we note that the equation (??) becomes singular at $Re = 0$. In such cases, we solve the non-dimensionalised incompressible Navier-Stokes equations based on thermal length, velocity and temporal scales derived in Appendix A.2.

3.2.2 Numerical Methods

The governing equations are solved numerically using an open-source spectral/ hp -element package, Nektar++ [??]. The computational mesh consists of 2D quadrilateral elements in the $x - y$ plane generated using Gmsh [?] and then imported into Nektar++ using Nekmesh [?]. We discretise the spatial domain based on the quasi-3D approach, employing spectral/ hp elements in the $x - y$ plane and Fourier expansions in the z [?]. We emphasise that the streamwise direction is in z . The

discretised equations are solved using a velocity correction scheme, based on a second-order stiffly splitting scheme, where the nonlinear advection and forcing terms are treated explicitly, while the pressure and diffusion terms are treated implicitly [?]. The 3/2 and polynomial de-aliasing rule for the Fourier expansions and spectral/ hp elements are applied during the evaluation of the nonlinear advection terms. We refer to the solution obtained at the end of the velocity correction scheme as the homogenous velocity, \mathbf{u}_h .

3.2.3 Ra - Re sweep

We consider fifty-two numerical experiments at $Re = 0, 0.1, 1, 10, 100, 500, 750, 1000, 1050, 2000$, and $Ra = 0, 2000, 3000, 5000, 8000, 10000$ at $Pr = 1$ with a large aspect ratio of $\Gamma = 4\pi$. Their spatial and temporal numerical resolutions and time-integration horizon, T , are described in the Appendix A.4. The initial conditions of all cases are sampled from a statistically stationary solution. Laminar solutions are obtained for $Ra = 0$, $Re \leq 1000$, and are omitted from the analysis. For all of the cases considered here, we maintain the same spatial resolution except $Re = 2000$, where the number of Fourier expansions was doubled. The temporal resolution between the numerical experiments differs due to time scales arising from the different flow physics, as we shall see later. We have also considered a mesh independence study for the end case of $Ra = 10000$, $Re = 2000$, where doubling the number of Fourier modes or increasing the polynomial order by 1 led to a $< 1\%$ change in near-wall transport properties defined by the Nusselt number, $Nu = -\langle d\theta/dy|_{y=-h} \rangle_{x,z} d/\Delta T$, and shear, $\langle dw/dy|_{y=-h} \rangle_{x,z}$, where $\langle \cdot \rangle_{x,z} = 1/(L_x L_z) \int_{z,x} \cdot dx dz$ refer to the plane averaged operator.

3.2.4 Linear Stability Analysis

In §3.4, we will perform numerical experiments where small disturbances are added along the unstable manifolds of longitudinal rolls. To determine the unstable manifolds, we consider a small disturbance about the longitudinal roll state,

$$\mathbf{u}(\mathbf{x}, t) = \mathbf{u}_{LR}(\mathbf{x}) + \hat{\mathbf{u}}(\mathbf{x}, t), \quad (3.3a)$$

$$\theta(\mathbf{x}, t) = \theta_{LR}(\mathbf{x}) + \hat{\theta}(\mathbf{x}, t), \quad (3.3b)$$

$$p(\mathbf{x}, t) = p_{LR}(\mathbf{x}) + \hat{p}(\mathbf{x}, t), \quad (3.3c)$$

where $\mathbf{q} = [\mathbf{u}, \theta, p]^T$, $\mathbf{q}_{LR} = [\mathbf{u}_{LR}, \theta_{LR}, p_{LR}]^T$ and $\hat{\mathbf{q}} = [\hat{\mathbf{u}}, \hat{\theta}, \hat{p}]^T$ refers to solution vector, the longitudinal state and the disturbances respectively. We substitute equation (3.3) into (3.1) and neglect the nonlinear terms, leading to the linearised equations,

$$\frac{\partial \hat{\mathbf{q}}}{\partial t} = \mathcal{A}(\mathbf{q}_{LR}; Re, Ra, Pr)\hat{\mathbf{q}}, \quad (3.4a)$$

where

$$\mathcal{A}(\mathbf{q}_{LR}; Re, Ra, Pr) = \begin{pmatrix} -(\mathbf{u}_{LR} \cdot \nabla) - (\nabla \mathbf{u}_{LR} \cdot) + 1/Re \nabla^2 & \frac{Ra}{8Re^2Pr} \hat{\mathbf{j}} & -\nabla \\ -(\nabla \theta_{LR} \cdot) & -(\mathbf{u}_{LR} \cdot \nabla) + \nabla^2 & 0 \\ \nabla \cdot & 0 & 0 \end{pmatrix}. \quad (3.4b)$$

Out of convenience, we will only consider longitudinal rolls invariant along the z -direction, which are also assumed to be periodic in x -direction, and the following form of normal-mode solution can be considered,

$$\hat{\mathbf{q}}(\mathbf{x}, t) = \check{\mathbf{q}}(x, y) e^{i(\alpha x + \beta z) + \lambda t} + \text{c.c}, \quad (3.5)$$

where λ , α and β are the complex frequency, the spanwise wavenumber (or the Floquet exponent), and the stream wavenumber, respectively. Using the periodic nature of $\check{\mathbf{q}}(x, y)$ in the x -direction, (3.5) can also be written as

$$\hat{\mathbf{q}}(\mathbf{x}, t) = \left[\sum_{n=-\infty}^{\infty} \check{\mathbf{q}}_n(y) e^{i \frac{2\pi}{L_x} (n+\epsilon)x} \right] e^{i\beta z + \lambda t} + \text{c.c}, \quad (3.6)$$

where $\epsilon (= \alpha L_x / (2\pi))$ is the Floquet detuning parameter with $0 \leq \epsilon \leq 1/2$. In this study, we will only consider the identification of the unstable manifolds of longitudinal rolls in a fixed computational domain, hence, the fundamental mode, $\epsilon = 0$, is of sole interest. Substituting equation (3.6) into (3.4) result to a discretised eigenvalue problem with the eigenvalue λ . The wavenumber, β , is restricted to discrete values of $\beta = 2\pi m / L_z$, and m is a positive integer, for the given computational domain. The resulting eigenvalue problems are solved using a time-stepper-based iterative Arnoldi algorithm implemented in Nektar++ [?].

3.3 *Ra-Re* Phase Space

3.3.1 Classification

We present the results obtained from the DNS of transitional RBP flows, focusing on the parameter space defined by Rayleigh numbers in the range $Ra \in [0, 10000]$, and Reynolds numbers in the range of $Re \in [0, 2000]$ (see Appendix A.4 for the full details). At opposite ends of the Re -spectrum, the onset of SDC and subcritical shear-driven turbulence are shown. Figure 3.1 shows the terminal midplane temperature snapshots, $\theta(x, z)|_{y=0}$, of different flow regimes. The solid blue curves refer to the approximate neutral stability boundaries for the longitudinal and transverse rolls as $Ra_{\parallel} = 1708$, and $Ra_{\perp} = f(Re)$ respectively [?]. In the absence of shear at $Re = 0$, these curves merge onto the classical critical RBC instability at $Ra_{cr} = 1708$, as ISRs become rotationally invariant about the wall-normal axis. Additionally, a red arrow indicates the secondary neutral stability curve, marking the onset of oscillatory instabilities of ISRs within $5000 < Ra < 8000$ at $Re = 0$ [?]. The phase diagram in figure 3.1 is not plotted to scale but serves as a conceptual reference for distinguishing different flow states.

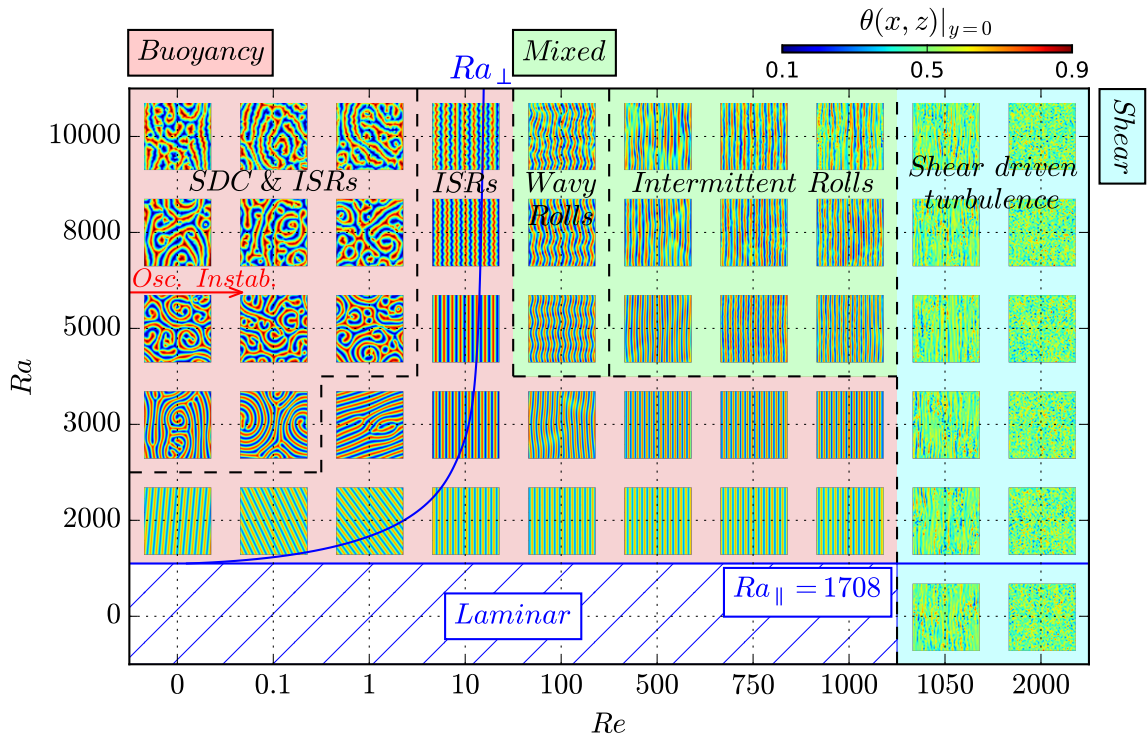


Figure 3.1: The $Ra - Re$ phase space illustrates the terminal midplane temperature snapshots, $\theta(x, z)|_{y=0}$ for $Re \in [0, 2000]$ and $Ra \in [0, 10000]$, classified into five distinct regimes: (1) SDC & ISRs, (2) ISRs, (3) wavy rolls, (4) intermittent rolls and (5) shear-driven turbulence. The blue solid curves refer to primary neutral curves of the longitudinal and transverse rolls Ra_{\parallel} , Ra_{\perp} . The red curve refers to secondary oscillatory instability of ISRs at $Re = 0$ [?]. Shades of red, green and blue indicate their dominant mechanism, whether driven by buoyancy or shear (or mixed). The plot is not to scale.

In this Ra - Re phase space, we categorise the flow behaviour into five distinct regimes: (1) bistability between SDC and ISRs (SDC & ISRs), (2) ideal straight rolls (ISRs), (3) wavy rolls, (4) intermittent rolls, and (5) shear-driven turbulence. The categories are defined based on common flow structures (patterns), and/or dynamical characteristics, ranging from equilibrium solutions to intermittent and chaotic dynamics. Furthermore, we classify these states based on their first and second-order statistical properties, where they appear independent of Re in the buoyancy-dominated regime (shaded in red), and Ra in the shear-dominated regime (shaded in blue), discussed in Appendix A.5. In the mixed regime shaded in green, both Ra and Re are important.

In the buoyancy-dominated regime, the flow structures are predominantly described by convection rolls, such as SDC, transverse, oblique, longitudinal rolls (and ISRs with no mean flow) or oscillatory rolls. The bistability between SDC and ISRs is preserved for $Ra \geq 3000$ at $Re = 0.1$, and $Re = 1$ for $Ra \geq 5000$. This points towards a Re_s -threshold where SDC disappears, which depends on Ra , demarcated by the black dotted lines on the left-hand side of figure 3.1. However, computing this Re_s -threshold is beyond the scope of this work. Notably, a transverse roll with a ‘hooked-like’ defect is observed at $Re = 1$, $Ra = 3000$, reminiscent of the multiple ‘non-ISR’ states in RBC (see references in §3.1.2). At $Re = 10$, SDC disappears and longitudinal rolls appear. As Re is increased further to 1000, the longitudinal rolls emerge as the preferred solution at $Ra = 2000, 3000$. Notably, the non-dimensionalised spanwise wavenumber of these longitudinal rolls is approximately $\alpha d \approx 1.65$, which happens to lie outside of the stability boundaries of the Busse balloon in RBC [?]. This may suggest that the stability boundaries may expand as Re increases. Further evidence comes from the skewed-varicose longitudinal roll structure at $Re = 100$, $Ra = 3000$, which resembles a skewed-varicose instability, a secondary instability related to the Busse balloon boundaries [?].

As Re approaches 100, the longitudinal rolls undergo a secondary wavy instability [??], leading to the emergence of wavy longitudinal rolls depicted in figure 3.1. The wavelength of streamwise waviness and spanwise periodic longitudinal roll appears across approximately three intervals of streamwise length, $\Lambda_z \sim L_z/3$, and twelve intervals of spanwise length, $\Lambda_x \sim L_x/12$, respectively. The ratio between the wavelength of streamwise waviness and spanwise roll is about ~ 4 , around the ballpark reported by ?.

3.3.2 Spatiotemporal intermittent rolls

As Re approaches $Re = 500$, wavy rolls disappear. Instead, a new regime, referred to as intermittent rolls, is observed. In this regime, the longitudinal rolls remain as the dominant convection structure, interspersed with a spatiotemporal intermittent breakdown towards the laminar state. For $Ra = 8000$, $Re = 500$, this behaviour is illustrated in the temporal intermittency of the near-wall transport properties such as the plane averaged shear, $\langle dw/dy|_{y=-h} \rangle_{x,z}$, and the Nusselt number, Nu , in figure 3.2(a). The breakdown from the longitudinal rolls towards the laminar state is evident in figure 3.2(b), where the bright and dark regions in the spacetime plot of near-wall spanwise and wall-normal perturbation kinetic energy, $\mathcal{E}_{u'+v'} = 1/2 \left[u'|_{(y^+,z)=(15,8\pi)}^2 + v'|_{(y^+,z)=(15,8\pi)}^2 \right]$ (where $\mathbf{u}' = \mathbf{u} - W_{lam}(y)$, $y^+ = u_\tau y_0 / \nu$, $u_\tau = \sqrt{\langle \gamma/h \rangle_t}$, $y_0 = h - y = 0.44$, refer to perturbation velocities, dimensionless height, frictional velocity, wall-normal height respectively), highlight the presence

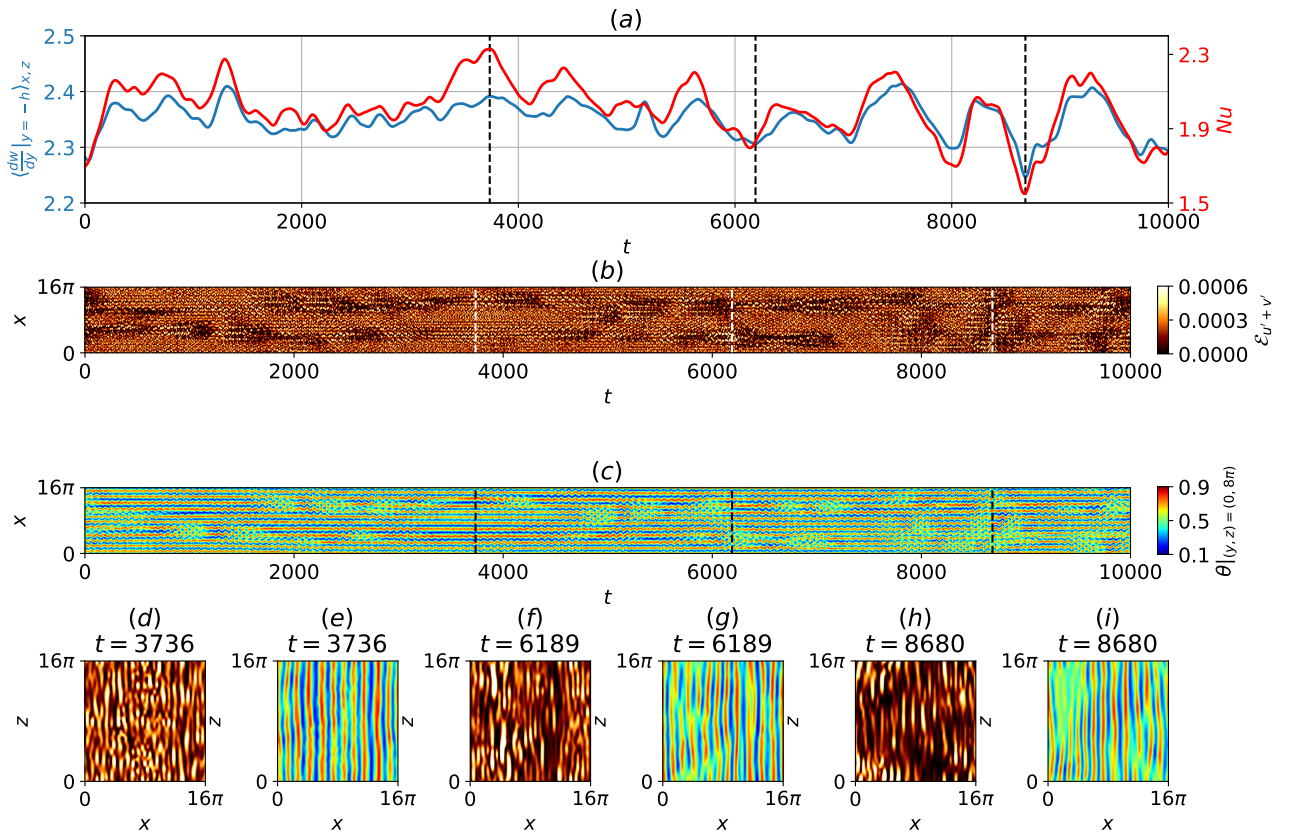


Figure 3.2: The intermittent rolls regime at $Ra = 8000$, $Re = 500$, $t \in [0, 10000]$. The time history of (a) Nusselt number, and shear, (b) near-wall wall-normal and spanwise perturbation kinetic energy, (c) midplane temperature spacetime plot, and their corresponding near-wall and midplane temporal planar snapshots at (d,e) $t = 3736$, (f,g) $t = 6189$, and (h,i) $t = 8680$.

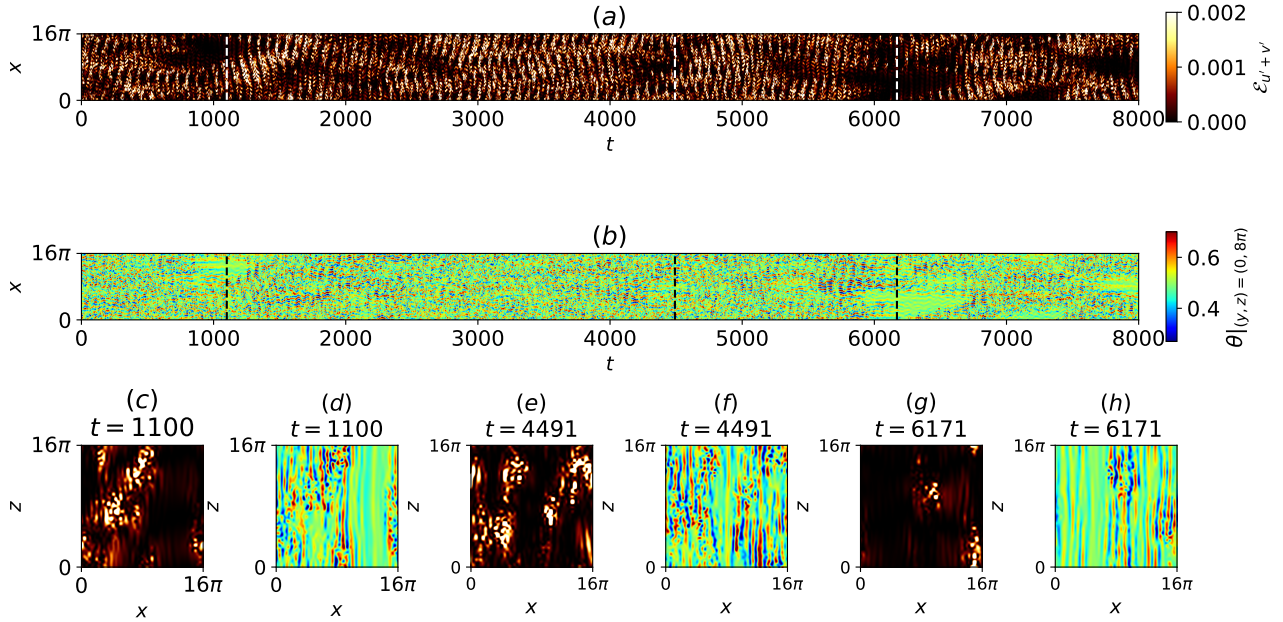


Figure 3.3: Shear-driven turbulence regime at $Ra = 0, Re = 1050, t \in [0, 8000]$. Spacetime plots of (a) near-wall wall-normal and spanwise perturbation kinetic energy, (b) midplane temperature spacetime plot, and near-wall and midplane temporal planar snapshots at (c,d) $t = 1100$, (e,f) $t = 4491$, and (g,h) $t = 6171$, highlighting a prolonged laminar patch.

of longitudinal rolls and spatially-localised laminar states. Figure 3.2(c) describes the spacetime plot of midplane temperature, $\theta|_{(y,z)=(0,8\pi)}$, where elongated red/blue lines correspond to regions of longitudinal rolls, while green spots indicate spatially-localised laminar states, highlighting the breakdown process. The near-wall transport properties, such as the Nusselt number and shear, exhibit strong correlations, peaking at $t = 3736$, corresponding to a spatially coherent longitudinal roll structure in figure 3.2(d,e). This is followed by a dip at $t = 6189$ and $t = 8680$, indicative of the breakdown towards the laminar state shown in figures 3.2(f,g) and 3.2(h,i) respectively. In other words, the longitudinal rolls enhance heat and momentum transfer across the wall, which is briefly disrupted by its breakdown towards the laminar state. However, exploring the spatiotemporal intermittency of this regime remains challenging in a large extended domain. To overcome this challenge, we consider a confined domain, $\Gamma = \pi/2$, where spatial intermittency could be artificially suppressed and discuss its temporal intermittent dynamics in §3.4.2.

3.3.3 Coexistence with turbulent bands

As Re approaches $Re = 1050$, shear-driven turbulence emerges as spatiotemporal intermittent turbulent-laminar bands, where turbulent and laminar regions can coexist (see references in §3.1.3). In the absence of buoyancy ($Ra = 0$), these bands emerge clearly, as shown in figure 3.3. The spacetime plot of the near-wall wall-normal and spanwise perturbation kinetic energy, $\mathcal{E}_{u'+v'}$, in figure 3.3(a) highlights this coexistence, where the turbulent and laminar regions are indicated by dark and bright areas, respectively. Notably, a period of prolonged laminar state is observed at $t = 1100, 4491, 6171$, represented by localised green regions in the midplane temperature spacetime plot, $\theta|_{(y,z)=(0,8\pi)}$, in

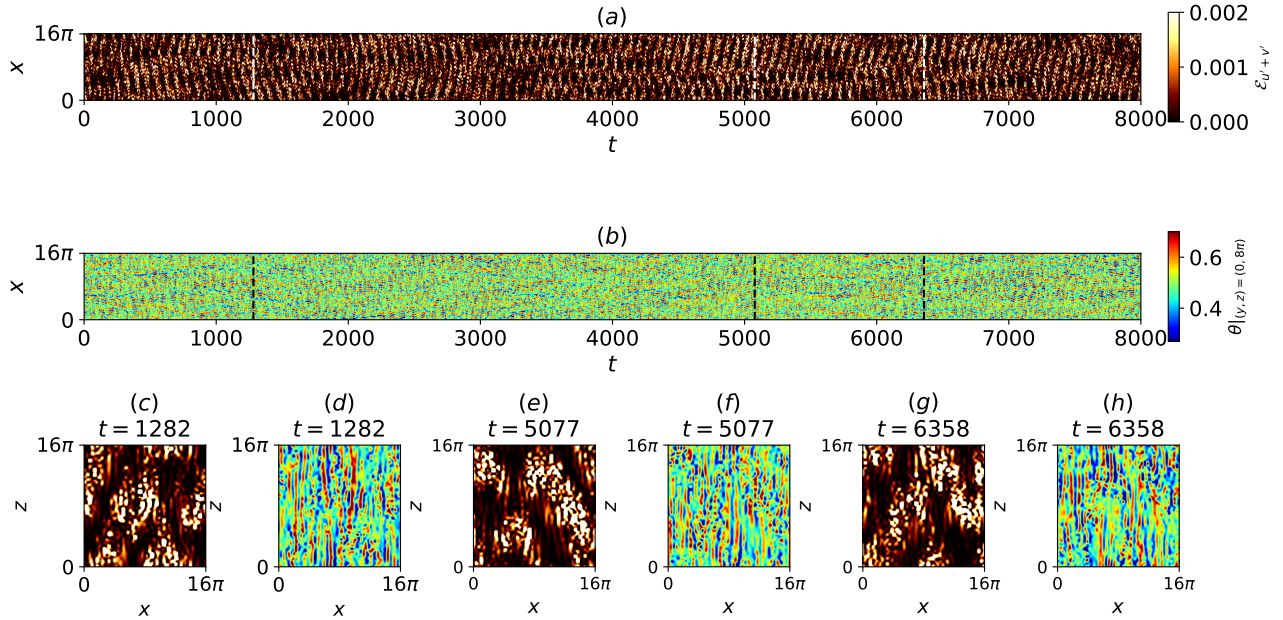


Figure 3.4: Shear-driven turbulence regime at $Ra = 100000$, $Re = 1050$, $t \in [0, 8000]$. Spacetime plots of (a) near-wall wall-normal and spanwise perturbation kinetic energy, (b) midplane temperature spacetime plot, and their corresponding near-wall and midplane temporal $x - z$ planar snapshots at (c,d) $t = 1282$, (e,f) $t = 5077$, and (g,h) $t = 6358$, highlighting the coexistence of longitudinal rolls and turbulent bands.

figure 3.3(b). The prolonged laminar states are also evident in the near-wall and midplane temporal snapshots of figures 3.3(c-h), shown as large pockets of dark and green regions filling approximately half of the spatial domain. Next, we consider the influence of buoyancy on the turbulent-laminar bands and compare cases at $Ra = 0$ and $Ra = 10000$ at $Re = 1050$. At $Ra = 10000$, the features of the turbulent-laminar bands appearing as alternate dark and bright bands are visually consistent in the spacetime plot of near-wall wall-normal and spanwise perturbation kinetic energy, $\mathcal{E}_{u'+v'}$, in figure 3.4(a). However, key differences between the $Ra = 0$ case emerge. Notably, the midplane temperature snapshots, $\theta|_{(y,z)=(0,0.8\pi)}$, at $t = 1282, 5077, 6358$ in figures 3.4(d,f,g) reveal localised regions of streamwise-aligned red and blue stripes, indicating the presence of longitudinal rolls, which are absent in $Ra = 0$. These longitudinal roll regions are located next to neighbouring turbulent (bright) regions in the near-wall perturbation kinetic energy snapshots in figures 3.4(c,e,g), suggesting that longitudinal rolls coexist with turbulent patches at $Ra = 10000$. However, we caution that similar red and blue stripes are also observed in $Ra = 0$, where longitudinal rolls are not expected, likely suggesting the presence of quasi-streamwise rollers, shown in figure 3.3(f). Nonetheless, turbulence occurs more spatially intermittently at $Ra = 0$, containing prolonged pockets of laminar regions, while the turbulent-laminar bands at $Ra = 10000$ appear more visibly consistently (compare figures 3.3(a) and 3.4(a)). In other words, the presence of longitudinal rolls may promote turbulence locally, where prolonged regions of laminar patches do not appear. However, investigating this remains challenging due to the spatiotemporal nature of a large extended domain. To address this, we focus our analysis to a confined domain, $\Gamma = \pi/2$, where turbulent bands and longitudinal bands cannot coexist, thereby reducing spatial intermittency discussed further in §3.4.

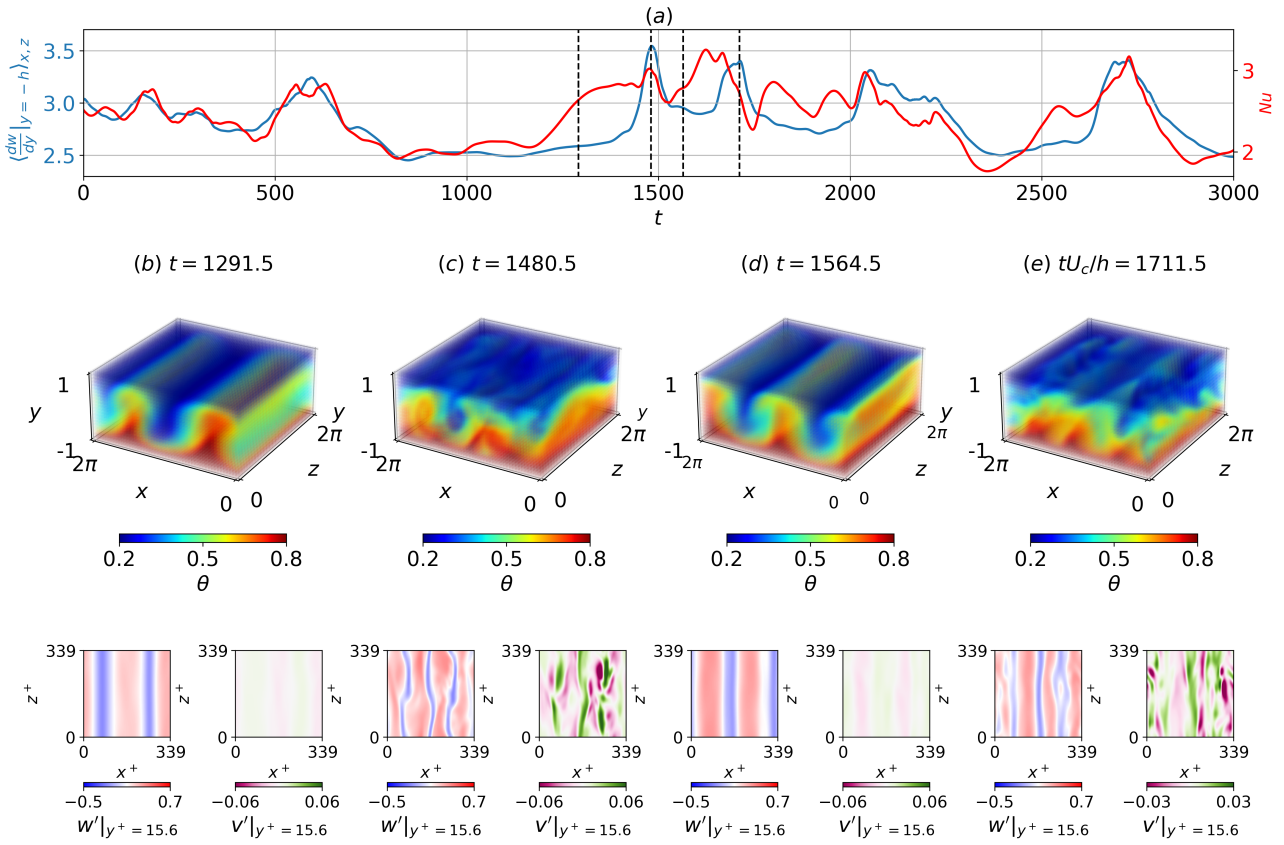


Figure 3.5: Intermittent dynamics in a confined domain at $Ra = 10000$, $Re = 1050$, $t \in [0, 3000]$, $\Gamma = \pi/2$. The time history of the (a) Nusselt number and shear. Temporal snapshots of volumetric temperature, planar near-wall streamwise and spanwise perturbations at (b) $t = 1291.5$, (c) $t = 1480.5$, (d) $t = 1564.5$, (e) $t = 1711.5$. Longitudinal rolls and transient turbulence are observed at (b,d) and (c,e), respectively.

3.4 The role of longitudinal rolls

3.4.1 The thermally-assisted sustaining process (TASP) in a confined domain

Motivated by the minimal flow unit (MFU) approach to study turbulence [?], we consider simulations confined to a confined domain defined by $\Gamma = \pi/2$, where the longitudinal rolls and localised turbulence could be spatially isolated. We first consider a numerical simulation at $Ra = 10000$, $Re = 1050$, in $\Gamma = \pi/2$, time integrated for $t \in [0, 3000]$. The initial condition has been sampled from a statistically stationary turbulent field at $Re = 2000$, which is then lowered slowly to $Re = 1050$. The time history from $t \in [0, 3000]$ of the near-wall transport properties such as the Nusselt number, Nu , shear, $\langle dw/dy|_{y=-h}\rangle_{x,z}$, volumetric temperature, $\theta(x)$, and near-wall streamwise and spanwise perturbation velocities snapshots, $w'|_{y^+=15.6}$, $v'|_{y^+=15.6}$, are presented in figure 3.5. In this confined domain, the dynamics of the system exhibit temporal intermittency, where the solution trajectory appears to wander between the longitudinal rolls and turbulent dynamics, marked by high and low near-wall transport properties, respectively. The turbulent dynamics mentioned here refer to chaotic trajectories (see §3.1.3) marked by a disordered volumetric temperature field and high near-wall transport quantities.

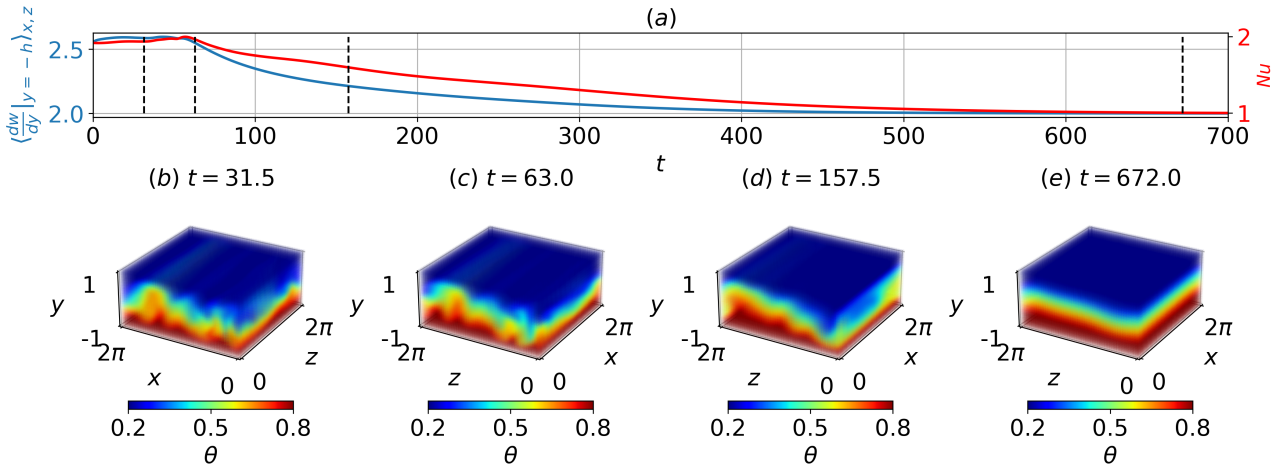


Figure 3.6: Relaminarisation in a confined domain at $Ra = 0$, $Re = 1050$, $t \in [0, 3000]$, $\Gamma = \pi/2$. The time history of the (a) Nusselt number and shear. Temporal snapshots of volumetric temperature at (b) $t = 31.5$, (c) $t = 63$, (d) $t = 157.5$, (e) $t = 672$.

Starting from a longitudinal roll state of spanwise wavenumber of $\alpha d = 4$ at $t = 1291.5$ in figure 3.5(b), the solution erupts into turbulence at $t = 1480.5$, marked by a disordered temperature field in figure 3.5(c). During this breakdown, the near-wall snapshots of streamwise perturbation velocity, $w'|_{y+=15}$, and wall-normal perturbation velocity, $v'|_{y+=15}$, illustrated in the bottom panels of figures 3.5(c), reveal three pairs of high- and low-speed streaks, each with an average spanwise wavelength of $\Lambda_x^+ \approx 339/3 = 113$ (where $\Lambda_x^+ = u_\tau \Lambda_x / \nu$ refers to non-dimensionalised wavelength), close to the mean streak spacing ($\Lambda^+ \sim 100$) commonly reported in shear flow turbulence [????]. These streaks appear to be meandering, negatively correlated with wall-normal perturbation velocities, reminiscent of a streak breakdown process [?], or a bursting event [?], where high- and low-speed streaks are brought close to and away from the wall, respectively, enhancing near-wall transport quantities. Indeed, this is reflected by large increments of the Nusselt number and shear of roughly 40% at $t = 1480.5$ in figure 3.5(a). Subsequently, the solution trajectory returns to a longitudinal roll state at $t = 1564.5$, before erupting into turbulence at $t = 1711.5$ (see figures 3.5(d,e) respectively). This suggests that the turbulence has a finite lifetime, occurring transiently before decaying towards the laminar state at $Re = 1050$ [??], which is linearly unstable, leading to the onset of longitudinal rolls where transient turbulence could be re-excited again.

To test this hypothesis, we consider a numerical simulation at $Ra = 0$, $Re = 1050$, in $\Gamma = \pi/2$, where longitudinal rolls cannot appear. The initial condition is taken from a stationary turbulent solution at $Ra = 0$, $Re = 2000$, which is then lowered slowly to $Re = 1050$, and then time integrated for $t \in [0, 700]$. The time history of Nusselt number, Nu , shear, $\langle dw/dy|_{y=-h} \rangle_{x,z}$, and the volumetric temperature snapshots, $\theta(\mathbf{x})$, are reported in figure 3.6. Turbulence occurs transiently, which decays towards the laminar solution in $t \in [0, 700]$ within the confined domain. As we compare the results between $Ra = 0$ and $Ra = 10000$, we propose that the longitudinal rolls at $Ra = 10000$ could provide a transition mechanism towards transient turbulence, which could be sustained indefinitely.

Next, we investigate the impact of longitudinal rolls on this proposed mechanism at different Ra .

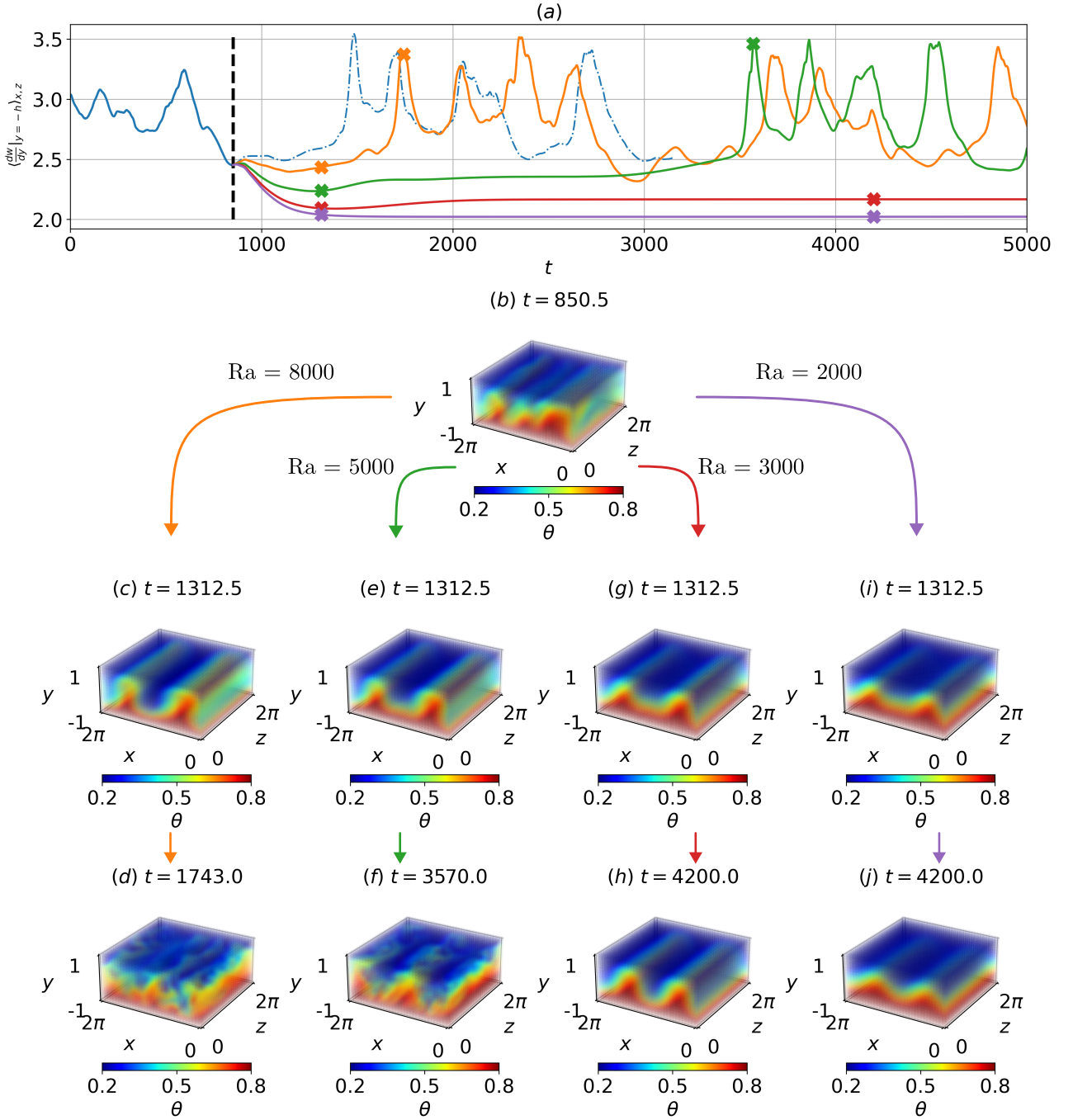


Figure 3.7: Ra -quenching experiments for $Ra = 8000, 5000, 3000, 2000$, $Re = 1050$, $\Gamma = \pi/2$, $t \in [850.5, 5000]$. The time history of (a) shear and (b) volumetric temperature snapshots of the initial condition at $t = 850.5$. Volumetric temperature snapshots for $Ra = 8000$ at (c,d) $t = 1312.5, 1743$, and $Ra = 5000$ at (e,f) $t = 1312.5, 3570$, revealing a longitudinal roll and a turbulent state, respectively. Stable longitudinal rolls emerge for $Ra = 3000$ at (g,h) $t = 1312.5, 4200$, and $Ra = 2000$ at (j,k) $t = 1312.5, 4200$.

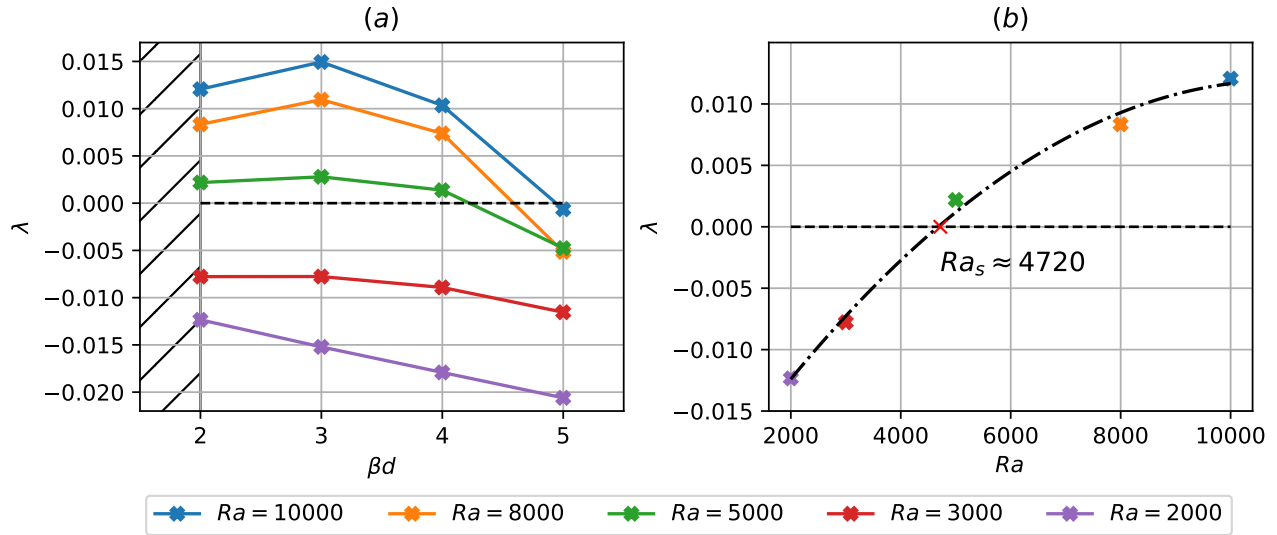


Figure 3.8: The growth rates of infinitesimal perturbations linearised about longitudinal rolls, \mathbf{q}_{LR} , of spanwise wavenumber of $\alpha d = 4$, against (a) streamwise wavenumber λ , and (b) Ra for $\beta d = 1$. The hatches in (a) refer to wavenumbers smaller than those admissible in $\Gamma = \pi/2$. The dash-dotted line in (b) is a standard quadratic regression yielding $Ra_s \approx 4720$.

We perform four numerical simulations with an initial condition taken from $Ra = 10000$, $Re = 1050$, at $t = 850.5$ (before the onset of longitudinal rolls, see figure 3.5), which is lowered instantaneously to $Ra = 8000, 5000, 3000, 2000$ respectively. The initial conditions are time-integrated further to $t \in [850.5, 5000]$, and the time history of the shear, $\langle dw/dy|_{y=-h} \rangle_{x,z}$, and the temperature volumetric temporal snapshots, $\theta(\mathbf{x})$, of these ‘Ra-quenching’ experiment are presented in figure 3.7. The time history of shear is visibly intermittent for $Ra = 8000, 5000$, depicted as the orange and green trajectories in figure 3.7(a), similar to $Ra = 10000$. At $Ra = 8000, 5000$, the longitudinal rolls emerge at $t = 1312.5$ (see figures 3.7(d,f)), before erupting into turbulence at $t = 1743$ and $t = 3570$ in figures 3.7(e,g) respectively. This is then accompanied by a large spike in the near-wall transport properties before dipping briefly in figure 3.7(a). As Ra is lowered to $Ra = 3000, 2000$, the transients begin to decay into a longitudinal state from $t = 850.5$ to $t = 1312.5$, which remains asymptotically stable until $t = 4200$, represented as the red and purple trajectories of figures 3.7(i,k) respectively. This suggests that the longitudinal rolls become linearly unstable for $Ra = 8000, 5000$, leading to turbulence, while remaining stable for $Ra = 3000, 2000$. Notably, the longitudinal rolls state at $Ra = 5000$ remained saturated over a longer period $t \in [1500, 3400]$ (green curve of figure 3.7), suggesting an underlying linear instability with a smaller growth rate compared to $Ra = 8000$. We note that the longitudinal rolls in figure 3.7 have a spanwise wavenumber of $\alpha d = 4$, which corresponds to the wavenumber of the dominant primary instability (see Appendix A.6), indicating that it is the preferred wavenumber within the confined domain.

To determine the stability characteristics of the longitudinal rolls, we perform linear stability analysis about the longitudinal roll state ($\alpha d = 4$), at $Ra = 10000, 8000, 5000, 3000, 2000$. The details of linear stability analysis are described in §3.2.4, where λ and $\hat{\mathbf{s}}_\beta e^{i\beta z}$ refer to the eigenvalue and eigenmode. The longitudinal roll (base) states, \mathbf{q}_{LR} , are obtained by time integrating an initial

condition consisting of the laminar (conduction) state, superimposed by the primary eigenmode, $ad = 4$, at $Ra = 10000, 8000, 5000, 3000, 2000$, in a two-dimensional $x - y$ plane, suppressing any three-dimensional perturbations numerically. The growth rates as a function of discrete streamwise wavenumbers, $2 \leq \beta d \leq 5$, are presented in figure 3.8. We note that the admissible streamwise wavenumbers within $\Gamma = \pi/2$ are $\beta d = m$, where m is a positive even integer, $m = 2, 4, \dots$, and $\beta d = 3, 5$ are included for completeness. The longitudinal rolls are linearly unstable for $Ra \geq 5000$, while they remain stable for $Ra \leq 3000$, confirming our hypothesis earlier. Notably, the growth rates between $Ra = 5000$ and $Ra = 10000$ differ by an order of magnitude, which could explain the prolonged period of saturation in the green curve of figure 3.7(a,b). The dominant secondary instability of longitudinal rolls in $\Gamma = \pi/2$ has a streamwise wavenumber of $\beta d = 2$. Using a standard quadratic regression, the critical Rayleigh number for disturbances with $\beta d = 2$ is approximately $Ra_s \approx 4720$, presented in figure 3.8(b).

Following this, we examine the dominant unstable manifold ($\beta d = 2$) of the longitudinal rolls, by considering an initial condition,

$$\mathbf{q}_0(\mathbf{x}, t = 0) = \mathbf{q}_{LR}(x, y) + \hat{\mathbf{q}}_\beta(x, y)e^{i\beta z}, \quad (3.7)$$

which is prescribed to equation (3.1). Here, $\hat{\mathbf{q}}_\beta e^{i\beta dz}$ is an eigenmode at βd , and the amplitude of which was scaled such that its total energy is defined by,

$$\delta = \frac{1}{V} \int_{\Omega} \hat{\mathbf{u}}(\mathbf{x})^T \hat{\mathbf{u}}(\mathbf{x}) + \frac{Ra}{8Re^2Pr} \hat{\theta}(\mathbf{x})^2 d\Omega \approx O(10^{-3}) \quad (3.8)$$

is considered. We have also considered that $\delta = 10^{-2}, 10^{-4}$, where $\delta = 10^{-3}$ was found to be sufficiently small enough to ensure linear growth, while large enough to be computationally practical.

The initial condition is time integrated from $t \in [0, 8000]$, and its time history of near wall transport properties such as the Nusselt number, Nu and shear, $\langle dw/dy|_{y=-h} \rangle_{x,z}$, midplane temperature spacetime plot, $\theta|_{(y,z)=(0,\pi)}$, volumetric temperature, $\theta(\mathbf{x})$, and near-wall streamwise and spanwise perturbation velocities snapshots, $w'|_{y^+=15}, v'|_{y^+=15}$, are presented in figure 3.9. The intermittent trajectory is visually present, oscillating between the longitudinal rolls and transient turbulence over four cycles $t = [0, 8000]$, marked by regions of low and high near-wall transport quantities in figure 3.9(a) and alternating between organised and disorganised longitudinal rolls in figure 3.9(b). The snapshots of figure 3.9 illustrate the volumetric temperature field, planar near-wall streamwise and wall-normal perturbations, resembling the longitudinal rolls ($LR1 - 4$), and transient turbulent states ($T1 - 4$). As the solution emerges from the unstable manifold of the longitudinal roll state, ($LR1$) in figure 3.9(c), the trajectory erupts into turbulence at $t = 1512$, marked by a disordered volumetric temperature field with high- and low-speed streaks in snapshot ($T1$) in figure 3.9(c). These high- and low-speed streaks are negatively spatially-correlated with wall-normal perturbation velocities in figure 3.9(d), reminiscent of sweeps and ejection events commonly found in turbulent shear flows [??]. Notably, the flow structures in snapshot $T1$ in figure 3.9(d), appear visibly symmetric along the centerline of the channel, $x^+ \approx 162$ (where $x^+ = u_\tau x / \nu$ refers to the non-dimensionalised spanwise coordinate), comparable to the invariant states identified in transition shear flows [?????]. Turbulence

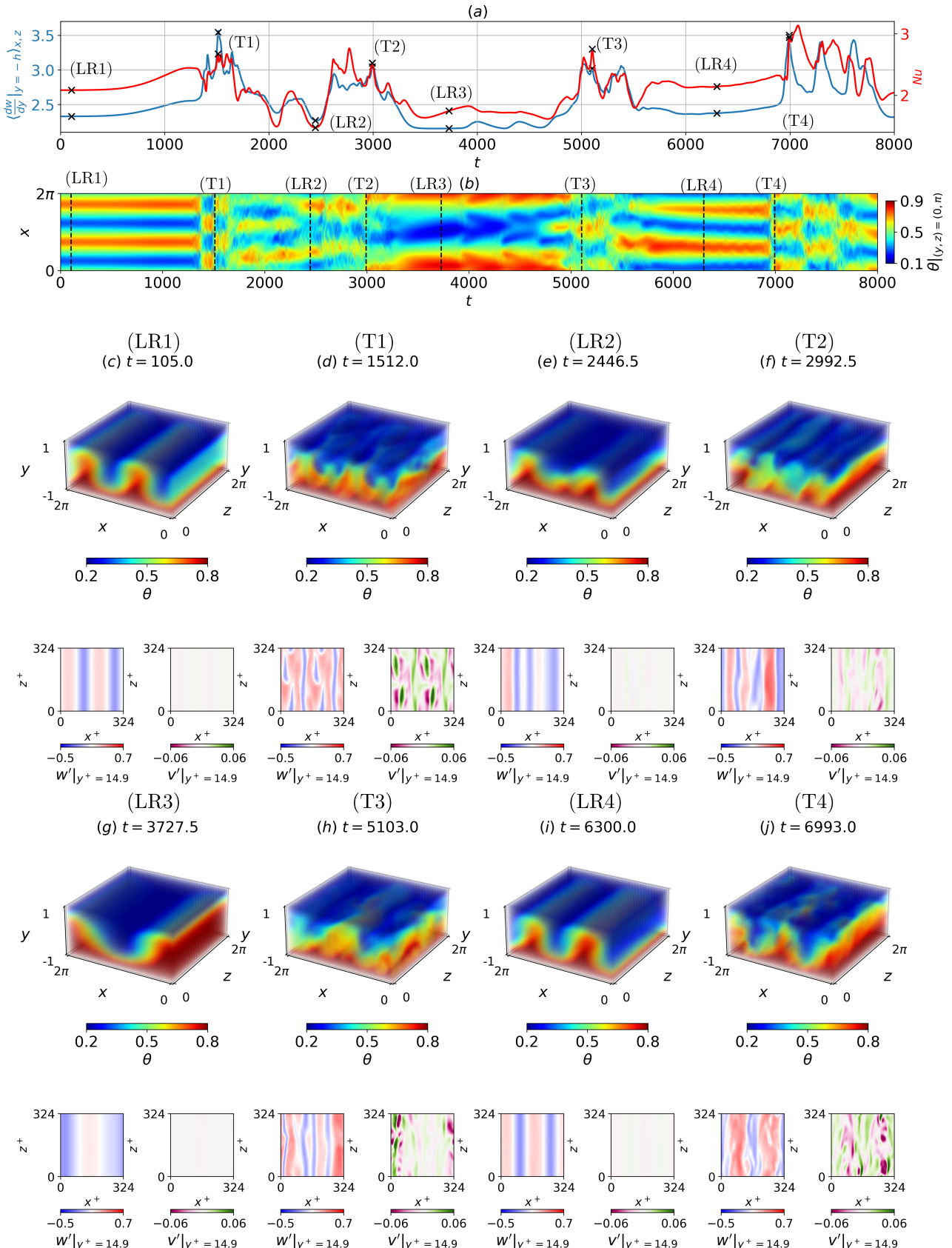


Figure 3.9: Integrating along the dominant unstable manifold, $\beta d = 2$, of the longitudinal rolls at $Ra = 5000$, $Re = 1050$, $\Gamma = \pi/2$, $t \in [0, 8000]$. Time history of the (a) Nusselt number and shear, and (b) midplane temperature spacetime plot. This system oscillates between the longitudinal rolls ($LR1 - 4$) and turbulence ($T1 - 4$) over four intervals. Snapshots of volumetric temperature and near-wall streamwise and spanwise velocity perturbations at (b) $t = 105$, (c) $t = 1512$, (d) $t = 2446.5$, (e) $t = 2992.5$, (f) $t = 3727.5$, (g) $t = 5103$, (h) $t = 6300$, (i) $t = 6993$.

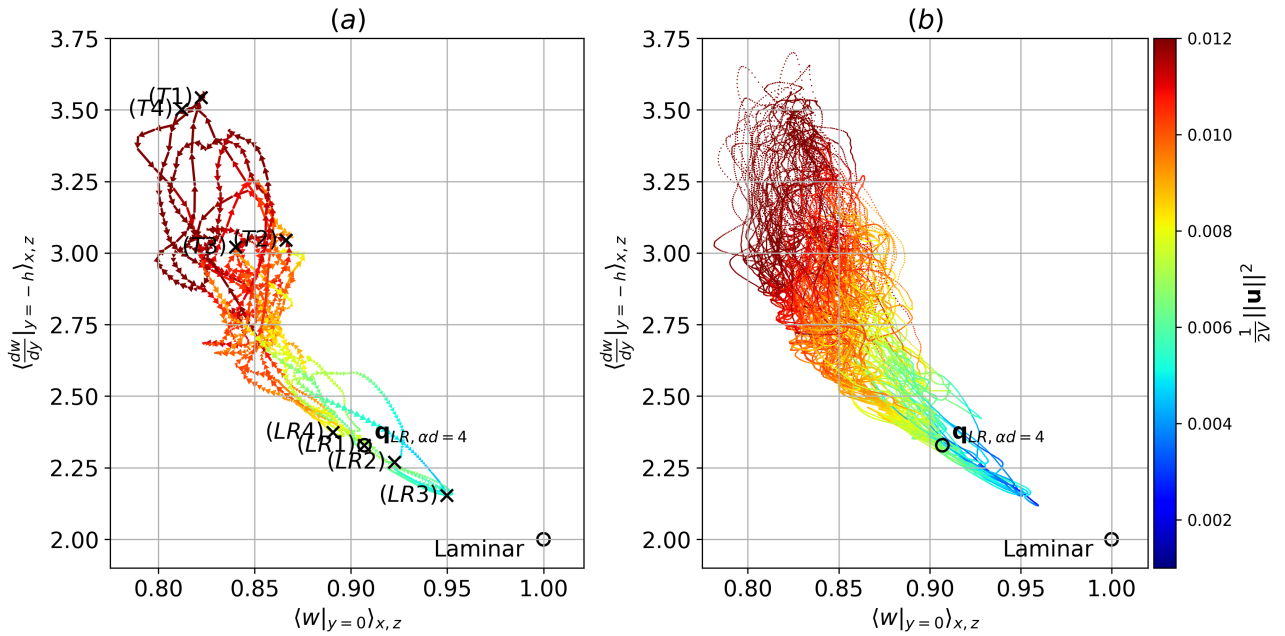


Figure 3.10: State space projection based on the planar averaged centerline velocity and shear, coloured by the volume normalised perturbation kinetic energy at $Ra = 5000$, $Re = 1050$, $\Gamma = \pi/2$, (a) $t \in [0, 800]$, (b) $t \in [0, 68750]$. The open black circles represent the unstable equilibria of longitudinal rolls and the laminar state. Note that the black-crosses, labelled by (T1-4) and (LR1-4), refer to temporal snapshots in figure 3.9, not equilibria solutions.

occurs transiently, and the solution decays towards a longitudinal roll-like state at $t = 2446.5$, shown by snapshot (LR2) in figure 3.9(e), thereby completing one single cycle. We note that the snapshot (LR2) does not strictly resemble the longitudinal roll state at snapshot (LR1), however, we show that they are similar and reside close by in state space, as we shall see later. The intermittent cycle repeats over three subsequent intervals, where the turbulent dynamics and longitudinal rolls emerge at $t = 2992.5, 5103, 6993$, and $t = 3727.5, 6300$, represented as snapshots (T2, 3, 4) and (LR3, 4) in figures 3.9(f,h,j) and 3.9(g,i) respectively.

Here, we showed that the dominant unstable manifold of the longitudinal rolls is linked to turbulent dynamics, a transition mechanism based on linear instability. Interestingly, a ‘single’ longitudinal roll with $\alpha d = 2$ emerges after turbulence decays, shown as snapshot (LR3). This suggests that other unstable manifolds may be linked to the transition to transient turbulence.

To visualise the temporal dynamics in figure 3.9 with better clarity, we project the solution trajectory onto state observables using the planar averaged centerline velocity, $\langle w|_{y=0} \rangle_{x,z}$, shear, $\langle dw/dy|_{y=-h} \rangle_{x,z}$ coloured by the volume normalised perturbation kinetic energy, $1/(2V)||\mathbf{u}'||^2$, in figure 3.10. These observables seek to distinguish the region of turbulent dynamics, longitudinal roll state, and laminar state residing in near $(0.82, 3.2)$, $(0.90, 2.32)$ and $(1, 2)$, respectively. This separation is further supported by the location of the temporal snapshots between (T1 – 4) and (LR1 – 4), organised near the turbulent dynamics and in longitudinal roll state, $\mathbf{q}_{LR,\alpha d=4}$, setting them apart. We emphasise that the unstable longitudinal roll state, $\mathbf{q}_{LR,\alpha d=4}$, and laminar states denoted by open circles are unstable equilibria, while the snapshots longitudinal roll, (LR1 – 4), and turbulent

snapshots, ($T1 - 4$), denoted by black crosses, are not.

The solution trajectory emerges from the unstable manifold of the longitudinal rolls, $\mathbf{q}_{LR_{\alpha d=4}}$, evolving towards turbulent dynamics around $(0.85, 3.2)$, denoted by high shear. Turbulence is transient, occurring with a finite lifetime [??], eventually decaying towards the laminar state. As the solution trajectory approaches the laminar solution $(1, 2)$, it abruptly reverses towards the longitudinal roll state near $(0.95, 2.15)$, $(LR3)$. Subsequently, the solution trajectory could depart along the unstable manifold of the longitudinal rolls again, leading to the onset of turbulence, where the cycle repeats.

To determine if this cycle could be sustained indefinitely, we consider a longer time horizon, $t \in [0, 68750]$, illustrated in figure 3.10(b). The solution trajectory wanders between the ‘cloud’ of chaotic transient turbulence at the top left corner (in red), and longitudinal roll and laminar state (in blue) in the bottom right, forming a basin of attraction between the unstable longitudinal rolls, transient turbulence and the laminar state. We suggest that this basin of attraction, is likely established above a critical Ra as the longitudinal rolls become linearly unstable (i.e $Ra \gtrsim Ra_s \approx 4720$, see figure 3.8(b)), providing an intermediate pathway towards transient turbulence, which could be regenerated again - a ‘self-sustaining’ dynamical process. We refer to this sustaining process as the *thermally-assisted sustaining process (TASP)*, inspired by the self-sustaining process (SSP) from turbulent shear flows [?].

3.4.2 Variation of Ra and Re on the thermally sustained turbulent process within $\Gamma = \pi/2$

In this section, we explore the behaviour of the *TASP* as Re and Ra are varied. We consider eight different cases at $Ra = 8000, 4000$ and $Re = 600, 700, 1000, 1400$. The results of these eight cases, where longitudinal rolls are either unstable at $Ra = 8000$ or stable at $Ra = 4000$, are shown in figure 3.11, depicting the spacetime plots of midplane temperature, $\theta|_{y=0}(x, t)$, time history of the Nusselt number, Nu , and shear, $\langle dw/dy|_{y=-h} \rangle_{x,z}$ and state space projection using the planar averaged centerline velocity, $\langle w|_{y=0} \rangle_{x,z}$, shear, coloured by the volume normalised perturbation kinetic energy, $\frac{1}{2V} \|\mathbf{u}'\|^2$. For all cases except $Ra = 4000$, $Re = 1000$ and $Re = 1400$, their initial conditions are prepared from the laminar state, superimposed by a random noise based on a Gaussian distribution with zero mean and unit variance, scaled to a total energy of $\delta = 10^{-3}$ (see definition in equation (3.8)). For the exceptional cases at $Ra = 4000$, $Re = 1000$ and $Re = 1400$, where subcritical turbulence and stable longitudinal rolls are expected, their initial conditions are obtained by gradually lowering Re from a statistically stationary turbulent solution at $Re = 2000$. We note that we have not explicitly performed a linear stability analysis of the longitudinal rolls for the parameter regime in figure 3.11, however, they appear to be unstable at $Ra = 8000$, while being stable at $Ra = 4000$ from DNS.

At $Ra = 8000$, $Re = 1000$, $t \in [0, 10000]$ in figure 3.11(c), the trajectory visits the transient turbulent regime near $t = 7200$, which decays towards the longitudinal roll state, \mathbf{q}_{LR} , at $t = 7400$, which could be regenerated again, consistent with the *TASP* in §3.4.1. As Ra is lowered to 4000, the solution trajectory decays towards the longitudinal roll state, \mathbf{q}_{LR} , where the *TASP* disappears. In this case, the longitudinal rolls are linearly stable, confirming our hypothesis earlier that the *TASP* is only established when longitudinal rolls become linearly unstable above a certain Ra -threshold (i.e

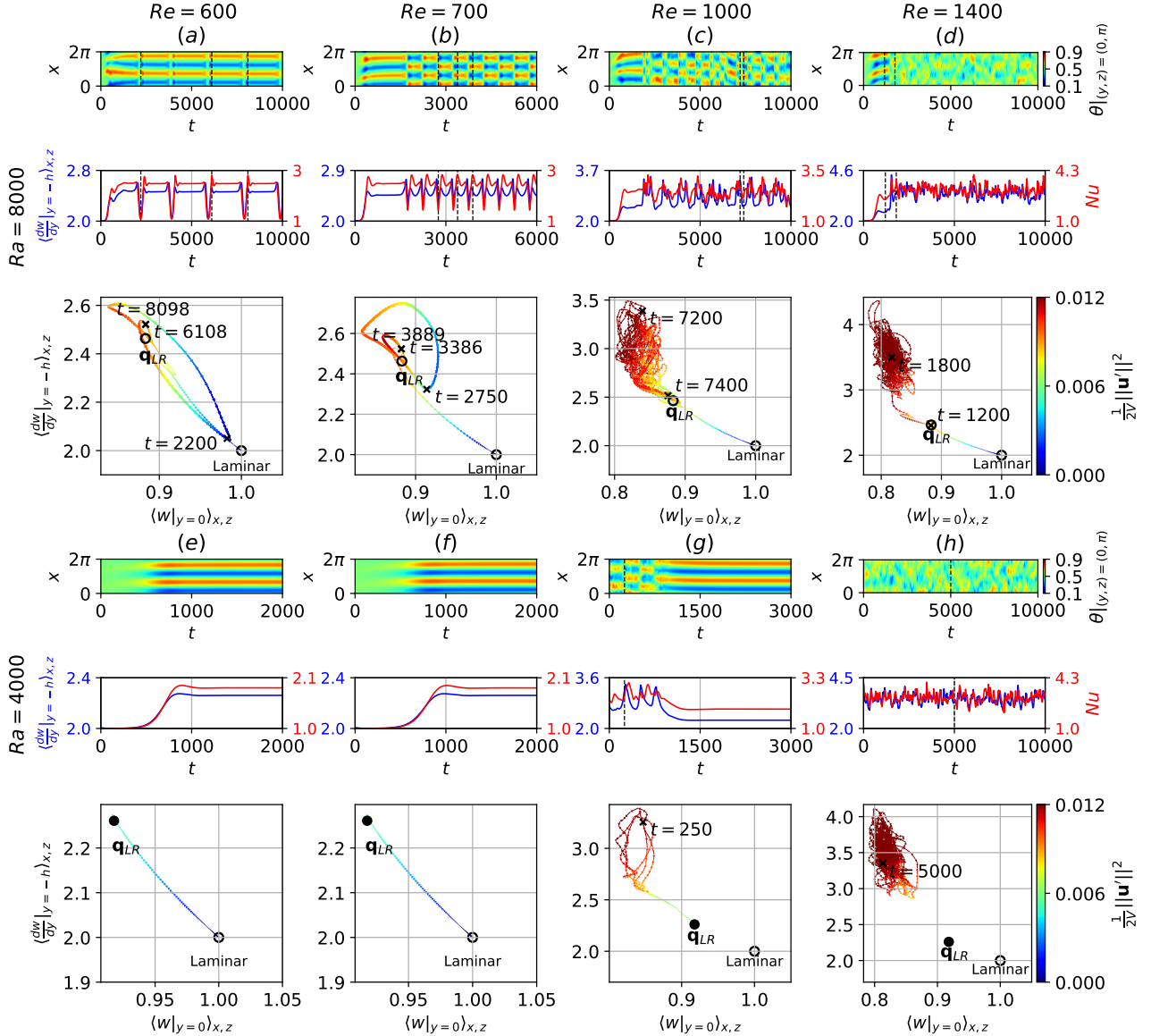


Figure 3.11: The behaviour of the unstable and stable longitudinal rolls at $Ra = 8000, 4000$ for (a,e) $Re = 600$, (b,f) $Re = 700$, (c,g) $Re = 1000$ and (d,h) $Re = 1400$ within $\Gamma = \pi/2$. Each parameter regime consist of three panels from the top to bottom, depicting the midplane temperature spacetime plot, $\theta|_{(y,z)=(0,\pi)}$, time history of the Nusselt number and shear, and state space projection based on the planar averaged centerline velocity and shear, coloured by the volume normalised perturbation kinetic energy.

$Ra \gtrsim Ra_s \approx 4720$).

At $Re = 1400$, $Ra = 4000$, the solution trajectory remains within the turbulent ‘cloud’ near $(0.8, 3.8)$ illustrated in figure 3.11(h), suggesting that turbulence might be sustained indefinitely, in which the turbulent chaotic saddle at $Re = 1000$ could be transformed into a chaotic attractor at $Re = 1400$. As Ra is increased to 8000, the solution trajectory originating from the laminar state, evolves towards the unstable longitudinal roll state, \mathbf{q}_{LR} at $t = 1550$, transitioning into sustained turbulence at $t = 1800$. Therefore, the linearly unstable longitudinal rolls serve as an intermediate transitional pathway between the laminar state and subcritical turbulence, whereas at $Ra = 4000$, a bistability between stable longitudinal rolls (not shown) and turbulence is established.

Next, we examine the behaviour of *TASP* as Re decreases towards the intermittent regime at $Re = 600, 700$, where a periodic orbit emerges between the longitudinal roll and the laminar state. At $Re = 600, Ra = 8000$ in figure 3.11(a), the solution trajectory initially evolves towards the longitudinal roll state, \mathbf{q}_{LR} , which is linearly unstable and breaks down towards the laminar state at $t = 2200$. This breakdown is evidenced by the trajectory’s proximity to the laminar state in state space and the presence of a narrow green patch in the midplane temperature spacetime plot. The longitudinal roll state is regenerated again, forming a periodic orbit with a period of $T_{period} = 8098 - 6108 = 1990$, oscillating between the longitudinal roll and laminar state over five intervals within $t \in [0, 10000]$. As Re increases slightly to 700, the periodic orbit persists over a shorter period of $T_{period} = 3889 - 3386 = 503$. A notable difference is observed in the regenerated longitudinal rolls, which is continuously translated by $L_x/2$ in the x -direction. Additionally, as Re increases from 600 to 700, the trajectory moves further away from the laminar state during breakdown, suggesting an increasing attraction towards the longitudinal roll state, \mathbf{q}_{LR} (compare $t = 2200$ in figure 3.11(a) and $t = 2750$ in figure 3.11(b)). When Ra is lowered to $Ra = 4000$, the periodic orbit disappears and the trajectory stabilises into the longitudinal roll state, \mathbf{q}_{LR} , at $Re = 600, 700$.

To summarise the dynamical processes identified in figure 3.11, we present a state space sketch of it in figure 4.21. At $Ra = 8000$, $Re = 600$ and $Re = 700$, the longitudinal rolls become linearly unstable, breaking down into the laminar state before being regenerated, forming a periodic orbit illustrated enclosed by black dotted paths in figures 4.21(a,b). For $Re = 700$, the regenerated longitudinal roll is continuously translated by $L_x/2$, suggestive a possible merger of two periodic orbits into one sketched in figure 3.11(b). Future bifurcation studies are required to establish this, providing an avenue for future work. As Ra is lowered to $Ra = 4000$, the laminar state stabilises into the longitudinal rolls in figure 4.21(e). This regime may contain invariant solutions [?], denoted as saddle points here. Integrating along the unstable manifold of longitudinal rolls at $Ra = 8000, Re = 1000$ leads to transient turbulence, which eventually decays to the laminar state before regenerating into longitudinal rolls again, forming the *TASP* in figure 4.21(c). In contrast, at $Ra = 4000, Re = 1000$, the longitudinal rolls become linearly stable, eliminating the intermediate (orange) pathway toward turbulence where transient turbulence stabilises into longitudinal rolls shown as the black-dashed trajectory in figure 4.21(f). For $Ra = 8000, Re = 1400$, the linearly unstable longitudinal rolls provide an intermediate pathway towards turbulence from the laminar state sketched in figure 4.21(d), breaking the bistability between the laminar state and subcritical turbulence seen at $Ra = 4000$ in

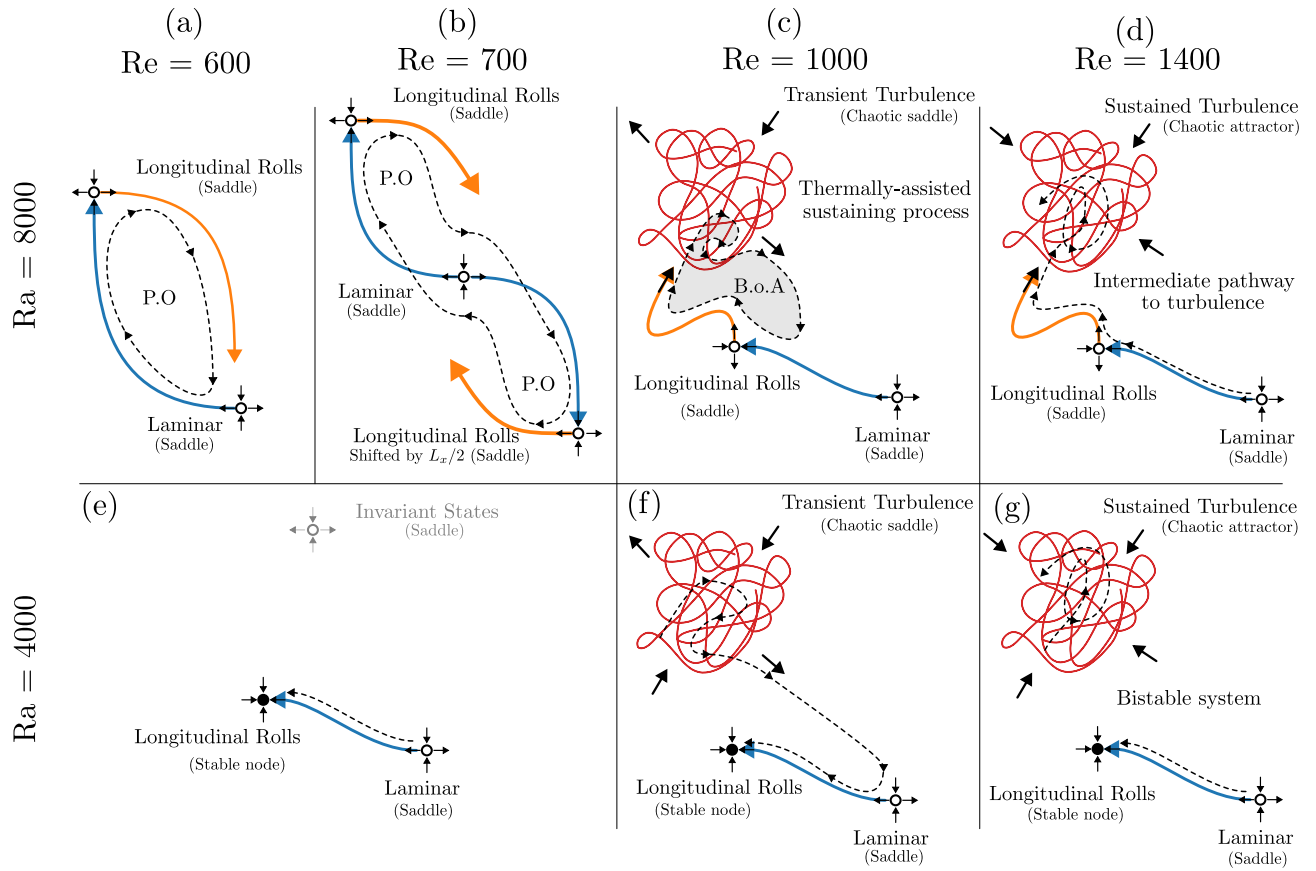


Figure 3.12: A state space sketch of figure 3.11 at $Ra = 8000$, (a) $Re = 600$, (b) $Re = 700$, (c) $Re = 1000$, (d) $Re = 1400$ and $Ra = 4000$ at (e) $Re = 600, 700$, (f) $Re = 1000$, (g) $Re = 1400$. The longitudinal roll is linearly unstable (saddle) at $Ra = 8000$, and is stable at $Ra = 4000$, whereas the laminar state is always linearly unstable (saddle). The blue and orange solid arrows refer to the unstable manifold of longitudinal rolls and the laminar state. The red solid lines denote the chaotic trajectories of turbulence, likely forming a chaotic saddle at $Re = 1000$ and a chaotic attractor at $Re = 1400$. The black-dashed trajectories refer to possible solution trajectories, forming a periodic orbit (P.O.) at $Ra = 8000$, $Re = 600, 700$, and a basin of attraction (B.o.A.) at $Ra = 8000$, $Re = 1000$. We note that invariant states could exist at $Ra = 4000$, $Re = 600, 700$, labelled as a saddle here [?].

figure 4.21(g). This behaviour resembles the nature of subcritical turbulence in shear-driven flow, highlighting the contribution of unstable longitudinal rolls towards the transition to turbulence within $\Gamma = \pi/2$.

We examined the dynamics of unstable longitudinal rolls as the Reynolds number, Re , and Rayleigh number, Ra , are varied, identifying three key dynamical processes: (1) periodic orbits between longitudinal rolls and the laminar state (figure 4.21(a,b)), (2) the *TASP*, where transient turbulence can be sustained (figure 4.21(c)) and (3) an intermediate transitional pathway towards sustained turbulence (figure 4.21(d)). To establish a connection between these processes and understand their transitional boundaries, we conduct a parameter sweep over $Ra \in [4000, 10000]$ and $Re \in [600, 1400]$ within $\Gamma = \pi/2$. Figure 3.13 presents the midplane temperature spacetime plot alongside the time history of shear, $\langle dw/dy|_{y=-h} \rangle_{x,z}$ and the Nusselt number, Nu . For all simulations, the initial conditions are prepared from the laminar state, superimposed with a random noise based on a Gaussian distribution with zero mean and unit variance, scaled to a total energy of $\delta = 10^{-3}$ (see definition in equation (3.8)). Due to the subcritical nature of turbulence and expected stable longitudinal rolls, exceptions are made for $Ra = 4000$, $Re \in [900, 1400]$, where initial conditions are taken from gradually lowering Re from a statistically stationary turbulent state at $Re = 2000$. The *thermally-assisted sustaining process* is highlighted in green for $Ra \in [5000, 10000]$ and $Re \in [900, 1200]$, where temporally intermittent shear and Nusselt number fluctuations are observed, accompanied by a mixture of organised and disorganised flow structures in the temperature spacetime plots. In this regime, the longitudinal rolls provide an intermediate pathway towards transient turbulence, which appears linearly unstable for $Ra \geq 5000$. Below this threshold, transient turbulence decays into stable longitudinal rolls, as observed at $Ra = 4000$, $Re \in [900, 1200]$ labelled as 'transient turbulence'. Periodic orbits between longitudinal rolls and the laminar state occur for $Ra \in [6000, 10000]$ and $Re \in [600, 800]$, establishing above a critical $Ra - Re$ threshold, below which solutions stabilise into longitudinal rolls shaded in red. Notably at $Re = 800$, the periodic orbit becomes increasingly quasi-periodic, likely related to the *TASP* near $Re \sim 900$. Despite longitudinal rolls being linearly stable at $Ra = 4000$, $Re = 1400$ (not shown), turbulence is sustained, shaded in blue across $Re = 1400$. In this case, a bistable system forms between longitudinal rolls and turbulence at $Ra = 4000$, while the longitudinal rolls provide an intermediate pathway towards turbulence for $Ra \geq 5000$. Figure 3.13 underscores the role of unstable longitudinal rolls in transitional RBP flows within confined domains.

3.4.3 Extending to large domains, $\Gamma = 4\pi$.

In this section, we bridge the gap between the confined and large domains by discussing the relevance of dynamical processes within the confined domains to the large domains, $\Gamma = 4\pi$. We will focus on the intermittent roll and shear-driven turbulence regime at $Ra = 500, 750, 1000, 1050$ for $Ra = 10000$ presented by figure 3.14, illustrating their spacetime plots of midplane temperature, $\theta|_{(y,z)=(0,8\pi)}$, and near-wall wall-normal and spanwise perturbation kinetic energy, $\mathcal{E}_{u'+v'}$. Additionally, we also examine the probability distribution functions based on the centreline-velocity normalised midplane velocity and temperature, $f(w|_{y=0}, \theta|_{y=0})$. At $Ra = 10000$, $Re = 500$, the breakdown of longitudinal rolls towards the laminar state is observed, highlighted by spatially-localised green spots in the midplane

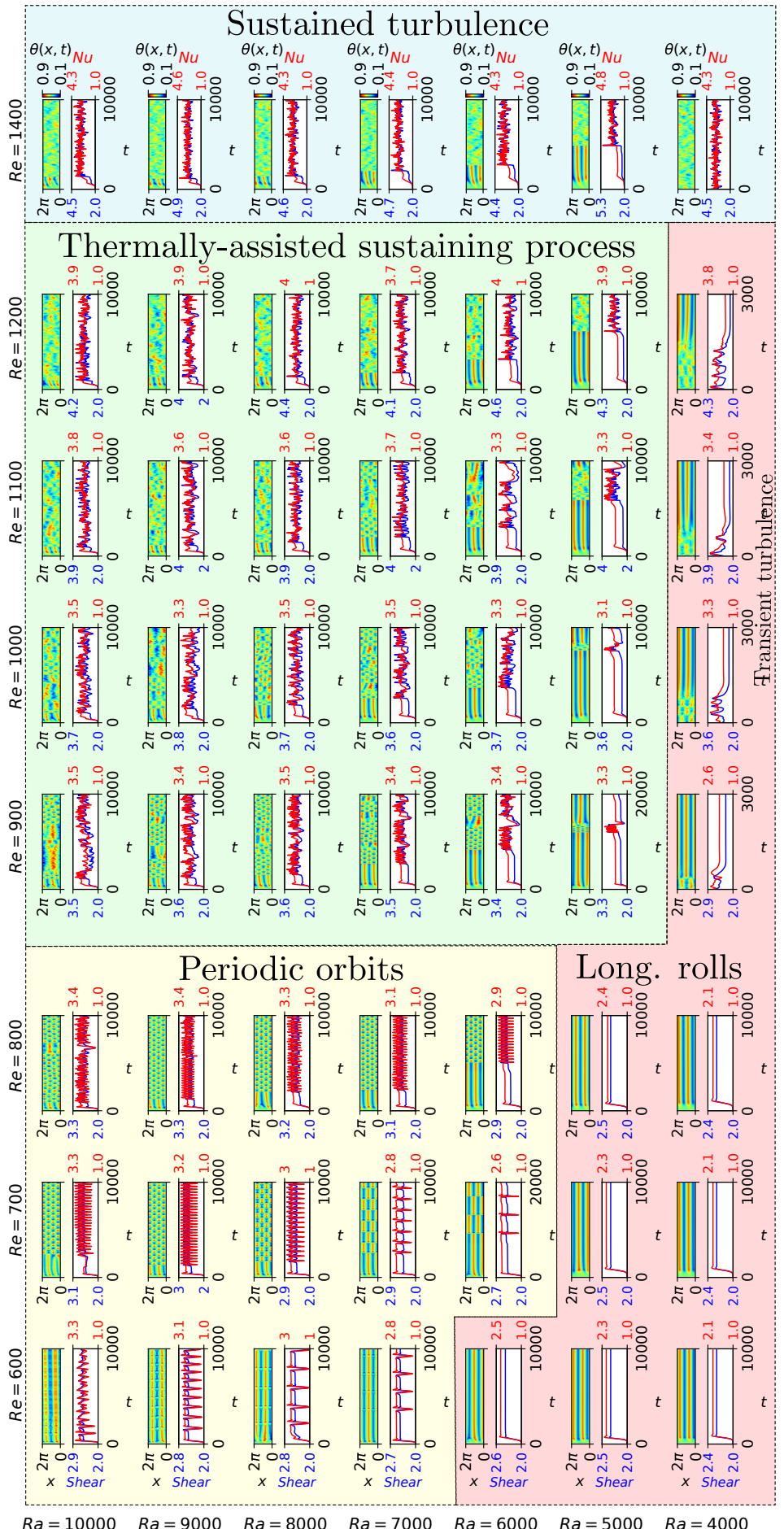


Figure 3.13: The temperature spacetime plots and time history of shear and the Nusselt number for $Ra \in [5000, 10000]$, $Re \in [600, 1400]$ within $\Gamma = \pi/2$. Unstable longitudinal rolls lead to the onset of (1) periodic orbits (yellow), (2) the *thermally-assisted sustaining process* (green), and (3) sustained turbulence (blue), occurring beyond an $Ra - Re$ boundary, below which longitudinal rolls remain stable (red).

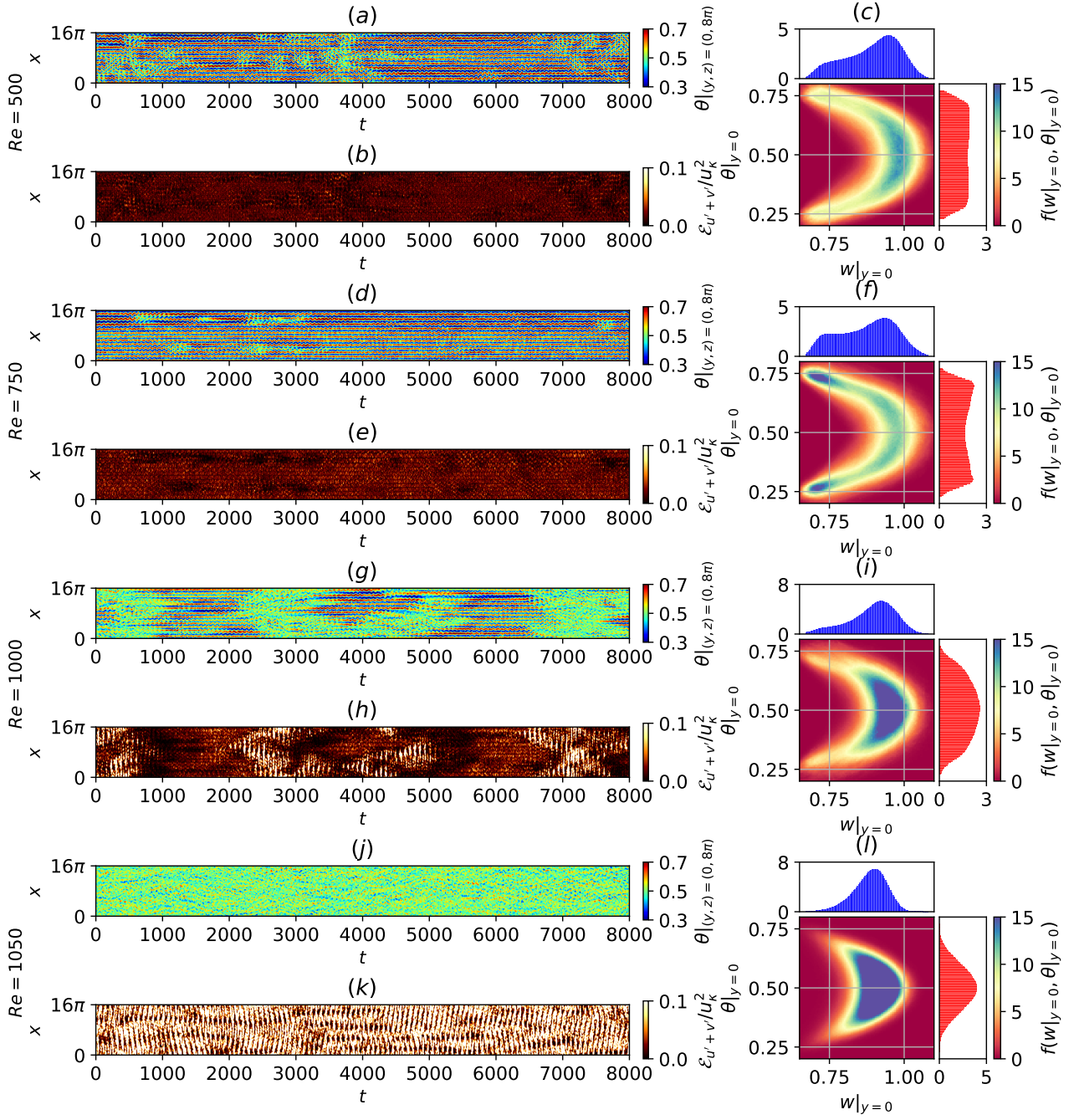


Figure 3.14: The midplane temperature spacetime plot, and near-wall wall-normal and spanwise perturbation kinetic energy by normalised by thermal velocity scale, u_κ , and the probability density functions based on planar-averaged centerline velocity and the midplane temperature at $Ra = 10000$, (a,b,c) $Re = 500$, (d,e,f) $Re = 750$, (g,h,i) $Re = 1000$, (j,k,l) $Re = 1050$.

temperature plots, and dark regions in the near-wall perturbation kinetic energy spacetime plot near $t = 500, 3800$ in figure 3.14(a,b) respectively. As Re increases from 500 to 750, the breakdown towards the laminar state remains visually apparent. The spatiotemporal dynamics between longitudinal rolls and the laminar state within the intermittent regime in the large domain are reminiscent of the periodic orbit identified between them in a confined domain. There is a noticeable decrease in the number of green and dark regions between figures 3.14(a,b) and (d,e), suggesting fewer laminar events at $Re = 750$. Indeed, this difference is further reflected in their PDFs, where the probability of laminar events, at $(w|_{y=0}, \theta|_{y=0}) = (1, 0)$, depicted as the ‘head’ of the ‘arc-shaped’ PDF decreasing from $Re = 500$ (figure 3.14(c)) to $Re = 750$ (figure 3.14(f)). This likely suggests fewer laminar state events and more occurrences of the longitudinal roll state, as the solution trajectory becomes increasingly attracted towards the longitudinal roll state from $Re = 600$ and $Re = 700$ at $Ra = 8000$ in the confined domain presented in figures 3.11(a,b).

At $Re = 1000$, we observe the coexistence of the laminar state, the longitudinal rolls and transient turbulence appearing as dark, bright and very bright regions in the near-wall wall-normal and spanwise perturbation velocities, normalised by thermal velocity scale, $\mathcal{E}_{u'+v'}/u_\kappa^2$ (where $u_\kappa = \kappa/d$) in figure 3.14(h). Starting at $t = 2000$, the longitudinal rolls appearing as red/blue elongated strips in figure 3.14(g) erupt into turbulence at $t = 2500$, appearing as very bright spots in figure 3.14(h). Turbulence is transient, decaying towards the laminar state at $t = 3000$, as indicated by the dark patches in figure 3.14(h). By $t = 4000$, longitudinal rolls are regenerated, appearing as red/blue elongated strips in figure 3.14(g). This process resembles TASP in a confined domain (figure 4.21(c)), suggesting that a similar process may be present in the large domain.

As Re approaches $Re = 1050$, turbulence becomes sustained, forming distinct turbulent-laminar bands as seen in figure 3.14(k,h). The increase in turbulent events is reflected by the PDFs, where a ‘D’-shaped PDF absent in $Re = 750$, gradually increases in intensity from $Re = 1000$ to $Re = 1050$. The lack of prolonged laminar spots, previously identified for $Ra = 0$ (figure 3.3 suggests that the longitudinal rolls provide an intermediate pathway towards turbulence in a small domain (figure 3.11(d)).

3.5 Conclusions

We conclude by summarising the key findings of transitional RBP from figure 3.1, where we identify five different regimes and their transition boundaries. First, we examined the bistability between SDC and ISRs in RBP flows, which persists up to $Re = 1$, beyond which only ISR solutions are observed. The critical Re_s at which SDC disappears likely depends on Re and remains an avenue for future study. At $Re = 10$, the wavenumber of the stable ISRs adheres to the stability boundaries of the Busse balloon, and we observe longitudinal rolls as well as oscillatory longitudinal rolls, expected from the secondary instabilities of RBC [?]. Wavy rolls appear at $Re = 100$, $Ra \geq 5000$ [??], but disappear for $Re \geq 500$, where a new regime referred to as the intermittent rolls emerges. This regime is characterised by the spatiotemporal intermittent breakdown of longitudinal rolls towards the laminar state, before being regenerated again. Similar to the wavy rolls regime, intermittent rolls only appear

above a Ra -threshold, $Ra \geq 5000$ (see figure 3.1), below which longitudinal rolls persists. Notably, the wavenumber of these longitudinal rolls lies outside of the stability boundaries of the Busse balloon for RBC ($Re = 0$), suggesting the stability boundaries are modified as Re increases, a potential avenue for future work. As Re approaches the shear-driven turbulent regime, we observe the coexistence of longitudinal rolls with neighbouring turbulent bands at $Ra = 10000$, highlighting the role of the spatiotemporal nature of longitudinal rolls in transitional RBP.

To investigate the role of longitudinal rolls in transitional RBP, we consider a confined domain, $\Gamma = \pi/2$, where spatial intermittency can be artificially suppressed. Integrating along the unstable manifold of longitudinal rolls in the confined domain leads to transient turbulence, which eventually decays towards the laminar state before longitudinal rolls re-emerge again. Transient turbulence can be sustained here, referred to as the *thermally-assisted sustaining process (TASP)*. To understand TASP further, we explore its behaviour as Re and Ra are varied. As Re decreases towards the intermittent rolls regime, a periodic orbit emerges, oscillating between the longitudinal roll and a laminar state. In contrast, as Re increases, shear-driven turbulence becomes sustained, with the longitudinal rolls providing an intermediate route towards the transition to turbulence from the laminar state. Our investigation of the role of unstable longitudinal rolls within confined domains revealed three dynamical processes: the onset of (1)periodic orbits, (2) the TASP, and (3) providing an intermediate route towards turbulence. It was also shown that the stability of longitudinal rolls largely depends on Re and Ra , below which only stable longitudinal rolls are observed. Furthermore, the connection between the dynamical process identified here to the onset of wavy rolls warrants further investigation. We also acknowledge that more spatially subharmonic instabilities may arise as the domain size increases.

Finally, we assess the relevance of our findings in the confined domain and their connection to the large domain. We suggest that the breakdown towards the laminar state in the intermittent roll regime bears qualitative similarities to the periodic orbit between them in the confined domain. Furthermore, transient turbulence that is sustained by longitudinal rolls is also evident in the large domain, where the flow transitions between transient turbulence, longitudinal rolls and the laminar state in figures 3.14(g,h). At $Re = 1050$, the turbulent-laminar bands dominate, weakly dependent on Ra , as suggested by figure A.2. It may be possible that these turbulent-laminar bands decay spontaneously towards the laminar state [??], and their lifetime statistics may depend on Ra , which warrants further investigation. However, if the TASP persists above a critical Ra providing a pathway to turbulence, then the turbulent-laminar bands could be sustained indefinitely. As Re approaches 2000, featureless turbulence emerges, with the first- and second-order statistics becoming independent of Re , indicating fully developed turbulence. It is likely that the range of $Ra \in [0, 10000]$ considered here is too low to significantly influence shear-driven turbulence at $Re = 2000$, suggested by the studies of turbulent RBP [?].

Chapter 4

The state space structure of Spiral Defect Chaos

4.1 Introduction

Rayleigh-Bénard convection (RBC) concerns the fluid motion confined between two parallel walls, separated by a distance d , heated from below. The motion of the fluid is effectively driven by unstable stratification due to temperature gradients ($\Delta T/d$) across the walls. Given a large enough temperature gradient, a non-trivial fluid motion occurs, often developing into a spatially varying structure known as a convection pattern. This motion is described in terms of the Rayleigh number $Ra = \alpha g d^3 \Delta T / \nu \kappa$, Prandtl number $Pr = \nu / \kappa$ and aspect ratio of the experimental/computational domain $\Gamma = L/d$, where $\alpha, g, \Delta T, \nu, \kappa, L$ refers to the thermal expansion coefficient, acceleration due to gravity, temperature difference between the bottom and top wall, kinematic viscosity thermal diffusivity, domain's length and span respectively. An important question that underpins RBC is often as follows: Given the Rayleigh number (Ra), Prandtl number (Pr) and aspect ratio (Γ) of a fluid system, what convection pattern arises and what is its associated heat flux?

4.1.1 Multiple convection states

While the Busse balloon describes the stability of ISRs over a continuum of wavenumbers (at given Ra and Pr), predicting the wavenumber of an ISR state remains an ongoing challenge ?. Experimental investigations of RBC in moderate domains ($\Gamma \geq 7$) showed that ISRs in rectangular (straight rolls) and cylindrical (concentric rolls) domains are stable. Consider $\varepsilon (\equiv (Ra - Ra_c) / Ra_c)$, where Ra_c is the critical Ra for the onset of linear instability for ISRs) as a control parameter referred to as the reduced Rayleigh number. As ε is increased continuously from below the onset, the initial ISRs become unstable and transform into another set of ISRs with a different wavelength. With the marginal increase of ε , this process is repeated and the ISRs undergo hysteretic transverse wavelength adjustments, adhering to the stability boundaries of the Busse balloon ???. When ISRs become unstable, roll dislocations and defects can be nucleated near the boundary or bulk, modifying the effective roll wavenumber as they travel through the domain ?. This observation implies that the wavenumber of an ISR state depends

on the state's history or the system's initial condition ?.

It is worth noting that the solutions in the form of ISRs appear to be an exception rather than the rule ?. The coexistence of multiple ‘non-ISR’ states, in the form of squares, travelling/stationary targets, giant rotating spirals, and oscillatory convection patterns have been found over several years ??????. Investigation of cylindrical RBC with small aspect-ratio ($\Gamma = 2$) revealed eight stationary states (at the same $Ra = 142000$), and two oscillatory states ($Ra > 14200$) ?. These findings were later supported by numerical experiments and bifurcation analyses ????. In particular, bifurcation analyses performed by ?, revealed twelve stable branches in the form of symmetric and asymmetric convection rolls near onset ($Ra \leq 2500$), with the potential emergence of hundreds of branches at higher Rayleigh numbers, $Ra \leq 30000$?. In larger domains ($\Gamma \geq 28$), giant rotating spirals were identified and thoroughly investigated ?. Experimental and numerical studies of RBC with varying sidewall boundary conditions (i.e. thermally insulating, conducting and no-slip) ????, non-Boussinesq convection ??, and rotational effects ? were investigated, where multiple states were also reported. More recently, ?? computed up to sixteen stable and unstable invariant states and identified heteroclinic orbits between the multiple states in an inclined RBC.

4.1.2 Spiral defect chaos

Convection rolls exhibiting spatio-temporal chaotic behaviour known as spiral defect chaos (SDC) are found in the same parameter space of ε , where ISRs were expected ???????????. It is well established that SDC exists as an intrinsic state of RBC, independent of sidewall conditions ?. SDC has also been found in numerical simulations of the two-dimensional Swift-Hohenberg equations ?????. Some investigations into quantifying the onset of SDC in terms of Rayleigh number remain inconclusive. The critical reduced Rayleigh number for the onset of SDC, ε_s , has been observed to decrease with increasing Γ , and increase with increasing Pr ?????. It is worth noting that SDC has been reported in larger domains ($\Gamma \geq 20$) only, implying that there exists a minimal Γ for SDC to occur ?, further supporting the dependence of ε_s on Γ mentioned above. This is also consistent with the leading Lyapunov exponents, which become smaller with decreasing aspect ratios, Γ , albeit at larger $\varepsilon = 2.5$?. Investigations into the spatial-temporal characteristics of SDC, such as the quantification of the averaged roll-curvature ??, probability of spirals ?? and correlation length-/time-scales ??? have been studied. Specifically, the correlation length-scales ??? of SDC appear to scale exponentially as ε is increased. Furthermore, spatio-temporal chaotic behaviour reminiscent to SDC has been found in other pattern-formation systems such as rotational RBC ?, dielectric barrier discharge ? and chemical systems ?.

Given the co-existence of ISRs and SDC in the parameter space of ε , it is known that they form bistability at $Pr \approx 1$ in a spatially extended domain, supported by experiments over a range of $\varepsilon (> 0)$?. Only carefully prepared experiment setups led to ISRs while most initial conditions yield SDC. In other words, the asymptotic state of RBC depends on its initial conditions, reminiscent of the hysteretic behaviour of RBC discussed in §4.1.1. The chaotic state of SDC is unstable at $Pr = 4$, where multiple spiral patterns coarsen into a single spiral, before evolving into straight-curved rolls over a long period ?. This implies that the behaviour of SDC depends on Pr .

4.1.3 Scope of this study

The bistability between SDC and ISR is well established, but this also opens a question of how it is connected with the previous findings of multiple stable states. It is worth noting that a possible parameter in exploring this connection appears to be the domain size. Bistability has been reported in domains much larger ($\Gamma = 50$) than the multiple states found in small-to-moderate domains ($\Gamma \leq 10$) [?](#). Furthermore, giant rotating spirals have been found in domains comparable to the horizontal length scale of SDC [??](#). Under this premise, the scope of this study is to explore how SDC, ISRs and multiple states are linked within the state space, where stable/unstable equilibria and their manifolds (or linear stability) could provide useful physical insights into the state transition dynamics.

Motivated by the observation that SDC consists of several localised structures that resemble multiple states (i.e. travelling waves, spirals, asymmetric states), we first seek to isolate these states by minimising the domain systematically. Confined within the minimal domain, SDC is found to appear only transiently and does not sustain for a long time. The transient SDC state eventually stabilises into a large number of stable multiple states, which will be referred to as the ‘elementary’ states of SDC, and they are subsequently found within the minimal domain. As we shall see later, these elementary states remarkably resemble local structures of SDC observed in wide computational domains, indicating that they possibly underpin the formation of SDC. Next, the state-space boundaries between SDC and ISRs are explored by employing the edge-tracking technique [??](#), unveiling the existence of multiple edge states sitting on the boundaries. Finally, to understand the role of the unstable ISRs outside the Busse balloon, we perform a series of numerical experiments, in which a small perturbation is added along the unstable manifolds of several (unstable) ISRs outside of the Busse balloon. We shall see that some of their unstable manifolds are connected to stable ISRs within the Busse balloon, while the others are linked to transient SDC, which is subsequently stabilised into an elementary state. This suggests that some of the unstable ISRs act as signposts for the state-space boundary between stable ISRs and SDC (and/or elementary states).

The main contributions of the present study can be briefly summarised as follows:

1. Discovery of a number of stable invariant solutions which underpin the localised structures of SDC by minimising the computational domain for SDC (section [4.3](#));
2. Computation of some of multiple ‘edge states’ sitting on the separatrix between SDC and ISRs (section [4.4](#));
3. Several heteroclinic orbits connecting unstable ISRs and stable ISRs near the boundaries of the Busse balloon (section [4.5.1](#));
4. The role of unstable ISRs far from the Busse balloon acting as a signpost between ISRs and SDC (section [4.5.2](#)).

4.2 Problem formulation

4.2.1 Rayleigh-Benard convection (RBC)

We consider a buoyancy-driven flow of an incompressible fluid separated by a vertical height of d , confined between an upper wall of uniform temperature T_U , and a lower wall of uniform temperature T_L . The temperature of the lower wall is higher than the temperature of the upper wall ($\Delta T = T_L - T_U > 0$) such that the fluid is unstably stratified. The fluid has a density of ρ , a thermal diffusivity of κ , and a kinematic viscosity of ν . The non-dimensionalised governing equations with the Boussinesq approximation for buoyancy-driven flows are given by

$$\frac{\partial \mathbf{u}}{\partial t} + (\mathbf{u} \cdot \nabla) \mathbf{u} = -\nabla p + Pr \nabla^2 \mathbf{u} + Ra Pr \theta \mathbf{j}, \quad (4.1a)$$

$$\frac{\partial \theta}{\partial t} + (\mathbf{u} \cdot \nabla) \theta = \nabla^2 \theta, \quad (4.1b)$$

$$\nabla \cdot \mathbf{u} = 0, \quad (4.1c)$$

with the following boundary conditions at the wall,

$$\mathbf{u}|_{y=0,1} = 0, \quad \theta|_{y=0} = 1, \quad \theta|_{y=1} = 0, \quad (4.2a)$$

and the periodic boundary condition in the horizontal direction. Here, t denotes the time scaled by the vertical thermal diffusion time, d^2/κ , and $\mathbf{x} (= (x, y, z))$ is the spatial coordinates non-dimensionalised by d , where x and z are two orthogonal horizontal directions and y is the vertical direction. $\mathbf{u} (= (u, v, w))$ is the velocity vector scaled with κ/d , p the pressure scaled with $\rho\kappa^2/d^2$, $\theta (\equiv (T - T_U)/\Delta T)$ the non-dimensional temperature with T being the absolute temperature, and \mathbf{j} denotes the unit vector in y -direction. The Rayleigh number and the Prandtl numbers are defined as in §4.1: $Ra = \alpha g d^3 \Delta T / \nu \kappa$, Prandtl number $Pr = \nu/\kappa$. Throughout this study, $Pr = 1$ is set.

4.2.2 Numerical method

The governing equations are solved numerically using Nektar++, an open-source spectral/ hp -element method framework ?. An initial computational mesh, composed of quadrilateral elements, in the x - y plane is generated using Gmsh ? and then refined by Nekmesh, the mesh generator available in Nektar++. Several computational domains of different sizes are prepared: $(L_x, L_y, L_z) = (32\pi, 1, 32\pi), (16\pi, 1, 16\pi), (8\pi, 1, 8\pi), (4\pi, 1, 4\pi)$. The spatial domain is discretised using a quasi-3D approach with spectral/ hp elements in x - y domain and Fourier expansions in z -direction. The discretised equations are subsequently solved using a velocity-correction method based on a second-order implicit-explicit temporal scheme ??. Since different computational domain sizes were considered, the spatial distribution of spectral/ hp elements in the x - y plane and Fourier expansions along z was kept constant. A spatial resolution of $(\Delta x, \Delta y|_{y=0,d}, \Delta y|_{y=d/2}, \Delta z) = (0.1\pi, 0.0549, 0.367, 0.25\pi)$

with polynomial order $P = 4$, and temporal resolution of $\Delta t = 0.0125$ was sufficient to establish numerical independence – for example, the Nusselt number, $Nu(= - \int_{x,z} \frac{\partial \theta}{\partial y} |_{y=0} dx dz)$, varies less than 10^{-5} when P was increased to $P = 5$.

4.2.3 Linear stability analysis of ISRs

As discussed in §4.1.3, we will perform a set of numerical experiments, in which a small perturbation about several unstable ISRs is added along their unstable manifolds. To obtain the direction of the unstable manifolds (i.e. linear instability eigenfunctions), we consider a small perturbation about the ISR (base) state:

$$\mathbf{u}(\mathbf{x}, t) = \mathbf{u}_{ISR,q}(\mathbf{x}) + \mathbf{u}'(\mathbf{x}, t), \quad (4.3a)$$

$$\theta(\mathbf{x}, t) = \theta_{ISR,q}(\mathbf{x}) + \theta'(\mathbf{x}, t), \quad (4.3b)$$

$$p(\mathbf{x}, t) = p_{ISR,q}(\mathbf{x}) + p'(\mathbf{x}, t), \quad (4.3c)$$

where $\mathbf{s} = [\mathbf{u}, \theta, p]^T$, $\mathbf{s}_{ISR,q} = [\mathbf{u}_{ISR,q}, \theta_{ISR,q}, p_{ISR,q}]^T$ and $\mathbf{s}' = [\mathbf{u}', \theta', p']^T$ refers to solution vector, the ISR (base) state of a given wavenumber, q , and the perturbation respectively. Substitution of (4.3) into (4.1) leads to the following linearised equations:

$$\frac{\partial \mathbf{s}'}{\partial t} = \mathcal{A}(\mathbf{s}_{ISR,q}; Ra, Pr)\mathbf{s}', \quad (4.4a)$$

where

$$\mathcal{A}(\mathbf{s}_{ISR,q}; Ra, Pr) = \begin{pmatrix} -(\mathbf{U} \cdot \nabla) - (\nabla \mathbf{U} \cdot) + Pr \nabla^2 & Ra Pr \hat{\mathbf{j}} & -\nabla \\ -(\nabla \Theta \cdot) & -(\mathbf{U} \cdot \nabla) + \nabla^2 & 0 \\ \nabla \cdot & 0 & 0 \end{pmatrix}. \quad (4.4b)$$

For the sake of simplicity here, we will only consider the ISRs invariant along z -direction. Since the ISRs are also assumed periodic in x -direction, the following form of normal-mode solution can be considered:

$$\mathbf{s}'(\mathbf{x}, t) = \check{\mathbf{s}}(x, y)e^{i(\alpha x + \beta z) + \lambda t} + \text{c.c}, \quad (4.5)$$

where λ , α and β are the complex frequency, the streamwise wavenumber (or the Floquet exponent), and the spanwise wavenumber, respectively. Using the periodic nature of $\check{\mathbf{s}}(x, y)$ in x -direction, (4.5) can also be written as

$$\mathbf{s}'(\mathbf{x}, t) = \left[\sum_{n=-\infty}^{\infty} \check{\mathbf{s}}_n(y) e^{i \frac{2\pi}{L_x} (n+\epsilon)x} \right] e^{i\beta z + \lambda t} + \text{c.c}, \quad (4.6)$$

where $\epsilon (= \alpha L_x / (2\pi))$ is the Floquet detuning parameter with $0 \leq \epsilon \leq 1/2$. Since the stability analysis here will be limited to the identification of unstable manifolds of ISRs in a fixed computational domain, $\epsilon = 0$ (fundamental mode) is considered only - note that the modes associated with $\epsilon \neq 0$ are only

observed in the x domains greater than L_x .

Substituting (4.6) into (4.4) leads to a discretised eigenvalue problem in terms of the eigenvalue λ , where the wavenumber in the z -direction must be restricted to be $\beta = 2\pi m/L_z$, and m is a positive integer, for the given computational domain. The resulting eigenvalue problems are solved using a time-stepper-based iterative Arnoldi algorithm ?, implemented in Nektar++, which has been verified in various applications ?. The eigenvalues of primary instabilities of RBC computed in Nektar++ are also verified against those obtained with a Chebyshev-collocation method in Appendix A.7.

4.3 Transient SDC and elementary states in minimal domain

In this section, we seek to capture localised structures of SDC using a minimal domain by systematically reducing the domain by half in the homogeneous (x - z) directions. A random noise, characterised by Gaussian white noise (0 mean and 1 variance), generated with a total energy of

$$\delta = \frac{1}{V} \int_{\Omega} \tilde{\mathbf{u}}(\mathbf{x})^T \tilde{\mathbf{u}}(\mathbf{x}) + RaPr\tilde{\theta}(\mathbf{x})^2 d\Omega \approx O(10^{-3}), \quad (4.7)$$

where $\tilde{\mathbf{u}}(\mathbf{x})$ and $\tilde{\theta}(\mathbf{x})$ refer to the perturbation velocity and temperature about the base state $\mathbf{U}(\mathbf{x}) = \mathbf{0}$ and $\Theta(y) = 1 - y$, is introduced as an initial condition to the system. Here, we note that the first term of the integrand in (4.7) is the kinetic energy of the perturbation velocity and the second one measures the potential energy from the perturbation temperature.

The system is time integrated for 300 units of vertical thermal diffusion time $t (= d^2/\kappa)$. The resulting mid-plane temperature snapshots $\theta(x, z)|_{y=d/2}$ at $t = 300$ exhibit features of spiral defect chaos, as shown in figure 4.1. When the domain size is large, for instance, $\Gamma = 8\pi$ shown in figure 4.1(a), features of SDC consist of many repeating localised spirals, defects and dislocations. Reducing the domain in half to $\Gamma = 4\pi$, shown in figure 4.1(b), led to a spatially less extensive chaotic state, revealing a single spiral, with some defects and dislocations. Surprisingly, a further reduction of the domain in half, $\Gamma = 2\pi$, does not lead to sustained SDC, but rather, a transient SDC state before settling into stable ‘elementary’ states. These elementary states are identified as *pacman* (PM), *spiral-defect* (SD), *hooked* (HK), and *peanut* (PN) states in figure 4.1 (c-f), which resemble the localised features of SDC (see the coloured bounding boxes in figures 4.1(a,b)). These states represent stable invariant solutions of (4.1). Specifically, PM state represents a steady equilibrium, SD and HK states are characterised by relative periodic orbits, and the PN state is a periodic orbit ?.

An example of a transient SDC state is shown in figure 4.2(a), where spirals, a typical feature of SDC ?, form spontaneously with a chaotic transient (figures 4.2(c-e)), before stabilising into SD state with a period of $T \approx 73$ (figures 4.2(f,g)). In addition to the elementary states presented in figures 4.1(c-f), we have identified ten additional elementary states, each independently preceded by a transient SDC state, and fourteen stable ISRs of varying wavenumbers (see Appendix A.8). In total, we have identified 28 states with $\Gamma = 2\pi$. Minimising the domain further to $\Gamma = \pi$ only led to stable ISRs at least for the random initial conditions we have examined in this study. We therefore consider $\Gamma = 2\pi$ as the minimal domain, in which both transient SDC and elementary states exist. It is worth

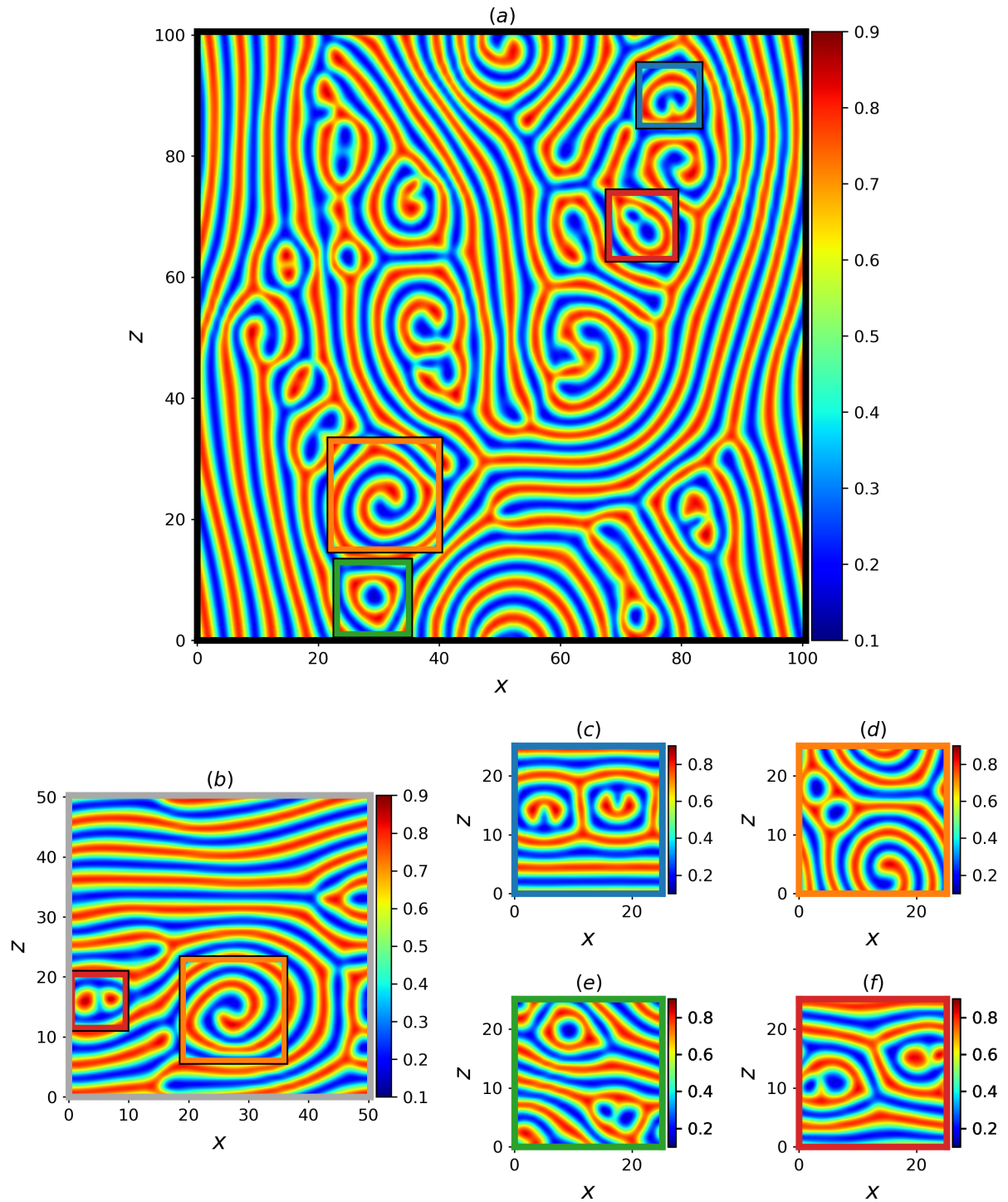


Figure 4.1: Midplane temperature snapshots, $\theta(x, z)|_{y=d/2}$, of spiral defect chaos (SDC) for a domain aspect ratio of (a) $\Gamma = 8\pi$ and (b) 4π . Elementary states of SDC captured when $\Gamma = 2\pi$: (c) steady *pacman* (PM), (d) relative periodic orbit *spiral-defect* (SD), (e) relative periodic orbit *hooked* (HK), and (f) periodic *peanut* (PN) elementary state. Note that the localised structures indicated by bounding boxes in (a,b) resemble structures in (c-f).

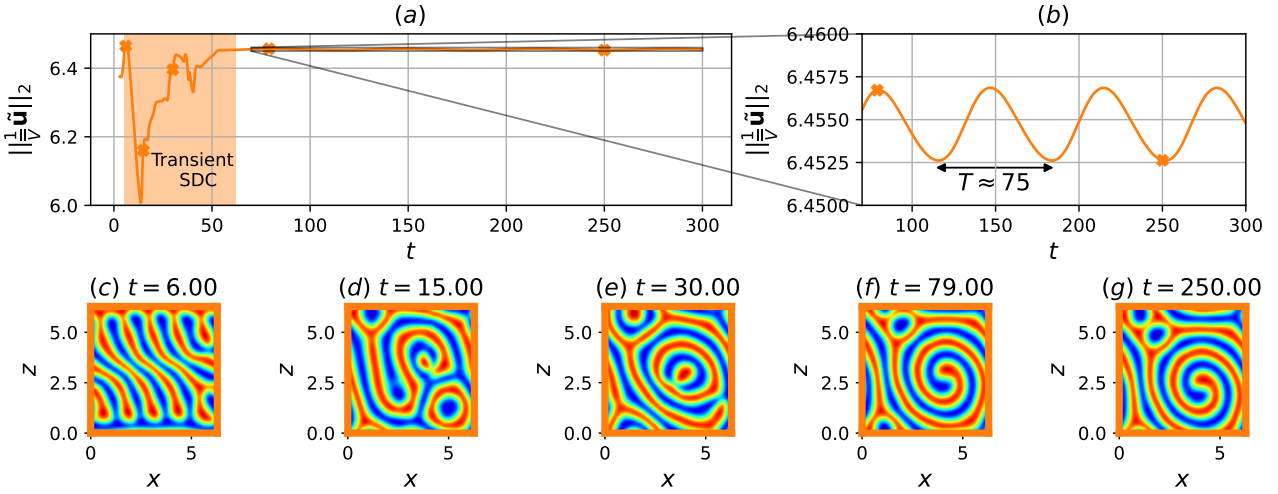


Figure 4.2: (a,b) Time history of the volume ($\bar{V} = L_x L_y L_z$) normalised L2-norm of velocity perturbations from a random initial condition with $\delta = 0.001$ and (c-g) Mid-plane temperature snapshots at $t = 6, 15, 30, 79, 250$. Here, transient chaotic SDC lasts up to $t \approx 70$, before stabilising into an SD state, emerging as a relative periodic orbit with the time period $T \approx 73$ propagating diagonally in the negative x - and z -directions.

mentioning that solutions to multiple states were obtained in smaller domains with $\Gamma = 2$, but in a cylindrical domain ??.

To show whether SDC and elementary states are related, we compare their state space trajectories, and the averaged wall-normal temperature profiles. Figure 4.3 presents the two chaotic trajectories of SDC from $\Gamma = 8\pi, 4\pi$, four of fourteen transient SDC trajectories obtained and fourteen stable fixed-points of ISRs from $\Gamma = 2\pi$ on a two-dimensional state portrait based on the volume ($\bar{V} = L_x L_y L_z$) normalised L2-norms of velocity ($\|\frac{1}{V}\tilde{\mathbf{u}}\|_2$) and temperature ($\|\frac{1}{V}RaPr\tilde{\theta}\|_2$) perturbations. The trajectories begin from $t = 3$, as those for $t < 3$ contain artificial transients and are omitted for clarity. The state space trajectories of SDC ($\Gamma = 8\pi, 4\pi$) and the transient SDC states for $\Gamma = 2\pi$ are visibly attracted toward a region, where $\|\frac{1}{V}\tilde{\mathbf{u}}\|_2 \approx 6.3$ and $\|\frac{1}{V}RaPr\tilde{\theta}\|_2 \approx 8.6$, as shown in figure 4.3(b). This suggests that they are presumably the same type of SDC emerging in different domains. The closely packed chaotic trajectories are in contrast to the ISRs populating sparsely.

The transient SDC trajectories eventually stabilise into fourteen elementary states in figure 4.4, where the transient SDC trajectories from figure 4.3 are now omitted. Obscured by the transient SDC trajectories initially, the elementary states in figure 4.4(b) emerge as seven steady states (■), two travelling waves (×), one periodic orbit (dash-dotted line) and four relative periodic orbits (solid line). All the SDC trajectories for $\Gamma = 8\pi, 4\pi, 2\pi$ are organised around the fourteen elementary states (figure 4.4(b)). Notably, the state space trajectories of SDC and the elementary states are in close vicinity to the ISR of wavenumbers $q = 2.5/d$ (see figures 4.3 and 4.4), which corroborates with the averaged wavenumber of SDC, $q_{avg} \approx 2.5/d$??.

The comparison between the time-averaged mean temperature profile, mean-squared temperature fluctuations, and mean-squared velocity fluctuations of SDC (figures 4.1(a,b)) and elementary states (figures 4.1(c-f) and figure A.6) are presented in figure 4.5. In figure 4.5(c), we present the sum

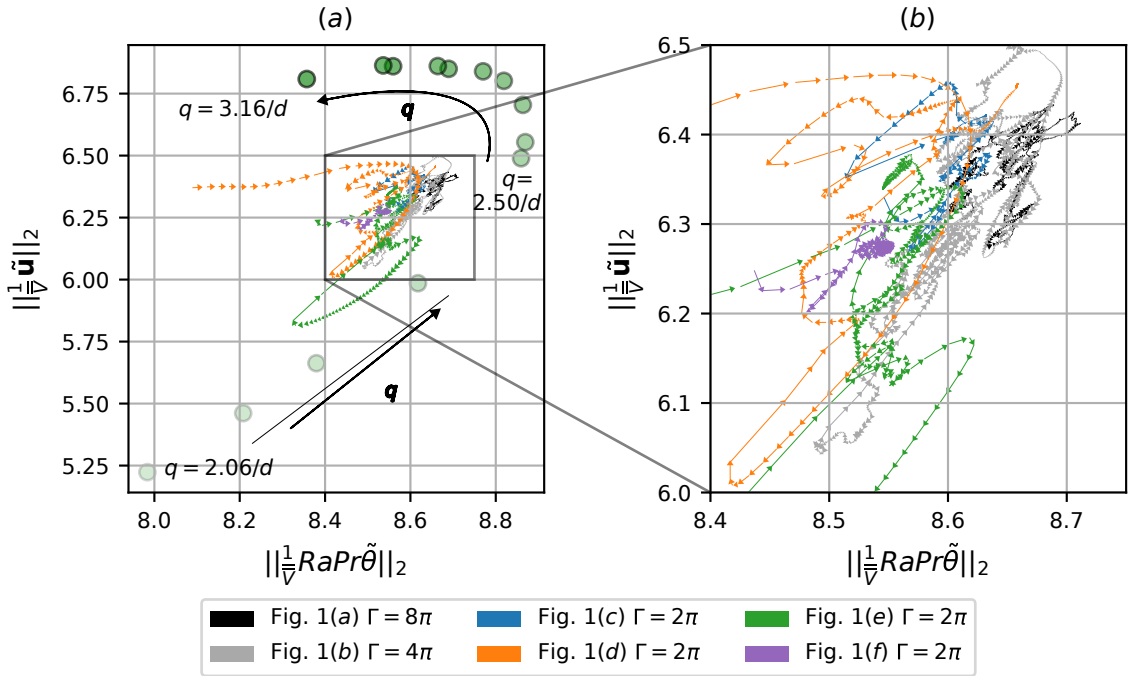


Figure 4.3: (a) State-space portrait in the plane of $\|\frac{1}{V}\tilde{u}\|_2$ and $\|\frac{1}{V}RaPr\tilde{\theta}\|_2$ for SDC from $\Gamma = 8\pi, 4\pi$ (figures 4.1(a,b)), four transient SDC state proceeding to stable elementary states (figures 4.1(c-f), A.6), and fourteen stable stationary ISRs of wavenumbers $2.0 \leq qd \leq 3.35$. Here, the magnitude of q is denoted by the opacity of the filled symbol (\bullet), increasing from the bottom left and turning toward the top left shown as arrows; (b) Zoomed-in view of (a). The legend refers to the figures for respective trajectories preceding snapshots in figure 4.1.

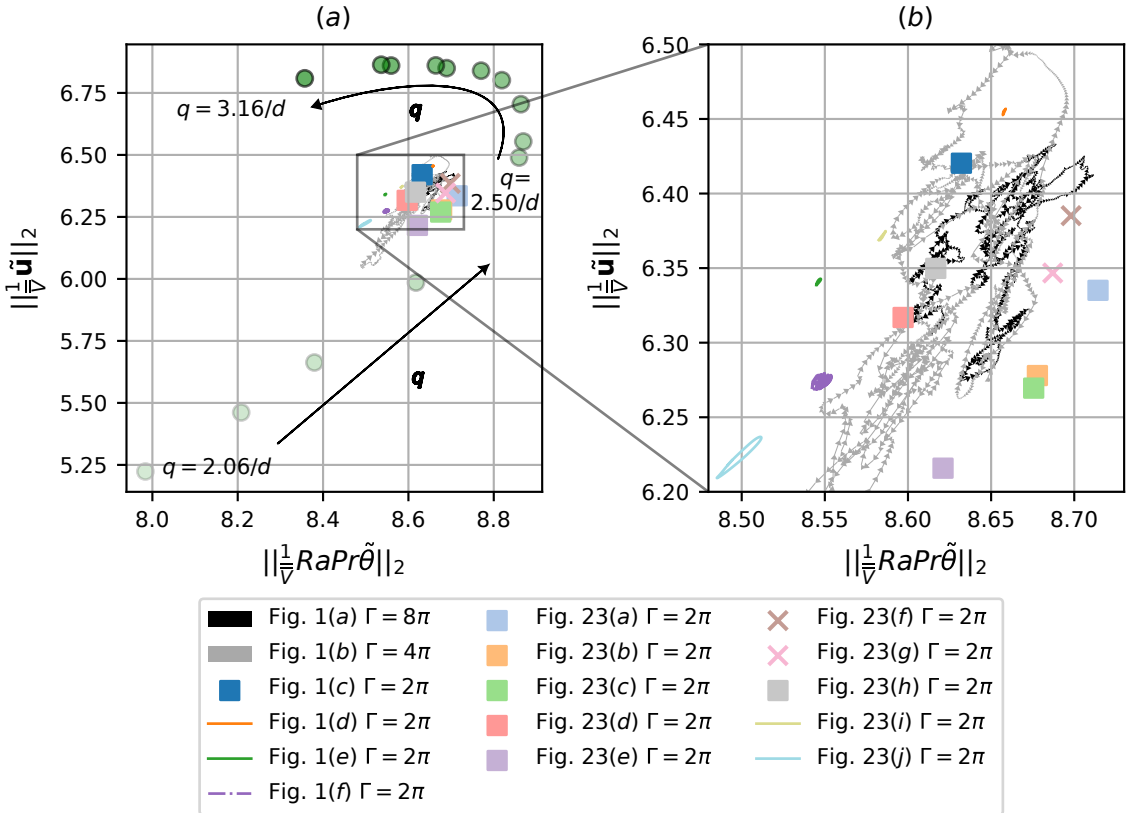


Figure 4.4: (a) State-space portrait (from figure 3) highlighting the transient SDC states for $\Gamma = 2\pi$ proceeding toward stable elementary states (see figures 4.1(c-f), A.6): steady states (■), travelling waves (×), periodic orbit (dash-dotted line) and relative periodic orbits (solid lines). Here, ISRs are denoted by the varying opacity of the filled symbol (●) increasing from the bottom left and turning toward the top left shown as arrows; (b) Zoomed-in view of (a).

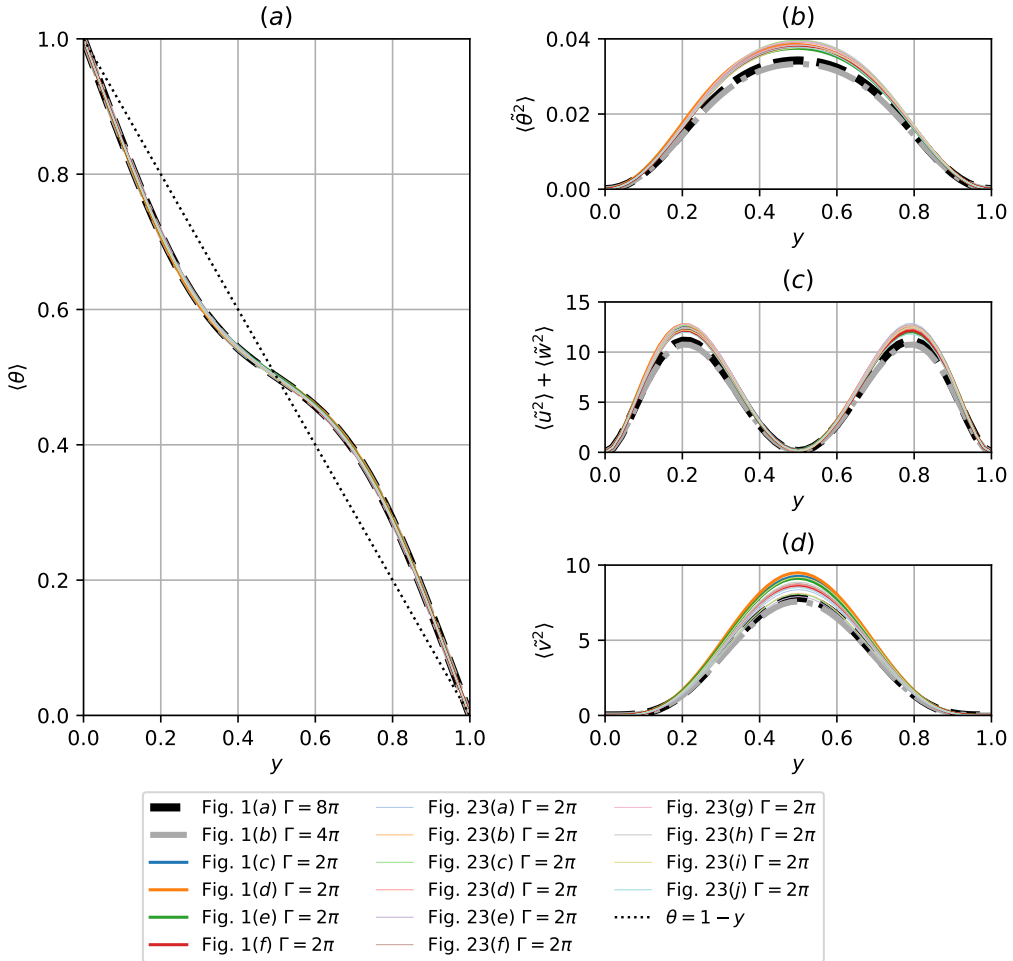


Figure 4.5: Profiles of (a) averaged temperature, (b) root-mean-squared temperature fluctuation, (c) sum of root-mean-squared $x-z$ velocity fluctuations and (d) root-mean-squared wall-normal velocity fluctuations for the SDC and elementary states shown in figures 4.1(a-f) and in Appendix A.8. Note that $\langle \cdot \rangle = \frac{1}{T L_x L_z} \int_{t,x,z} dt dx dz$ refers to the time and plane averaged operator, where T was chosen to be sufficiently long to ensure temporal convergence.

of mean-squared x - and z - velocity fluctuations due to horizontal isotropy. The mean temperature profiles of the elementary states closely match those of SDC (figure 4.5(a)). Notably, the mean-squared temperature and velocity fluctuations between SDC states (grey and black dashed curves) of figures 4.5(b-d) are similar. The mean-squared temperature and velocity fluctuations profiles of elementary states are comparable to those of SDC but are in general, slightly larger in magnitudes.

The spatial-temporal complexity of SDC reduces when the domain size is reduced from $\Gamma = 8\pi$ to $\Gamma = 4\pi$, i.e. less disordered spatial features. Reducing the domain from $\Gamma = 4\pi$ to $\Gamma = 2\pi$ led to transient SDC before stabilising into many elementary states. From the conventional view, especially made in the context of shear flow turbulence, this is unexpected as the chaotic state (i.e. turbulence) is commonly described as solution trajectories wandering around unstable invariant solutions ?????. However, in this particular case observed in RBC, the chaotic state (i.e. SDC) is instead stabilised into stable invariant solutions (elementary states). Despite this distinguished feature of the state space, each of the elementary states is still seen to emerge in a spatially localised manner of SDC in an extended domain (figure 4.1), and their spatially-averaged statistics are remarkably similar to those of SDC in extended domains (figure 4.5). Therefore, we consider the elementary states in the minimal domain to be the ‘building blocks’ structure of SDC.

4.4 Multiplicity of edge states

The stable nature of many ISRs and elementary states underpinning SDC implies the existence of state-space boundaries between them (i.e. edge). In this section, we perform the edge tracking between the stable manifolds of ISRs and elementary states to compute the attractors on the edge (i.e edge states). For the edge tracking, we use the bisection method ???, with an initial condition given by

$$\mathbf{s}_0(\mathbf{x}, t=0) = \chi \mathbf{s}_{ISR,q} + (1 - \chi) \mathbf{s}_{elementary}, \quad (4.8)$$

where $\mathbf{s}_0(= [\mathbf{u}_0, \theta_0, p_0]^T)$ refers to an initial condition consisting of a weighted sum, $\chi \in [0, 1]$, between a stable ISR state, $\mathbf{s}_{ISR,q}$ of a wavenumber q , and an elementary state, $\mathbf{s}_{elementary}$ where the subscript refers to its names in figures 4.1(c-f).

Given the large number of stable ISRs and elementary states, we shall focus on the computation of the edge states considering three of the stable ISRs and two of the elementary states. However, in principle, the edge tracking is technically possible with other stable ISRs and elementary states. As such, in general, multiple edge states are expected. The three ISRs are related to three different wavenumbers, denoted by $\mathbf{s}_{ISR,q=2.06/d}$, $\mathbf{s}_{ISR,q=2.24/d}$, $\mathbf{s}_{ISR,q=3.16/d}$ (figures A.7(b,d,j)) respectively, and the two elementary states are SD state, $\mathbf{s}_{spiral-defect}$ (figure 4.1(c)), and PM state, \mathbf{s}_{pacman} (figure 4.1(d)). Using this set of stable ISRs and elementary states, we aim to track the edge near $\mathbf{s}_{ISR,q}$ in the direction of $\mathbf{s}_{elementary}$ by bisecting the initial condition with χ in (4.8), whereby one of the two trajectories across the edge decays toward $\mathbf{s}_{ISR,q}$ and the other is attracted toward transient chaotic state (i.e. SDC), referred to as the ‘lower’ and ‘upper’ trajectories respectively. The bisection of the initial condition is carried out by monitoring the difference in two trajectories with Nu (i.e. ΔNu). When the two trajectories reach a certain time at which $\Delta Nu > 0.0007$, the bisection of the initial

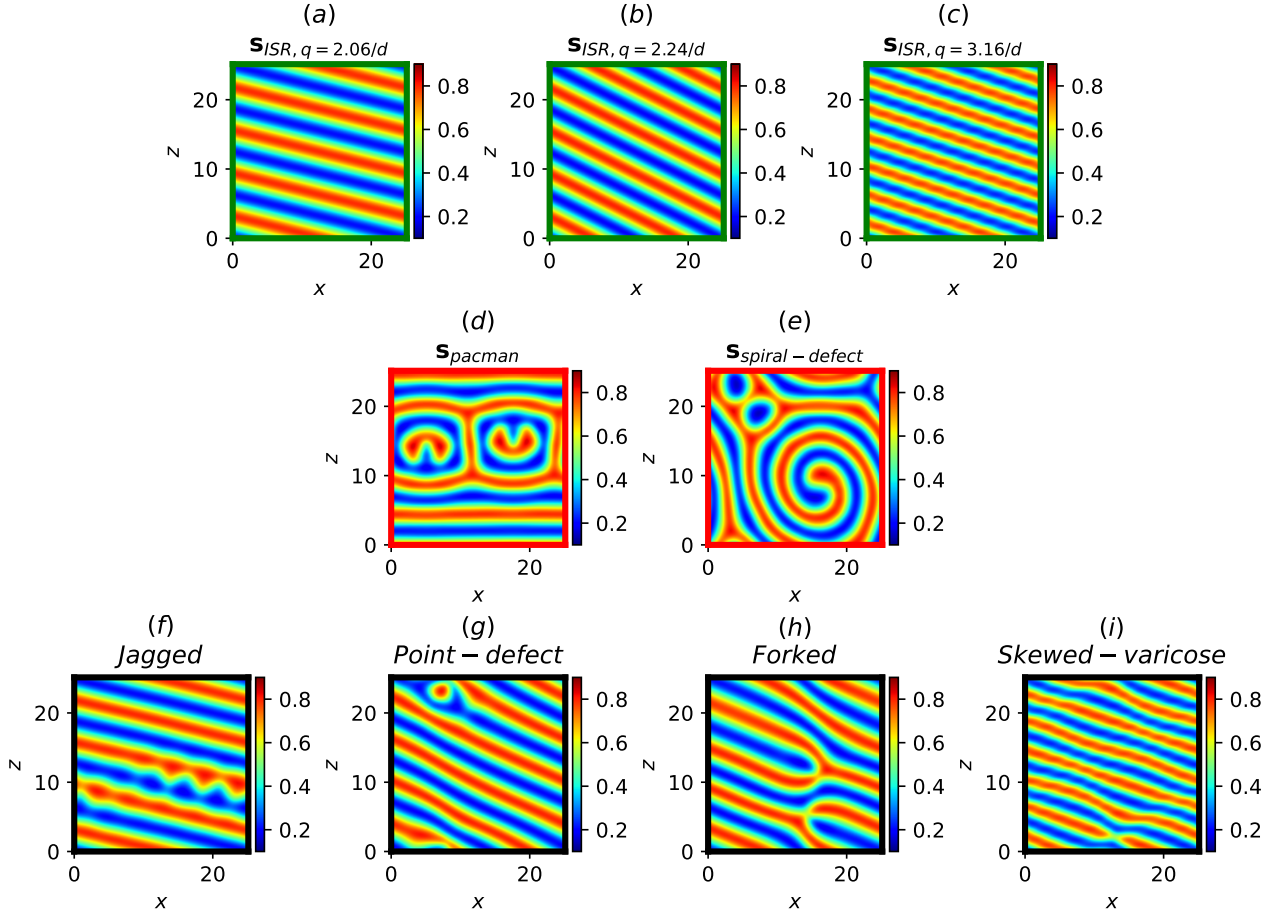


Figure 4.6: Mid-plane temperature fields of ISRs and elementary states used in Eq. (4.8), and the resulting edge states. Here, ISRs (green borders): (a) $s_{ISR,q}=2.06/d$, (b) $s_{ISR,q}=2.24/d$, (c) $s_{ISR,q}=3.16/d$; elementary states: (d) s_{pacman} , (e) $s_{spiral-defect}$; edge states (black borders): (f) *jagged*, (g) *point-defect*, (h) *forked* and (i) *skewed-varicose* edge state.

condition is repeated using the flow fields from the two different trajectories by replacing $s_{ISR,q}$ and $s_{elementary}$ in (4.8) with them. This process is repeated until the edge trajectory reaches an attractor (i.e. an edge state).

Table 4.1 summarises the edge states and their dynamical properties computed from six combinations of $s_{ISR,q}$ and $s_{elementary}$ states, and they are visualised with the mid-plane temperature field in figure 4.6. The convection patterns of edge states are often featured with mild spatial complexity compared to SDC and the elementary states. In particular, their patterns contain the underlying convection pattern of $s_{ISR,q}$ with spatially localised defects. We obtained four edge states: specifically, the *jagged* and *skewed-varicose* edge states are stationary, and the *point-defect* and *forked* edge states are travelling wave and a relative periodic orbit respectively. The *jagged*, *skewed-varicose* and *forked* edge states lie on the boundary, separating the basins of attraction of stable $s_{ISR,q}$ from transient SDC. In the case of the *point-defect* edge state, the solution trajectory is found to bypass the transient SDC state, directly settling into a stable elementary state characterised by bubble-like convection roll defects, $s_{bubble-defect}$. Since the *jagged*, *skewed-varicose*, *forked* edge states are similar in nature, acting as separatrices between $s_{ISR,q}$ states and transient SDC, we will focus our analysis on the *jagged* edge

$s_{ISR,q}$	$s_{elementary}$	Edge state	State transitioned
$s_{ISR,q}=2.06/d$	$s_{spiral-defect}$	<i>Jagged</i> (Stationary)	Transient Chaos
$s_{ISR,q}=2.06/d$	s_{pacman}	<i>Jagged</i> (Stationary)	Transient Chaos
$s_{ISR,q}=2.24/d$	$s_{spiral-defect}$	<i>Point-defect</i> (Travelling wave)	$s_{bubble-defect}$
$s_{ISR,q}=2.24/d$	s_{pacman}	<i>Forked</i> (Relative Periodic Orbit)	Transient Chaos
$s_{ISR,q}=3.16/d$	$s_{spiral-defect}$	<i>Skewed-varicose</i> (Stationary)	Transient Chaos
$s_{ISR,q}=3.16/d$	s_{pacman}	<i>Skewed-varicose</i> (Stationary)	Transient Chaos

Table 4.1: A summary of the edge states computed. The first two columns denote the pair of initial conditions considered for edge tracking in Eq. (4.8). The names and classification of the edge states are described in the third column. The last column describes the state transitioned from $s_{ISR,q}$ for sufficiently large χ in Eq. (4.8).

state only, alongside the *point-defect* edge state.

Using Nu as an observable, successive bisections between $s_{ISR,q}=2.06/d$ and $s_{spiral-defect}$ reveal the trajectory along the edge, as illustrated in figure 4.7. The trajectory along the edge spans from $t \approx 0 - 15$, and is initially characterised by a ‘speckled’ defect (figure 4.7(b)). The ‘speckled’ defect grows into a spatially localised jagged-like defect as the trajectory is attracted to the *jagged* stationary edge state from $t \approx 6.5$ onwards (figures 4.7(c-e)). We further examine the two trajectories in the opposite directions along the unstable manifold of the *jagged* edge state in figure 4.8, where the ‘upper’ trajectory evolves into a transient SDC and the ‘lower’ trajectory decays into the original stable $s_{ISR,q}=2.06/d$ state. Starting from the ‘upper’ trajectory (figure 4.8(a)), the spatially localised jagged defect grew in the direction normal to the roll orientation at $t = 80.5$ (figure 4.8(b)), contaminating the adjacent roll structure and propagating through the domain where transient SDC emerges from $t > 80.5$, lasting up to $t \approx 120$ (a snapshot of transient chaotic SDC regime at $t = 90.5$ is shown in figure 4.8(c)). The trajectory subsequently stabilises into a travelling-wave PM elementary state described by ‘pac-man’ like patterns, propagating along the $-x$ direction from $t = 125.5$ to $t = 170.5$ (figures 4.8(d,e)). This is reminiscent of a secondary cross-roll instabilities experienced by low-wavenumber ISRs (such as $s_{ISR,q}=2.06/d$ considered here), where a defect propagates in the direction perpendicular to the rolls ?. Along the ‘lower’ trajectory (figure 4.8(f)), the jagged defects diffuse from $t = 70.5$ to $t = 75.5$, decaying into the stable $s_{ISR,q}=2.06/d$ state at $t = 80.5$ (figures 4.8(g-j)).

Next, we analyse the edge trajectory obtained bisecting between $s_{spiral-defect}$ and $s_{ISR,q}=2.24$ in figure 4.9. The trajectory along the edge from $t = 4$ (figure 4.9(b)) is described by time-dependent convection structures. The edge trajectory began to be stabilised into the *point-defect* edge state from $t = 13$ onwards (figure 4.9(c)), propagating along x direction from $t = 22.5$ (figures 4.9(d,e)). It is characterised by the convection structure of the $s_{ISR,q}=2.24$ state with a pointed defect structure, hence referred to as the *point-defect* edge state. The upper and lower trajectories through two opposite directions of the unstable manifold of the travelling wave *point-defect* edge state are subsequently examined in figure 4.10. Integrating along the upper trajectory (figure 4.10(a)), the spatially localised point-defect structure grew from $t = 43$ to $t = 83$ (figures 4.10(b-d)), saturating into a stationary elementary state at $t = 163$ (figure 4.10(e)) characterised by $s_{ISR,q}=2.24$ with a large bubble defect. Along the lower trajectory (figure 4.10(f)), the spatially localised point defect merged onto the adjacent convection roll from $t = 38$ to $t = 44.5$ (figures 4.10(g,h,i)), stabilising into the $s_{ISR,q}=2.24/d$ state at

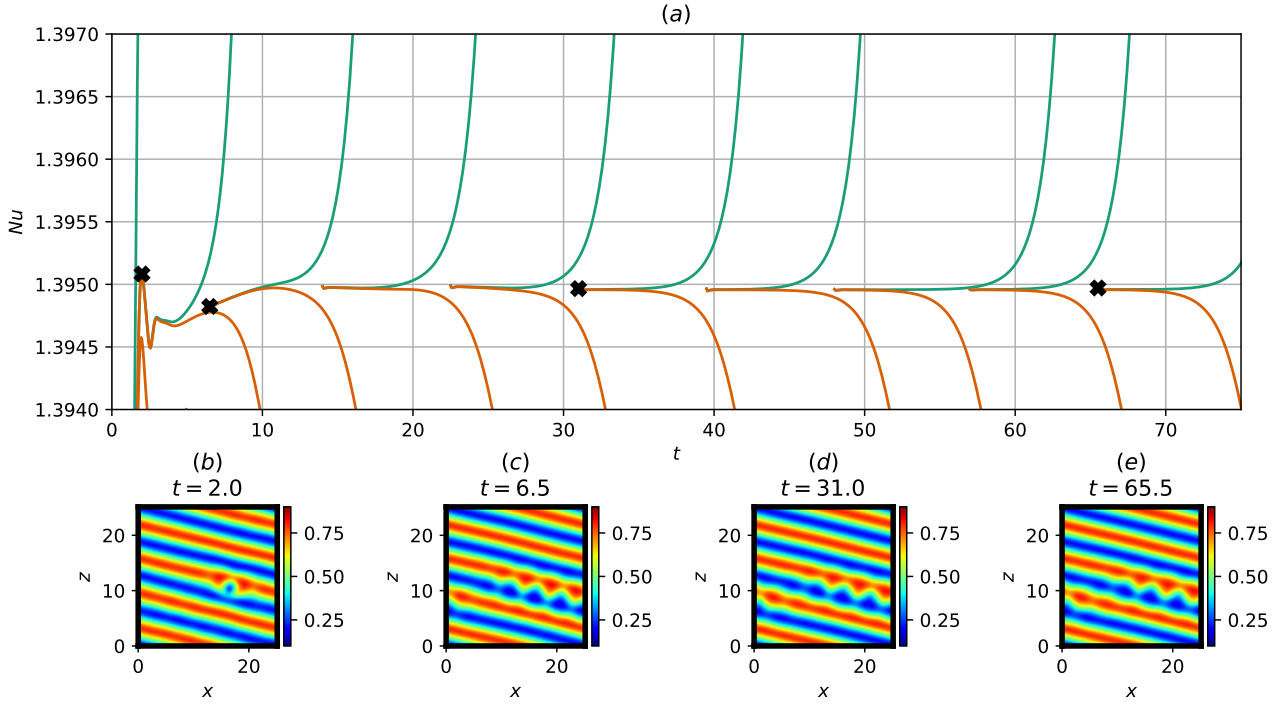


Figure 4.7: (a) Time history of Nu and (b-e) the corresponding mid-plane temperature field snapshots at $t = 2.0, 6.5, 31.0, 65.5$ along the edge trajectory obtained by bisecting $s_{ISR,q=2.06/d}$ and $s_{spiral-defect}$.

$t = 53$ (figure 4.10(j)). It is worth noting that, in this particular case, no chaotic transient in the form of SDC has been observed.

Finally, figure 4.11 depicts a state space portrait of stable ISRs, SDC and the edge/elementary states found here. As seen previously, SDC and elementary states are seen to be clustered around the region of $\|\frac{1}{V}\tilde{\mathbf{u}}\|_2 \approx 6.3$ and $\|\frac{1}{V}RaPr\tilde{\theta}\|_2 \approx 8.6$, whereas stable ISRs are distributed along a horseshoe-shaped band (green line). The edge states found in this study are located not far from the (green) horseshoe-shaped band of ISRs, as they presumably lie in a smaller (grey) horseshoe-shape band situated between ISRs and SDC or elementary states. While we have identified four edge states, we expect that there are more edge states, presumably distributed along the (grey) horseshoe-shaped band. It is also worth mentioning that the edge states we found here contain the underlying ISR structure ($s_{q=2.06/d, 2.24/d, 3.16/d}$) modified by spatially localised defects and ‘pinches’ between rolls, supporting its proximity with ISRs in the state space. This feature is also reminiscent of spatially localised edge states identified in boundary layer flows ?. Lastly, we would like to emphasise that we have only considered initial conditions from the states between $s_{ISR,q}$ and $s_{elementary}$ and not strictly between $s_{ISR,q}$ and a transient SDC state. Nevertheless, three of the edge states are found to lie on the boundary separating the stable ISRs from transient SDC, supporting previous findings that the transient chaotic SDC are related to elementary states.

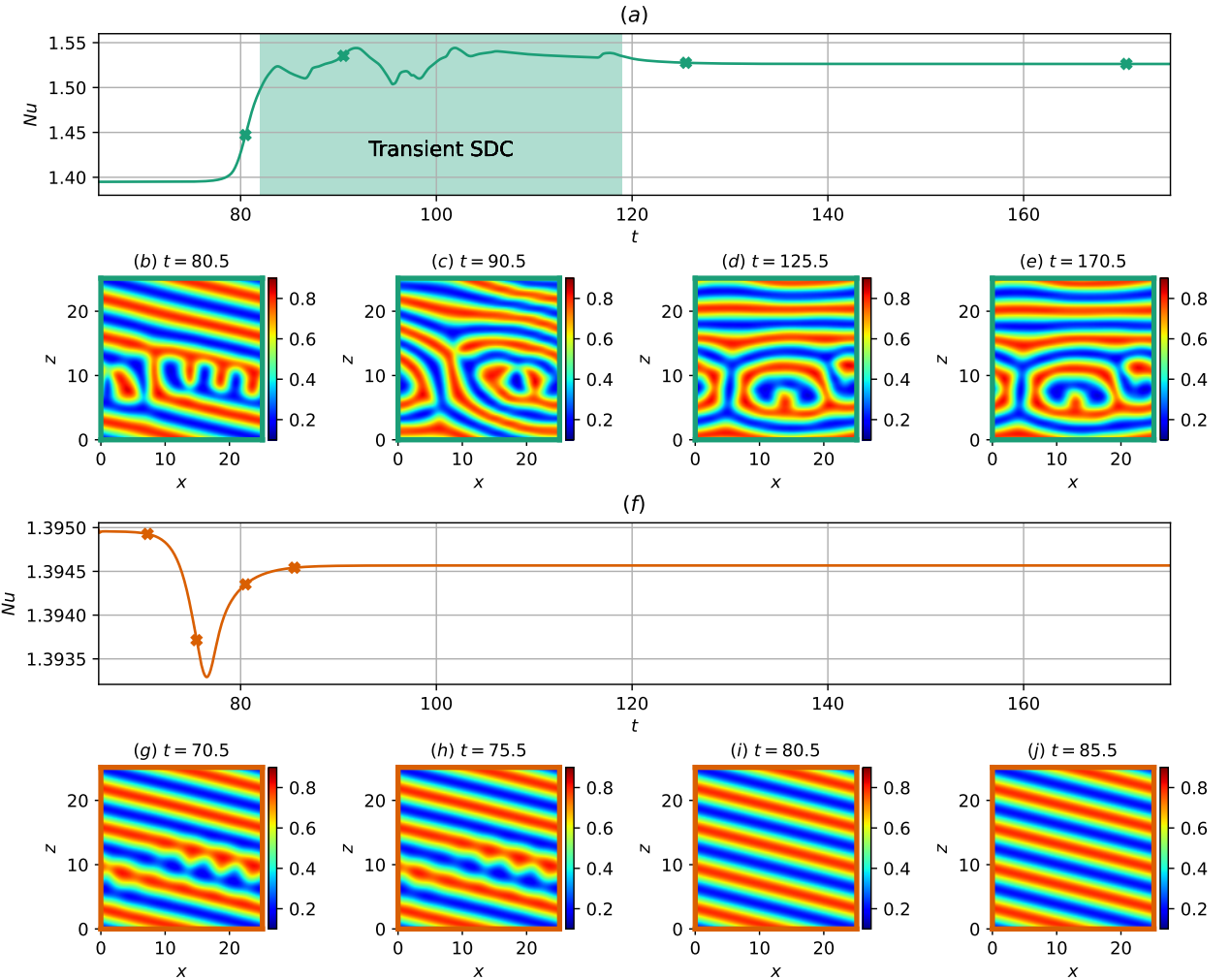


Figure 4.8: Time history of Nu along two opposite directions along the unstable manifold of the jagged edge state: (a) ‘upper’ trajectory leading to a transient SDC for $t \approx 85 - 120$ and subsequently to PM state for $t > 120$ and (f) ‘lower’ trajectory stabilising into $s_{ISR,q=2.06/d}$. Mid-plane temperature fields are visualised in (b-e) along the upper trajectory at $t = 80.5, 90.5, 125.5, 170.5$, and in (g-j) along the lower trajectory at $t = 70.5, 75.5, 80.5, 85.5$.

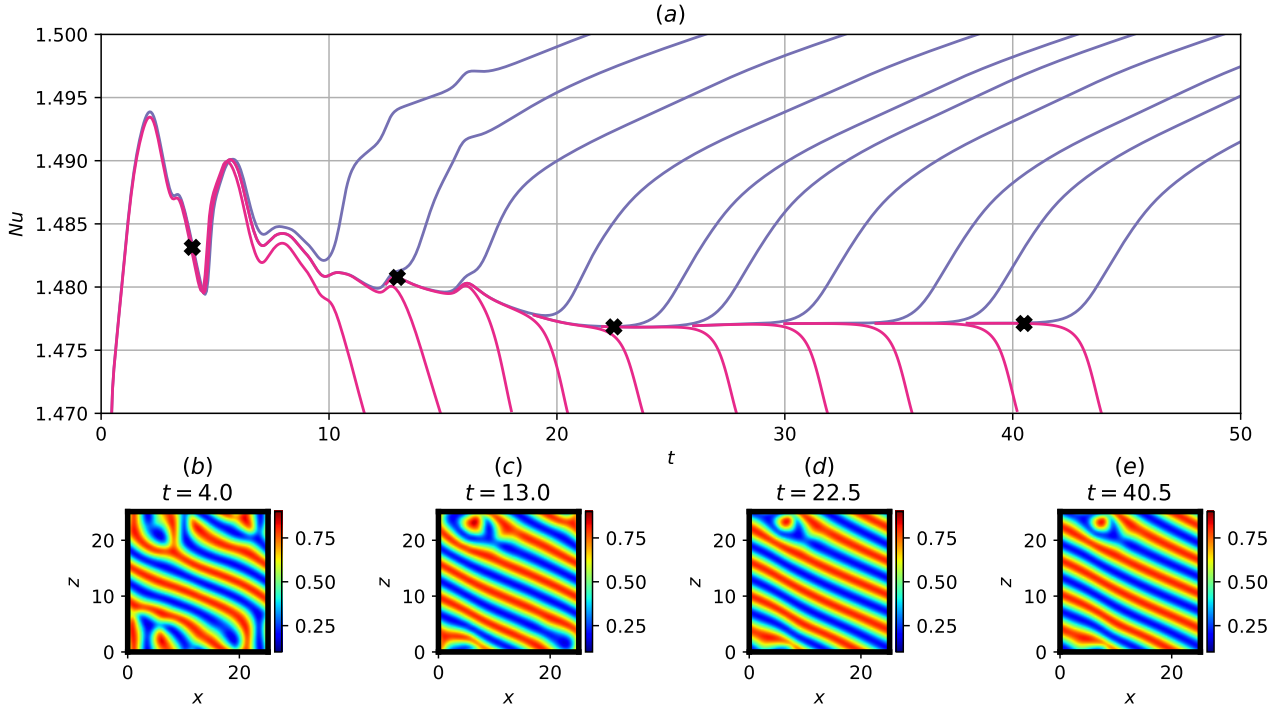


Figure 4.9: a) Time history of $\bar{N}u$ and (b-e) the corresponding mid-plane temperature field snapshots at $t = 4, 13, 22.5, 40.5$ along the edge trajectory obtained by bisecting $s_{ISR,q=2.24}$ and $s_{spiral-defect}$.

4.5 Unstable ideal straight rolls

Thus far, we have studied the edge and the edge states between some of the stable ISRs and elementary states. The dynamics associated with the unstable ISRs outside of the Busse balloon, however, remain unclear ?. Given that the stable ISRs and SDC form a bistable system, it is expected that some of the unstable ISRs near the Busse balloon would asymptotically reach one of the stable ISRs as the difference between the stable and unstable ISRs would be sufficiently small ???. On the other hand, the unstable ISRs, which exist far from the boundary of the Busse balloon, may well have a sufficiently large deviation from the stable ISRs, implying that they are possibly associated with a state-space route to the SDC. The purpose of this section is to test this hypothesis by examining the long-term behaviour of the linear instabilities of the unstable ISRs.

We consider the linear instabilities of 3 unstable ISRs on the right side of the Busse balloon, with increasing wavenumber of $q = 3.5/d, 4.0/d, 4.5/d$, as shown in figure 4.12(a). The identification of the linear instability mode (or unstable manifold) with the different spanwise wavenumbers β is considered (see (4.6)). Figure 4.12(b) presents the unstable eigenvalues as a function of β . There are 2, 4 and 7 unstable manifolds ($\Re(\lambda) > 0$) for unstable ISRs of $q = 3.5/d, 4.0/d, 4.5/d$ respectively, forming total 13 unstable manifolds. In general, the growth rate and the number of linear instability modes (i.e. the repelling strength and the number of unstable manifolds) increase as q increases. It is worth mentioning that the solutions of unstable ISRs of $s_{ISR,q}(x, y)$ (required for linear stability analysis) are obtained by restricting the computational domain to the 2D $x-y$ plane which artificially suppresses 3D linear instabilities. We also note that the stability analysis of the unstable ISR, $q = 5.0/d$

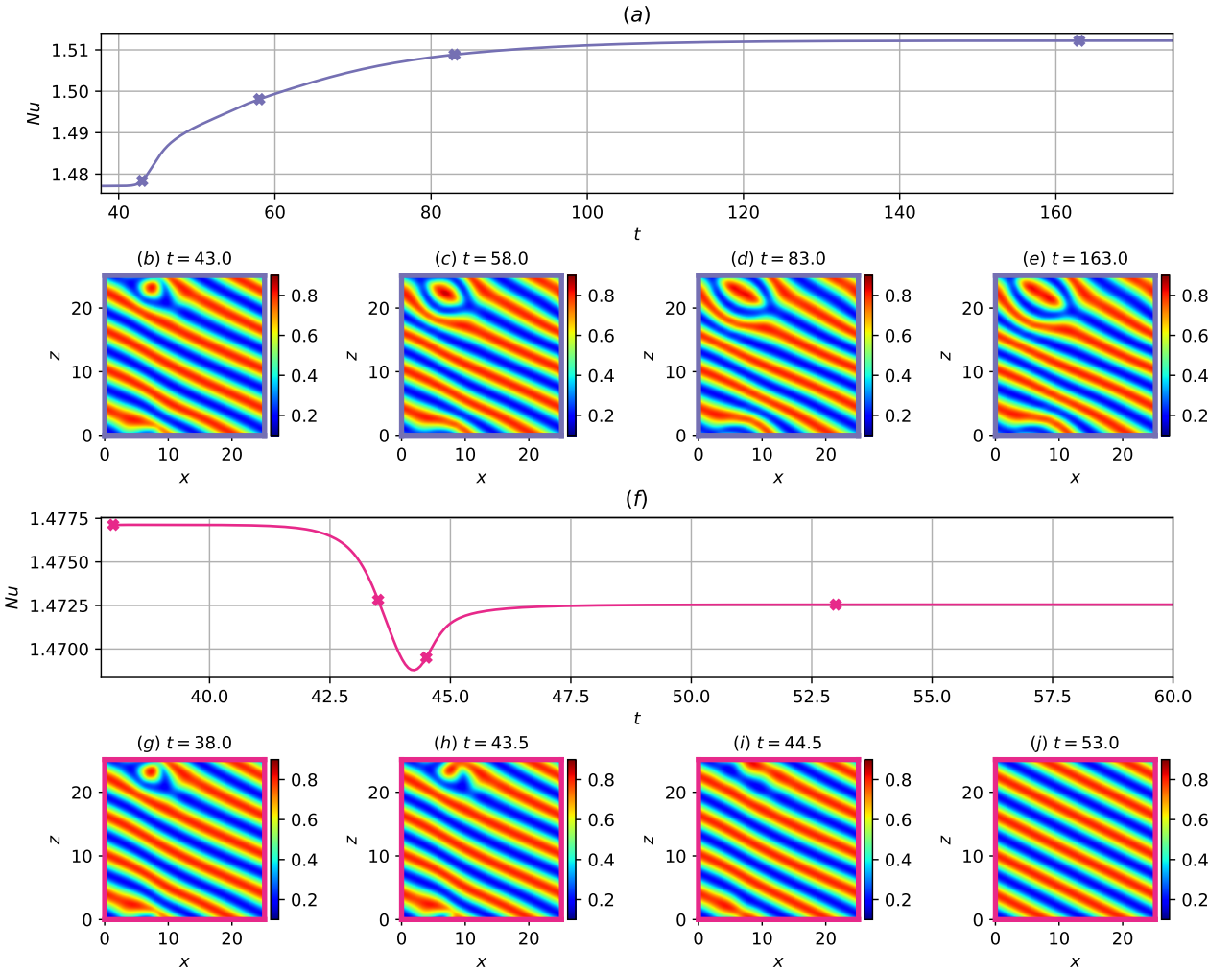


Figure 4.10: Time history of Nu along two opposite directions of the unstable manifold of the *point-defect* edge state: (a) ‘upper’ trajectory leading a stationary elementary state with bubble defect from $t \approx 43 - 163$ and (f) ‘lower’ trajectory decaying to the stable $s_{ISR,q=2.24}$ state. Mid-plane temperature fields are visualised in (b-e) along the upper trajectory at $t = 43.0, 58.0, 83.0, 163.0$, and in (g-j) along the lower trajectory at $t = 38.0, 43.5, 44.5, 53.0$.

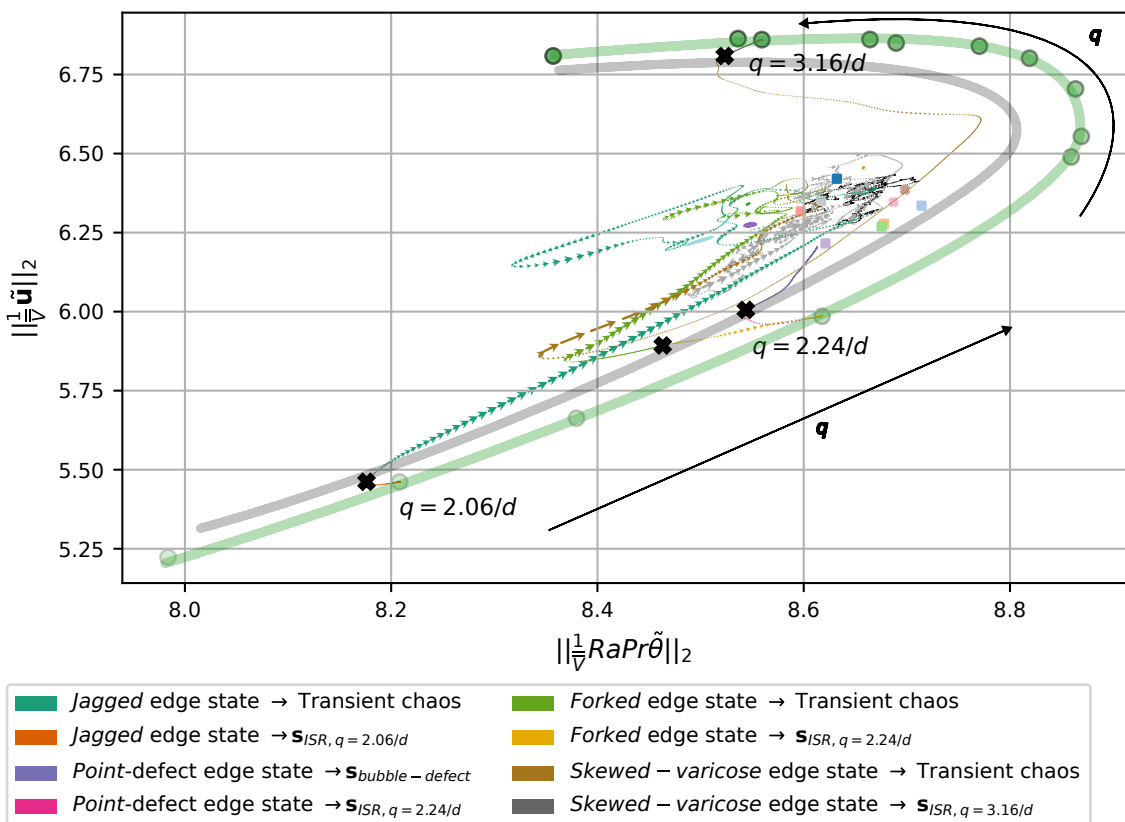


Figure 4.11: Phase portrait of the *jagged*, *point-defect*, *defect* and *skewed-varicose* edge states, along with stable ISRs, elementary states and transient SDC. Green and grey horseshoe lines are the regions, where stable ISRs and edge attractors are expected to be distributed when different sizes of the computational domain are considered.

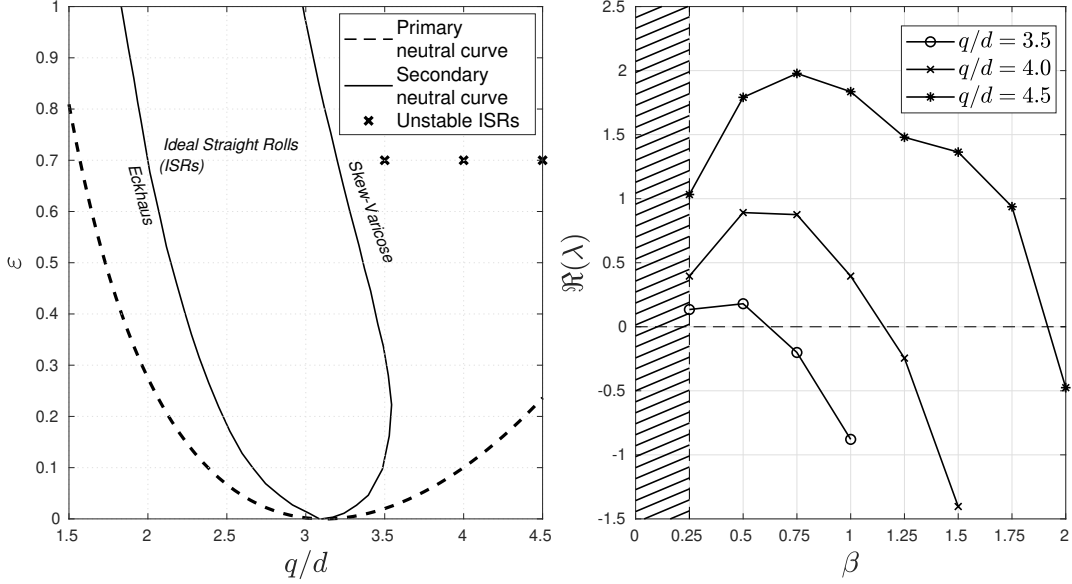


Figure 4.12: (a) Primary and secondary (Busse balloon from figure 1 ?) stability curves and unstable ISRs with $q = 3.5/d, 4.0/d, 4.5/d$; (b) Variation of the growth rate of instabilities of unstable ISRs as a function of spanwise wavenumber β . (Note that there are a total 13 unstable eigenmodes.)

Cases	$\beta = 0.25$	$\beta = 0.50$	$\beta = 0.75$	$\beta = 1.00$	$\beta = 1.25$	$\beta = 1.50$	$\beta = 1.75$
$q = 3.5/d$	ISR _{3.04}	(a) ISR _{2.50}	Stable	Stable	Stable	Stable	Stable
$q = 4.0/d$	ISR _{2.50}	(b) ISR _{3.16}	ISR _{3.00}	ISR _{2.83}	Stable	Stable	Stable
$q = 4.5/d$	ISR _{2.50}	ISR _{2.50}	(c) ISR _{3.00}	ISR _{3.20}	(d) Elementary	ISR _{2.50}	(e) Elementary

Table 4.2: Asymptotic state of secondary linear instabilities of $q = 3.5/d, 4.0/d, 4.5/d$. Subscripts in ISR refer to asymptotic wavenumber q , e.g., ISR_{2.5} refers to ideal straight rolls with wavenumber of $q = 2.5/d$. The asymptotic behaviours of (a-c) and (d,e) are discussed further in §4.5.1 and §4.5.2 respectively.

was not considered as it quickly evolved into an unstable ISR of $q = 3.5/d$, which will be discussed in section §4.5.1.

To consider the long-term behavior in the direction of the unstable manifolds, an initial condition,

$$\mathbf{s}_0(\mathbf{x}, t=0) = \mathbf{s}_{ISR,q}(\mathbf{x}) + \hat{\mathbf{s}}_\beta(x, y)e^{i\beta z}, \quad (4.9)$$

is prescribed to equation (4.1). Here, $\hat{\mathbf{s}}_\beta e^{i\beta z}$ is the unstable eigenmode, the amplitude of which was scaled such that its total energy (defined in (4.6)) of $\delta = 10^{-5}, 10^{-4}, 10^{-3}$ were considered. The total energy of the eigenmode, $\delta = 10^{-4}$ was found to be sufficiently small enough to ensure linear growth, while large enough to prevent other eigenmodes from being excited. Next, the initial condition is time integrated over an extended period until an asymptotic state is reached. Table 4.2 shows the asymptotic states of 13 linear instabilities, depicted in figure 4.12(b), of which 11 linear instabilities led to ISRs states, forming a network of heteroclinic orbits which will be discussed in §4.5.1. Only the remaining 2 instabilities led to a transient SDC state before settling into an elementary state discussed further in §4.5.2.

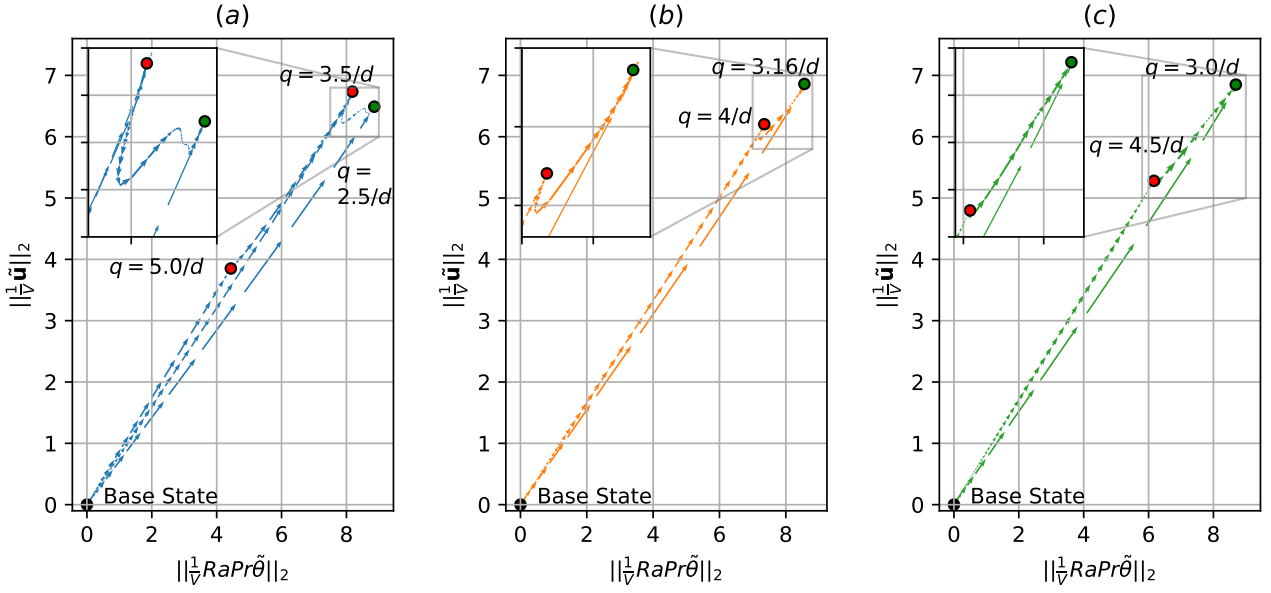


Figure 4.13: The phase-space solution trajectories connecting: (a) unstable base (conductive) state between 10 unstable rolls ($q = 5/d$), 7 unstable rolls ($q = 3.5/d$) and 5 stable rolls ($q = 2.5/d$); (b) unstable base (conductive) state between 8 unstable rolls ($q = 5/d$) and 6 stable rolls ($q = 3.16/d$); (c) unstable base (conductive) state between 9 unstable rolls ($q = 4.5/d$) and 6 stable rolls ($q = 3/d$). Here, the size of the arrows indicates the speed of the solution trajectory (or flow).

4.5.1 Pathways leading to ISRs - heteroclinic orbits

In this section, the asymptotic behaviour of the most unstable linear instabilities of ISRs (tab 4.2(a-c)) will be discussed. Figure 4.13 depicts the state space plot of volume normalised L2-norms of velocity and temperature. It reveals a number of heteroclinic orbits, connecting the base state (●), stable (●) and unstable (●) ISRs. Figure 4.13(a) exhibits several solution trajectories linking the base state, stable and unstable ISRs: three orbits connecting the base state to all the stable and unstable ISRs shown, one from the ISR of $q = 3.5/d$ to that of $q = 2.5/d$, and one from the ISR of $q = 5.0/d$ to that of $q = 3.5/d$. Here, caution will need to be taken in interpreting each of the connections as a heteroclinic orbit, because there appears to be an invariant state at which the speed of the solution trajectory nearly vanishes (a sign of the existence of unstable invariant states or ghost states ?): for example, see the solution trajectory between the ISR of $q = 3.5/d$ to that of $q = 2.5/d$ (in the inset of figure 4.13(a)), which will be discussed below with figure 4.14. Starting from the primary base state, the system saturates into an ISR of wavenumber $q = 5.0/d$. Since this ISR is linearly unstable, it evolves into another unstable ISR of $q = 3.5/d$, before ultimately stabilising into an ISR of $q = 2.5/d$. Next, figure 4.13(b) shows three solution trajectories connecting the base state, an unstable and stable ISR. Starting from the base state, the system transitions into an unstable ISR of $q = 4/d$ before stabilising into an ISR of $q = 3.16/d$. Lastly, figure 4.13(c) presents three solution trajectories connecting the base state, a stable and unstable ISR. Starting from the base state, it can evolve to an unstable ISR of $q = 4.5/d$ before settling into a stable ISR of $q = 3.0/d$. Figure 4.13 suggests that each of the stable ISRs within the Busse balloon has the basin of attraction, characterised by a web of heteroclinic orbits connecting some of the unstable ISRs outside of the Busse balloon. It is worth emphasising that

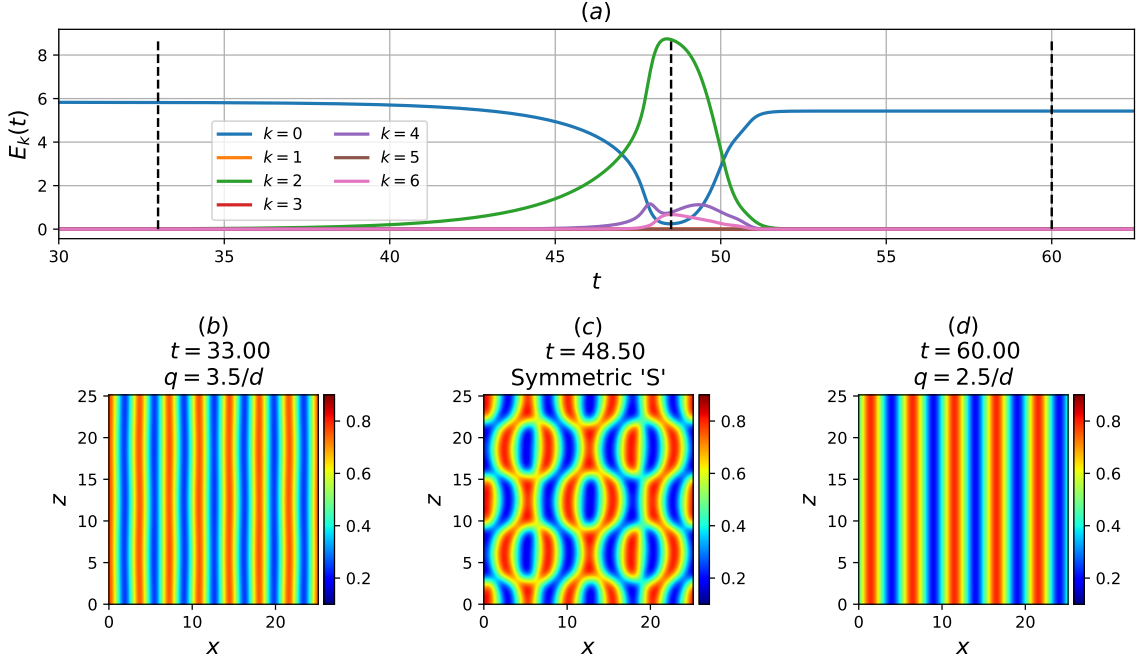


Figure 4.14: Asymptotic behaviour of the linear instability ($\hat{q}_{\beta=0.50}$) about unstable ISR $q = 3.5/d$. (a) Modal energy $E_k(t)$, and temperature snapshots, $\theta(x, z)|_{y=d/2}$ at (b) $t = 33$, (c) $t = 48.5$, (d) $t = 60$.

the connections between the solutions presented here were obtained by time-integrating the dominant unstable manifolds of ISRs. In practice, there are many more unstable manifolds (see table 4.2) which have not been presented, potentially leading to more complex networks of heteroclinic orbits that form the basin of attraction for each stable ISR.

Figure 4.14 describes the asymptotic behaviour with the most unstable eigenmode for $q = 3.5/d$ (table 4.2(a)) in detail, corresponding to the connection between the unstable ISR of $q = 3.5/d$ and the stable ISR of $q = 2.5/d$ in figure 4.13(a). To observe the linear instability defined in Eq. (4.9), we report contribution of modal energy (figure 4.14(a)) as

$$E_k(t) = \frac{1}{2} \int_{\Omega} |\hat{\mathbf{u}}_k(t)|^2 d\Omega, \quad (4.10)$$

where $\hat{\mathbf{u}}_k$ refers to the k -th Fourier coefficient in z -direction. Initially, the simulation starts from the ISR state of 7 rolls ($t = 33$), corresponding to a roll-wavenumber of $q = 3.5/d$. The unstable eigenmode $\hat{s}_{\beta=0.50}$ grows exponentially before peaking at $t = 48.50$, forming an ‘S’-liked symmetric state (figure 4.14(c)). Note that, at this point, the time derivative of $E_k(t)$ nearly vanishes, indicating that the snapshot taken at $t = 48.50$ is potentially close to an unstable invariant state. Finally, the modal energy of $N_z = 2$ decays and the system settles into an ISR state of $q = 2.5/d$ (5 rolls aligned in the x -direction), which is within the Busse balloon.

Figure 4.15 illustrates the asymptotic behaviour with the most unstable eigenmode for $q = 4.0/d$ (table 4.2b), also depicted in the solution trajectory connecting the unstable ISR of $q = 4.0/d$ to the stable ISR of $q = 3.16/d$ in figure 4.13(b). Figure 4.15(a) shows the contribution of modal energy from each Fourier z component. From $t = 5 - 10$, the system experiences an exponential growth,

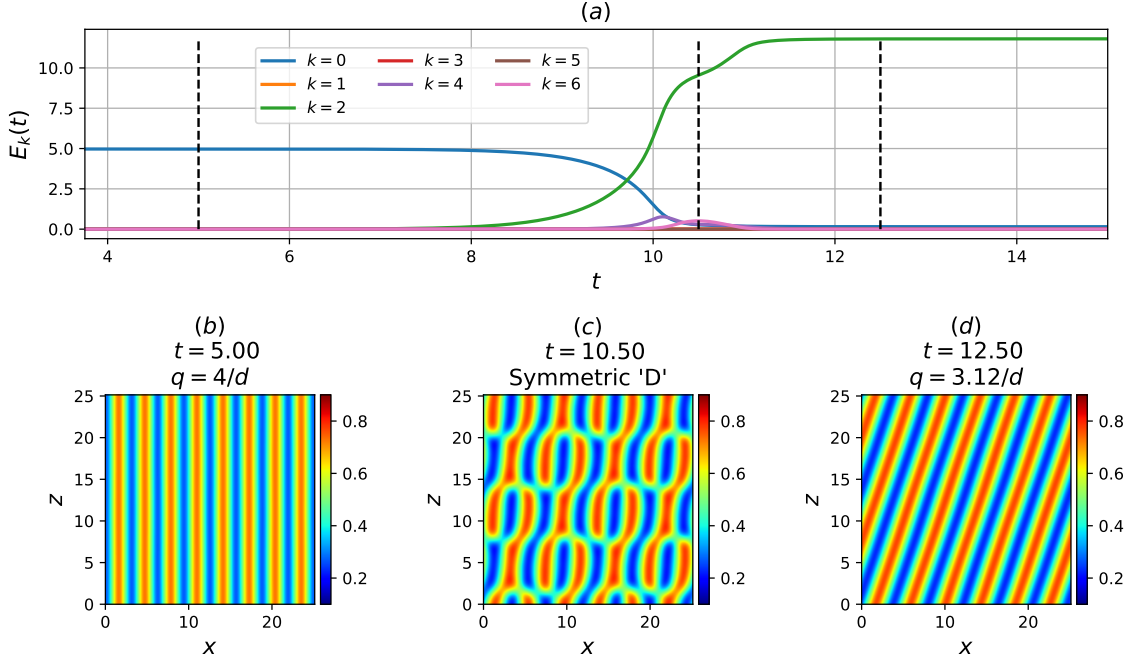


Figure 4.15: Asymptotic behaviour along the linear instability $\hat{s}_{\beta=0.50}$ about unstable ISR $q = 4.0/d$. (a) Modal energy $E_k(t)$, and temperature snapshots, $\theta(x, z)|_{y=d/2}$ at (b) $t = 5$, (c) $t = 10.5$, (d) $t = 12.5$.

guided by its dominant secondary eigenmode $\hat{s}_{\beta=0.50}$, where the 8 rolls ISRs ‘disintegrates’ into a convection pattern characterised by a symmetric ‘D’ convection pattern. Finally, the system stabilises into an ISR state with wavenumber $q = 3.16/d$.

Figure 4.16 presents the asymptotic behaviour with the most unstable eigenmode for $q = 4.5$ (table 4.2(c)), corresponding to the connection between the unstable ISR ($q = 4.5/d$) and the stable ISR ($q = 3/d$) in figure 4.13(c). Figure 4.16(a) shows the contribution of modal energy from each Fourier z component. Initially, the system begins as an ISR state of 9 rolls ($t = 1.25$). Next, the secondary eigenmode $\hat{s}_{\beta=0.75}$ grows exponentially and peaks at $t = 4.50$, leading to an intermediate state characterised by a symmetric ‘O’ convection rolls with small $dE_k(t)/dt$ (fig 4.16(c)). Finally, the system evolved into an ISR state of $q = 3/d$ as an asymptotic state.

All three cases examined here show that the transition from an unstable ISR to a stable ISR involves an intermediate state, at which $dE_k(t)/dt$ is seen to be relatively small. In the transition pathway from the unstable to stable ISR, it is presumable that there exists an unstable equilibrium (i.e. fixed point/travelling-waves etc.) in the form of the original unstable ISR with its nonlinearly saturated instability, or ghost states ?. The existence of such a stationary solution can probably be computed with a typical Newton iteration or variational methods [??], but this is beyond the scope of the present study. In any case, the numerical experiments here suggest that each of the stable ISR has a basin of attraction composed of a network of heteroclinic orbits involving connections between the base state and unstable ISRs.

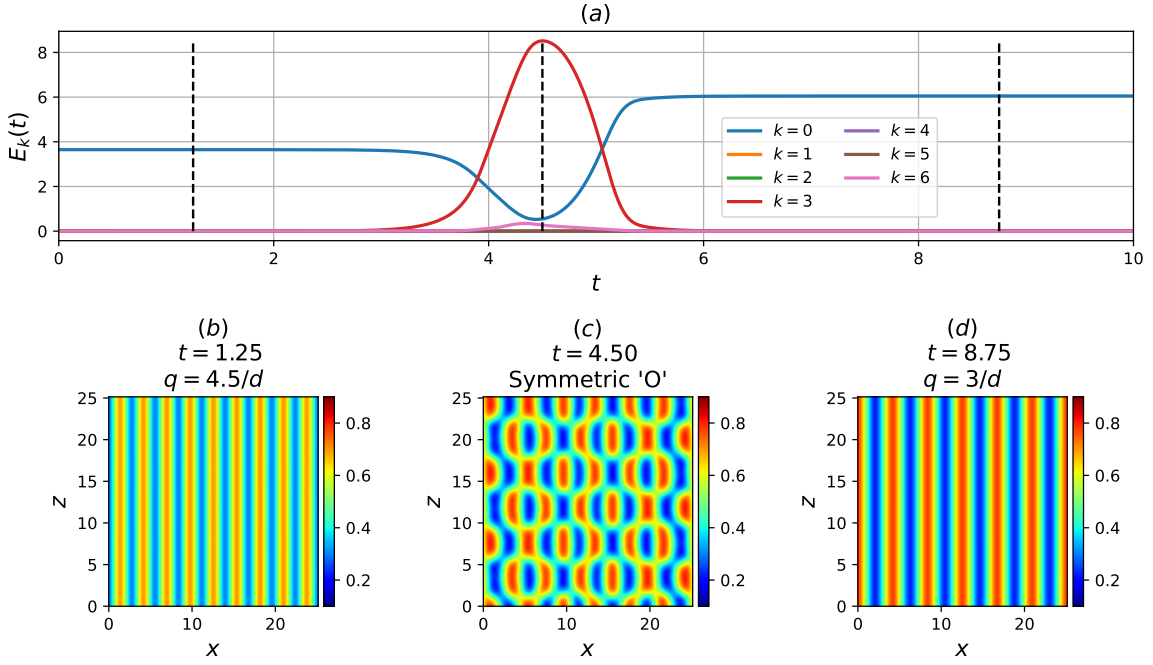


Figure 4.16: Asymptotic behaviour along the linear instability of $\hat{s}_{\beta=0.75}$ about unstable ISR of $q = 4.5/d$. (a) Modal energy $E_k(t)$, and temperature snapshots, $\theta(x, z)|_{y=d/2}$ at (b) $t = 1.25$, (c) $t = 4.50$, (d) $t = 8.75$.

4.5.2 Pathways leading to elementary states

Now, we discuss the asymptotic behaviour with linear instabilities of $\hat{s}_{\beta=1.25}$ and $\hat{s}_{\beta=1.75}$ about the unstable ISR of $q = 4.5/d$ (tab 4.2(d,e)). Contrary to the transitions presented in the previous section, the asymptotic states did not result in ISRs, but transient SDC before settling into an elementary state for case (e) (table 4.2(e)), and an elementary directly for case (d) (table 4.2(d)). The asymptotic behavior with $\hat{s}_{\beta=1.25}$ for unstable ISR $q = 4.5/d$ (table 4.2(d)) is presented in figure 4.17. At $t = 1.25$, the unstable ISR state ($q = 4.5/d$) is characterised by 9 rolls aligned along x direction. Subsequently, the state experiences the linear instability triggered ($t = 5$, figure 4.17(c)), shown as an exponential growth of the brown curve figure 4.17(a)), corresponding to the fifth Fourier modal energy (or $\beta = 1.25$). At $t = 6.75$, the system transitions into a saturated state temporarily (albeit unstable), characterised by square-like alternating convection patterns (figure 4.17(d)), and saturates briefly at $t = 8.75$, forming ‘S’-like convection patterns in figure 4.17(e). Finally, it settles into an oscillatory elementary state (i.e. stable periodic orbit) with an oscillation period of $T \approx 3.25$ (figures 4.17(f,g)).

The asymptotic behavior with $\hat{s}_{\beta=1.75}$ of unstable ISR $q = 4.5/d$ (table 4.2(e)) is presented in figure 4.18. Starting from $t = 1.25$, the unstable ISR state is characterised by 9 convection rolls aligned along the x -axis. The state experiences the linear instability imposed from $t = 1.25$ to $t = 7$, corresponding to an exponential growth in the grey curve ($E_7(t)$ in figure 4.18(a)), marked by cross-convection rolls in figure 4.18(c). Subsequently, the state exhibits a transient SDC behaviour from $t \approx 7$ to $t \approx 80$, characterised by an ‘O’-ring and ‘pac-man’ liked convection pattern illustrated in figure 4.18(d). Following this, the system stabilises into a short-period ($T \approx 1.8$) oscillatory behaviour

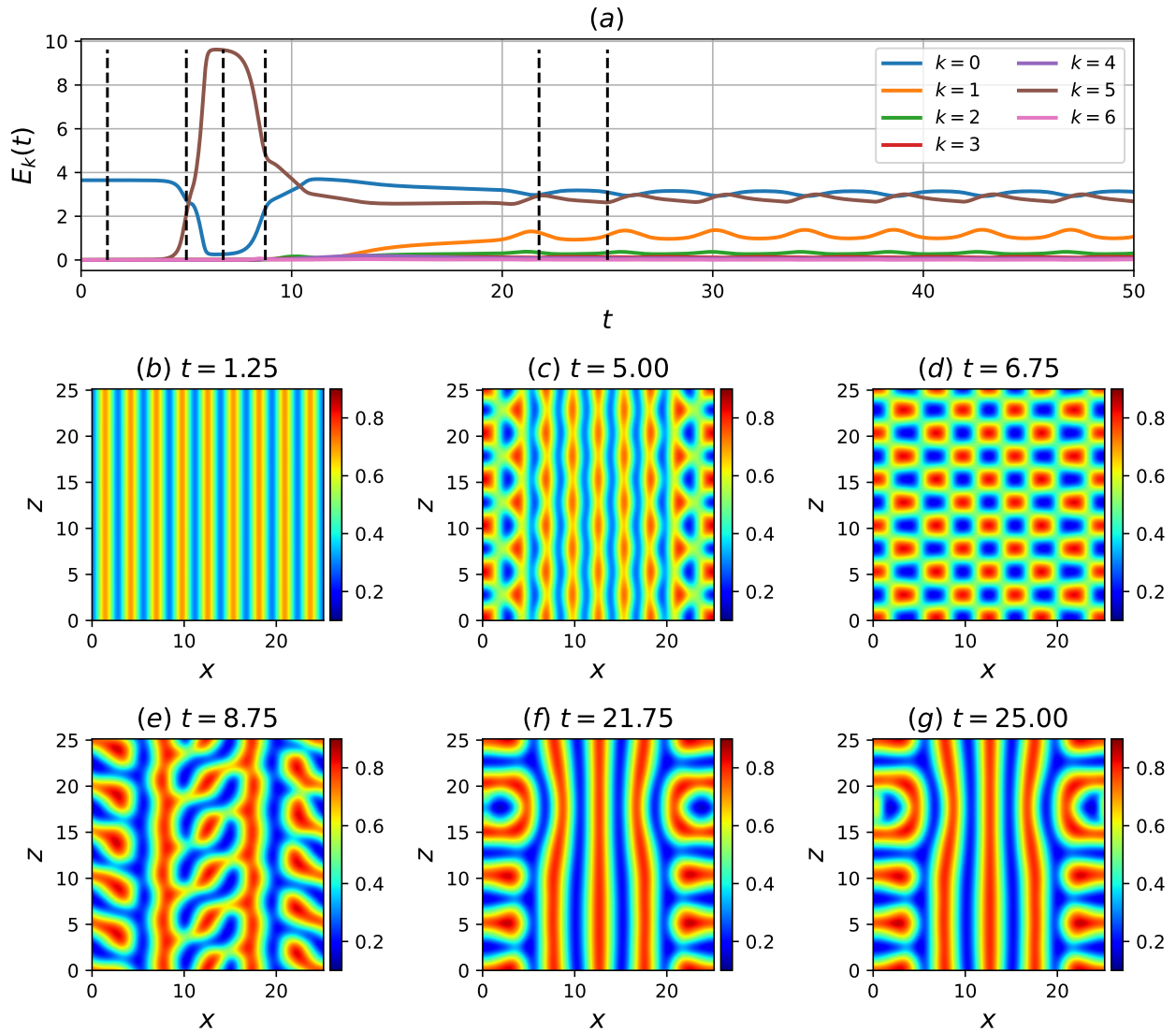


Figure 4.17: Asymptotic behaviour along the unstable manifold of $q = 4.5/d$, $\beta = 1.25$. (a) Modal energy $E_k(t)$ plot, and temperature snapshots $\theta(x, z)|_{y=d/2}$ at (b) $t = 1.25$, (c) $t = 5$, (d) $t = 6.75$, (e) $t = 8.75$, (f) $t = 21.75$ and (g) $t = 25$

between $t = 90$ and $t = 110$ (figure 4.18(e)), before transitioning into a long-period time-periodic state from $t = 110$ to $t = 201.75$ (figure 4.18(a) *cont.*), with a period of $T = 51.75$. The convection pattern appears to be travelling diagonally in the negative x - z directions (compare figures 4.18(f,g)), indicating that this state is a relative periodic orbit.

Figure 4.19 presents the state space trajectories of two pathways discussed above, represented by the volume-normalised L2-norms of velocity perturbations, temperature perturbations and Nusselt number. These trajectories are superimposed upon the state space trajectories of SDC (figures 4.1(a,b)), elementary states (figures 4.1(c-f)) and the fixed-point attractors of ISRs (figure 4.4). The purple trajectory represents the one along the linear instability direction (i.e. the unstable manifold) of $q = 4.5/d$ with $\beta = 1.25$. Originating from the unstable ISR ($q = 4.5/d$), briefly saturates at $\|\frac{1}{V}\tilde{\mathbf{u}}\| \approx 6.25$ and $\|\frac{1}{V}RaPr\tilde{\theta}\|_2 \approx 8$, before stabilising into a periodic orbit near the *spiral-defect* elementary state (see figure 4.1, represented by the orange trajectory in figure 4.4). The case of $q = 4.5/d$ along the linear instability direction for $\beta = 1.75$ is represented by the brown trajectory. Emanating from the unstable ISR ($q = 4.5/d$), the trajectory experiences a period of transient SDC behaviour in the vicinity of elementary states before converging onto a relative periodic orbit, as expected from figure 4.18. It is evident that the two trajectories arising from linear instabilities about the unstable ISR ($q = 4.5/d$) lie within the vicinity of SDC.

4.5.3 A pathway to SDC in an extended domain $\Gamma = 4\pi$

In §4.5.2, we have identified two distinct pathways to elementary states along some unstable manifolds from an unstable ISR. In particular, one of the trajectories evolved into transient SDC before stabilising into an elementary state. This is reminiscent of a chaotic saddle, but with a considerably short lifetime. The transient SDC behaviour observed within the minimal domain implies that if the same initial condition is added in an extended computational domain, it would trigger a chaotic state at least with a longer lifetime. This chaotic state is expected to be SDC in an extended domain, given the analysis in §4.5.2. To examine this hypothesis, we conduct a numerical simulation with an initial condition from the case of table 4.2(e) (i.e. the unstable ISR $q = 4.5/d$ with the instability mode of $\hat{s}_{\beta=1.75}$) in a domain twice larger than each horizontal direction ($\Gamma = 12.58$).

The solution trajectory along the unstable manifold, $s_{\beta=1.75}$, of ISR $q = 4.5/d$ in an extended domain ($\Gamma = 4\pi$) is presented in figure 4.20. The state, characterised by 18 convection rolls (figure 4.20(b)), experiences the linear instability from $t = 1.25$ to $t = 7$, marked by cross-convection rolls shown in figure 4.20(c). Subsequently, the state exhibits a prolonged period of chaotic behaviour, starting from $t = 7$ and lasting beyond $t = 200$. This is in stark contrast to the transient SDC behaviour observed in the minimal domain (figure 4.18), confirming the hypothesis above. Finally, it is interesting to note that the convection patterns of figures 4.20(f,g) contain localised structures that bear resemblance with the stationary *pac-man* (figure 4.1(c)) and oscillatory *peanut* (figure 4.1(f)) elementary states.

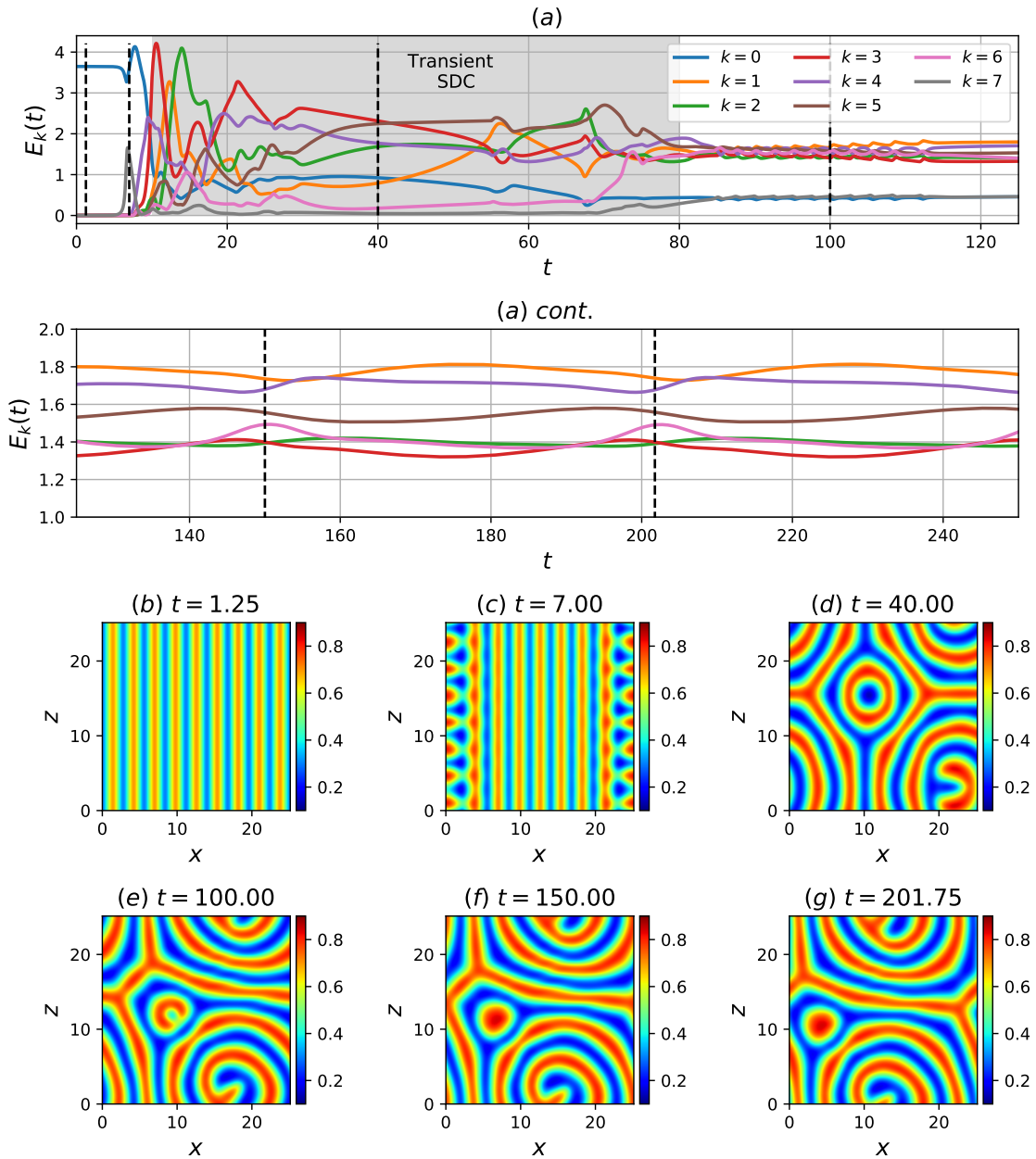


Figure 4.18: Asymptotic behaviour along the linear instability of $\hat{s}_{\beta=1.75}$ about unstable ISR $q = 4.5/d$. (a) Modal energy $E_k(t)$, and temperature snapshots $\theta(x, z)|_{y=d/2}$ at the onset of secondary instability at (b) $t = 1.25$, (c) $t = 7$, following a transient SDC behaviour at (d) $t = 40$, and settling into a elementary state at (e) $t = 100$, (f) $t = 150$ and (g) $t = 201.75$.

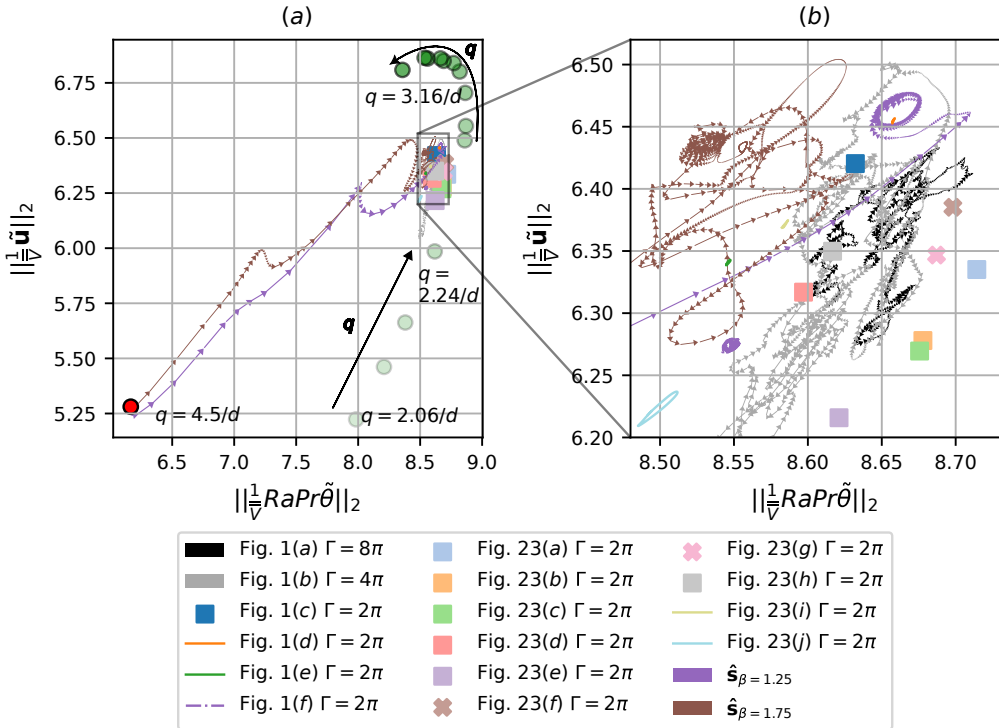


Figure 4.19: State space visualisations using (a) $\|\frac{1}{V}\tilde{\mathbf{u}}\|_2$ and $\|\frac{1}{V}RaPr\tilde{\theta}\|_2$, for SDC shown in figure 4.1(a,b), 4 elementary states shown in figures 4.1(c-f), linear instabilities (purple) $\hat{s}_{\beta=1.25}$, (brown) $\hat{s}_{\beta=1.75}$ about an unstable ISR $q = 4.5/d$ (figures 4.17, 4.18), and stable fixed-points of ISRs for wavenumber $q \in (2.0/d, 3.35/d)$ with the magnitude of q is depicted by the opacity of the filled symbol (●), with arrows denoting direction of increasing q . Figure (b) is a magnified plot of (a).

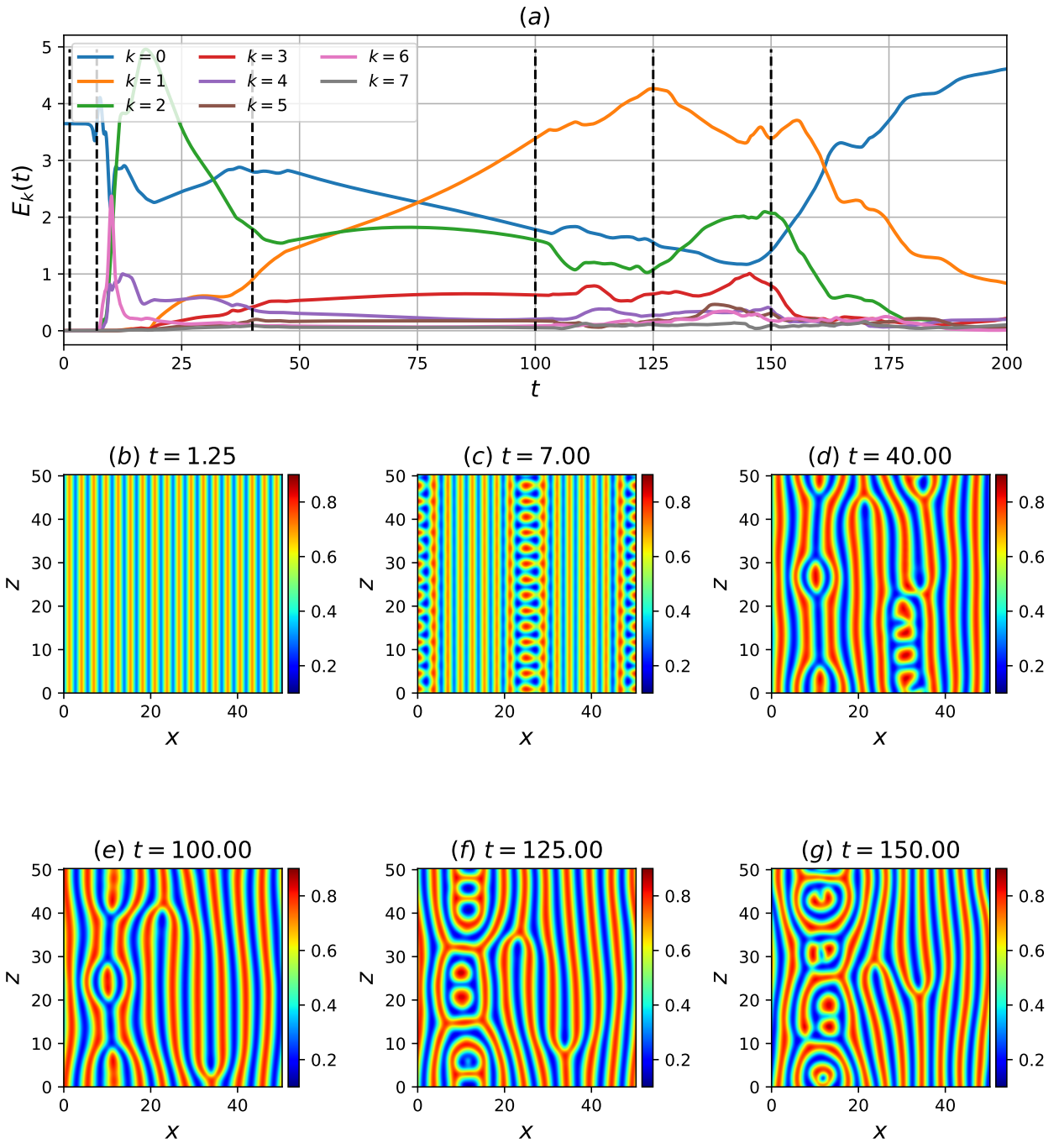


Figure 4.20: Asymptotic behaviour along the linear instability $\hat{s}_{\beta=1.75}$ about unstable ISR $q = 4.50/d$, in an extended domain $\Gamma = 4\pi$. (a) Modal energy $E_k(t)$, and temperature snapshots $\theta(x, z)|_{y=d/2}$, at (b) $t = 1.25$, (c) $t = 7$, (d) $t = 40$, (e) $t = 100$, (f) $t = 125$, (g) $t = 150$.

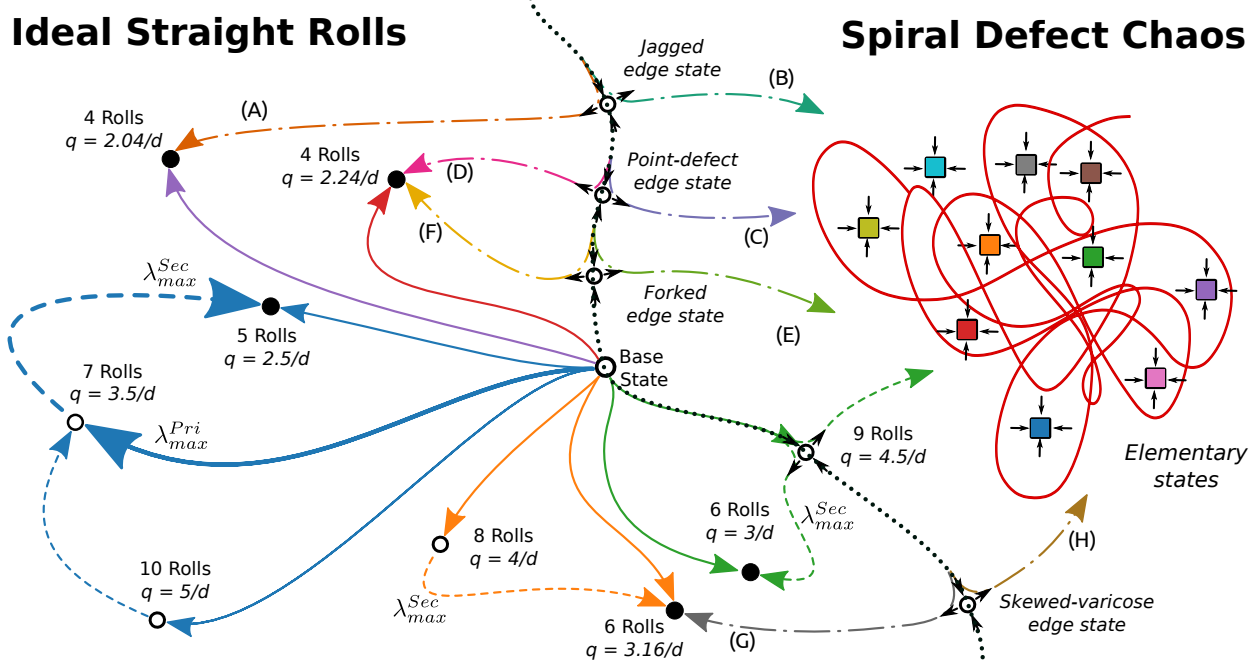


Figure 4.21: State space sketch containing the base, stable and unstable ISRs, edge, elementary states and SDC in a confined domain. Open circles, (\circ) and filled circles/squares (\bullet , \blacksquare) refer to unstable and stable states. Solid $(-)$ and dashed lines $(--)$ are the solution trajectories along the primary and secondary instabilities respectively, $\lambda_{max}^{Pri,Sec}$ refers to the most unstable primary and secondary linear instability manifolds. Blue, orange and green trajectories denote heteroclinic connections leading toward stable ISRs (trajectories labelled (A-G) and colors adapted from figure 4.13). Dashed-dotted trajectories $(-\cdot-)$ refer to solution trajectories emerging from the edge states (color-coded from figure 4.11). The dotted line (\cdots) represents the boundary between ISRs and SDC, consisting of many stable elementary states.

4.6 Concluding remarks

SDC has been considered one of the bistable states within a large spatial domain in Rayleigh-Bénard convection. However, existing studies have also shown the presence of multiple stable states in small and large domains, puzzling one's understanding of the bistable system in an extended spatial domain. Starting with numerical simulation in an extended domain ($\Gamma = 8\pi$), we have systematically reduced the computational domain, such that the fundamental patterns of SDC can be isolated. Through numerical experiments confined within a minimal domain of $\Gamma = 2\pi$, we have identified transient SDC before stabilising into a stable elementary states of SDC, and 14 different elementary states have been found in this way. From the conventional view of turbulence in shear flow, chaotic trajectories (representing turbulence) are expected to visit a set of unstable invariant solutions before eventually decaying to the base (laminar) state. However, in contrast to this expectation, the solution trajectory, once tangled into SDC stabilises into an non-trivial elementary state instead of returning to the base (ISR) state ???. This finding is new and challenges the understanding of transition from a dynamical system viewpoint. Despite this, the elementary states are still situated around the chaotic trajectories of SDC in the state space (figure 4.4), and their statistical properties (figure 4.5) are remarkably similar to those of SDC. This suggests that the computed elementary states may serve as ‘building block’ structures of SDC that interact with each other to form SDC in an extended domain.

To further understand the state space structure of SDC, ISRs and possible gateways toward SDC, we furnish a state space sketch of the solution trajectories connecting the base, stable and unstable ISRs, edge, elementary states and SDC, shown in figure 4.21. Starting from the base state, time-integrating along the unstable manifold guided by primary instabilities leads to either stable or unstable ISRs, denoted by solid trajectories. Notably, the most unstable primary instability leads to a 7 roll ISR ($q = 3.5/d$), before saturating into a stable 5 roll ISR ($q = 2.5/d$), following the most unstable secondary instability, depicted by dashed trajectories. These solution trajectories form a network of heteroclinic orbits, connecting the base state with stable ($q = 2.5/d$) and unstable ($q = 3.5/d, 5/d$) ISRs, represented in blue. Further from the boundaries of the Busse balloon, we have identified two more heteroclinic orbits that form a basin of attractor between the base state, and stable, unstable ISRs, labelled as a group of orange and green trajectories. These heteroclinic orbits are expected in experimental settings where initial conditions and background noise can be controlled precisely. In practice, where precise controls are inaccessible, it is more likely to observe SDC ($\Gamma = 4\pi, 8\pi$) or stable elementary states ($\Gamma = 2\pi$), which are embedded in the chaotic trajectories of SDC (see coloured ■), supporting the notion that SDC is underpinned by elementary states presumably interacting with each other. By examining the edge states between stable ISRs and elementary states, we have identified 4 edge states that lie on the boundary between stable ISRs and transient SDC, where the upper and lower trajectories emerging from their unstable manifold are represented by dash-dotted trajectories. Further from the Busse balloon, we have identified an unstable manifold of a 9 roll ($q = 4.5/d$) ISR, leading to the onset of SDC. Consequently, the unstable base state is also expected to lie on the boundary, as a controlled initial condition could guide the system toward the unstable 9-roll ISR, and subsequently the onset of SDC. Finally, the dotted line represents the boundary between ISRs and SDC, consisting of the base state, edge states and unstable 9 roll ISR ($q = 4.5/d$), illustrating

four possible routes toward SDC. Although we have considered the unstable manifolds of ISRs for $\Gamma = 2\pi$, we acknowledge that the dimension of such manifolds depends on the domain size and that the presence of spatially subharmonic instabilities may arise as the domain size increases. Additionally, there may well be other unstable ISRs and edge states along the boundary. However, the investigation into the existence of such states is challenging due to the daunting computational efforts required. Recent advances, such as the framework proposed in ?, may help to accelerate linear stability analysis and facilitate further investigations.

Chapter 5

Conclusions

Appendix A

Appendices

A.1 Non-dimensionalisation

The non-dimensionalised incompressible Navier-Stokes equations with Boussinesq approximations for buoyancy describe the motion of a fluid of RBP. where $\nabla^* = (\partial/\partial x^*, \partial/\partial y^*, \partial/\partial z^*)$ and t^* refer to the differential operators and time with dimensions in per unit space, m^{-1} , and time, s . $\mathbf{u}^*(\mathbf{x}^*), T(\mathbf{x}^*), p^*(\mathbf{x}^*)$ refers to the three-dimensional fluid velocity, temperature, pressure fields, in dimensional form, while T_0, \mathbf{f}_b refers to a reference temperature and body-forcing terms. To reduce the number of control parameters, we can suitably nondimensionalise the primitive variables by a velocity scale u_c , length scale, L_x , and time scale u_c/L_x , where u_c refers to the centreline velocity of a laminar flow and L_x refers to the streamwise length of the domain.

$\rho, \nu, \kappa, g, \gamma$ refers the fluid's density, kinematic viscosity and thermal diffusivity, gravity, thermal expansion coefficient, properties specific to a given a fluid. We note that that for a given pressure gradient, ΔP^* , a laminar centerline velocity forms as $w^*(y^*) = W_{lam}^*(1 - y^2/h^2)$. Here, we have a total of nine dimensional quantities $W_{lam}^*, \Delta T, h, \kappa, \nu, \rho, \gamma, g$ that describes the behaviour of the fluid motion. However, utilise the buckingham pi theorem where we can reduce the equations to less dependenc

A.2 Governing equations for Rayleigh-Bénard convection

The governing equations for Rayleigh-Bénard convection are the non-dimensionalised equations with the Boussinesq approximation for buoyancy-driven flow, given by

$$\frac{\partial \mathbf{u}}{\partial t} + (\mathbf{u} \cdot \nabla) \mathbf{u} = -\nabla p + Pr \nabla^2 \mathbf{u} + \frac{Ra Pr}{8} \theta \mathbf{j}, \quad (\text{A.1a})$$

$$\frac{\partial \theta}{\partial t} + (\mathbf{u} \cdot \nabla) \theta = \nabla^2 \theta, \quad (\text{A.1b})$$

$$\nabla \cdot \mathbf{u} = 0, \quad (\text{A.1c})$$

subjected to the following boundary conditions at the walls,

$$\mathbf{u}|_{y=\pm h} = 0, \quad \theta|_{y=-h} = 1, \quad \theta|_{y=h} = 0, \quad (\text{A.2a})$$

and the periodic boundary conditions imposed in the planar x and z directions. Here, t denotes the time scaled by the vertical thermal diffusion time, d^2/κ , and $\mathbf{x} (= (x, y, z))$ represents the spatial coordinates non-dimensionalised by depth, d . The horizontal directions are x and z , while y is the vertical direction. The velocity vector is given by $\mathbf{u} (= (u, v, w))$ and is scaled by thermal velocity, κ/d , p . The pressure is scaled by $\rho\kappa^2/d^2$, while $\theta (\equiv (T - T_U)/\Delta T)$ refers to the non-dimensional temperature with T being the absolute temperature, and \mathbf{j} denotes the unit vector in y -direction. The Rayleigh number Ra , and the Prandtl number, Pr , are defined as in §???. In this study, we set $Pr = 1$.

A.3 Projection methods for Navier-Stokes equations

In this section, we describe the projection methods for solving the incompressible Navier Stokes equations. The projection methods belong to a general class of splitting methods, where the solution step for obtaining the velocity and pressure from the incompressible Navier Stokes are uncoupled. The premise for being able to do this is because the pressure terms act as a Lagrange multiplier which enforces the incompressibility constraint. Suppose we want to find the function u that minimises the functional,

$$\min_{\mathbf{u} \neq 0} \frac{\nu}{2} (\nabla \mathbf{u}, \nabla \mathbf{u}) - (f, \mathbf{u}), \quad \text{s.t. } \nabla \cdot \mathbf{u} = 0 \quad (\text{A.3})$$

where $(\mathbf{x}, \mathbf{y}) = \int_{\Omega} \mathbf{x}^T \mathbf{y} d\Omega$ refers to a suitable inner product. To solve this optimisation problem, we use the method of Lagrange multipliers which handles the constrain, by converting the equation above into an unconstrained optimisation problem defined by the Lagrangian

$$\mathcal{L} = \frac{\nu}{2} (\nabla \mathbf{u}, \nabla \mathbf{u}) - (f, \mathbf{u}) - (p, \nabla \cdot \mathbf{u}) \quad (\text{A.4})$$

Taking the variation $\delta\mathcal{L}$, with respect $\delta\mathbf{u}$, we get

$$\frac{\delta\mathcal{L}}{\delta\mathbf{u}} = \nu(\nabla \mathbf{u}, \nabla \delta\mathbf{u}) - (f, \delta\mathbf{u}) - (p, \nabla \cdot \delta\mathbf{u}), \quad (\text{A.5})$$

$$= -\nu(\nabla^2 \mathbf{u}, \delta\mathbf{u}) - (f, \delta\mathbf{u}) + (\nabla p, \delta\mathbf{u}) \quad (\text{A.6})$$

$$= (-\nu\nabla^2 \mathbf{u} - f + \nabla p, \delta\mathbf{u}). \quad (\text{A.7})$$

and with respect to δp , we get,

$$-\frac{\delta\mathcal{L}}{\delta p} = (\delta p, \nabla \cdot \mathbf{u}). \quad (\text{A.8})$$

The optimal condition is defined by vanishing variations, hence, we recover the Stokes equations,

$$\nu\nabla^2 \mathbf{u} + \nabla p = -f \quad (\text{A.9a})$$

$$\nabla \cdot \mathbf{u} = 0 \quad (\text{A.9b})$$

In other words, the role of pressure is to serve as a constrain to enforce incompressibility, where we can consider a velocity field that is not divergence free, which is then corrected by pressure later - the splitting method. To witness this in action, we consider the basic approach of Chorin's projection which is a two step method,

$$\frac{\mathbf{u}^* - \mathbf{u}^n}{\Delta t} = -(\mathbf{u}^n \cdot \nabla) \mathbf{u}^n + \nu \nabla^2 \mathbf{u}^n \quad (\text{A.10a})$$

then,

$$\mathbf{u}^{n+1} = \mathbf{u}^* + \Delta t \nabla p^{n+1}. \quad (\text{A.10b})$$

The idea of projection stems of taking the weak formulation of the second equation with $\mathbf{v} \in \mathbf{V} := \mathbf{v} \in H_0^1(\Omega) : \nabla \cdot \mathbf{v} = 0$,

$$(\mathbf{u}^*, \mathbf{v}) = (\mathbf{u}^{n+1}, \mathbf{v}) + (\nabla p^{n+1}, \mathbf{v}) \quad (\text{A.11})$$

Taking integration by parts we get,

$$(\mathbf{u}^*, \mathbf{v}) = (\mathbf{u}^{n+1}, \mathbf{v}) - \underbrace{(\nabla p^{n+1}, \nabla \cdot \mathbf{v})}_{=0}, \quad (\text{A.12})$$

Hence,

$$(\mathbf{u}^*, \mathbf{v}) = (\mathbf{u}^{n+1}, \mathbf{v}) \quad (\text{A.13})$$

A.4 Simulation parameters for Ra - Re sweep

The spectral/ hp quadrilateral element width, heights and polynomial order are kept constant for all simulations, $(\Delta x, \Delta y|_{y=\pm h}, \Delta y|_{y=0}, P) = (0.1\pi, 0.0549, 0.367, 4)$. To resolve the high gradients, the quadrilateral element heights are bunched near the wall, $\Delta y|_{y=\pm h}$, and expanded in the channel center, $\Delta y|_{y=0}$. The basis type employed here consists of the modified Jacobi polynomials, known as the *modified* basis [?]. Table A.1 describes the number of Fourier expansions, N_z , and temporal resolution of 52 numerical experiments at $Re = 0, 0.1, 1, 10, 100, 500, 750, 1000, 1050, 2000$, and $Ra = 0, 2000, 3000, 5000, 8000, 10000$ with $Pr = 1$ and a large aspect ratio, $\Gamma = 4\pi$. The initial conditions of all numerical experiments were sampled from a statistically stationary solution based on the time history of the Nusselt number and shear. The laminar solution obtained for $Ra = 0$, $Re \leq 1000$ has been omitted in table A.1.

Ra	Re	N_z	dt	T	$\frac{d}{\kappa}$
0	1050	64	0.1	8000	-
0	2000	128	0.02	3000	-
2000	0	64	0.05	50	25
2000	0.1	64	0.005	5	25
2000	1	64	0.01	50	25
2000	10	64	0.05	50	2.5
2000	100	64	0.1	50	0.25
2000	500	64	0.1	50	0.05
2000	750	64	0.1	50	0.033
2000	1000	64	0.1	50	0.025
2000	1050	64	0.1	8000	3.81
2000	2000	128	0.02	2800	0.75
3000	0	64	0.05	3000	1500
3000	0.1	64	0.005	300	1500
3000	1	64	0.05	100	50
3000	10	64	0.05	50	2.5
3000	100	64	0.1	10000	50
3000	500	64	0.1	50	0.05
3000	750	64	0.1	50	0.033
3000	1000	64	0.1	50	0.025
3000	1050	64	0.1	8000	3.81
3000	2000	128	0.02	2800	0.75
5000	0	64	0.005	1200	600
5000	0.1	64	0.001	800	4000
5000	1	64	0.01	2500	1250
5000	10	64	0.05	500	25
5000	100	64	0.1	1000	5
5000	500	64	0.05	8000	8
5000	750	64	0.05	8000	5.33
5000	1000	64	0.02	8000	4
5000	1050	64	0.02	8000	3.81
5000	2000	128	0.02	2800	0.75
8000	0	64	0.0025	600	300
8000	0.1	64	0.0005	600	3000
8000	1	64	0.005	600	300
8000	10	64	0.05	500	25
8000	100	64	0.1	5000	25
8000	500	64	0.05	10000	10
8000	750	64	0.05	8000	5.33
8000	1000	64	0.02	8000	4
8000	1050	64	0.02	8000	3.81
8000	2000	128	0.02	2800	0.75
10000	0	64	0.0025	1000	500
10000	0.1	64	0.00025	800	4000
10000	1	64	0.0025	600	300
10000	10	64	0.05	12000	600
10000	100	64	0.1	8000	40
10000	500	64	0.05	8000	8
10000	750	64	0.05	8000	5.33
10000	1000	64	0.02	8000	4
10000	1050	64	0.02	8000	3.81
10000	2000	128	0.02	2800	0.75

Table A.1: The summary of the spatial and temporal resolution for a given Re , Ra . N_z denotes the number of Fourier expansions in the z -direction. $dt, T, d/\kappa$ denotes the timestep, final time and the final time scaled by the thermal timescale.

A.5 First- and second-order statistics of the buoyancy- and shear-driven regime

A.5.1 Buoyancy-driven regime

We present the first- and second-order statistics of the buoyancy-dominated regime (shaded in red), consisting of the (1) SDC & ISRs, and (2) ISRs states in figure A.1, illustrating its temporal and plane-averaged streamwise velocity, $\langle w \rangle_{x,z,t}$, temperature, $\langle \theta \rangle_{x,z,t}$, fluctuating wall-normal velocity squared normalised by thermal velocity scale, $\langle \tilde{v}\tilde{v} \rangle_{x,z,t}/u_\kappa^2$, fluctuating temperature squared, $\langle \tilde{\theta}\tilde{\theta} \rangle_{x,z,t}$ and fluctuating span- and streamwise velocities squared normalised by thermal velocity scale, $\langle \tilde{u}\tilde{u} + \tilde{w}\tilde{w} \rangle_{x,z,t}/u_\kappa^2$. We note that the fluctuating components are defined about a temporal-planar averaged quantity, i.e $\tilde{\mathbf{u}} = \mathbf{u} - \langle \mathbf{u} \rangle_{x,z,t}$. The mean temperature profiles (figure A.1(b)), and the fluctuating span- and streamwise velocities (figure A.1(f)) are visually similar for the same Ra , and are nearly independent of Re . However, we observe the dependence on Re at $Ra = 3000$ in the fluctuating temperature squared (figure A.1(d)), and fluctuating wall-normal velocities (figure A.1(c)), likely due to variations in convection structures, particularly in the convection roll wavenumbers. A detailed analysis of how the statistical properties vary with roll wavenumber is beyond the scope of this work. We propose that the underlying flow structure, consisting of convection rolls, describes the buoyancy-driven regime, shaded in red in figure 3.1. In this regime, the strength of the convection is primarily controlled by Ra , akin to RBC, and remains independent of Re .

A.5.2 Shear-driven regime

As Re falls within the range of $1050 \leq Re \leq 2000$, shear-driven turbulence dominates, where the impact of Ra on the first- and second-order statistics is weakly dependent on Ra in figure A.2. Figure A.2 describes the temporal and plane-averaged streamwise velocity, $\langle w \rangle_{x,z,t}$, temperature, $\langle \theta \rangle_{x,z,t}$, fluctuating streamwise velocity squared, $\langle \tilde{w}\tilde{w} \rangle_{x,z,t}$, fluctuating wall-normal velocity squared, $\langle \tilde{v}\tilde{v} \rangle_{x,z,t}$, fluctuating spanwise velocities squared, $\langle \tilde{u}\tilde{u} \rangle_{x,z,t}$, fluctuating Reynolds stresses $\langle \tilde{v}\tilde{w} \rangle_{x,z,t}$, and fluctuating temperature squared, $\langle \tilde{\theta}\tilde{\theta} \rangle_{x,z,t}$ at $Re = 2000, 1050$ for $Ra \in [0, 10000]$. The flow structures appear as uniform, featureless turbulence [?] at $Re = 2000$, independent of Ra . The spacetime figure of near-wall ($y^+ = 15$), wall-normal and spanwise perturbation kinetic energy, $\mathcal{E}_{u'+v'}$, at $Re = 2000$, $t \in [0, 2800]$, illustrating spatially uniform featureless turbulence, visually distinguishable with $Ra \in [0, 10000]$, corroborating with their Ra -independent first- and second-order statistics in figure A.2. In other words, the dominant physical mechanism is shear-driven turbulence at $Re = 2000$, independent of Ra .

As Re approaches $Re = 1050$, the midplane temperature in figure 3.1 shows regions of spatially localised structures, indicating the presence of turbulent-laminar bands, described in figure 3.3 and 3.4 later. The mean streamwise velocity and temperature gradients at both ends of the wall, and second-order statistics, are enhanced slightly from $Ra = 0$ to $Ra = 10000$. This enhancement could be due to the coexistence of longitudinal rolls with turbulent bands at $Ra = 10000$, discussed in §??. Notably, we have also included the statistics for a subcritical case ($Ra < Ra_{\parallel}$) at $Ra = 1000$,

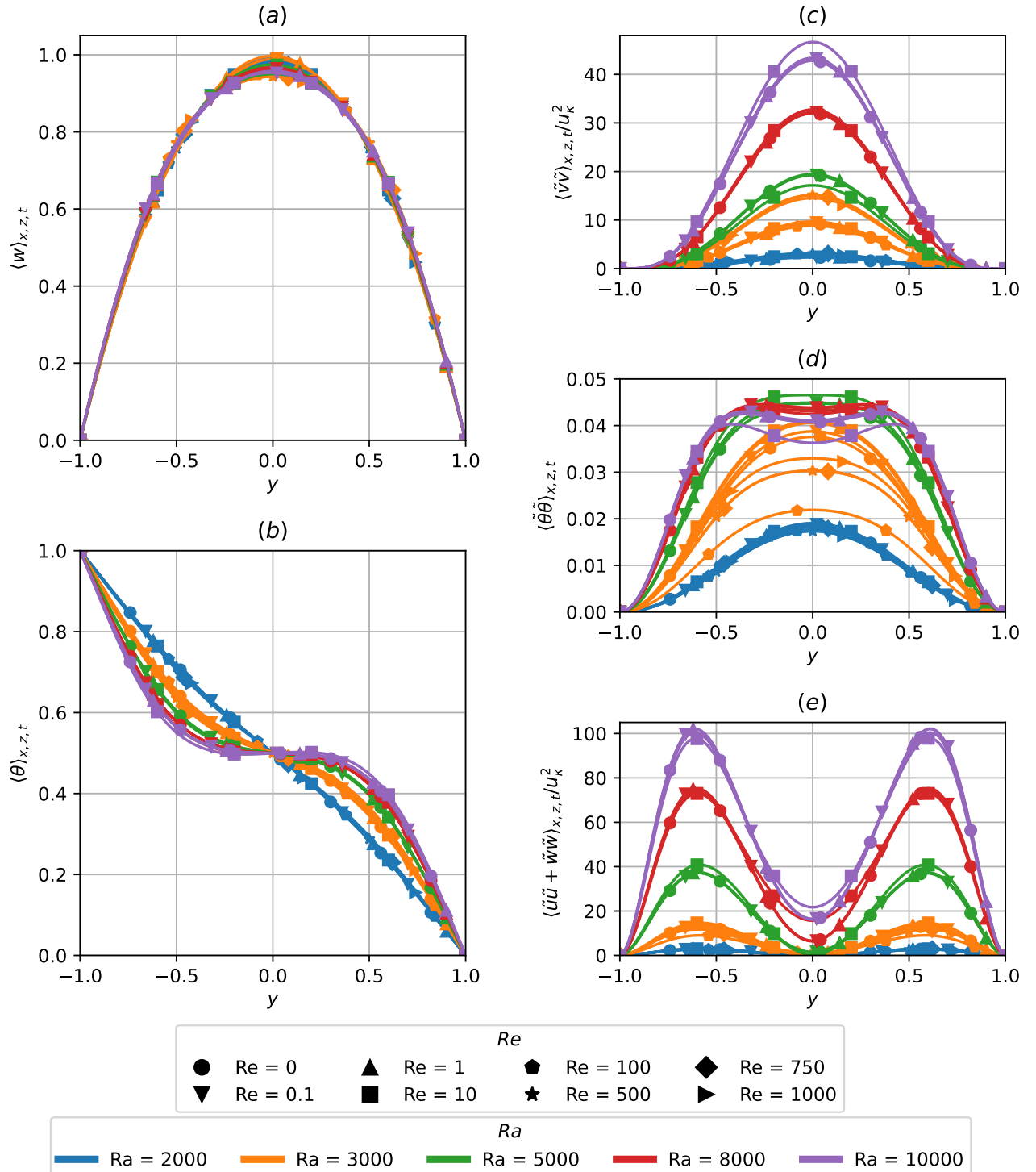


Figure A.1: The wall-normal distribution of temporal and plane- averaged (a) streamwise velocity, (b) temperature, (c) fluctuating wall-normal velocity squared normalised by thermal velocity scale, (d) fluctuating temperature squared and (e) fluctuating span- and streamwise velocities squared normalised by thermal velocity scale of buoyancy-driven regime shaded in red in figure 3.1.

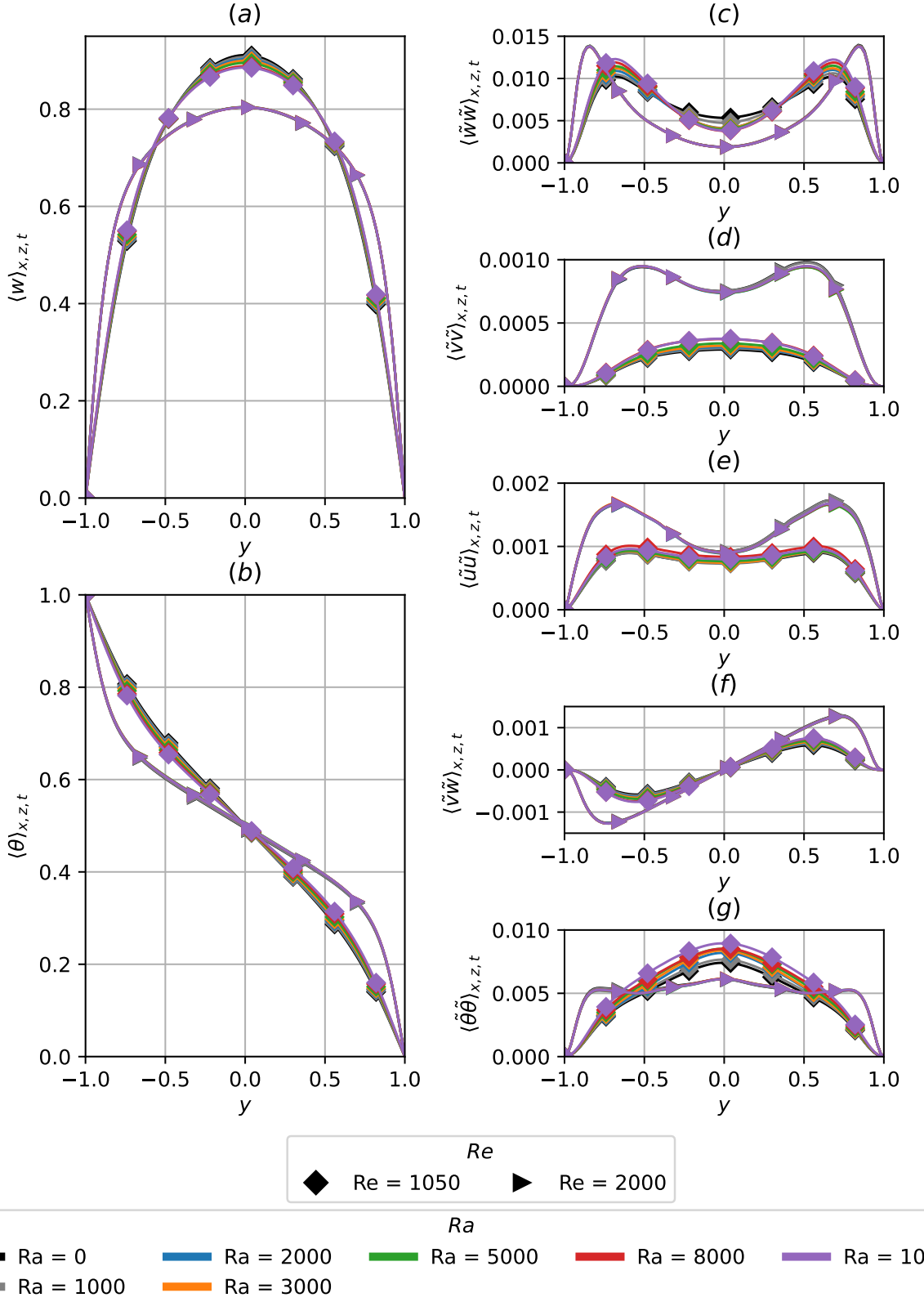


Figure A.2: The wall-normal distribution of temporal and plane- averaged (a) streamwise velocity, (b) temperature, (c) fluctuating streamwise velocity squared, (d) fluctuating wall-normal velocity squared, (e) fluctuating spanwise velocities squared, (f) fluctuating Reynolds stresses and (g) fluctuating temperature squared in the shear-driven regime shaded in blue in figure 3.1.

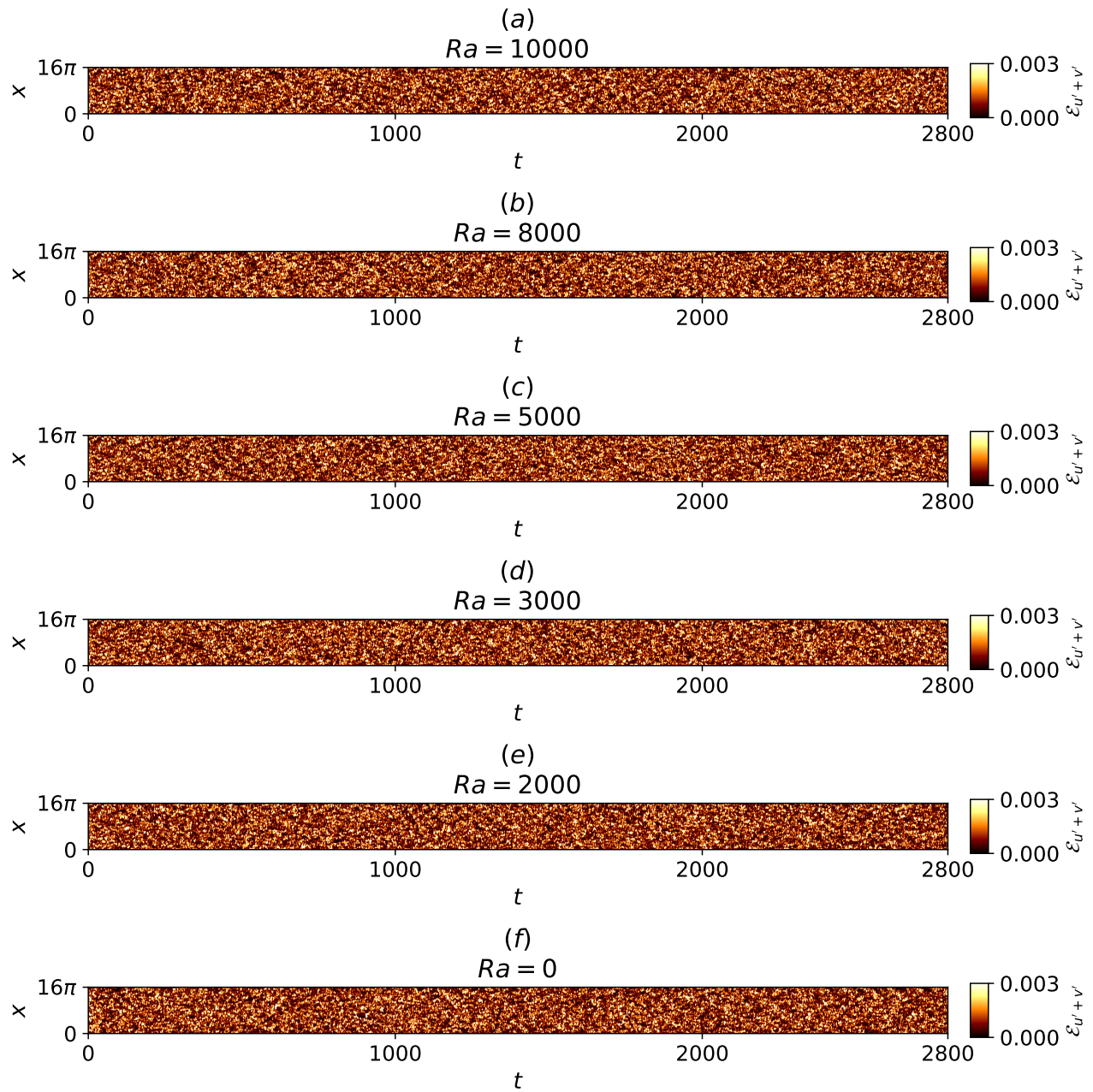


Figure A.3: Spacetime plots of near-wall, wall-normal and spanwise perturbation kinetic energy for $Re = 2000$, $t \in [0, 2800]$, $\Gamma = 4\pi$ at (a) $Ra = 10000$, (b) $Ra = 8000$, (c) $Ra = 5000$, (d) $Ra = 3000$, (e) $Ra = 2000$, (f) $Ra = 0$.

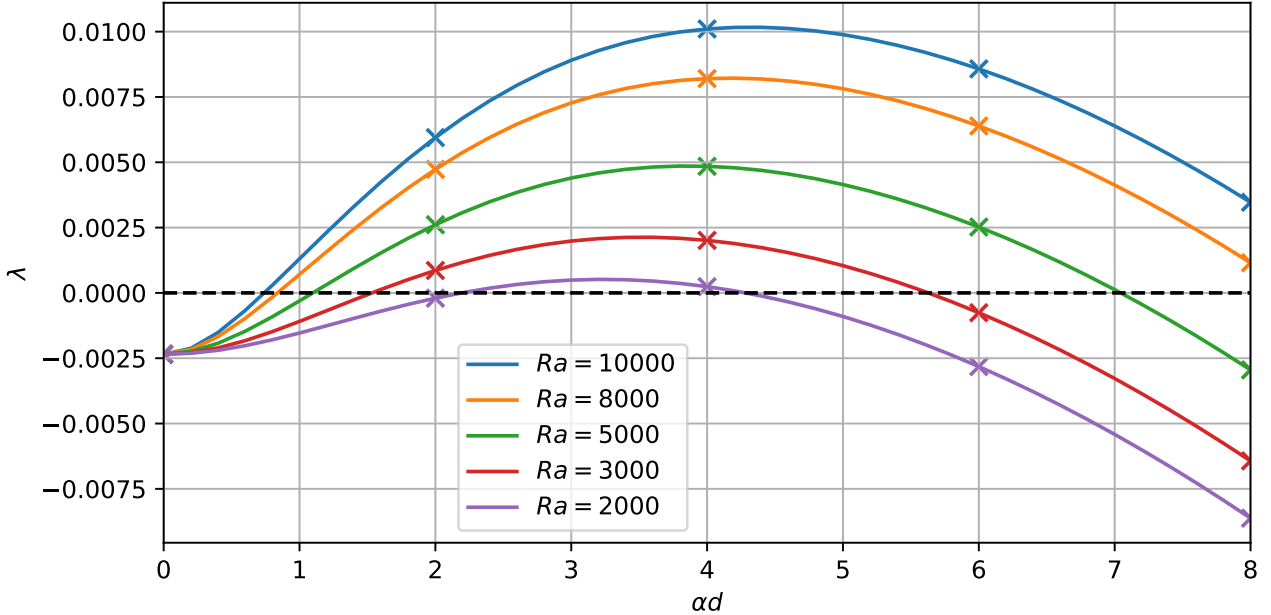


Figure A.4: Growth rates of primary instabilities at $Ra = 10000, 8000, 5000, 3000, 2000$ leading to the onset of longitudinal rolls against spanwise wavenumber of αd at $Re = 1050$.

indicating the presence of subcritical effects as the statistics are slightly enhanced from $Ra = 0$ to $Ra = 1000$, reported by ?. Nonetheless, there is a distinct change of state between $Re = 1000$ to 1050 (see figure 3.1), marked by the transition from the longitudinal/intermittent roll regime to shear-driven turbulence at $Re \geq 1050$, thus, shaded in blue in figure 3.1.

A.6 Growth rates of primary instabilities

Figure A.4 shows the eigenvalues of the primary instabilities as a function of its spanwise wavenumber αd , leading to the onset of longitudinal rolls at $Re = 1050$. The results are obtained using a Chebyshev-collocation method discretised by 51 Chebyshev polynomials [?]. The crosses denote the spanwise wavenumbers admissible within the domain $\Gamma = \pi/2$, where $\alpha d = 4$ corresponds to the dominant eigenmode.

A.7 Verification of linear stability analysis

Figure A.5 shows the eigenvalues as a function of spanwise wavenumber β of RBC at $\varepsilon = 0.7$. The results are obtained using Nektar++ and compared against a Chebyshev-collocation method discretised by 101 Chebyshev polynomials ?.

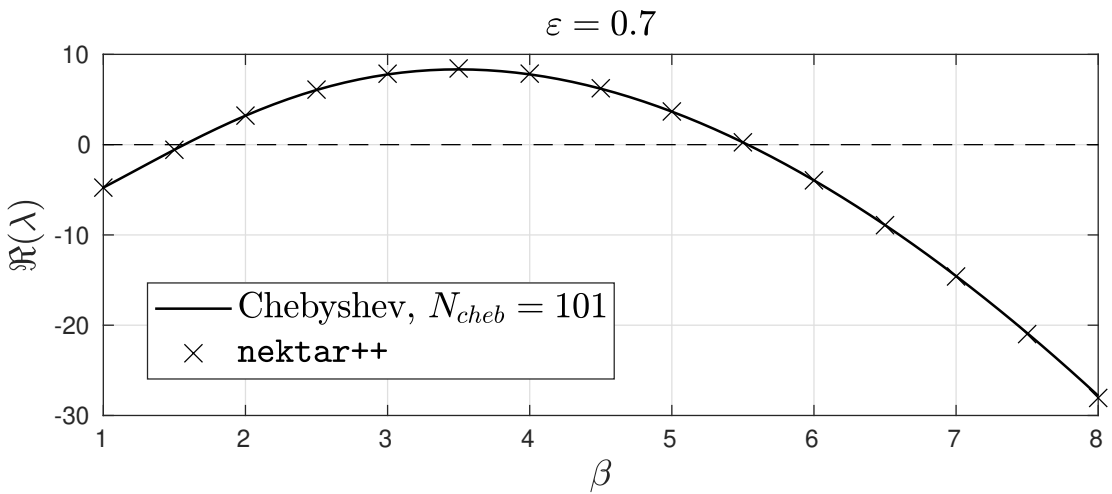


Figure A.5: Eigenvalues of primary instabilities of RBC at $\varepsilon = 0.7$ computed in Nektar++ compared against a Chebyshev-collocation method with 101 Chebyshev expansions.

A.8 Other elementary states and ISRs

Figure A.6 presents snapshots of temperature slices ($\theta(x, z)|_{d/2}$), depicting ten distinct elementary states. These states are obtained within a minimal domain $\Gamma = 2\pi$, consisting of eight stationary states (figures A.6(a-h)) and two travelling-wave states (figures A.6(i,j)). Figure A.7 features a snapshot of fourteen ideal straight rolls (ISRs), and they satisfy rotational symmetry about the y -axis and mirror symmetries about the x - and z -axes due to the horizontal isotropy of the present system. These ISRs represent stable fixed-points in the state space of figures 4.3, 4.4, 4.11, 4.19.

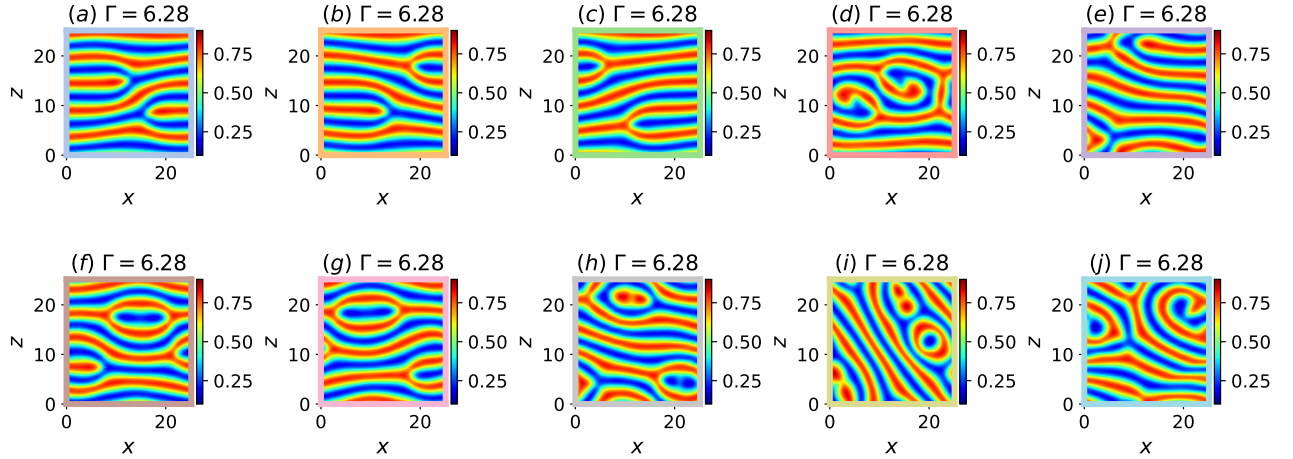


Figure A.6: Temperature snapshots, $\theta(x, z)|_{y=d/2}$, of 10 elementary states confined within a minimal domain $\Gamma = 2\pi$: (a) steady ‘forked-A’ state, (b) steady ‘forked-B’ state, (c) steady ‘forked-c’ state, (d) steady ‘twin-armed’ state, (e) steady ‘tri-rolls’ state, (f) travelling-wave ‘O-a’ state, (g) travelling-wave ‘O-b’ state, (h) steady ‘keyhole’ state, (i) relative periodic orbit ‘eye’ state, (j) relative periodic orbit ‘S’ state

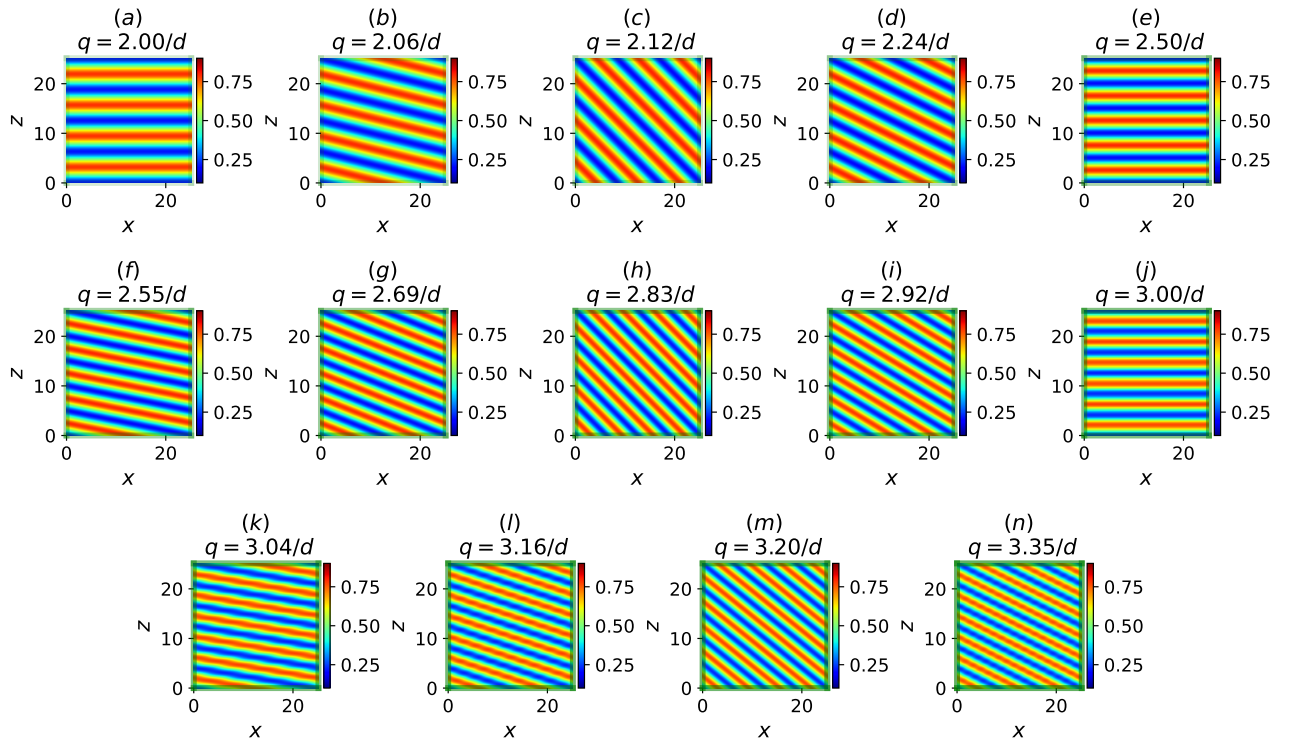


Figure A.7: Temperature snapshots, $\theta(x, z)|_{y=d/2}$, of 14 stable ideal straight rolls (ISRs) confined within a minimal domain, $\Gamma = 6.28$. Plots (a-n) are ordered in increasing wavenumbers, $q \in (2/d, 3.35/d)$.

Bibliography

Clouds streets and comma clouds near svalbard. <https://earthobservatory.nasa.gov/images/87749/clouds-streets-and-comma-clouds-near-svalbard>.

H. Affan and R. Friedrich. Spiral defect chaos in an advection-reaction-diffusion system. *Physical Review E*, 89(6):062920, June 2014. ISSN 1539-3755, 1550-2376. doi: 10.1103/PhysRevE.89.062920. URL <https://link.aps.org/doi/10.1103/PhysRevE.89.062920>.

Guenter Ahlers. Experiments on spatio-temporal chaos.

Mitsunobu Akiyama, Guang-Jyh Hwang, and KC Cheng. Experiments on the onset of longitudinal vortices in laminar forced convection between horizontal plates. 1971. ISSN 0022-1481.

Edward Anderson, Zhaojun Bai, Christian Bischof, L Susan Blackford, James Demmel, Jack Dongarra, Jeremy Du Croz, Anne Greenbaum, Sven Hammarling, and Alan McKenney. *LAPACK users' guide*. SIAM, 1999. ISBN 0-89871-447-8.

Walter Edwin Arnoldi. The principle of minimized iterations in the solution of the matrix eigenvalue problem. *Quarterly of applied mathematics*, 9(1):17–29, 1951. ISSN 0033-569X.

Kerstin Avila, David Moxey, Alberto De Lozar, Marc Avila, Dwight Barkley, and Björn Hof. The Onset of Turbulence in Pipe Flow. *Science*, 333(6039):192–196, July 2011. ISSN 0036-8075, 1095-9203. doi: 10.1126/science.1203223. URL <https://www.science.org/doi/10.1126/science.1203223>.

Marc Avila, Ashley P. Willis, and Björn Hof. On the transient nature of localized pipe flow turbulence. *Journal of Fluid Mechanics*, 646:127–136, March 2010. ISSN 0022-1120, 1469-7645. doi: 10.1017/S0022112009993296. URL https://www.cambridge.org/core/product/identifier/S0022112009993296/type/journal_article.

Marc Avila, Dwight Barkley, and Björn Hof. Transition to Turbulence in Pipe Flow. *Annual Review of Fluid Mechanics*, 55(1):575–602, January 2023. ISSN 0066-4189, 1545-4479. doi: 10.1146/annurev-fluid-120720-025957. URL <https://www.annualreviews.org/doi/10.1146/annurev-fluid-120720-025957>.

Kapil M. S. Bajaj, David S. Cannell, and Guenter Ahlers. Competition between spiral-defect chaos and rolls in Rayleigh-Bénard convection. *Physical Review E*, 55(5):R4869–R4872, May 1997. ISSN

1063-651X, 1095-3787. doi: 10.1103/PhysRevE.55.R4869. URL <https://link.aps.org/doi/10.1103/PhysRevE.55.R4869>.

D. Barkley, H. M. Blackburn, and S. J. Sherwin. Direct optimal growth analysis for timesteppers. *International Journal for Numerical Methods in Fluids*, 57(9):1435–1458, July 2008. ISSN 0271-2091, 1097-0363. doi: 10.1002/fld.1824. URL <https://onlinelibrary.wiley.com/doi/10.1002/fld.1824>.

Dwight Barkley and Laurette S. Tuckerman. Computational Study of Turbulent Laminar Patterns in Couette Flow. *Physical Review Letters*, 94(1):014502, January 2005. doi: 10.1103/PhysRevLett.94.014502. URL <https://link.aps.org/doi/10.1103/PhysRevLett.94.014502>. Publisher: American Physical Society.

Dwight Barkley and Laurette S Tuckerman. Mean flow of turbulent–laminar patterns in plane Couette flow. *Journal of Fluid Mechanics*, 576:109–137, 2007. ISSN 1469-7645. Publisher: Cambridge University Press.

Myron J. Block. Surface Tension as the Cause of Bénard Cells and Surface Deformation in a Liquid Film. *Nature*, 178(4534):650–651, September 1956. ISSN 0028-0836, 1476-4687. doi: 10.1038/178650a0. URL <https://www.nature.com/articles/178650a0>.

Eberhard Bodenschatz, David S. Cannell, John R. De Bruyn, Robert Ecke, Yu-Chou Hu, Kristina Lerman, and Guenter Ahlers. Experiments on three systems with non-variational aspects. *Physica D: Nonlinear Phenomena*, 61(1-4):77–93, December 1992. ISSN 01672789. doi: 10.1016/0167-2789(92)90150-L. URL <https://linkinghub.elsevier.com/retrieve/pii/016727899290150L>.

Eberhard Bodenschatz, Werner Pesch, and Guenter Ahlers. Recent Developments in Rayleigh-Bénard Convection. *Annual Review of Fluid Mechanics*, 32(1):709–778, January 2000. ISSN 0066-4189, 1545-4479. doi: 10.1146/annurev.fluid.32.1.709. URL <https://www.annualreviews.org/doi/10.1146/annurev.fluid.32.1.709>.

Katarzyna Borońska and Laurette S. Tuckerman. Extreme multiplicity in cylindrical Rayleigh-Bénard convection. I. Time dependence and oscillations. *Physical Review E*, 81(3):036320, March 2010a. ISSN 1539-3755, 1550-2376. doi: 10.1103/PhysRevE.81.036320. URL <https://link.aps.org/doi/10.1103/PhysRevE.81.036320>.

Katarzyna Borońska and Laurette S. Tuckerman. Extreme multiplicity in cylindrical Rayleigh-Bénard convection. II. Bifurcation diagram and symmetry classification. *Physical Review E*, 81(3):036321, March 2010b. ISSN 1539-3755, 1550-2376. doi: 10.1103/PhysRevE.81.036321. URL <https://link.aps.org/doi/10.1103/PhysRevE.81.036321>.

N. Boullié, V. Dallas, and P. E. Farrell. Bifurcation analysis of two-dimensional Rayleigh-Bénard convection using deflation. *Physical Review E*, 105(5):055106, May 2022. ISSN 2470-0045,

2470-0053. doi: 10.1103/PhysRevE.105.055106. URL <https://link.aps.org/doi/10.1103/PhysRevE.105.055106>.

Luca Brandt. The lift-up effect: The linear mechanism behind transition and turbulence in shear flows. *European Journal of Mechanics - B/Fluids*, 47:80–96, September 2014. ISSN 09977546. doi: 10.1016/j.euromechflu.2014.03.005. URL <https://linkinghub.elsevier.com/retrieve/pii/S0997754614000405>.

F. H. Busse. The oscillatory instability of convection rolls in a low Prandtl number fluid. *Journal of Fluid Mechanics*, 52(1):97–112, March 1972. ISSN 0022-1120, 1469-7645. doi: 10.1017/S0022112072002988. URL https://www.cambridge.org/core/product/identifier/S0022112072002988/type/journal_article.

F H Busse. Non-linear properties of thermal convection. *Reports on Progress in Physics*, 41(12):1929–1967, December 1978. ISSN 0034-4885, 1361-6633. doi: 10.1088/0034-4885/41/12/003. URL <https://iopscience.iop.org/article/10.1088/0034-4885/41/12/003>.

F. H. Busse and J. A. Whitehead. Instabilities of convection rolls in a high Prandtl number fluid. *Journal of Fluid Mechanics*, 47(2):305–320, May 1971. ISSN 0022-1120, 1469-7645. doi: 10.1017/S0022112071001071. URL https://www.cambridge.org/core/product/identifier/S0022112071001071/type/journal_article.

Kathryn M. Butler and Brian F. Farrell. Three-dimensional optimal perturbations in viscous shear flow. *Physics of Fluids A: Fluid Dynamics*, 4(8):1637–1650, August 1992. ISSN 0899-8213. doi: 10.1063/1.858386. URL <https://pubs.aip.org/pof/article/4/8/1637/402702/Three-dimensional-optimal-perturbations-in-viscous>.

Henri Bénard. Les tourbillons cellulaires dans une nappe liquide. - Méthodes optiques d’observation et d’enregistrement. *Journal de Physique Théorique et Appliquée*, 10(1):254–266, 1901. ISSN 0368-3893. doi: 10.1051/jphystab:0190100100025400. URL <http://www.edpsciences.org/10.1051/jphystab:0190100100025400>.

Reha V. Cakmur, David A. Egolf, Brendan B. Plapp, and Eberhard Bodenschatz. Bistability and Competition of Spatiotemporal Chaotic and Fixed Point Attractors in Rayleigh-Bénard Convection. *Physical Review Letters*, 79(10):1853–1856, September 1997a. ISSN 0031-9007, 1079-7114. doi: 10.1103/PhysRevLett.79.1853. URL <https://link.aps.org/doi/10.1103/PhysRevLett.79.1853>.

Reha V. Cakmur, David A. Egolf, Brendan B. Plapp, and Eberhard Bodenschatz. Transition from Spatiotemporal Chaos to Ideal Straight Rolls in Rayleigh-Benard Convection, February 1997b. URL <http://arxiv.org/abs/patt-sol/9702003>. arXiv:patt-sol/9702003.

Philippe Carrière and Peter A. Monkewitz. Convective versus absolute instability in mixed Rayleigh–Bénard–Poiseuille convection. *Journal of Fluid Mechanics*, 384:243–262, April 1999. ISSN 0022-1120, 1469-7645. doi: 10.1017/

S0022112098004145. URL https://www.cambridge.org/core/product/identifier/S0022112098004145/type/journal_article.

K.-H. Chiam, M. R. Paul, M. C. Cross, and H. S. Greenside. Mean flow and spiral defect chaos in Rayleigh-Bénard convection. *Physical Review E*, 67(5):056206, May 2003. ISSN 1063-651X, 1095-3787. doi: 10.1103/PhysRevE.67.056206. URL <https://link.aps.org/doi/10.1103/PhysRevE.67.056206>.

Alexandre Joel Chorin. A numerical method for solving incompressible viscous flow problems. *Journal of Computational Physics*, 2(1):12–26, August 1967. ISSN 00219991. doi: 10.1016/0021-9991(67)90037-X. URL <https://linkinghub.elsevier.com/retrieve/pii/002199916790037X>.

Douglas C. Chu and George Em Karniadakis. A direct numerical simulation of laminar and turbulent flow over riblet-mounted surfaces. *Journal of Fluid Mechanics*, 250:1–42, May 1993. ISSN 0022-1120, 1469-7645. doi: 10.1017/S0022112093001363. URL https://www.cambridge.org/core/product/identifier/S0022112093001363/type/journal_article.

R. M. Clever and F. H. Busse. Instabilities of longitudinal rolls in the presence of Poiseuille flow. *Journal of Fluid Mechanics*, 229(-1):517, August 1991. ISSN 0022-1120, 1469-7645. doi: 10.1017/S0022112091003142. URL http://www.journals.cambridge.org/abstract_S0022112091003142.

A. Cloot and G. Lebon. A nonlinear stability analysis of the Bénard–Marangoni problem. *Journal of Fluid Mechanics*, 145(-1):447, August 1984. ISSN 0022-1120, 1469-7645. doi: 10.1017/S0022112084003013. URL http://www.journals.cambridge.org/abstract_S0022112084003013.

Vincent Croquette. Convective pattern dynamics at low Prandtl number: Part I. *Contemporary Physics*, 30(2):113–133, March 1989a. ISSN 0010-7514, 1366-5812. doi: 10.1080/00107518908225511. URL <http://www.tandfonline.com/doi/abs/10.1080/00107518908225511>.

Vincent Croquette. Convective pattern dynamics at low Prandtl number: Part II. *Contemporary Physics*, 30(3):153–171, May 1989b. ISSN 0010-7514, 1366-5812. doi: 10.1080/00107518908222594. URL <http://www.tandfonline.com/doi/abs/10.1080/00107518908222594>.

R. B. Dean. Reynolds Number Dependence of Skin Friction and Other Bulk Flow Variables in Two-Dimensional Rectangular Duct Flow. *Journal of Fluids Engineering*, 100(2):215–223, June 1978. ISSN 0098-2202, 1528-901X. doi: 10.1115/1.3448633. URL <https://asmedigitalcollection.asme.org/fluidsengineering/article/100/2/215/409704/Reynolds-Number-Dependence-of-Skin-Friction-and>.

W. Decker, W. Pesch, and A. Weber. Spiral defect chaos in Rayleigh-Bénard convection. *Physical Review Letters*, 73(5):648–651, August 1994. ISSN 0031-9007. doi: 10.1103/PhysRevLett.73.648. URL <https://link.aps.org/doi/10.1103/PhysRevLett.73.648>.

Lifang Dong, Fucheng Liu, Shuhua Liu, Yafeng He, and Weili Fan. Observation of spiral pattern and spiral defect chaos in dielectric barrier discharge in argon/air at atmospheric pressure. *Physical Review E*, 72(4):046215, October 2005. ISSN 1539-3755, 1550-2376. doi: 10.1103/PhysRevE.72.046215. URL <https://link.aps.org/doi/10.1103/PhysRevE.72.046215>.

Y. Duguet, P. Schlatter, and D. S. Henningson. Formation of turbulent patterns near the onset of transition in plane Couette flow. *Journal of Fluid Mechanics*, 650:119–129, May 2010. ISSN 0022-1120, 1469-7645. doi: 10.1017/S0022112010000297. URL https://www.cambridge.org/core/product/identifier/S0022112010000297/type/journal_article.

Robert E. Ecke, Yuchou Hu, Ronnie Mainieri, and Guenter Ahlers. Excitation of Spirals and Chiral Symmetry Breaking in Rayleigh-Bénard Convection. *Science*, 269(5231):1704–1707, September 1995. ISSN 0036-8075, 1095-9203. doi: 10.1126/science.269.5231.1704. URL <https://www.science.org/doi/10.1126/science.269.5231.1704>.

Wiktor Eckhaus. *Studies in Non-Linear Stability Theory*, volume 6 of *Springer Tracts in Natural Philosophy*. Springer Berlin Heidelberg, Berlin, Heidelberg, 1965. ISBN 978-3-642-88319-4 978-3-642-88317-0. doi: 10.1007/978-3-642-88317-0. URL <http://link.springer.com/10.1007/978-3-642-88317-0>.

David A. Egolf, Ilarion V. Melnikov, and Eberhard Bodenschatz. Importance of Local Pattern Properties in Spiral Defect Chaos. *Physical Review Letters*, 80(15):3228–3231, April 1998. ISSN 0031-9007, 1079-7114. doi: 10.1103/PhysRevLett.80.3228. URL <https://link.aps.org/doi/10.1103/PhysRevLett.80.3228>.

David A. Egolf, Ilarion V. Melnikov, Werner Pesch, and Robert E. Ecke. Mechanisms of extensive spatiotemporal chaos in Rayleigh–Bénard convection. *Nature*, 404(6779):733–736, April 2000. ISSN 0028-0836, 1476-4687. doi: 10.1038/35008013. URL <https://www.nature.com/articles/35008013>.

T. Ellingsen and E. Palm. Stability of linear flow. *The Physics of Fluids*, 18(4):487–488, April 1975. ISSN 0031-9171. doi: 10.1063/1.861156. URL <https://pubs.aip.org/pfl/article/18/4/487/459138/Stability-of-linear-flow>.

Greg Evans and Ralph Greif. Unsteady three-dimensional mixed convection in a heated horizontal channel with applications to chemical vapor deposition. *International Journal of Heat and Mass Transfer*, 34(8):2039–2051, August 1991. ISSN 00179310. doi: 10.1016/0017-9310(91)90215-Z. URL <https://linkinghub.elsevier.com/retrieve/pii/001793109190215Z>.

Brian F. Farrell. Optimal excitation of perturbations in viscous shear flow. *The Physics of Fluids*, 31(8):2093–2102, August 1988. ISSN 0031-9171. doi:

10.1063/1.866609. URL <https://pubs.aip.org/pfl/article/31/8/2093/966463/Optimal-excitation-of-perturbations-in-viscous>.

Keisuke Fukui, Masamoto Nakajima, and Hiromasa Ueda. The longitudinal vortex and its effects on the transport processes in combined free and forced laminar convection between horizontal and inclined parallel plates. *International Journal of Heat and Mass Transfer*, 26(1):109–120, January 1983. ISSN 00179310. doi: 10.1016/S0017-9310(83)80013-1. URL <https://linkinghub.elsevier.com/retrieve/pii/S0017931083800131>.

K. S. Gage and W. H. Reid. The stability of thermally stratified plane Poiseuille flow. *Journal of Fluid Mechanics*, 33(1):21–32, July 1968. ISSN 0022-1120, 1469-7645. doi: 10.1017/S0022112068002326. URL https://www.cambridge.org/core/product/identifier/S0022112068002326/type/journal_article.

J. F. Gibson, J. Halcrow, and P. Cvitanović. Visualizing the geometry of state space in plane Couette flow. *Journal of Fluid Mechanics*, 611:107–130, September 2008. ISSN 0022-1120, 1469-7645. doi: 10.1017/S002211200800267X. URL https://www.cambridge.org/core/product/identifier/S002211200800267X/type/journal_article.

J. F. Gibson, J. Halcrow, and P. Cvitanović. Equilibrium and travelling-wave solutions of plane Couette flow. *Journal of Fluid Mechanics*, 638:243–266, November 2009. ISSN 0022-1120, 1469-7645. doi: 10.1017/S0022112009990863. URL https://www.cambridge.org/core/product/identifier/S0022112009990863/type/journal_article.

Gene H Golub and Charles F Van Loan. *Matrix computations*. JHU press, 2013. ISBN 1-4214-0859-7.

Sébastien Gomé, Laurette S. Tuckerman, and Dwight Barkley. Statistical transition to turbulence in plane channel flow. *Physical Review Fluids*, 5(8):083905, August 2020. ISSN 2469-990X. doi: 10.1103/PhysRevFluids.5.083905. URL <https://link.aps.org/doi/10.1103/PhysRevFluids.5.083905>.

Michael D. Graham and Daniel Floryan. Exact Coherent States and the Nonlinear Dynamics of Wall-Bounded Turbulent Flows. *Annual Review of Fluid Mechanics*, 53(1):227–253, January 2021. ISSN 0066-4189, 1545-4479. doi: 10.1146/annurev-fluid-051820-020223. URL <https://www.annualreviews.org/doi/10.1146/annurev-fluid-051820-020223>.

J. Halcrow, J. F. Gibson, P. Cvitanović, and D. Viswanath. Heteroclinic connections in plane Couette flow. *Journal of Fluid Mechanics*, 621:365–376, February 2009. ISSN 0022-1120, 1469-7645. doi: 10.1017/S0022112008005065. URL https://www.cambridge.org/core/product/identifier/S0022112008005065/type/journal_article.

James M. Hamilton, John Kim, and Fabian Waleffe. Regeneration mechanisms of near-wall turbulence structures. *Journal of Fluid Mechanics*, 287:317–348, March 1995. ISSN 0022-1120, 1469-7645. doi: 10.1017/S0022112095000978. URL https://www.cambridge.org/core/product/identifier/S0022112095000978/type/journal_article.

Ronald D. Henderson and Dwight Barkley. Secondary instability in the wake of a circular cylinder. *Physics of Fluids*, 8(6):1683–1685, June 1996. ISSN 1070-6631, 1089-7666. doi: 10.1063/1.868939. URL <https://pubs.aip.org/pof/article/8/6/1683/260183/Secondary-instability-in-the-wake-of-a-circular>.

Thorwald Herbert. PARABOLIZED STABILITY EQUATIONS. *Annual Review of Fluid Mechanics*, 29(1):245–283, January 1997. ISSN 0066-4189, 1545-4479. doi: 10.1146/annurev.fluid.29.1.245. URL <https://www.annualreviews.org/doi/10.1146/annurev.fluid.29.1.245>.

C.Q Hoard, C.R Robertson, and A Acrivos. Experiments on the cellular structure in bénard convection. *International Journal of Heat and Mass Transfer*, 13(5):849–856, May 1970. ISSN 00179310. doi: 10.1016/0017-9310(70)90130-4. URL <https://linkinghub.elsevier.com/retrieve/pii/0017931070901304>.

B. Hof, P. G. J. Lucas, and T. Mullin. Flow state multiplicity in convection. *Physics of Fluids*, 11(10):2815–2817, October 1999. ISSN 1070-6631, 1089-7666. doi: 10.1063/1.870178. URL <https://pubs.aip.org/pof/article/11/10/2815/254396/Flow-state-multiplicity-in-convection>.

M. Z. Hossain and J. M. Floryan. Drag reduction in a thermally modulated channel. *Journal of Fluid Mechanics*, 791:122–153, March 2016. ISSN 0022-1120, 1469-7645. doi: 10.1017/jfm.2016.42. URL https://www.cambridge.org/core/product/identifier/S0022112016000422/type/journal_article.

M. Z. Hossain and J. M. Floryan. On the role of surface grooves in the reduction of pressure losses in heated channels. *Physics of Fluids*, 32(8):083610, August 2020. ISSN 1070-6631, 1089-7666. doi: 10.1063/5.0018416. URL <https://pubs.aip.org/pof/article/32/8/083610/1060903/On-the-role-of-surface-grooves-in-the-reduction-of>.

M. Z. Hossain, D. Floryan, and J. M. Floryan. Drag reduction due to spatial thermal modulations. *Journal of Fluid Mechanics*, 713:398–419, December 2012. ISSN 0022-1120, 1469-7645. doi: 10.1017/jfm.2012.465. URL https://www.cambridge.org/core/product/identifier/S002211201200465X/type/journal_article.

Yuchou Hu, Robert Ecke, and Guenter Ahlers. Convection near threshold for Prandtl numbers near 1. *Physical Review E*, 48(6):4399–4413, December 1993. ISSN 1063-651X, 1095-3787. doi: 10.1103/PhysRevE.48.4399. URL <https://link.aps.org/doi/10.1103/PhysRevE.48.4399>.

Yuchou Hu, Robert Ecke, and Guenter Ahlers. Convection for Prandtl numbers near 1: Dynamics of textured patterns. *Physical Review E*, 51(4):3263–3279, April 1995. ISSN 1063-651X, 1095-3787. doi: 10.1103/PhysRevE.51.3263. URL <https://link.aps.org/doi/10.1103/PhysRevE.51.3263>.

Yuchou Hu, Robert E. Ecke, and Guenter Ahlers. Convection under rotation for Prandtl numbers near 1: Linear stability, wave-number selection, and pattern dynamics. *Physical Review E*, 55(6):

6928–6949, June 1997. ISSN 1063-651X, 1095-3787. doi: 10.1103/PhysRevE.55.6928. URL <https://link.aps.org/doi/10.1103/PhysRevE.55.6928>.

O. Iida and Y. Nagano. The Relaminarization Mechanisms of Turbulent Channel Flow at Low Reynolds Numbers. *Flow, Turbulence and Combustion*, 60(2):193–213, 1998. ISSN 13866184. doi: 10.1023/A:1009999606355. URL <http://link.springer.com/10.1023/A:1009999606355>.

Harold Jeffreys. Some cases of instability in fluid motion. *Proceedings of the Royal Society of London. Series A, Containing Papers of a Mathematical and Physical Character*, 118(779):195–208, March 1928. ISSN 0950-1207, 2053-9150. doi: 10.1098/rspa.1928.0045. URL <https://royalsocietypublishing.org/doi/10.1098/rspa.1928.0045>.

Klavs F. Jensen, Erik O. Einset, and Dimitrios I. Fotiadis. Flow Phenomena in Chemical Vapor Deposition of Thin Films. *Annual Review of Fluid Mechanics*, 23(1):197–232, January 1991. ISSN 0066-4189, 1545-4479. doi: 10.1146/annurev.fl.23.010191.001213. URL <https://www.annualreviews.org/doi/10.1146/annurev.fl.23.010191.001213>.

J. John Soundar Jerome, Jean-Marc Chomaz, and Patrick Huerre. Transient growth in Rayleigh-Bénard-Poiseuille/Couette convection. *Physics of Fluids*, 24(4):044103, April 2012. ISSN 1070-6631, 1089-7666. doi: 10.1063/1.4704642. URL <https://pubs.aip.org/pof/article/24/4/044103/257562/Transient-growth-in-Rayleigh-Benard-Poiseuille>.

A. Karimi, Zhi-Feng Huang, and M. R. Paul. Exploring spiral defect chaos in generalized Swift-Hohenberg models with mean flow. *Physical Review E*, 84(4):046215, October 2011. ISSN 1539-3755, 1550-2376. doi: 10.1103/PhysRevE.84.046215. URL <https://link.aps.org/doi/10.1103/PhysRevE.84.046215>.

George Karniadakis and Spencer J Sherwin. *Spectral/hp element methods for computational fluid dynamics*. Oxford University Press, 2005. ISBN 0-19-852869-8.

George Em Karniadakis, Moshe Israeli, and Steven A Orszag. High-order splitting methods for the incompressible Navier-Stokes equations. *Journal of Computational Physics*, 97(2):414–443, December 1991. ISSN 00219991. doi: 10.1016/0021-9991(91)90007-8. URL <https://linkinghub.elsevier.com/retrieve/pii/0021999191900078>.

Genta Kawahara and Shigeo Kida. Periodic motion embedded in plane Couette turbulence: regeneration cycle and burst. *Journal of Fluid Mechanics*, 449:291–300, December 2001. ISSN 0022-1120, 1469-7645. doi: 10.1017/S0022112001006243. URL https://www.cambridge.org/core/product/identifier/S0022112001006243/type/journal_article.

R.E. Kelly. The Onset and Development of Thermal Convection in Fully Developed Shear Flows. In *Advances in Applied Mechanics*, volume 31, pages 35–112. Elsevier, 1994. ISBN 978-0-12-002031-7. doi: 10.1016/S0065-2156(08)70255-2. URL <https://linkinghub.elsevier.com/retrieve/pii/S0065215608702552>.

K.J. Kennedy and A. Zebib. Combined free and forced convection between horizontal parallel planes: some case studies. *International Journal of Heat and Mass Transfer*, 26(3):471–474, March 1983. ISSN 00179310. doi: 10.1016/0017-9310(83)90052-2. URL <https://linkinghub.elsevier.com/retrieve/pii/0017931083900522>.

T. Khapko, T. Kreilos, P. Schlatter, Y. Duguet, B. Eckhardt, and D. S. Henningson. Edge states as mediators of bypass transition in boundary-layer flows. *Journal of Fluid Mechanics*, 801:R2, August 2016. ISSN 0022-1120, 1469-7645. doi: 10.1017/jfm.2016.434. URL https://www.cambridge.org/core/product/identifier/S0022112016004341/type/journal_article.

John Kim, Parviz Moin, and Robert Moser. Turbulence statistics in fully developed channel flow at low Reynolds number. *Journal of Fluid Mechanics*, 177:133–166, April 1987. ISSN 0022-1120, 1469-7645. doi: 10.1017/S0022112087000892. URL https://www.cambridge.org/core/product/identifier/S0022112087000892/type/journal_article.

E.L. Koschmieder and S.G. Pallas. Heat transfer through a shallow, horizontal convecting fluid layer. *International Journal of Heat and Mass Transfer*, 17(9):991–1002, September 1974. ISSN 00179310. doi: 10.1016/0017-9310(74)90181-1. URL <https://linkinghub.elsevier.com/retrieve/pii/0017931074901811>.

P. D. Lax and A. N. Milgram. IX. Parabolic Equations. In *Contributions to the Theory of Partial Differential Equations. (AM-33)*, pages 167–190. Princeton University Press, December 1955. ISBN 978-1-4008-8218-2. doi: 10.1515/9781400882182-010. URL <https://www.degruyter.com/document/doi/10.1515/9781400882182-010/html>.

P. Le Gal, A. Pocheau, and V. Croquette. Square versus Roll Pattern at Convective Threshold. *Physical Review Letters*, 54(23):2501–2504, June 1985. ISSN 0031-9007. doi: 10.1103/PhysRevLett.54.2501. URL <https://link.aps.org/doi/10.1103/PhysRevLett.54.2501>.

Richard B Lehoucq, Danny C Sorensen, and Chao Yang. *ARPACK users' guide: solution of large-scale eigenvalue problems with implicitly restarted Arnoldi methods*. SIAM, 1998. ISBN 0-89871-407-9.

Jun Liu and Guenter Ahlers. Spiral-Defect Chaos in Rayleigh-Bénard Convection with Small Prandtl Numbers. *PHYSICAL REVIEW LETTERS*, 77(15), 1996.

Mary Lowe and J. P. Gollub. Pattern Selection near the Onset of Convection: The Eckhaus Instability. *Physical Review Letters*, 55(23):2575–2578, December 1985. ISSN 0031-9007. doi: 10.1103/PhysRevLett.55.2575. URL <https://link.aps.org/doi/10.1103/PhysRevLett.55.2575>.

J-M Luijkx, Jean Karl Platten, and J Cl Legros. On the existence of thermoconvective rolls, transverse to a superimposed mean Poiseuille flow. *International Journal of Heat and Mass Transfer*, 24(7):1287–1291, 1981. ISSN 0017-9310. Publisher: Elsevier.

Dong-Jun Ma, De-Jun Sun, and Xie-Yuan Yin. Multiplicity of steady states in cylindrical Rayleigh-Bénard convection. *Physical Review E*, 74(3):037302, September 2006. ISSN 1539-3755,

1550-2376. doi: 10.1103/PhysRevE.74.037302. URL <https://link.aps.org/doi/10.1103/PhysRevE.74.037302>.

Paul Manneville. Rayleigh-Bénard Convection: Thirty Years of Experimental, Theoretical, and Modeling Work. In Gerhard Höhler, Johann H. Kühn, Thomas Müller, Joachim Trümper, Andrei Ruckenstein, Peter Wölfle, Frank Steiner, Innocent Mutabazi, José Eduardo Wesfreid, and Etienne Guyon, editors, *Dynamics of Spatio-Temporal Cellular Structures*, volume 207, pages 41–65. Springer New York, New York, NY, 2006. ISBN 978-0-387-40098-3 978-0-387-25111-0. doi: 10.1007/978-0-387-25111-0_3. URL http://link.springer.com/10.1007/978-0-387-25111-0_3. Series Title: Springer Tracts in Modern Physics.

Á. Meseguer and L.N. Trefethen. Linearized pipe flow to Reynolds number 107. *Journal of Computational Physics*, 186(1):178–197, March 2003. ISSN 00219991. doi: 10.1016/S0021-9991(03)00029-9. URL <https://linkinghub.elsevier.com/retrieve/pii/S0021999103000299>.

Stephen W. Morris, Eberhard Bodenschatz, David S. Cannell, and Guenter Ahlers. Spiral defect chaos in large aspect ratio Rayleigh-Bénard convection. *Physical Review Letters*, 71(13):2026–2029, September 1993. ISSN 0031-9007. doi: 10.1103/PhysRevLett.71.2026. URL <https://link.aps.org/doi/10.1103/PhysRevLett.71.2026>.

Stephen W. Morris, Eberhard Bodenschatz, David S. Cannell, and Guenter Ahlers. The spatio-temporal structure of spiral-defect chaos. *Physica D: Nonlinear Phenomena*, 97(1-3):164–179, October 1996. ISSN 01672789. doi: 10.1016/0167-2789(96)00096-6. URL <https://linkinghub.elsevier.com/retrieve/pii/0167278996000966>.

H. W. Müller, M. Lücke, and M. Kamps. Transversal convection patterns in horizontal shear flow. *Physical Review A*, 45(6):3714–3726, March 1992. ISSN 1050-2947, 1094-1622. doi: 10.1103/PhysRevA.45.3714. URL <https://link.aps.org/doi/10.1103/PhysRevA.45.3714>.

M. Nagata. Three-dimensional finite-amplitude solutions in plane Couette flow: bifurcation from infinity. *Journal of Fluid Mechanics*, 217:519–527, August 1990. ISSN 0022-1120, 1469-7645. doi: 10.1017/S0022112090000829. URL https://www.cambridge.org/core/product/identifier/S0022112090000829/type/journal_article.

M. Nagata. Three-dimensional traveling-wave solutions in plane Couette flow. *Physical Review E*, 55(2):2023–2025, February 1997. ISSN 1063-651X, 1095-3787. doi: 10.1103/PhysRevE.55.2023. URL <https://link.aps.org/doi/10.1103/PhysRevE.55.2023>.

X. Nicolas, A. Mojtabi, and J. K. Platten. Two-dimensional numerical analysis of the Poiseuille–Bénard flow in a rectangular channel heated from below. *Physics of Fluids*, 9(2):337–348, February 1997. ISSN 1070-6631, 1089-7666. doi: 10.1063/1.869235. URL <https://pubs.aip.org/pof/article/9/2/337/259822/Two-dimensional-numerical-analysis-of-the>.

X. Nicolas, J.-M. Luijckx, and J.-K. Platten. Linear stability of mixed convection flows in horizontal rectangular channels of finite transversal extension heated from below. *International Journal of Heat*

and Mass Transfer, 43(4):589–610, February 2000. ISSN 00179310. doi: 10.1016/S0017-9310(99)00099-X. URL <https://linkinghub.elsevier.com/retrieve/pii/S001793109900099X>.

Xavier Nicolas. Revue bibliographique sur les écoulements de Poiseuille-Rayleigh-Bénard : écoulements de convection mixte en conduites rectangulaires horizontales chauffées par le bas. *International Journal of Thermal Sciences*, 41(10):961–1016, October 2002. ISSN 12900729. doi: 10.1016/S1290-0729(02)01374-1. URL <https://linkinghub.elsevier.com/retrieve/pii/S1290072902013741>.

Xavier Nicolas, Shihe Xin, and Noussaiba Zoueidi. Characterisation of a Wavy Convective Instability in Poiseuille-Rayleigh-Be'nard Flows: Linear Stability Analysis and Non Linear Numerical Simulations Under Random Excitations. In *2010 14th International Heat Transfer Conference, Volume 7*, pages 203–208, Washington, DC, USA, January 2010. ASMEDC. ISBN 978-0-7918-4942-2 978-0-7918-3879-2. doi: 10.1115/IHTC14-22256. URL <https://asmedigitalcollection.asme.org/IHTC/proceedings/IHTC14/49422/203/360332>.

Xavier Nicolas, Noussaiba Zoueidi, and Shihe Xin. Influence of a white noise at channel inlet on the parallel and wavy convective instabilities of Poiseuille-Rayleigh-Bénard flows. *Physics of Fluids*, 24(8):084101, August 2012. ISSN 1070-6631, 1089-7666. doi: 10.1063/1.4737652. URL <https://pubs.aip.org/pof/article/24/8/084101/258132/Influence-of-a-white-noise-at-channel-inlet-on-the>.

William M'F. Orr. The Stability or Instability of the Steady Motions of a Perfect Liquid and of a Viscous Liquid. Part II: A Viscous Liquid. *Proceedings of the Royal Irish Academy. Section A: Mathematical and Physical Sciences*, 27:69–138, 1907. ISSN 00358975. URL <http://www.jstor.org/stable/20490591>. Publisher: Royal Irish Academy.

Steven A. Orszag. Accurate solution of the Orr–Sommerfeld stability equation. *Journal of Fluid Mechanics*, 50(4):689–703, December 1971. ISSN 0022-1120, 1469-7645. doi: 10.1017/S0022112071002842. URL https://www.cambridge.org/core/product/identifier/S0022112071002842/type/journal_article.

Steven A. Orszag, Moshe Israeli, and Michel O. Deville. Boundary conditions for incompressible flows. *Journal of Scientific Computing*, 1(1):75–111, 1986. ISSN 0885-7474, 1573-7691. doi: 10.1007/BF01061454. URL <http://link.springer.com/10.1007/BF01061454>.

S. Ostrach and Y. Kamotani. Heat Transfer Augmentation in Laminar Fully Developed Channel Flow by Means of Heating From Below. *Journal of Heat Transfer*, 97(2):220–225, May 1975. ISSN 0022-1481, 1528-8943. doi: 10.1115/1.3450344. URL <https://asmedigitalcollection.asme.org/heattransfer/article/97/2/220/416581/Heat-Transfer-Augmentation-in-Laminar-Fully>.

MT Ouazzani, Jean-Paul Caltagirone, Gilles Meyer, and Abdelkader Mojtabi. Etude numerique et expérimentale de la convection mixte entre deux plans horizontaux à températures différentes.

International journal of heat and mass transfer, 32(2):261–269, 1989. ISSN 0017-9310. Publisher: Elsevier.

MT Ouazzani, Jean Karl Platten, and Abdelkader Mojtabi. Etude expérimentale de la convection mixte entre deux plans horizontaux à températures différentes—II. *International journal of heat and mass transfer*, 33(7):1417–1427, 1990. ISSN 0017-9310. Publisher: Elsevier.

Hervé Pabiou, Xavier Nicolas, Shihe Xin, and Sophie Mergui. Observations d'une instabilité convective apparaissant sous la forme de rouleaux sinueux dans un écoulement de Poiseuille–Rayleigh–Bénard. *Mécanique & industries*, 4(5):537–543, 2003. ISSN 1296-2139. Publisher: Elsevier.

Hervé Pabiou, Sophie Mergui, and Christine Bénard. Wavy secondary instability of longitudinal rolls in RayleighPoiseuille flows. *Journal of Fluid Mechanics*, 542(-1):175, October 2005. ISSN 0022-1120, 1469-7645. doi: 10.1017/S0022112005006154. URL http://www.journals.cambridge.org/abstract_S0022112005006154.

Chaitanya S Paranjape. Onset of turbulence in plane Poiseuille flow. 2019. Publisher: IST Austria Klosterneuburg, Austria.

Chaitanya S. Paranjape, Yohann Duguet, and Björn Hof. Oblique stripe solutions of channel flow. *Journal of Fluid Mechanics*, 897:A7, August 2020. ISSN 0022-1120, 1469-7645. doi: 10.1017/jfm.2020.322. URL https://www.cambridge.org/core/product/identifier/S0022112020003225/type/journal_article.

Chaitanya S. Paranjape, Gökhan Yalnız, Yohann Duguet, Nazmi Burak Budanur, and Björn Hof. Direct Path from Turbulence to Time-Periodic Solutions. *Physical Review Letters*, 131(3):034002, July 2023. ISSN 0031-9007, 1079-7114. doi: 10.1103/PhysRevLett.131.034002. URL <https://link.aps.org/doi/10.1103/PhysRevLett.131.034002>.

V. C. Patel and M. R. Head. Some observations on skin friction and velocity profiles in fully developed pipe and channel flows. *Journal of Fluid Mechanics*, 38(1):181–201, August 1969. ISSN 0022-1120, 1469-7645. doi: 10.1017/S0022112069000115. URL https://www.cambridge.org/core/product/identifier/S0022112069000115/type/journal_article.

Anthony T Patera. A spectral element method for fluid dynamics: Laminar flow in a channel expansion. *Journal of Computational Physics*, 54(3):468–488, June 1984. ISSN 00219991. doi: 10.1016/0021-9991(84)90128-1. URL <https://linkinghub.elsevier.com/retrieve/pii/0021999184901281>.

M. R. Paul, M. I. Einarsson, P. F. Fischer, and M. C. Cross. Extensive chaos in Rayleigh-Bénard convection. *Physical Review E*, 75(4):045203, April 2007. ISSN 1539-3755, 1550-2376. doi: 10.1103/PhysRevE.75.045203. URL <https://link.aps.org/doi/10.1103/PhysRevE.75.045203>.

M.R. Paul, K.-H. Chiam, M.C. Cross, P.F. Fischer, and H.S. Greenside. Pattern formation and dynamics in Rayleigh–Bénard convection: numerical simulations of experimentally realistic geometries. *Physica D: Nonlinear Phenomena*, 184(1-4):114–126, October 2003. ISSN 01672789. doi: 10.1016/S0167-2789(03)00216-1. URL <https://linkinghub.elsevier.com/retrieve/pii/S0167278903002161>.

Anne Pellew and Richard Vynne Southwell. On maintained convective motion in a fluid heated from below. *Proceedings of the Royal Society of London. Series A. Mathematical and Physical Sciences*, 176(966):312–343, November 1940. ISSN 0080-4630, 2053-9169. doi: 10.1098/rspa.1940.0092. URL <https://royalsocietypublishing.org/doi/10.1098/rspa.1940.0092>.

Sergio Pirozzoli, Matteo Bernardini, Roberto Verzicco, and Paolo Orlandi. Mixed convection in turbulent channels with unstable stratification. *Journal of Fluid Mechanics*, 821:482–516, June 2017. ISSN 0022-1120, 1469-7645. doi: 10.1017/jfm.2017.216. URL https://www.cambridge.org/core/product/identifier/S0022112017002166/type/journal_article.

Brendan B Plapp and Eberhard Bodenschatz. Core dynamics of multi-armed spirals in Rayleigh–Bénard convection. *Physica Scripta*, T67:111–116, January 1996. ISSN 0031-8949, 1402-4896. doi: 10.1088/0031-8949/1996/T67/022. URL <https://iopscience.iop.org/article/10.1088/0031-8949/1996/T67/022>.

Brendan B. Plapp, David A. Egolf, Eberhard Bodenschatz, and Werner Pesch. Dynamics and Selection of Giant Spirals in Rayleigh-Bénard Convection. *Physical Review Letters*, 81(24):5334–5337, December 1998. ISSN 0031-9007, 1079-7114. doi: 10.1103/PhysRevLett.81.5334. URL <https://link.aps.org/doi/10.1103/PhysRevLett.81.5334>.

Brendan Bryce Plapp. Spiral pattern formation in Rayleigh-Benard convection. *Ph.D. Thesis*, page 3118, December 1997. URL <https://ui.adsabs.harvard.edu/abs/1997PhDT.....105P>.

A. Prigent and O. Dauchot. "Barber pole turbulence" in large aspect ratio Taylor-Couette flow. *Physical Review Letters*, 89(1):014501, June 2002. ISSN 0031-9007, 1079-7114. doi: 10.1103/PhysRevLett.89.014501. URL <http://arxiv.org/abs/cond-mat/0009241>. arXiv:cond-mat/0009241.

Arnaud Prigent, Guillaume Grégoire, Hugues Chaté, and Olivier Dauchot. Long-wavelength modulation of turbulent shear flows. *Physica D: Nonlinear Phenomena*, 174(1-4):100–113, January 2003. ISSN 01672789. doi: 10.1016/S0167-2789(02)00685-1. URL <https://linkinghub.elsevier.com/retrieve/pii/S0167278902006851>.

Subhashis Ray and J. Srinivasan. Analysis of conjugate laminar mixed convection cooling in a shrouded array of electronic components. *International Journal of Heat and Mass Transfer*, 35(4):815–822, April 1992. ISSN 00179310. doi: 10.1016/0017-9310(92)90249-R. URL <https://linkinghub.elsevier.com/retrieve/pii/001793109290249R>.

Lord Rayleigh. LIX. *On convection currents in a horizontal layer of fluid, when the higher temperature is on the under side.* *The London, Edinburgh, and Dublin Philosophical Magazine and Journal of Science*, 32(192):529–546, December 1916. ISSN 1941-5982, 1941-5990. doi: 10.1080/14786441608635602. URL <https://www.tandfonline.com/doi/full/10.1080/14786441608635602>.

Satish C. Reddy and Dan S. Henningson. Energy growth in viscous channel flows. *Journal of Fluid Mechanics*, 252:209–238, July 1993. ISSN 0022-1120, 1469-7645. doi: 10.1017/S0022112093003738. URL https://www.cambridge.org/core/product/identifier/S0022112093003738/type/journal_article.

Satish C. Reddy, Peter J. Schmid, and Dan S. Henningson. Pseudospectra of the Orr–Sommerfeld Operator. *SIAM Journal on Applied Mathematics*, 53(1):15–47, February 1993. ISSN 0036-1399, 1095-712X. doi: 10.1137/0153002. URL <http://pubs.siam.org/doi/10.1137/0153002>.

Florian Reetz and Tobias M. Schneider. Invariant states in inclined layer convection. Part 1. Temporal transitions along dynamical connections between invariant states. *Journal of Fluid Mechanics*, 898:A22, September 2020. ISSN 0022-1120, 1469-7645. doi: 10.1017/jfm.2020.317. URL https://www.cambridge.org/core/product/identifier/S0022112020003171/type/journal_article.

Florian Reetz, Tobias Kreilos, and Tobias M. Schneider. Exact invariant solution reveals the origin of self-organized oblique turbulent-laminar stripes. *Nature Communications*, 10(1):2277, May 2019. ISSN 2041-1723. doi: 10.1038/s41467-019-10208-x. URL <https://doi.org/10.1038/s41467-019-10208-x>.

Florian Reetz, Priya Subramanian, and Tobias M. Schneider. Invariant states in inclined layer convection. Part 2. Bifurcations and connections between branches of invariant states. *Journal of Fluid Mechanics*, 898:A23, September 2020. ISSN 0022-1120, 1469-7645. doi: 10.1017/jfm.2020.318. URL https://www.cambridge.org/core/product/identifier/S0022112020003183/type/journal_article.

Osborne Reynolds. XXIX. An experimental investigation of the circumstances which determine whether the motion of water shall be direct or sinuous, and of the law of resistance in parallel channels. *Philosophical Transactions of the Royal Society of London*, 174:935–982, December 1883. ISSN 0261-0523, 2053-9223. doi: 10.1098/rstl.1883.0029. URL <https://royalsocietypublishing.org/doi/10.1098/rstl.1883.0029>.

Osborne Reynolds. IV. On the dynamical theory of incompressible viscous fluids and the determination of the criterion. *Philosophical Transactions of the Royal Society of London*. (A.), 186:123–164, December 1895. ISSN 0264-3820, 2053-9231. doi: 10.1098/rsta.1895.0004. URL <https://royalsocietypublishing.org/doi/10.1098/rsta.1895.0004>.

Gabriele Rocco. Advanced Instability Methods using Spectral/hp Discretisations and their Applications to Complex Geometries. 2014.

H. T. Rossby. A study of Bénard convection with and without rotation. *Journal of Fluid Mechanics*, 36(2):309–335, April 1969. ISSN 0022-1120, 1469-7645. doi: 10.1017/S0022112069001674. URL https://www.cambridge.org/core/product/identifier/S0022112069001674/type/journal_article.

Sten Rüdiger and Fred Feudel. Pattern formation in Rayleigh-Bénard convection in a cylindrical container. *Physical Review E*, 62(4):4927–4931, October 2000. ISSN 1063-651X, 1095-3787. doi: 10.1103/PhysRevE.62.4927. URL <https://link.aps.org/doi/10.1103/PhysRevE.62.4927>.

A. Scagliarini, H. Einarsson, Á. Gylfason, and F. Toschi. Law of the wall in an unstably stratified turbulent channel flow. *Journal of Fluid Mechanics*, 781:R5, October 2015. ISSN 0022-1120, 1469-7645. doi: 10.1017/jfm.2015.498. URL https://www.cambridge.org/core/product/identifier/S002211201500498X/type/journal_article.

Andrea Scagliarini, Armann Gylfason, and Federico Toschi. Heat flux scaling in turbulent Rayleigh-Bénard convection with an imposed longitudinal wind. *Physical Review E*, 89(4):043012, April 2014. ISSN 1539-3755, 1550-2376. doi: 10.1103/PhysRevE.89.043012. URL <http://arxiv.org/abs/1311.4598>. arXiv:1311.4598 [physics].

H. Schlichting. Zur Entstehung der Turbulenz bei der Plattenströmung. *Nachrichten von der Gesellschaft der Wissenschaften zu Göttingen, Mathematisch-Physikalische Klasse*, 1933:181–208, 1933. URL <http://eudml.org/doc/59420>.

Hermann Schlichting and Klaus Gersten. Onset of Turbulence (Stability Theory). In *Boundary-Layer Theory*, pages 415–496. Springer Berlin Heidelberg, Berlin, Heidelberg, 2017. ISBN 978-3-662-52917-1 978-3-662-52919-5. doi: 10.1007/978-3-662-52919-5_15. URL http://link.springer.com/10.1007/978-3-662-52919-5_15.

A. Schlüter, D. Lortz, and F. Busse. On the stability of steady finite amplitude convection. *Journal of Fluid Mechanics*, 23(01):129, September 1965. ISSN 0022-1120, 1469-7645. doi: 10.1017/S0022112065001271. URL http://www.journals.cambridge.org/abstract_S0022112065001271.

Peter J. Schmid. Nonmodal Stability Theory. *Annual Review of Fluid Mechanics*, 39(1):129–162, January 2007. ISSN 0066-4189, 1545-4479. doi: 10.1146/annurev.fluid.38.050304.092139. URL <https://www.annualreviews.org/doi/10.1146/annurev.fluid.38.050304.092139>.

Peter J. Schmid and Dan S. Henningson. *Stability and Transition in Shear Flows*, volume 142 of *Applied Mathematical Sciences*. Springer New York, New York, NY, 2001. ISBN 978-1-4612-6564-1 978-1-4613-0185-1. doi: 10.1007/978-1-4613-0185-1. URL <http://link.springer.com/10.1007/978-1-4613-0185-1>.

Rainer Schmitz, Werner Pesch, and Walter Zimmermann. Spiral-defect chaos: Swift-Hohenberg model versus Boussinesq equations. *Physical Review E*, 65(3):037302, March 2002. ISSN 1063-651X, 1095-3787. doi: 10.1103/PhysRevE.65.037302. URL <https://link.aps.org/doi/10.1103/PhysRevE.65.037302>.

Tobias M. Schneider, Bruno Eckhardt, and James A. Yorke. Turbulence transition and the edge of chaos in pipe flow. *Physical Review Letters*, 99(3):034502, July 2007. ISSN 0031-9007, 1079-7114. doi: 10.1103/PhysRevLett.99.034502. URL <http://arxiv.org/abs/nlin/0703067>. arXiv:nlin/0703067.

Masaki Shimizu and Paul Manneville. Bifurcations to turbulence in transitional channel flow. *Physical Review Fluids*, 4(11):113903, November 2019. doi: 10.1103/PhysRevFluids.4.113903. URL <https://link.aps.org/doi/10.1103/PhysRevFluids.4.113903>. Publisher: American Physical Society.

Jennifer H. Siggers. Dynamics of target patterns in low-Prandtl-number convection. *Journal of Fluid Mechanics*, 475:357–375, January 2003. ISSN 0022-1120, 1469-7645. doi: 10.1017/S0022112002002896. URL https://www.cambridge.org/core/product/identifier/S0022112002002896/type/journal_article.

Joseph D. Skufca, James A. Yorke, and Bruno Eckhardt. Edge of Chaos in a Parallel Shear Flow. *Physical Review Letters*, 96(17):174101, May 2006. ISSN 0031-9007, 1079-7114. doi: 10.1103/PhysRevLett.96.174101. URL <https://link.aps.org/doi/10.1103/PhysRevLett.96.174101>.

Arnold Sommerfeld. *Ein Beitrag zur hydrodynamischen Erklarung der turbulenten Flussigkeitsbewegungen*. 1909.

Baofang Song, Dwight Barkley, Bjorn Hof, and Marc Avila. Speed and structure of turbulent fronts in pipe flow. *Journal of Fluid Mechanics*, 813:1045–1059, February 2017. ISSN 0022-1120, 1469-7645. doi: 10.1017/jfm.2017.14. URL https://www.cambridge.org/core/product/identifier/S0022112017000143/type/journal_article.

Herbert Brian Squire. On the stability for three-dimensional disturbances of viscous fluid flow between parallel walls. *Proceedings of the Royal Society of London. Series A, Containing Papers of a Mathematical and Physical Character*, 142(847):621–628, November 1933. ISSN 0950-1207, 2053-9150. doi: 10.1098/rspa.1933.0193. URL <https://royalsocietypublishing.org/doi/10.1098/rspa.1933.0193>.

J. Swift and P. C. Hohenberg. Hydrodynamic fluctuations at the convective instability. *Physical Review A*, 15(1):319–328, January 1977. ISSN 0556-2791. doi: 10.1103/PhysRevA.15.319. URL <https://link.aps.org/doi/10.1103/PhysRevA.15.319>.

J. J. Tao, Bruno Eckhardt, and X. M. Xiong. Extended localized structures and the onset of turbulence in channel flow. *Physical Review Fluids*, 3(1):011902, January 2018. doi: 10.1103/PhysRevFluids.3.

011902. URL <https://link.aps.org/doi/10.1103/PhysRevFluids.3.011902>. Publisher: American Physical Society.

Vassilios Theofilis. Advances in global linear instability analysis of nonparallel and three-dimensional flows. *Progress in Aerospace Sciences*, 39(4):249–315, May 2003. ISSN 03760421. doi: 10.1016/S0376-0421(02)00030-1. URL <https://linkinghub.elsevier.com/retrieve/pii/S0376042102000301>.

W. Tollmien. Über die Entstehung der Turbulenz. 1. Mitteilung. *Nachrichten von der Gesellschaft der Wissenschaften zu Göttingen, Mathematisch-Physikalische Klasse*, 1929:21–44, 1928. URL <http://eudml.org/doc/59276>.

Lloyd N. Trefethen. Pseudospectra of Linear Operators. *SIAM Review*, 39(3):383–406, January 1997. ISSN 0036-1445, 1095-7200. doi: 10.1137/S0036144595295284. URL <http://pubs.siam.org/doi/10.1137/S0036144595295284>.

Takahiro Tsukahara, Kaoru Iwamoto, Hiroshi Kawamura, and Tetsuaki Takeda. DNS of heat transfer in a transitional channel flow accompanied by a turbulent puff-like structure, September 2014a. URL <http://arxiv.org/abs/1406.0586>. arXiv:1406.0586 [physics].

Takahiro Tsukahara, Yasuo Kawaguchi, and Hiroshi Kawamura. An experimental study on turbulent-stripe structure in transitional channel flow, 2014b. URL <https://arxiv.org/abs/1406.1378>. Version Number: 2.

Takahiro Tsukahara, Yohji Seki, Hiroshi Kawamura, and Daisuke Tochio. DNS of turbulent channel flow at very low Reynolds numbers, September 2014c. URL <http://arxiv.org/abs/1406.0248>. arXiv:1406.0248 [physics].

Laurette S. Tuckerman and Dwight Barkley. Global Bifurcation to Traveling Waves in Axisymmetric Convection. *Physical Review Letters*, 61(4):408–411, July 1988. ISSN 0031-9007. doi: 10.1103/PhysRevLett.61.408. URL <https://link.aps.org/doi/10.1103/PhysRevLett.61.408>.

Laurette S. Tuckerman and Dwight Barkley. Bifurcation Analysis for Timesteppers. In *Numerical Methods for Bifurcation Problems and Large-Scale Dynamical Systems*, volume 119, pages 453–466. Springer New York, New York, NY, 2000. ISBN 978-1-4612-7044-7 978-1-4612-1208-9. doi: 10.1007/978-1-4612-1208-9_20. URL http://link.springer.com/10.1007/978-1-4612-1208-9_20. Series Title: The IMA Volumes in Mathematics and its Applications.

Laurette S Tuckerman and Dwight Barkley. Patterns and dynamics in transitional plane Couette flow. *Physics of Fluids*, 23(4), 2011. ISSN 1070-6631. Publisher: AIP Publishing.

Laurette S. Tuckerman, Tobias Kreilos, Hecke Schrobsdorff, Tobias M. Schneider, and John F. Gibson. Turbulent-laminar patterns in plane Poiseuille flow. *Physics of Fluids*, 26(11):114103, November 2014. ISSN 1070-6631, 1089-7666. doi: 10.1063/1.4900874. URL <https://pubs.aip.org/pof/article/26/11/114103/315350/Turbulent-laminar-patterns-in-plane-Poiseuille>.

R. Témam. Sur l'approximation de la solution des équations de Navier-Stokes par la méthode des pas fractionnaires (II). *Archive for Rational Mechanics and Analysis*, 33(5):377–385, January 1969. ISSN 0003-9527, 1432-0673. doi: 10.1007/BF00247696. URL <http://link.springer.com/10.1007/BF00247696>.

Geoffrey K. Vallis, Douglas J. Parker, and Steven M. Tobias. A simple system for moist convection: the Rainy–Bénard model. *Journal of Fluid Mechanics*, 862:162–199, March 2019. ISSN 0022-1120, 1469-7645. doi: 10.1017/jfm.2018.954. URL https://www.cambridge.org/core/product/identifier/S0022112018009540/type/journal_article.

Milton Van Dyke and Milton Van Dyke. *An album of fluid motion*, volume 176. Parabolic Press Stanford, 1982.

D. Viswanath. Recurrent motions within plane Couette turbulence. *Journal of Fluid Mechanics*, 580:339–358, June 2007. ISSN 0022-1120, 1469-7645. doi: 10.1017/S0022112007005459. URL https://www.cambridge.org/core/product/identifier/S0022112007005459/type/journal_article.

Eduardo Vitral, Saikat Mukherjee, Perry H. Leo, Jorge Viñals, Mark R. Paul, and Zhi-Feng Huang. Spiral defect chaos in Rayleigh-Bénard convection: Asymptotic and numerical studies of azimuthal flows induced by rotating spirals. *Physical Review Fluids*, 5(9):093501, September 2020. ISSN 2469-990X. doi: 10.1103/PhysRevFluids.5.093501. URL <https://link.aps.org/doi/10.1103/PhysRevFluids.5.093501>.

Fabian Waleffe. Exact coherent structures in channel flow. *Journal of Fluid Mechanics*, 435:93–102, May 2001. ISSN 0022-1120, 1469-7645. doi: 10.1017/S0022112001004189. URL https://www.cambridge.org/core/product/identifier/S0022112001004189/type/journal_article.

Fabian Waleffe. Homotopy of exact coherent structures in plane shear flows. *Physics of Fluids*, 15(6):1517–1534, June 2003. ISSN 1070-6631, 1089-7666. doi: 10.1063/1.1566753. URL <https://pubs.aip.org/pof/article/15/6/1517/448391/Homotopy-of-exact-coherent-structures-in-plane>.

José Eduardo Wesfreid. Henri Bénard: Thermal convection and vortex shedding. *Comptes Rendus. Mécanique*, 345(7):446–466, June 2017. ISSN 1873-7234. doi: 10.1016/j.crme.2017.06.006. URL <https://comptes-rendus.academie-sciences.fr/mecanique/articles/10.1016/j.crme.2017.06.006/>.

G. E. Willis and J. W. Deardorff. The oscillatory motions of Rayleigh convection. *Journal of Fluid Mechanics*, 44(04):661, December 1970. ISSN 0022-1120, 1469-7645. doi: 10.1017/S0022112070002070. URL http://www.journals.cambridge.org/abstract_S0022112070002070.

Hao-wen Xi, J. D. Gunton, and Jorge Viñals. Spiral defect chaos in a model of Rayleigh-Bénard convection. *Physical Review Letters*, 71(13):2030–2033, September 1993. ISSN 0031-9007. doi: 10.1103/PhysRevLett.71.2030. URL <https://link.aps.org/doi/10.1103/PhysRevLett.71.2030>.

Haowen Xi and J. D. Gunton. Spatiotemporal chaos in a model of Rayleigh-Bénard convection. *Physical Review E*, 52(5):4963–4975, November 1995. ISSN 1063-651X, 1095-3787. doi: 10.1103/PhysRevE.52.4963. URL <https://link.aps.org/doi/10.1103/PhysRevE.52.4963>.

Xiangkai Xiao and Baofang Song. The growth mechanism of turbulent bands in channel flow at low Reynolds numbers. *Journal of Fluid Mechanics*, 883:R1, January 2020. ISSN 0022-1120, 1469-7645. doi: 10.1017/jfm.2019.899. URL https://www.cambridge.org/core/product/identifier/S0022112019008991/type/journal_article.

Shihe Xin, Xavier Nicolas, and Patrick Le Quéré. Stability analyses of Longitudinal Rolls of Poiseuille-Rayleigh-Bénard Flows in Air-Filled Channels of Finite Transversal Extension. *Numerical Heat Transfer, Part A: Applications*, 50(5):467–490, July 2006. ISSN 1040-7782, 1521-0634. doi: 10.1080/10407780600620079. URL <http://www.tandfonline.com/doi/abs/10.1080/10407780600620079>.

Xiangming Xiong, Jianjun Tao, Shiyi Chen, and Luca Brandt. Turbulent bands in plane-Poiseuille flow at moderate Reynolds numbers. *Physics of Fluids*, 27(4):041702, April 2015. ISSN 1070-6631, 1089-7666. doi: 10.1063/1.4917173. URL <https://pubs.aip.org/pof/article/27/4/041702/1019208/Turbulent-bands-in-plane-Poiseuille-flow-at>.